

2015

Advanced transition metal oxide materials as electrodes for lithium ion batteries

Mohammad Ihsan
University of Wollongong

Follow this and additional works at: <https://ro.uow.edu.au/theses>

University of Wollongong

Copyright Warning

You may print or download ONE copy of this document for the purpose of your own research or study. The University does not authorise you to copy, communicate or otherwise make available electronically to any other person any copyright material contained on this site.

You are reminded of the following: This work is copyright. Apart from any use permitted under the Copyright Act 1968, no part of this work may be reproduced by any process, nor may any other exclusive right be exercised, without the permission of the author. Copyright owners are entitled to take legal action against persons who infringe their copyright. A reproduction of material that is protected by copyright may be a copyright infringement. A court may impose penalties and award damages in relation to offences and infringements relating to copyright material.

Higher penalties may apply, and higher damages may be awarded, for offences and infringements involving the conversion of material into digital or electronic form.

Unless otherwise indicated, the views expressed in this thesis are those of the author and do not necessarily represent the views of the University of Wollongong.

Recommended Citation

Ihsan, Mohammad, Advanced transition metal oxide materials as electrodes for lithium ion batteries, Doctor of Philosophy thesis, Institute for Superconducting and Electronic Materials, University of Wollongong, 2015. <https://ro.uow.edu.au/theses/4601>



Innovative silicon detectors for dosimetry in external beam radiotherapy

This thesis is presented as part of the requirements for the
Award of the Degree of
Doctor of Philosophy

From

University of Wollongong

By

Abdullah Hamad A Aldosari
BSc. and MSc. MedPhys

Centre for Medical Radiation Physics, Engineering Physics
Faculty of Engineering and Information Sciences

2015

ABSTRACT

Silicon diodes have been widely used in radiation therapy quality assurance applications because they have a number of attractive qualities, including real-time feedback (compared to film), high spatial resolution, high linearity, radiation hardness and a small size (compared to ionisation chambers). This work describes three dosimetry systems based on silicon detectors that were developed and manufactured at the Centre for Medical Radiation Physics for Quality Assurance in external beam radiation therapy.

The first part of this study is focused on the characterisation of a single pad detector based on a p-type silicon epitaxial layer, used to assemble a 2-D array of diodes, named MagicPlate-121, for dosimetry and fluence measurement of MV photon beams. The single detector has been tested in terms of radiation hardness and its radiation damage mechanism simulated by Technology CAD modelling. The epitaxial detectors were readout by the TERA, application-specific integrated circuit chip designed for ion chambers. The detector showed unusual total dose radiation response as a function of the irradiation dose, and also showed stabilization of the response within $\pm 2.5\%$ for 12 kGy of gamma irradiation dose (Co-60). The photoneutron radiation damage was also tested and showed a decreased response within 0.5%/100 Gy. The EPI detector demonstrated high radiation hardness for used in clinical quality assurance (QA).

The second detector tested in this work is a monolithic two-dimensional array silicon detector called MagicPlate-512 (MP512). The MP512 was designed for small field beams and consisted of 512 pixels implanted on a p-type substrate, with the size of each pixel being $0.5 \times 0.5 \text{ mm}^2$. The radiation hardness characterisation by photons

and photoneutrons of the MP samples were tested and showed $\pm 5\%$ of response stabilization and decreased response due to photoneutrons within 2.6%/300 Gy. The MP512 was employed to measure the dose distribution in a solid water phantom and has been successfully characterised for QA in stereotactic body radiation therapy and stereotactic radiosurgery for beam sizes down to $0.5 \times 0.5 \text{ cm}^2$. SBRT and SRS treatments are modalities which require rotation of the beam around the patient for a full plan delivery. Therefore, in such modalities, it is important to characterise a detector also in terms of angular dependence. The intrinsic angular dependence of monolithic silicon devices such as MP512 has been minimised by building a cylindrical phantom which automatically align MP512 and keep the detector plane perpendicular to the irradiation beam. The design principles and the characterization of the phantom are presented with an experimental evaluation of its performance in terms of alignment with the rotating LINAC and bidirectional positioning accuracy which is ± 1 degree and ± 0.25 degree, respectively. The MP512 was successfully used in combination with the Radiofrequency tracking system named Calypso to measure dose distribution in different modalities (no motion, motion, and motion with a dynamic multileaf collimator tracking system) and compared with EBT3 film. Further, a dynamic wedge study was performed and dose distribution measured by the MP512 and by EBT3 film for comparison. Excellent agreement has been found with a discrepancy between MP512 and EBT3 film of less than 2% across the whole dynamic wedge profile.

The third detector tested in this thesis was the 'DUO', which contained 512 phosphorous ion implanted microstrips on a p-type silicon substrate. The total area of the silicon was $52 \times 52 \text{ mm}^2$, with $200 \text{ }\mu\text{m}$ strip pitch. The radiation hardness characterisation has been carried out by irradiation by photons and photoneutrons

and the response showed stabilization at 120 kGy of gamma irradiation dose (Co-60). The photoneutron damage was also tested and showed a decreased response within 11%/300 Gy.

DECLARATION OF ORIGINALITY

I, Abdullah Hamad Aldosari, declare that this thesis, submitted in fulfilment of the requirements for the award of Doctor of Philosophy, in the Centre for Medical Radiation Physics, Engineering and Information Sciences, University of Wollongong, is wholly my own work, unless otherwise referenced or acknowledged. The document has not been submitted for qualification at any other academic institution.

Abdullah Hamad A Aldosari

On: 04 March 2015

ACKNOWLEDGEMENTS

I wish to acknowledge all those who have supported and assisted me in the process of researching and completed my PhD. I would like to make the following particular acknowledgments.

First of all, Dr. Marco Petasecca has been my main supervisor. I extend my deepest thanks and appreciation to Dr. Marco who not only monitored me with constructive advice and generous time, but also with valued friendship and respect.

My thanks also to Professor Anatoly Rosenfeld, who has generously and consistently offered insightful and significant advice and guidance to my research. Professor Anatoly Rosenfeld is a wonderful mentor and supervisor.

I thank Associate Professor Michael Lerch, who also contributed support, advice and assistance to my project. Dr. Martin Carolan, Chief Physicist Illawarra Cancer Care Centre Wollongong Hospital, must be also acknowledge for his generous contribution of his time, advice and support.

I also extend thanks to my colleagues Mathew Newall, who shared, consulted and assisted me. Lolanda Fuduli, Anthony Espinoza and Sami Alshaika, I also acknowledge for their support and assistance.

My thanks also to the Saudi Arabia government for the financial support and Saudi Arabian Cultural Mission in Australia. I thank my family in Saudi Arabia for their support, love and encouragement.

My final acknowledgements and deepest thanks must be to my wife for her patient, support in every way, over these past six years.

This work is also dedicated to the spirit of my father, who was the first encourager and supporter to me in continuing my education.

CONTENTS

ABSTRACT	i
DECLARATION OF ORIGINALITY	iv
ACKNOWLEDGEMENTS.....	v
CONTENTS.....	vi
LIST OF FIGURES	xi
LIST OF TABLES	xvi
PEER REVIEWED JOURNAL PAPERS AND CONFERENCE PROCEEDINGS	xvii
LIST OF ABBREVIATIONS	xix
CHAPTER 1: INTRODUCTION.....	1
1.1 Introduction	1
1.2 Project goals	2
CHAPTER 2: LITERATURE REVIEW.....	4
2.1 Radiation therapy	4
2.1.1 IMRT.....	5
2.1.2 VMAT	6
2.1.3 SRT: SBRT and SRS	6
2.2 QA for SBRT and SRS requirements.....	8
2.2.1 Optimal specification of a 2-D dosimeter array for SRT	12
2.3 Organ movement and its management	13
2.3.1 Strategies to reduce motion effects	14
2.4 Radiation dosimetry and current QA of contemporary radiotherapy.....	17
2.4.1 Point dosimeters	18
2.4.1.1 <i>Ionisation chamber</i>	18
2.4.1.2 <i>Fibre optics dosimeters</i>	19
2.4.1.3 <i>Diamond dosimeter</i>	19
2.4.2 2-D dosimetry	20
2.4.2.1 <i>Film dosimeters</i>	21
2.4.2.2 <i>IC array</i>	21
2.4.2.3 <i>I'mRT MatriXX</i>	22
2.4.3 3-D dosimetry	22
2.4.3.1 <i>PRESAGE dosimeters</i>	23
2.4.4 Dosimetric verification of a DMLC.....	24
2.4.5 Summary	24
2.5 Silicon detectors can work as dosimeters for MV radiotherapy	27
2.5.1 2-D Silicon dosimeters.....	30
2.5.1.1 <i>MapCheck</i>	30
2.5.1.2 <i>MP121</i>	30
2.5.1.3 <i>Silicon segmented detector</i>	31
2.5.1.4 <i>Single-sided silicon strip detector</i>	31
2.5.2 3-D Silicon dosimeters.....	32
2.5.2.1 <i>Delta4</i>	32
2.5.2.2 <i>ArcCHECK</i>	32

2.6 Silicon detector limitations	33
2.7 Radiation damage in silicon	33
2.7.1 Silicon radiation detectors: radiation hardness and sensitivity variation ..	33
2.7.2 Bulk damage	38
2.7.3 Changing the detector properties	41
2.7.3.1 <i>Leakage current</i>	41
2.7.3.2 <i>Effective doping concentration (N_{eff})</i>	41
2.7.3.3 <i>Charge collection efficiency—trapping</i>	42
2.7.4 Surface damage	42
2.7.5 Photoneutron damage	44
2.8 CMRP semiconductor dosimetry solutions	45
CHAPTER 3: CHARACTERISING AN INNOVATIVE P-TYPE	
EPITAXIAL DIODE FOR DOSIMETRY IN MODERN EBRT	46
3.1 Introduction	46
3.2 Materials and methods	46
3.2.1 Design and fabrication	46
3.2.2 Detector packaging	47
3.2.3 TERA readout system	48
3.2.3.1 <i>Brief description of how TERA works</i>	49
3.2.3.2 <i>DAQ</i>	52
3.3 Pre-irradiation characterisation	53
3.3.1 Current-voltage characteristics	53
3.3.2 Experimental methods	55
3.3.3 Capacitance-voltage characteristics	57
3.3.4 Experimental methods	57
3.3.5 Diode response measurements	58
3.3.6 Radiation hardness characterisation	59
3.3.6.1 <i>Introduction</i>	59
3.3.6.2 <i>Radiation hardness study by photoneutrons</i>	60
3.3.7 Simulation	61
3.3.7.1 <i>Introduction</i>	61
3.3.7.2 <i>Detector simulation</i>	61
3.4 Results	63
3.4.1 Electrical characteristics	63
3.4.2 Damage rate calculation (α)	67
3.4.3 CCE	68
3.4.4 Radiation damage by 18 MV photon beam	74
3.5 Conclusion	75
CHAPTER 4: RADIATION HARDNESS FOR 2-D SILICON DIODE	
ARRAY (MP512) USED IN EBRT	76
4.1 Introduction	76
4.2 Materials and methods	76
4.2.1 MP512 array design and fabrication	76
4.2.2 Test structures design and fabrication	78
4.2.3 Readout system	80
4.2.4 I-V characteristics for test structure and MP512	80
4.2.5 Experimental method	80
4.2.6 C-V characteristics	83
4.2.7 Radiation hardness characterisation	84

4.2.7.1 Radiation hardness study by photons and photoneutrons for test structures	84
4.2.7.2 Photon damage—experimental method	85
4.2.7.3 Photoneutron damage—experimental method	85
4.2.7.4 Radiation hardness study by photons and photoneutrons for MP array (MP512)—experimental method	86
4.3 Results	87
4.3.1 Electrical and I-V characteristics for test structure	87
4.3.2 Electrical characterisation of MP512 full array	90
4.3.3 Capacitance characteristics (C-V) of test structures	92
4.3.4 Radiation damage for test structures and MP	99
4.3.4.1 Photon damage for test structure	99
4.3.4.2 Photoneutron damage for test structure	99
4.3.4.3 Photon damage for MP512 array	102
4.3.4.4 Photoneutron damage for MP512 array	105
4.4 Conclusion	106
CHAPTER 5: A TWO DIMENSIONAL SILICON DETECTORS ARRAY FOR QUALITY ACCURANCE IN SBRT—MAGICPLATE-512	109
5.1 Introduction	109
5.2 Materials and methods	109
5.2.1 MP detector array	109
5.2.2 DAQ	109
5.2.3 Detector packaging characterisation	110
5.2.4 Uniformity	111
5.2.5 Dose linearity measurement	112
5.2.6 Percentage depth dose measurements	113
5.2.7 Dose per pulse measurements	113
5.2.8 Beam profile measurement	114
5.2.9 Beam profile measurements by EBT3 film	114
5.2.10 OF measurements	116
5.3 Results	117
5.3.1 Uniformity	117
5.3.2 Dose linearity	118
5.3.3 Detector packaging	118
5.3.4 Percent depth dose	119
5.3.5 Dose per pulse dependence	119
5.3.6 Beam profile measurements	120
5.3.7 OF measurements	126
5.4 Conclusion	128
CHAPTER 6: ROTATABLE PHANTOM FOR AUTOMATIC ALIGNMENT OF MP512 WITH THE LINAC BEAM	130
6.1 Introduction	130
6.2 Rotatable phantom description	130
6.3 X-ray CT for rotatable cylindrical phantom	133
6.4 Mechanical and electronics parts of the rotatable phantom system	135
6.5 Slow control and DAQ digital design	137
6.6 Experimental results: control system tuning and comparison at the workbench	139
6.7 Experimental results using a medical LINAC	142

6.8 Conclusion.....	142
CHAPTER 7: A 2-D SILICON DETECTOR ARRAY (MP512) USED AS A TOOL TO STUDY MOVING TARGETS IN RADIOTHERAPY	144
7.1 Introduction	144
7.2 Method and materials	144
7.2.1 The detector system and packaging	144
7.2.2 Aluminium shielding calculation and simulations.....	145
7.2.3 Baseline study	148
7.2.4 Calypso four-dimensional (4-D) localisation system.....	148
7.2.5 Lung motion mimicking.....	149
7.2.6 HexaMotion six-dimensional (6-D) motion platform	150
7.2.7 Experimental setup.....	151
7.2.7.1 <i>Dynamic wedge study</i>	151
7.2.7.2 <i>Beam profile measurements using MP512</i>	152
7.2.7.3 <i>Beam profile measurements using EBT3 film</i>	154
7.3 Results	154
7.3.1 DAQ	154
7.4 2-D maps of MP512	155
7.4.1 Geant4 simulation of aluminium sheet effect and RF noise destruction performance	157
7.4.2 Dynamic wedge measurement	159
7.4.3 Beam profiles	160
7.5 Penumbra width	164
7.6 Conclusion.....	166
CHAPTER 8: HIGH SPATIAL RESOLUTION MONOLITHIC SILICON ARRAY FOR STEREOTACTIC RADIOSURGERY	169
8.1 Introduction	169
8.2 Materials and methods	169
8.2.1 Design and fabrication	169
8.2.2 Readout system	170
8.2.3 I-V characteristics	170
8.2.4 C-V characteristics	171
8.2.5 Uniformity.....	171
8.2.6 Dose linearity	171
8.2.7 Reproducibility.....	171
8.2.8 Damage rate calculation (α)	171
8.2.9 Radiation hardness study	172
8.2.9.1 <i>Photon damage</i>	172
8.2.9.2 <i>Photoneutron damage</i>	172
8.3 Results	172
8.3.1 Electrical characteristics (I-V and C-V).....	172
8.3.2 Uniformity.....	174
8.3.3 Dose linearity	174
8.3.4 Reproducibility.....	176
8.3.5 Damage rate calculation (α)	176
8.3.6 Photon damage	177
8.3.7 Radiation damage by 18 MV photon beam	178
8.4 Conclusion.....	179

CHAPTER 9: CONCLUSION.....	181
9.1 EPI diode	181
9.2 MP512	182
9.2.1 Radiation damage study	182
9.2.2 Radiation response and basic characteristics	184
9.2.3 MP512 used as dose verification for movable target	185
9.3 DUO512	185
REFERENCES.....	187
APPENDIX A	210

LIST OF FIGURES

Figure 2.1: Mass absorption coefficient ratio of silicon to water	28
Figure 2.2: Varian LINAC photon energy spectrum for 6 MV, FF= flattening filter exist and FFF=flattening filter free, without a flattening filter makes the spectrum softer (left) and Collisional stopping power ratio silicon (Z=14) to water (right)	29
Figure 2.3: Schematic of a silicon <i>p-n</i> junction diode [113].....	35
Figure 2.4: Displacement damage v. energy for neutrons, protons, pions and electrons plotted relative to 1 MeV neutrons [132]	39
Figure 2.5: Primary and secondary defects in silicon (Si) caused by fast neutrons [125]	39
Figure 2.6: Primary and secondary defects in silicon (Si) caused by Co-60 [125]....	40
Figure 2.7: The mechanism of surface damage in an MOS [150]	44
Figure 3.1: EPI diode schematic representation.....	47
Figure 3.2: EPI diode—(a) EPI shielded by aluminium and (b) EPI sensitive volume protected by Kapton	48
Figure 3.3: Schematic diagram of the TERA readout [159]	49
Figure 3.4: Charge subtraction waveforms [159]	50
Figure 3.5: Rad-X Dose View interface.....	53
Figure 3.6: Measurement of I-V circuit diagram—EPI without guard ring	56
Figure 3.7: Measurement of the C-V circuit diagram—EPI without guard ring	58
Figure 3.8: Experimental setup for EPI diodes with LINAC readout system (left) and TERA readout system (right)	59
Figure 3.9: I-V characteristics from a few samples of EPI diodes, without guard ring	64
Figure 3.10: C-V characteristics from a few samples of EPI diodes, without guard ring	65
Figure 3.11: Collection of I-V experimental results from a few samples, and comparison with the I-V of the simulation model	66
Figure 3.12: Collection of I-V experimental results from a few samples, and comparison of the measured and simulated C-V of the EPI diode	67

Figure 3.13: Average leakage current density of a set of 20 samples as a function of the total dose measured at 20 V	68
Figure 3.14: The space charge distribution and variation of the lateral depletion region as a function of the irradiation dose (white line)	69
Figure 3.15: Simulated CCE as a function of the concentration of positive charge trapped at the Si/SiO ₂ interface (left) and the experimental measure of the EPI diode response normalised to pre-irradiation CCE as a function of the accumulated dose (right)	71
Figure 3.16: TCAD simulation of the diffusion of the charge generated inside the silicon substrate by a Minimum Ionising Particle (MIP) corresponding to 80 Frenkel pairs per micron in silicon. a) Initial conditions with no event; b) generation of the charge at the moment of the event occurs; c-d-e-f-g) evolution of the charge diffusing toward the electrodes as a function of time	73
Figure 3.17: The response of the EPI diode as a function of the irradiation dose delivered by an 18 MV medical LINAC photon beam	74
Figure 4.1: Schematic of the M512 packaging between two PMMA slabs (not to scale) (left) and the MP512 detector mounted and wire-bonded to the thin PCB, with detector and wire bonding protected by a thin layer of epoxy resin (right)	77
Figure 4.2: Real and schematic diagram of the test structure with guard ring.....	79
Figure 4.3: Real and schematic diagram of the test structure without guard ring	79
Figure 4.4: Schematic of the I-V test for test structure without guard ring	81
Figure 4.5: Schematic of the I-V test for the test structure with a guard ring that is grounded (left) and floating (right).....	82
Figure 4.6: Schematic of the I-V test for the MP512 array.....	82
Figure 4.7: Locations of diodes tested on MP512	83
Figure 4.8: The setup of the response test for the arrays	87
Figure 4.9: I-V characteristics for all test structures without guard ring	88
Figure 4.10: I-V characteristics for 1 Ω -cm CMRP substrate, showing different ion implantations with guard ring grounded and floating	89
Figure 4.11: I-V characteristics for 10 Ω cm (KDB) substrate, different ion implantation with guard ring grounded and floating.....	90

Figure 4.12: I-V characteristics for both arrays from the MP512 CMRP and KDB substrates and same pixels are tested in both arrays in the positions of MP. MP with KDB substrate shows high leakage current compared to MP with CMRP substrate.....	91
Figure 4.13: C-V characteristics for the test structure of both substrates without a guard ring	93
Figure 4.14: Silicon detector parameters monograph [177]	95
Figure 4.15: C-V characteristics for test structure 1 Ω -cm CMRP with guard ring ..	96
Figure 4.16: C-V characteristics for test structure 10 Ω -cm CMRP with guard ring	97
Figure 4.17: C-V characteristics for test structure 10 Ω -cm KDB with guard ring...	98
Figure 4.18: Relative response for test structures as a function of accumulated dose	99
Figure 4.19: Relative response for test structures as result of photoneutrons.....	100
Figure 4.20: Relative response for MP512 sample #24 with KDB substrate at d_{\max}	103
Figure 4.21: Relative response for MP512 sample #21 with CMRP substrate at d_{\max}	104
Figure 4.22: Comparison of the response of the test structures and MP512 full array as a function of accumulated dose	105
Figure 4.23: A normalised response as a function of the irradiation dose using an 18 MV medical LINAC photon beam.....	106
Figure 5.1: Schematic of the M512 packaging, inserting the MP512 upside down	111
Figure 5.2: Schematic of the equalisation setup	112
Figure 5.3: Differential response of MP512 after equalisation.....	117
Figure 5.4: Accumulated dose response of the central pixel	118
Figure 5.5: PDD measured with MP512 of 6 MV photons and 10 x 10 cm ² field in comparison with a Markus ion chamber	119
Figure 5.6: DPP response for MP512 normalised to the DPP of 2.78×10^{-4} Gy/pulse	120
Figure 5.7: Beam profiles measured with MP512 and EBT3 films for radiation fields ranging from 0.5 x 0.5 to 10 x 10 cm ²	125
Figure 5.8: Field size dependence response of MP512, MOSkin and EBT3 film normalised to response at 10 x 10 cm ² field size	127

Figure 5.9: Comparison of output factor for a different detector type and size from Sauer et al. [187]	127
Figure 6.1: Final design of the rotatable cylindrical phantom by SolidWorks (left) and actual rotatable cylindrical phantom with an inclinometer attached to the LINAC head (right)	132
Figure 6.2: Phantom with mechanical parts under the LINAC gantry	133
Figure 6.3: CT image of the rotatable phantom in 3-D	134
Figure 6.4: 2-D isodose plan of the rotatable phantom	135
Figure 6.5: Schematic diagram of the rotatable phantom system	135
Figure 6.6: Simplified block diagram of the rotatable phantom architecture	138
Figure 6.7: PID tuning tracking mode	140
Figure 6.8: Timing parameters	140
Figure 6.9: Step response	141
Figure 7.1: Schematic of the MP512 with PMMA, solid water and an aluminium sheet	147
Figure 7.2: Principle of electromagnetism with beacon in the Calypso system	149
Figure 7.3: Lung trace motion in X (blue) and Y (green) coordinates	150
Figure 7.4: Experimental setup of the MP512 carried by the HexaMotion platform	151
Figure 7.5: Diagram of jaws defining the square field size	152
Figure 7.6: The final setup, showing the transponders (beacons) positioned on the foam top of the detector and localised relative to the room coordinate system	154
Figure 7.7: Graphical user interface of the data acquisition (left) and investigation of the initial LINAC beam characteristics (right)	155
Figure 7.8: 2-D dose distribution at d_{\max} of MP512 for different field sizes in three cases	156
Figure 7.9: Baseline fluctuation distribution acquired with Calypso on (with and without aluminium sheet shielding—blue and orange bars, respectively) compared to the baseline fluctuation with Calypso off (green bars)	157
Figure 7.10: Comparison of the Geant4 simulations of present depth dose (left) and dose profile (right) for 1 x 1, 2 x 2 and 3 x 3 cm ² field sizes with and without the aluminium sheet	158

Figure 7.11: Dynamic wedge integral dose profiles taken in the central Y axis of MP512 (upper plot) and the percentage difference that normalised to the no-motion peak integral dose response (lower plot)	159
Figure 7.12: MP512 dose profile in different cases comparing the data measured by EBT3 for field sizes of (a) $3 \times 3 \text{ cm}^2$, (b) $2 \times 2 \text{ cm}^2$ and (c) $1 \times 1 \text{ cm}^2$ in the Y direction	162
Figure 7.13: MP512 dose profile in different cases comparing the data measured by EBT3 for field sizes of (a) $3 \times 3 \text{ cm}^2$, (b) $2 \times 2 \text{ cm}^2$ and (c) $1 \times 1 \text{ cm}^2$ in the X direction	164
Figure 7.14: Comparison of penumbra width between MP512 and EBT3 film for field sizes 1×1 , 2×2 and $3 \times 3 \text{ cm}^2$ in the Y direction.....	165
Figure 7.15: Comparison of left hand profiles for 1×1 , 2×2 and 3×3 field sizes along the X- direction of EBT3 and MP512 measurements. Both the devices show the dose distribution generated by the leaf leakage with a minimal (within 2%) discrepancy	166
Figure 8.1: DUO512 pixel structure diagram (not to scale) (left) and DUO512 silicon detector array (right).....	170
Figure 8.2: Pre-irradiation leakage current of the selected pixels.....	173
Figure 8.3: Measurement of the C-V characteristic of the DUO512	173
Figure 8.4: Detector response before and after equalisation was applied.....	174
Figure 8.5: Measurement of the linearity of the central pixel, error bars are included but barely visible even considering a variation corresponding to two standard deviations over five repetitions.	176
Figure 8.6: Leakage current density as a function of irradiation dose, measured at negative 20 V bias.	177
Figure 8.7: Measurement of relative sensitivity as a function of pre-irradiation dose up to 14 Mrad.....	178
Figure 8.8: Normalised response of silicon detector array as a function of the irradiation dose delivered by an 18 MV medical LINAC photon beam .	179

LIST OF TABLES

Table 2.1: Comparison of characteristics of IMRT, VMAT, SRS and SBRT	8
Table 2.2: Commercial detectors for QA available in the market	25
Table 2.3: Different types of defect structures produced by different types of radiation [125]	40
Table 3.1: Two-level radiation damage model	62
Table 4.1: Ion implantation and resistivity of two arrays	77
Table 4.2: Amount of dopant concentrations for the samples used in this thesis	78
Table 4.3: The dose received of each samples from test structures	85
Table 4.4: The relative response alterations due to the photoneutrons	100
Table 5.1: EBT3 and MP512 FWHM and penumbra width (80%-20%) study for different square field sizes at 10 cm depth and isocentre.....	121
Table 6.1: Timing performances	141
Table 6.2: Timing parameters in three modalities in clinical environment using a LINAC	142
Table 7.1: Parameter values for calculating aluminium thickness.....	145
Table 7.2: Summary of calculations of FWHM and RHS penumbra width (80%- 20%) in the Y direction of all field sizes measured by MP512 and EBT3 film	162
Table 7.3: Summary of calculations of FWHM and RHS penumbra width (80%- 20%) in the X direction of all field sizes measured by MP512 and EBT3 film	164

**PEER REVIEWED JOURNAL PAPERS AND CONFERENCE
PROCEEDINGS**

1. M. L. F. Lerch, M. Petasecca, A. Cullen, **A. Hamad**, H. Requardt, E. Brauer-Krisch, A. Bravin, V. L. Perevertaylo and A. B. Rosenfeld, “Dosimetry of intensive synchrotron microbeams,” *Radiation. Measurements.* **46**, 1560–1565 (2011).
2. M. Petasecca, A. Cullen, L. Fuduli, A. Espinoza, C. Porumb, C. Stanton, **A. H. Aldosari**, E. Brauer-Krisch, H. Requardt, A. Bravin, V. Perevertaylo, A. B. Rosenfeld and M. L. F. Lerch, “X-Tream: A novel dosimetry system for synchrotron Microbeam radiation therapy,” *J. Instrumentation.* **7**, 1–15 (2012).
3. **A. H. Aldosari**, A. Espinoza, D. Robinson, L. Fuduli, C. Porumb, S. Alshaikh, M. Carolan, M. L. F. Lerch, V. Perevertaylo, A. B. Rosenfeld and M. Petasecca, “Characterization of an innovative p-type epitaxial diode for dosimetry in modern external beam radiotherapy,” *IEEE Trans. Nuclear. Sci.* **60**(6), 4705–4712 (2013).
4. L. Fuduli, C. Porumb, A. A. Espinoza, **A. H. Aldosari**, M. Carolan, M. L. F. Lerch, P. Metcalfe, A. B. Rosenfeld and M. Petasecca, “A comparative analysis multichannel data acquisition system for quality assurance in external beam radiation therapy,” *J. Instrumentation.* **9**(6), 1–12 (2014).
5. **A. H. Aldosari**, M. Petasecca, A. Espinoza, M. Newall, L. Fuduli, C. Porumb, S. Alshaikh, Z. A. Alrowaili, M. Weaver, P. Metcalfe, M. Carolan, M. L. F. Lerch, V. Perevertaylo and A. H. Aldosari, “A two dimensional silicon detectors array for quality assurance in stereotactic radiotherapy: MagicPlate-512,” *Med. Phys.* **41**(9), 1-10 (2014).
6. **A. H. Aldosari**, M. Petasecca, A. Espinoza, D. Robinson, L. Fuduli, C. Porumb, A. Cullen, V. Perevertaylo, S. Alshaika, M. Carolan, M. L. F. Lerch and A. B. Rosenfeld, “Radiation hardness of EPI silicon detector for 2D dosimetry in external radiation therapy,” Abstract in *Proceedings of IEEE-NSS/MIC/RTSD 2013: Institute of Electrical and Electronics Engineers*, October 27–November 2 2013, COEX, Seoul, South Korea.

7. C. S. Porumb, L. Fuduli, M. Petasecca, Z. A. Alrowaili, A. A. Espinoza, **A. H. Aldosari**, A. Cullen, V. L. Perevertaylo, M. Carolan, M. L. F. Lerch and A. B. Rosenfeld, “A novel dual-verification quality assurance system for external beam radiotherapy,” Abstract in *Proceedings of IEEE-NSS/MIC/RTSD 2013: Institute of Electrical and Electronics Engineers*, October 27–November 2 2013, COEX, Seoul, South Korea.
8. Claudiu S. Porumb, M. Petasecca, **A. H. Aldosari**, M. Newall, I. Fuduli, M. Carolan, D. Cutajar, D. Prokopovich, J. B. Davies, M. L. F. Lerch, A. B. Rosenfeld, “Characterisation of novel monolithic pixelated detectors for 2D dosimetry in external beam radiotherapy,” Abstract in *Proceedings of MMND-IPTC Conference 2014: Micro-Mini & Nano Dosimetry and Prostate Cancer Treatment*, 20–25 October 2014, Port Douglas, Queensland, Australia.
9. M. K. Newall, M. Petasecca, **A. H. Aldosari**, M. L. F. Lerch, M. Carolan, J. T. Booth, E. Colvill, P. Keall, M. Jackson, M. Barton, T. Kron, W. Tome, P. Metcalfe and A. B. Rosenfeld, “The serial dose magnifying glass: A unique tool for the study of moving targets in radiotherapy,” Presented at *CSM 2014: Combined Scientific Meeting*, 4–7 September 2014, Melbourne Convention and Exhibition Centre, Victoria, Australia.
10. M. Petasecca, M. K. Newall, J. T. Booth, M. Duncan, **A. H. Aldosari**, I. Fuduli, A. A. Espinoza, C. S. Porumb, S. Guatelli, P. Metcalfe, E. Colvill, D. Cammarano, M. Carolan, B. Oborn, M. L. F. Lerch, V. Perevertaylo, P. J. Keall, and A. B. Rosenfeld, “MagicPlate-512: A 2D silicon detector array for quality assurance of stereotactic motion adaptive radiotherapy,” *Med. Phys.* **42**(6), 2992-3004 (2015).
11. M. Petasecca, S. Alhujaili, **A. H. Aldosari**, I. Fuduli, M. K. Newall, C. S. Porumb, M. Carolan, K. Nitschke, M. L. F. Lerch, J. Kalliopuska, V. Perevertaylo, and A. B. Rosenfeld, “Angular independent silicon detector for dosimetry in external beam radiotherapy,” *Med. Phys.* **42**(8), 4708-4718 (2015).

LIST OF ABBREVIATIONS

2-D	two-dimensional
3-D	three-dimensional
4-D	four-dimensional
6-D	six-dimensional
ADAC	adaptive discrete angle control
ANSTO	Australian Nuclear Science and Technology Organisation
ASIC	application-specific integrated circuit
CAX	central axis pixel
CCE	charge collection efficiency
CMRP	Centre for Medical Radiation Physics
CT	computed tomography
C-V	capacitance-voltage
DAC	discrete angle control
DAQ	data acquisition system
DIL	dual in-line
DMLC	dynamic multileaf collimator
DPP	dose per pulse
EBRT	external beam radiation therapy
EPI	epitaxial
FPGA	field programmable gate array
FWHM	full width at half maximum
GATRI	Gamma Technology Research Irradiator
GR	generation/recombination
GRC	generation and recombination centre
GTV	gross tumour volume
IC	ionisation chamber
I-V	current-voltage
IMAT	intensity modulated arc therapy
KDB	silicon substrate from European silicon facility
IMRT	intensity modulated radiation therapy
LINAC	linear accelerator

MIP	minimum ionising particle
MLC	multileaf collimator
MOS	metal-oxide semiconductor
MOSFET	metal-oxide semiconductor field-effect transistor
MP	Magic Plate
MRI	magnetic resonance imaging
MU	monitor unit
MV	megavoltage
OF	output factor
OTA	operational transconductance amplifier
PCB	printed circuit board
PDD	percentage depth dose
PG	pulse generator
PID	proportional integral derivative
PMMA	polymethyl methacrylate
PTV	planning target volume
PXC	pixel-segmented ionisation chamber
QA	quality assurance
RF	radiofrequency
SBRT	stereotactic body radiation therapy
SD	standard deviation
SED	side equivalent distance
SHR	Shockley-Read-Hall
SPI	Serial Peripheral Interface
SRS	stereotactic radiosurgery
SRT	stereotactic radiation therapy
SSD	source-to-surface distance
TCAD	Technology Computer Aided Design
TE	tissue equivalent
VMAT	volumetric modulated arc therapy

CHAPTER 1: INTRODUCTION

1.1 Introduction

According to the World Health Organization, the number of deaths from cancer is continuing to increase and could reach 12 million by 2030 [1]. However, some cancers can be cured, or at least the suffering of patients minimised, particularly if diagnosed early. Three of the main cancer treatment options, which are often used in combination, are surgery, chemotherapy and radiotherapy. Of all cured patients, 30% are treated with radiotherapy, and more than half receive radiotherapy as part of their cancer management plan [1]. The prime objective of radiation therapy is the effective delivery of ionising radiation to a specific target, while avoiding the surrounding healthy tissues. New developments in delivery technology have introduced treatments such as intensity modulated radiation therapy (IMRT), volumetric modulated arc therapy (VMAT) and stereotactic body radiation therapy (SBRT). Verifying doses for IMRT, VMAT and SBRT involves measuring two-dimensional (2-D) or three-dimensional (3-D) dose distributions and comparing them with treatment planning system calculations [2]. Due to the ever-increasing complexity of treatment modalities in radiation therapy, there is a greater need for accurate determination of 2-D and 3-D dose distributions. This is frequently achieved by point dose measurements that use ion chambers or shielded single diodes, or by 2-D array dosimeters—such as radiochromic film, an array of ionising chambers or solid state detectors—to ensure the patient's treatment is performed correctly and safely [3]. This thesis focuses on developing silicon detectors, and improving and characterising their functionality and stability (radiation hardness) for use as quality assurance (QA) systems in medical applications.

1.2 Project goals

In this thesis, the research topics focus on detectors based on the silicon substrate. The work emphasises the development and characterisation of three new detector dosimeters for external beam radiation therapy (EBRT). The first detector examined in this thesis is an epitaxial (EPI) diode based on a *p*-type silicon epitaxial layer without a guard ring, designed by the Centre for Medical Radiation Physics at the University of Wollongong. It is a single pad detector that is used as a sensitive element of the sensor array called ‘Magic Plate (MP) 121’—an 11 x 11 array of diodes for 2-D and 3-D dosimetry in EBRT [4]. In Chapter 3 of this thesis, the EPI diode is successfully characterised, and demonstrates an unusual total dose radiation response.

The second detector system is referred to as the ‘Magic Plate 512’ (MP512). This is a monolithic 2-D array detector that contains 512 pixels and was designed for small field beam dosimetry. Chapter 4 explores the performance of the MP512. In order to characterise the radiation hardness of the detector, this study also tested single diode test structures fabricated on the same *p*-type wafer. Further, this study determined the basic characterisation of this detector via a medical linear accelerator (LINAC) (Chapter 5). A rotatable cylindrical phantom system was designed and machined precisely by the Centre for Medical Radiation Physics (CMRP) to avoid the angular dependence of the detector (Chapter 6). The MP512 was also tested for use in adaptive motion radiotherapy via a dynamic multileaf collimator (DMLC) tracking system based on the radiofrequency tracker Calypso and a movable platform (HexaMotion) (Chapter 7). This study is important to evaluate the effect of movement on the total dose deposited and calculated by the treatment planning

system, which does not take into account the intra- and inter-fraction movement of the target volume.

The third detector investigated in this thesis is the ‘DUO’—a monolithic 2-D strip detector consisting of 512 microstrips arranged in a cross-shaped geometry that is characterised in terms of radiation hardness (Chapter 8). Finally, Chapter 9 summarises the main outcomes of this thesis. It also presents the study’s advantages and weaknesses, as well as recommendations for the future development of single detector and 2-D array systems based on silicon substrates in small field dosimetry and EBRT in general.

CHAPTER 2: LITERATURE REVIEW

2.1 Radiation therapy

In 1895, Roentgen discovered the x-ray, which was the first step in radiation therapy and medical imaging history. Thereafter, Freund printed the first textbook on radiotherapy, and this field has since continued to be developed by physicists, radiographers and technologists [5]. Currently, over 50% of cancer patients receive radiation therapy during their treatment plan [6], with extensive use of imaging techniques for treatment guidance or planning. In particular, the introduction of computed tomography (CT) and the recent introduction of combined LINAC–magnetic resonance imaging (MRI) have enabled the development of more accurate treatment planning systems, and more effective determination of the target volume. In addition, blocks, wedges and radiation dosimetry tools have been incorporated into radiation delivery machines, which have radically improved patient treatment [5].

The complexity of contemporary radiation therapy continues growing with the introduction of modulation of beam intensity and shape [7]. The use of multileaf collimators (MLCs) protects normal tissue by shaping the beam, which was first achieved by conformal radiation therapy in 1965 by Takahashi [7, 8]. Conformal radiation therapy has the ability to reduce the volume of normal tissue that does not need to be irradiated. Further, using 3-D imaging in conformal radiation therapy enables higher precision in determining the target location, and increases the dose delivered to the tumour [9]. For patients suffering from prostate cancer, late side-effects are shown to decrease when treated with 3-D conformal radiation therapy, rather than conventional radiotherapy [9]. Brahme et al. developed the concept of shaping and modulating the beam intensity used in IMRT [7, 10]. The following

section presents a brief overview of the IMRT treatment modalities adopted currently for lung, liver and prostate cancers in order to define the specifications of the dosimetry systems required for such radiation delivery scenarios. IMRT and VMAT modalities are particularly relevant for this work, and stereotactic radiotherapy modalities—such as SBRT and SRS, which adopt a small field of irradiation (smaller than 4 cm side equivalent distance [SED])—represent very challenging scenarios for accurate dosimetry [11].

2.1.1 IMRT

IMRT enables accurate delivery of a high radiation dose (from 70 to 80 Gy in 15 to 30 fractions) to tumours, while sparing critical organs by modulating the radiation intensity in terms of shape and dose rate. The dose distribution in IMRT is non-uniform across the field. The intensity of the beam can be controlled by using MLCs, and can be stationary or rotating around the target volume. Two techniques can be used to deliver the dose. The first is the ‘step and shoot’ technique. In this technique, when the collimators are stationary, the beam is on, and multiple segments per field are given. The second technique is the ‘dynamic sliding window’. In this technique, the beam is on at all times, while the MLC leaves sweep through the field. When undertaking this, the radiation must be paused momentarily to allow the leaf to move into the correct position [12] from one segment to the subsequent segment.

Due to the complexity of treatment and need to improve the precision of delivering radiation and patient setup, QA tools are introduced to ensure the agreement between the planned dose and delivered dose. Further, the medical imaging is employed to ensure that the normal tissue is kept out of the radiation fluence.

2.1.2 VMAT

The first person to use intensity modulated arc therapy (IMAT) was Yn in 1995 [3, 13, 14]. IMAT is based on combining computer technology and LINAC to improve 3-D conformal radiotherapy and reduce the treatment delivery time, compared with IMRT [13, 15, 16]. However, in IMAT, the dose rate must be constant during the gantry rotation, which is the limitation of this technique [13, 14]. VMAT is a special technique of IMRT that delivers radiation by rotating the gantry continuously around the patient, with no interruption of the beam delivery, and with the field shape and MLC leaf positions changing during the treatment (with the beam fired at all times) [15].

2.1.3 SRT: SBRT and SRS

SRT is a technique that uses three dimensions (radiation is fired in several directions around the target volume) to deliver high ionising radiation via numerous beams to a small field (maximum field size of approximately $5 \times 5 \text{ cm}^2$) in the brain, lung, liver or prostate [17]. It can minimise toxicity and give highly effective treatment to stereotactic lesions [18]. There are many ways to deliver the dose in SRT, including via stereotactic brachytherapy and stereotactic external beam irradiation. Based on the number of fractions, stereotactic external beam irradiation can be categorised as either stereotactic radiosurgery (SRS) or SBRT. In SRS, the total amount of dose delivered to the patient is in one fraction, while, in SBRT, the dose delivery is in multiple fractions (between two and five). For patients with brain metastases, radiosurgery has demonstrated the greatest success for treatment [19]. However, delivering a high dose of radiation to a patient requires protecting any organs at risk (OARs) by using image guidance for the setup of the patient [18, 19].

The review presented in the previous sections about IMRT, VMAT and SRTs is summarised in Table 2.1, with particular emphasis on the main differences between the techniques.

Table 2.1: Comparison of characteristics of IMRT, VMAT, SRS and SBRT

Treatment modalities	Gantry rotating	Beam modulation	Dose/fraction Gy	No. of fractions	Margin	Organ	Field size
IMRT	X (The gantry is fixed for each segment)	✓	1.8–30	10–30 [20]	1 cm [20]	Whole body	Large field size ~10–20 cm
VMAT	✓ (The gantry is rotating)	✓	1.77–2.16 Gy (less monitor unit [MU] and time) [20, 21]	32 [21]	1 cm	Whole body	Large field size ~10–20 cm
SBRT	✓	✓	6–30	1–5 [22]	2 mm [20]	Lung, prostate, liver [22]	Less than 4 cm in diameter [23]
SRS	✓	X	10–35 [24]	1	2 mm [25]	Brain lesions [25]	Down to 2 mm

2.2 QA for SBRT and SRS requirements

In terms of small field beams, such as SRS and SBRT, the total amount of dose delivered to the patient is approximately 50 Gy or higher. Both these kinds of treatment require extremely high geometric accuracy, with a tight margin for planning target volume (PTV) and acute dose fall off [26] within a few millimetres. Due to the high dose delivered in one fraction by SRS, this technique is limited to small lesions of no larger than 4 cm in diameter [23].

In contrast, SBRT is increasingly used to treat large tumours. Using a small field size for radiation delivery is challenging due to the lateral electronic disequilibrium in the field [26]. This phenomenon is associated with the range of secondary electrons, and is usually present at the edge of the field. The presence of lateral electronic disequilibrium at the edge occurs because a large fraction of the secondary electrons produced by direct photons deposit their energy outside of the field. Indeed, the lateral electronic disequilibrium at the edge of the field has been shown to be

dominated by electron scattering rather than by the inward range of electrons [11, 27].

With a large field size, this effect can be considered negligible and the dose at the centre of the radiation field can be measured in charged particle lateral equilibrium conditions. Electronic equilibrium is influenced by several factors, such as the energy of the beam and the structure and density of the medium. With a small field size of less than 3 cm SED, the effect of lateral electronic disequilibrium is extreme, causing the total dose to be reduced at the centre of the radiation field. In this case, the effect of density inhomogeneous media—such as lung and air cavities or the cancer mass itself—will be high. Accordingly, in a low-density medium, the small field experiences substantial perturbations that are energy and density dependent [11]. Further, in small field radiotherapy modalities, systematic alignment errors that could be harmless in standard IMRT and VMAT treatments can have a significant clinical influence in SRT, resulting in severe over-radiation of (OARs) in a close PTV [26, 28-30]. This is worsened when the size of the radiation field is reduced and the dose gradient at the edges becomes steeper. In addition, the large amount of dose delivered in a small number of fractions limits the ability to adjust the error that occurs during a treatment session by modifying the following. According to the previous considerations, the main characteristics of a dosimetry QA tool in SRT must be:

- to resolve steep dose gradients (of around 1 mm)
- to measure high dynamic range to cope with the large dose/fraction.

According to Laub and Wong [31], the volume effect of detectors in the small fields used in radiation therapy has led to discrepancies of more than 10% between calculated cross-profiles and profiles measured with films. This is because of the

insufficient spatial resolution of the detector used to collect the beam data during commissioning of the IMRT planning tool [31]. Similarly, the penumbra width increases linearly with the size of the detector and does not depend on the beam energy [23, 32, 33]. To achieve accuracy of the dose delivered to the patient and maintain normal tissue sparing, medical physicists must have empirical beam data or use a Monte Carlo simulation [26]. Accurate basic parameters of the beam (percentage depth dose [PDD], output factor [OF] and beam profile) are required to tune the model of the beam used in the treatment planning systems for dose calculation or reverse calculation of the irradiation segments [29].

Thus, it is crucial to choose a suitable detector for small field dosimetry; however, this can be challenging for two reasons [34]. First, with a small field size—particularly for dimensions of less than 30 mm when using 6 megavoltage (MV) photons—the lateral electronic disequilibrium increases because the size of the field becomes similar to the secondary electron range. Therefore, measuring the dose in a single measurement at the centre is insufficient to distinguish the distribution [28]. Second, when the size of the detector is larger than the penumbra width, it is not able to adequately resolve the penumbra, which leads to systematic overestimation of the penumbra width.

To address the main problems confronted in small field dosimetry, the detectors should have the following characteristics:

1. be tissue equivalent and not perturb the radiation beam
2. have a small sensitive volume to avoid volume averaging effects, and be capable of high spatial resolution to resolve steep dose gradients at the beam edge

3. be able to overcome the problems of positioning accuracy that exist in small field dosimetry
4. exhibit energy, dose rate and directional response independence [29, 35]
5. have 2-D dose mapping capabilities.

Currently, no single detector fulfils all these criteria. In addition, using different types of detectors to measure the dose distribution of a small field radiation beam can cause difficulties with a high probability of significant errors. Semiconductor diode detectors that have been used for electrons and photon beams show a fast response and high spatial resolution with small sensitive volume, and do not need external bias. Further, silicon detectors are nearly independent of the stopping power ratio in comparison to water in the MV range of energy, but show larger attenuation in the photon energy range from 5 to 300 keV (large discrepancy in the mass absorption coefficient ratio between silicon and water largely due to the photoelectric effect). They also suffer angular, dose rate and temperature dependency. In order to use this detector and achieve accurate measurements, these effects must be well characterised and corrected [11].

Radiographic film dosimetry shows high spatial resolution, but is strongly energy dependent and not tissue equivalent. Radiochromic (Gafchromic) film is self-developing and has high spatial resolution, which makes it appropriate for high dose gradients and small field dosimetry. However, no film dosimeter is capable of absolute dose measurements and real-time results [36], unless the proper calibration is performed. Diamond detectors are fundamentally tissue equivalent for photon beams, and are thus energy independent. However, they are dependent on the exposed dose rate, even though a correction can be applied to the measurements [11, 23]. The BANG gel detector is energy dependent, is tissue equivalent and provides

high spatial resolution in three dimensions [37]. It has the ability to provide satisfactory data for small SRS cones without field perturbation [11, 38]. However, the main drawback of gel dosimetry is that it requires very expensive equipment to read out the optical density (such as optical CT gantry) and cannot be effectively operated by MRI due to artefacts [26, 38]. A thermoluminescent dosimeter (TLD) is an example of a dosimeter used in point dose measurements and *in vivo* dosimetry [39]. TLD material can be in several different forms, such as rods, chips or powder. However, the downside to TLD is that it exhibits energy and dose-rate dependence.

Further, the uncertainties resulting from the collimator, gantry and couch rotation could have a severe effect on the accuracy of the beam delivered to the specific lesion. Additionally, the positioning accuracy of the small detector may influence the measurements of the dose and lead to a large discrepancy. Based on these factors, McKerracher and Thwaites (1999) recommended using more than three detectors for fields larger than 12.5 mm, with dosimetry for smaller fields remaining a problem, especially when measuring OFs [28, 40].

2.2.1 Optimal specification of a 2-D dosimeter array for SRT

The main characteristic that separates SRS and SBRT is the delivery of large doses in a few fractions, which results in a different biological effectiveness of the dose delivered [41]. Given that SRS and SBRT are often used during lung and liver cancer treatment, they may also need to take into account organ motion management. When motion is taken into account, it is important to verify that the dose delivered to the patient during treatment is as close as possible to the dose stated in the treatment planning system, even if the cancer volume moves across the radiation field. The device required to verify such scenarios demands a total sensitive area large enough to encompass the magnitude of the range of motion of any target volume. It must

also contain enough channels with high spatial resolution—which is a combination of a small pixel pitch and small active volume—in order to ensure that the steep dose gradients can be incorporated and the movement of the cancer volume reconstructed accurately.

2.3 Organ movement and its management

IMRT has a greater ability to shape irregular target volumes than conventional radiotherapy [42-44]. In general, the improved physical features of IMRT can lead to better clinical results, as suggested by Zelefsky et al. [45]. There is concern regarding patient anatomy and position when treating with IMRT, especially when using a small field beam, which differs to some degree from that used for planning systems [46]. This is mostly due to imperfections in patient positioning, patient movement and organ motion [42, 46]. Unintended deviation in patient position or target movement can lead to under-dosage of the tumour volume, and over-dosage to normal tissues [46, 47]. To solve this issue, the PTV was introduced. This is defined by the clinical target volume (CTV) and surrounding margins [42, 46, 48]. This approach for treatment planning ensures that the desired dose is actually delivered to the CTV [48, 49]. However, this method potentially leads to irradiating large volumes of healthy tissue, and can be more complicated if there is any organ movement (intra-fraction movement) during the treatment delivery [42].

Intra-fraction organ motion is predominantly caused by respiratory and cardiac motion, and is natural and unpredictable. Tumours can move as much as 3 cm due to respiration [50]. However, these motions largely depend on the location of the tumour, and differ between patients [50]. Respiratory motion is one of the main sources of error in radiation therapy, and it also causes image artefacts [51]. Intra-fraction motion can lead to significant errors during the delivery of doses, such as

healthy tissue being exposed to high doses and under-dosage being delivered to the CTV [50]. To use SBRT, it is necessary to manage these sources of uncertainty in an effective manner.

2.3.1 Strategies to reduce motion effects

Some techniques have been implemented for motion management during simulation, planning and treatment. These techniques include deep inspiratory breath-hold (DIBH), forced shallow breathing and respiratory gating [47]. In the DIBH technique (active or voluntary), patients are asked to hold their breath during treatment. This minimises tumour motion and extends patients' lungs to their maximum volume, which pushes healthy lung tissue out of the primary radiation beam [47, 52]. However, this technique has limited applications for patients who suffer pulmonary function, which is likely to occur among people with lung cancer [47].

The aim of the forced shallow breathing technique is to restrict breathing motion and minimise organ movement by placing a plate on top of the patient's abdominal region [47, 53]. However, this technique causes the patient discomfort. Finally, the respiratory gating technique is used to allow patients to breathe normally, managing the emission of radiation only during the small displacement phase of the respiratory motion (exhalation phase) [54]. This technique records the respiration cycle while the patient breathes, and the recordings are used to gate the radiation beam [46]. Hence, tumour movement is restricted when the beam is on, and the margins of treatment volume are reduced accordingly [46]. Respiratory gating enables the gross tumour volume (GTV) to PTV margins to be reduced from 2 to 1 cm for liver cancer patients [55].

To improve the respiratory gating technique, it must include setup verification, such as by using a portal image. This combination reduces setup margins and the intra-fraction component of the internal margin [56]. In addition, the setup margin could be reduced by using positional verification, such as an electronic portal imaging device (EPID), which can be extremely effective if the GTV can be observed on the image [56]. However, this technique requires more time because treatment ceases when a patient's respiratory pattern fails to match the waveform acquired during simulation [50, 55]. In addition, the longer time required for imaging and treatment causes the patient to become uncomfortable and change position. Further, the LINAC is under mechanical stress due to the gantry starting and stopping quickly and repeatedly to follow the exact waveform of each patient.

The problem of organ motion, mainly for SBRT, can also be moderated by a respiratory-synchronised treatment technique based on a real-time tumour-tracking system [50]. The tumour should be in the relative site with respect to the beam when delivering the radiation. Setting up the radiation beam and robotic couch to adjust positioning in real time represents a solution to correcting tumour motion [57]. In terms of comparing the respiratory gating and tracking technique, the tracking system provides higher efficiency of dose delivery. Using DMLC for treatment has been shown to deliver a lower dose to healthy tissue, and possibly to reduce margins [49, 58]. This is still only 2-D compensation; however, it is possible to use a robotic arm built on the LINAC, such as a Cyberknife, for radiosurgery to achieve 3-D compensation [50, 59].

Several studies have been undertaken to determine the real-time position of tumours, such as using RapidArc combined with the 3-D DMLC tracking algorithm [49]. RapidArc is an optical tumour-tracking system that uses infrared cameras to detect

reflective markers attached to the patient [49]. In this study, the author used motion monitoring for the tumour, which was provided by the real-time position management system from Varian, combined with RapidArc [49]. The authors concluded that combining the RapidArc technique with a 3-D DMLC tracking algorithm was feasible and had the ability to improve the dose distribution delivered to a moving target.

Another promising method to monitor tumours in real time is using implanted markers in the tumour position or surrounding tissue. Implanted markers can be either passive radio opaque markers or emitting markers, such as electromagnetic markers [50]. Both markers are used not only for tracking in radiation therapy, but also for verifying the setup of the patient before the treatment begins. The first study using electromagnetic tracking was published by Houdek et al. in 1992 for SRT [60, 61]. Electromagnetic markers have since been used for many applications, such as SRT localisation [61], image-guided surgery and real-time tracking in radiation therapy [62].

Currently, the most commonly used electromagnetic tracking is the localisation and tracking which offered through Calypso system [60]. This system offers continuous monitoring of the target motion in real time with four dimensions via implanted resonant circuits called ‘beacons’. The Calypso system contains a magnetic array that is placed above the patient. The magnetic array excites the beacons and subsequently induces a small current. This response is detected by the array, and position data are sent to the DMLC system. The position of the Calypso array with respect to the LINAC is determined by infrared cameras in the treatment room. The accuracy of target detection in a phantom has been shown to be less than 1 mm [60, 62-64]. To use the Calypso system to localise and track the prostate, as an example, a minimum

of two transponders must be implanted [60]. The Calypso system was evaluated by Santanam et al., who found that it can be used in a clinical environment to localise and track the target in real time with an accuracy of 0.01 cm [62]. Another study performed by Kupelan et al. found that using the Calypso system is an effective and objective localisation technique for positioning prostate patients during radiation delivery [63].

Each of these treatment procedures require QA tools to guarantee that the treatment is safely delivered to patients. The following sections present the QA tools used for radiation therapy, including point, 2-D and 3-D dosimeters.

2.4 Radiation dosimetry and current QA of contemporary radiotherapy

In recent years, the complexity of treatment planning systems and treatment by small field radiation, such as SRT, has increased. Thus, it is extremely important to have comprehensive QA tools to assist in such complex radiation field scenarios, and accurately verify the plan calculated by the TPS [2]. The ideal dosimeter should demonstrate high spatial and timing resolution, a wide dynamic range, dose response linearity, and response insensitivity to dose rate and energy. Detectors should have high mechanical robustness and reliability. They should also be radiation hard so that their sensitivity does not decrease with use and frequent calibration is avoided. The dosimeter should become stable after an initial dose, independent of any supplementary accumulated doses.

Currently, the techniques used for dosimetry are mainly based on point dose measurements: the detector element can be an ionising chamber, TLD, diamond detector or metal-oxide semiconductor field-effect transistor (MOSFET). However, many types of 2-D tools are also used in radiation dosimetry, such as 2-D diode

arrays, Gafchromic film and gel dosimeters. The following section explores the alternatives available for dosimetry QA in EBRT and particularly for SBRT, where specific characteristics are required for the sensitive element of the detector system.

2.4.1 Point dosimeters

2.4.1.1 Ionisation chamber

The ionisation chamber (IC) is an example of a point dosimeter widely used in radiation therapy for its reliability, repetitiveness and easy calibration for absolute dosimetry [36, 65]. The basic idea of an IC is to measure the current generated by the ions collected at the electrodes and created in the active volume due to radiation. The IC consists of two electrode plates—the anode and cathode. The gap between these is filled with a non-conducting material, such as air or a liquid mixture. The voltage applied between the electrodes goes up to thousands of volts. When a radiation hit the detector, it ionises the material along its path to produce electron-ion pairs. The IC operates only when the amount of voltage is appropriate to collect all the ions produced in the active volume. Thereby, the negative and positive charge carriers drift across the sensitive volume to the electrodes (anode and cathode) via the electric field. Thus, a constant amount of current is produced and readout by an electrometer [66]. However, the IC indicates some volume averaging [36]. Volume averaging produces perturbations in the dose measurements, especially when using small fields, such as SRS, and this can be seen with penumbra measurements [36]. Further, the sensitive volume of the IC cannot be made too small because the amount of ionisation is proportional to the amount of material (air or liquid). Thus, the pitch between the IC cannot be small because the electrode materials require a lot of room and high voltages, which require a large isolation area.

2.4.1.2 Fibre optics dosimeters

A scintillating fibre dosimeter is plastic and water equivalent [67], with the scintillator combining with a fibre optic to collect the light and make it available for readout. The light is proportional to the absorbed dose and is measured by a photodetector [67]. Fibre optics dosimeters have the ability to measure doses in real time [68], and exhibit excellent spatial resolution and signal-to-noise ratio [67]. However, due to the interaction of the radiation beam with the fibre optic itself, Cerenkov light is produced, which represents a challenge to subtract that contribution from the signal generated by scintillation [69]. In addition, fibre optic dosimeters show large degradation of the response as a function of the radiation damage of the scintillating material. Combining this dosimeter with readout based on classical photomultiplier tubes makes it extremely sensitive to magnetic fields, and subsequently limits its use to combined modality treatments, such as LINAC-MRI or CT-MRI machines. Its use in combination with contemporary photodetectors, such as silicon photomultipliers (SiPM), makes it very sensitive to temperature variation, radiation damage and cross-calibration when used in a large number of channels.

2.4.1.3 Diamond dosimeter

The diamond dosimeter has been raised as a good candidate as a small beam dosimeter for SRT. This detector is nearly tissue equivalent due to its atomic number of $Z = 6$, which is close to human tissue of $Z_{\text{eff}} \approx 7.42$ [70, 71] for photon radiation modalities. Diamond dosimeters show high spatial resolution due to the small sensitive volume, which is especially helpful for small field beams, such as SRT, to measure high dose gradient regions [71]. Diamond dosimeters have also demonstrated that they are chemically stable, non-toxic and energy independent. It has much greater sensitivity compared to the ionisation chamber, which makes it

suitable for dosimetry in stereotactic and IMRT. In addition, the energy needed to generate the electron-hole pairs is 13 eV compared to the energy of silicon. This feature makes the diamond detector work like an insulator. Therefore, the diamond dosimeter is working under bias with very small current due to the large band gap. The diamond detector has the capability to be used in two configurations: on-line and off-line dosimeter. For on-line measurement, two electrodes are placed on an opposite side of the diamond plate and the incident radiation produces current through the crystal of the diamond. In this case, the current reading is proportional to the dose rate. However, this dosimeter has the limitations of being dose-rate dependent [23, 69], being expensive and requiring a long delivery time due to a very low fabrication yield.

2.4.2 2-D dosimetry

The verification of absolute dose distribution at single points has been achieved with point dosimeters, although the dose distribution for complex segments, such as those used in IMRT or SBRT, must be verified with higher dimensional measurements [36]. An advantage of 2-D verification is the ability to provide efficient and simultaneous measurement of the dose at multiple locations across the entire field of interest [72]. Provision of real-time feedback is also extremely important, although it is not always available. It is very important to have QA tools that help to check if the dose was delivered safely and accurately to the patients, which is why patient-specific QA is highly recommended for patients undergoing IMRT treatment [73]. This is also the reason it is important to have real-time feedback in a busy clinical scenario, such as contemporary hospitals. Currently, there are a few options for 2-D detectors that are used as dosimeters, such as films, arrays of ICs and silicon diodes. All these devices are briefly introduced in the following sections.

2.4.2.1 Film dosimeters

Radiographic film is an example of film dosimetry used in radiation therapy for 2-D radiation detection. However, radiographic film has certain properties that are not suitable for IMRT. These films have not shown any real-time measurements and have strong energy dependence (14 to 20 times) to low-energy photons [36]. The sensitivity of the film changes based on the production batch of the film, processor conditions and artefacts. Further, radiographic film is not tissue equivalent, and its variation in optical density has shown the greatest potential for causing dosimetry errors [74].

In contrast, radiochromic (Gafchromic) film is a film dosimeter that is widely diffused in radiotherapy that is nearly tissue equivalent [36, 75], is self-developing and potentially has high spatial resolution, which makes it appropriate for high dose gradients and small field dosimetry. Gafchromic EBT3 was developed recently with no orientation-dependence issues and better uniformity across the field of view due to the higher sensitivity of this material compared to Gafchromic MD-55 and the previous generation of EBT film [36]. In comparison to radiographic film, radiochromic film's optical density response can be determined without the need for a processor; however, it cannot provide absolute dose measurements, and should not be used to check MU outputs [36].

2.4.2.2 IC array

One example of a 2-D array is the pixel-segmented IC (PXC) introduced by Amerio et al. for 2-D dose verification [76]. The primary design inserted 1024 chambers with a sensitive volume of each pixel of 0.07 cm^3 over an area of $24 \times 24 \text{ cm}^2$, with a chamber diameter of 4 mm, height of 5.5 mm and pitch of 7.5 mm. The original detector array developed and evolved into the commercially available IMRT

MatriXX. The IC array was characterised in a polymethyl methacrylate (PMMA) phantom using Co-60 and 6 MV x-ray photon beams. The PXC showed good linearity in terms of dose and dose rate. The reproducibility of the PXC has been observed within 0.05% using Co-60. In terms of charge collection efficiency, it has shown 0.985 at a polarisation voltage of 400 V. The OF has been obtained by taking central detector in the PXC, and showed good agreement (of 0.4%) with a Farmer IC.

2.4.2.3 *I'mRT MatriXX*

Another type of commercially available 2-D detector array based on IC is the I'mRT MatriXX (Scanditronix Wellhofer GmbH, Germany) [77]. The I'mRT MatriXX contains 1020 pixels with a sensitive volume of 0.8 cm^3 covering an area of $23.6 \times 23.6 \text{ cm}^2$ with 0.76 cm detector spacing. The dose linearity of I'mRT MatriXX using 6 MV showed less than 1% errors for measured doses at 8 cGy; however, when the measured dose increased to an order of 1 cGy, the errors increased to 3% [77]. Further, the response of the array as a function of field size using 6 MV compared with measurement using IC (Farmer) exhibited agreement within 1%. According to Li et al., the I'mRT MatriXX does not show field size and source-to-surface distance (SSD) dependence using 6 MV and 18 MV, and demonstrated excellent performance for QA in radiotherapy. However, it showed a volume averaging of approximately 4.5 mm in diameter due to the detector size [77].

2.4.3 3-D dosimetry

An example of a 3-D dosimeter is radiochromic gel. Gel dosimetry involves a basic technique applied by medical physicists to verify spatial dose distributions delivered by radiotherapy equipment [78]. A polymer gel dosimeter is comprised of radiosensitive chemicals [79]. The first time gel was used as a dosimeter in radiation dosimetry was by Day and Stein in 1950 [79, 80]. A gel dosimeter can be read out

with several methods, such as via MRI, ultrasound, x-ray, CT and optical scanning [81]. The advantages of the gel dosimeter are that it is tissue equivalent and can record dose distribution in three dimensions, compared with one dimension for ICs and two dimensions for film. Gel dosimeters may be promising for future radiotherapy processes; however, some accuracy issues have not yet been effectively resolved. For example, as gel polymerises in the optical scanning process, it becomes more opaque with absorbed doses. Further, gel dosimeters are affected by MRI and their response is inhibited by the presence of oxygen [38, 82]. New gel dosimeters in 3-D have been developed and used for QA of treatment, such as the PRESAGE gel dosimeter. The next section briefly explores the advantages and disadvantages of this dosimeter.

2.4.3.1 PRESAGE dosimeters

The PRESAGE dosimeter is a 3-D dosimeter used as QA for radiation therapy. It contains polyurethane matrix and radiochromic components (leuco dye) that exhibit response (colour change) when exposed to ionisation radiation [83]. The value of this type of dosimeter is that it is not sensitive to oxygen, it is robust and it does not require an external container to maintain its shape [84]. Further, the light produced by the radiation is absorbed, rather than scattered, which makes measurement using the optical CT easier. The PRESAGE dosimeter has the ability to change its response by adjusting the properties of the radiochromic components (leuco dye) [83]. The PRESAGE has a solid plastic texture that can be cut or altered to different shapes for use in different applications. It has been shown that the PRESAGE gel dosimeter dose not exhibit a linear dose response [84, 85]. However, the PRESAGE mass density is exhibited as being higher within 10%, compared to water [86].





2.4.4 Dosimetric verification of a DMLC



When tumour tracking is adopted in radiotherapy, timing resolution is a requirement for the accurate assessment of the dose delivered to the target. Dose verification of treatment plans involving the use of DMLC tracking has been already performed in pioneer clinical studies via RapidArc, with verification performed using a biplanar diode array Delta⁴ funder (ScandiDos, Sweden) and 2-D ion chamber array called ‘Seven29’ (PTW-Freiburg, Germany) [49]. However, Seven29 has been shown to have higher uncertainty in the steep dose gradient region. In addition, using a 3-D detector, such as gel dosimetry, for the dose verification of dynamic radiotherapy is time consuming [87, 88].

2.4.5 Summary

IMRT and radiosurgery are complex radiotherapy techniques that are pushing the existing limits of dosimeter technology. These techniques use irregular 3-D dose maps formed by many small fields that require compact high-resolution dosimeters with small sensitive volumes that can be stacked and arrayed to provide 2-D and 3-D dose information. Current ICs often have their readouts compromised by the volume averaging effect, if their active volume is large in comparison to the field size. Chambers with a volume of fractions of mm³ are generally less sensitive, and subsequently require a longer irradiation time. Table 2.2 summarises some commercial chambers with other types of dosimeters available, with the main parameters of each device. As indicated by the review presented in the previous sections, it is important to use a suitable detector with high spatial resolution and small sensitive volumes for the dose verification of SRT, and silicon detectors represent a good candidate, as demonstrated in the following sections.

Table 2.2: Commercial detectors for QA available in the market

Vendors	Model/ design	Design	Sensitive volume (cm ³)	Active material	Angular dependence	Energy dependence	Field size dependence	Radiation hardness
IBA dosimetry 	IC CC13	Cylindrical	0.13	Air	No Due to the design	Yes For high energy range	Yes For small field beam	Yes
PTW 	IC Pinpoint T31006	Cylindrical	0.015	Air	No Due to the design	Yes	Yes For small field beam [89]	Yes [89]
PTW 	IC Farmer 30013	Cylindrical	0.6	Air	No Due to the design	No [90]	Yes For small field beam	Yes
PTW 	IC Seven29	Plane- parallel	0.5x0.5x 0.5	Air	No	Data not available	No [91]	Yes

ASHLAN D 	EBT3 film Gafchromi c	Plane	Single active area with thickness 27μm	Polyester	Yes [92]	No [93]	Yes	Yes
Best Medical 	MOSFET TN502RD mobile	Single	0.2 x 0.2 mm [94]	Silicon	Yes	Yes [95]	Yes [94]	No [94]

2.5 Silicon detectors can work as dosimeters for MV radiotherapy

Silicon detectors are extensively used in medical radiation dosimetry for radiation protection, imaging and radiotherapy by photon and electron beams because they demonstrate attractive properties—particularly their sensitivity, which enables reduction of the detector size and achieves high spatial resolution. They show high responsiveness compared to ICs (approximately 18000 times more sensitive with the same active volume) [96], fast charge collection due to high mobility, and a long mean free path of charge carriers. They can be fabricated via a reproducible and stable manufacturing technology that has been developed at the industrial level for many years. However, particular care must be taken to use silicon in dosimetry applications when considering the packaging strategy. Using low atomic number materials has an advantage because it avoids any edge effects and dose enhancement due to the scattering of surrounding materials. Silicon has a higher Z than does water (used to approximate tissue), which affects the absorption coefficient of x-rays by having an over-response over the energy range between 10 to 200 keV of approximately 800% when compared to water.

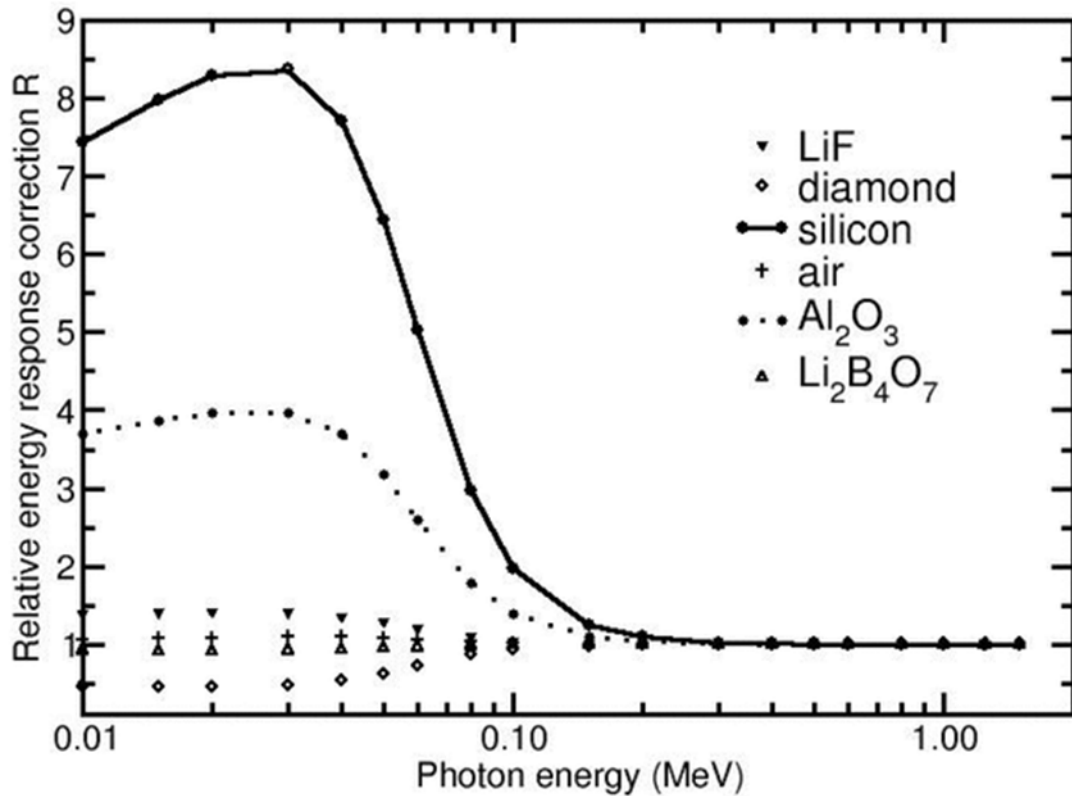


Figure 2.1: Mass absorption coefficient ratio of silicon to water

Figure 2.1 shows the mass absorption coefficient ratio of several materials, including the silicon-to-water ratio. This plot shows that photons with energy of approximately 35 to 50 keV show a large over-response of the silicon detector because of the photoelectric effect.

Photon energy spectrum emitted by a LINAC has a distribution typical for Bremsstrahlung, with the end point energy corresponding to the maximum energy of the accelerator (in this study, corresponding to 6 MV). Figure 2.2 (left) shows the energy spectrum of a LINAC at 6 MV with an average energy at 1.2 MeV. Considering the energy distribution of the photons emitted by a LINAC, the fraction of photons that have energy corresponding to the over-responding energy range in silicon is minimal.

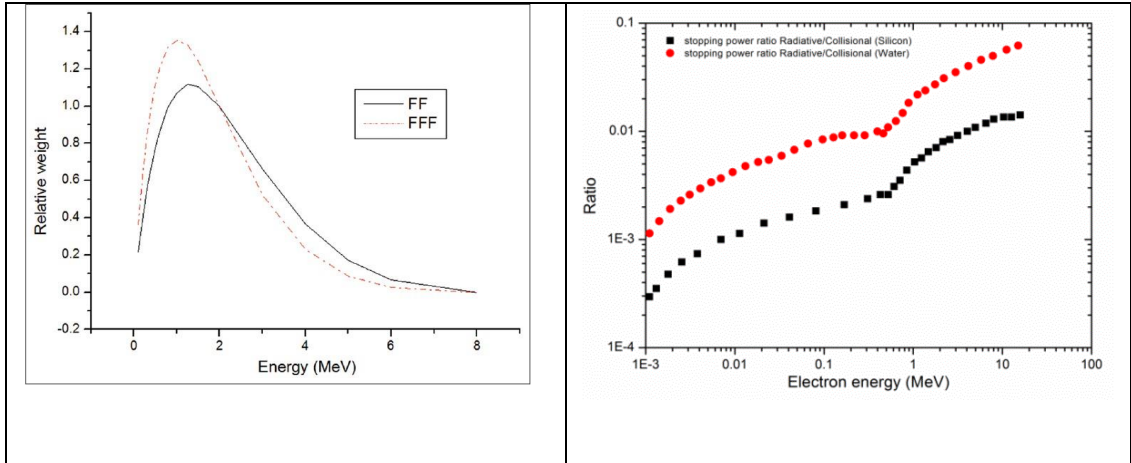


Figure 2.2: Varian LINAC photon energy spectrum for 6 MV, FF= flattening filter exist and FFF=flattening filter free, without a flattening filter makes the spectrum softer (left) and Collisional stopping power ratio silicon ($Z=14$) to water (right)

Use of silicon for accurate dosimetry, must considering that the main contribution to dose deposited in the silicon-sensitive volume is due to the secondary electrons scattered in the surrounding materials. The radiative/collisional stopping power ratio of electrons in silicon and water Figure.2.2 (right) remains constant in the 1.25 MeV energy range corresponding to the average energy of 6 MV photon beam [97].

The combination of the attenuation and stopping power characteristics of silicon makes this material a good candidate to be a relative dosimeter. After calibration to a reference point related to a tissue-equivalent absolute and calibrated dosimeter (such as a carbon calorimeter or calibrated ionising chamber), this could be used as a reliable and reproducible dosimeter for MV photon radiotherapy. Further, the energy required to create an electron-hole pair for a silicon diode is 10 times smaller (3.6 eV) than with an IC, which makes it suitable to be used in passive mode with no leakage current (which can deteriorate the signal-to-noise ratio) [96]. The following

section examines most of the recent silicon detector products available for 2-D and 3-D dosimetry.

2.5.1 2-D Silicon dosimeters

2.5.1.1 MapCheck

MapCheck is an example of a 2-D diode array made for the routine QA of planner IMRT dosimetry (Sun Nuclear, Melbourne, Australia) [98]. The device contains 445 *n*-type pixels covering an area of 22 x 22 cm². In the centre at 10 x 10 cm², the diode spacing is 7.07 mm, while, outside this area, the spacing increases to 14.14 mm, and the sensitive volume of each pixel is 0.8 x 0.8 mm². MapCheck was designed for absolute and relative dose measurements. The system was calibrated using a 25 x 25 cm² field size at a 100 cm SSD and build-up thickening of 5 cm. Letourneau et al. studied the characterisation of MapCheck and indicated that the array can be used for the routine QA of IMRT [98]. They observed linearity from the diode array response, recording doses of approximately 295 cGy. As most calibrations on the diodes are approximately $\pm 1\%$, the readings from MapCheck can be reproduced within a standard deviation (SD) of $\pm 0.15\%$. However, dose map calculations in relation to the planning system models show that this technique underestimates the dosage gradient around the penumbra area.

2.5.1.2 MP121

Wong et al. recognised the growing popularity of 2-D diode arrays as a suitable dosimeter and attributed this to its real-time feedback, as opposed to film dosimeters [4]. They described how a new MP (MP121) 2-D diode array can be characterised while acting as a planar detector and as a 2-D transmission detector in a solid water phantom. They found 2.1% reproducibility from the post-irradiated MP. Conversely, at high dose rates, the MP dose per pulse (DPP) is decreased, and at lower dose rates,

the MP shows to be dose rate independent. Based on conclusive results, Wong et al. found that, due to the low beam perturbing, the MP121 silicon array is suitable for 2-D radiation detection and simplified multipurpose use for verifying radiation therapy dosimetry, such as IMRT and VMAT.

2.5.1.3 Silicon segmented detector

A 2-D silicon segmented detector was designed for dose verification in radiotherapy. It contains 441 modular silicon detectors over an area of $6.29 \times 6.29 \text{ cm}^2$. The pixel is an *n*-type implantation on an epitaxial *p*-type layer, and has $2 \times 2 \text{ mm}^2$ with 3 mm detector spacing. The 441 detectors are connected to the readout electronic system, which contains 28 small boards. The dose linearity of the detector has shown a maximum SD of less than 1% [99]. The sensitivity of the detector to different dose rates was examined and demonstrated at an SD of 0.3%. This indicated that there is no dose rate dependence of the detector.

2.5.1.4 Single-sided silicon strip detector

The single-sided silicon strip detector is a combination of two single sided strip detectors arranged orthogonally each other and forming a thick 2-D array, suitable for radiotherapy treatment verification. It contains 16 Phosphorous doped silicon strips on a *p*+ material, with a total thickness of strips of 500 μm , mounted on a printed circuit board (PCB) [100]. The detector pitch is 3.1 mm and covers an active area of $50 \times 50 \text{ mm}^2$. All the strip detectors were connected to the readout electronic system using 16 conductor ribbon cables. The detector was characterised using 6 MV photons and showed a linearity deviation of 0.1% for a single strip. Further, the PDD was measured and compared with measurement using IC, and showed a maximum difference of 0.73% at a depth of 15 cm. The authors indicated that the detector setup

requires improvement due to the large number of channels by using a new electronic system based on an application-specific integrated circuit (ASIC).

2.5.2 3-D Silicon dosimeters

2.5.2.1 Delta⁴

The Delta⁴ system (Scandidos, Uppsala, Sweden) has been used for IMRT and VMAT verification [101]. The Delta⁴ consists of two crossing orthogonal planes with 1069 *p*-type silicon diodes surrounded by PMMA shaped as a cylinder. Dose reconstruction software can then produce 3-D dose maps. The diodes have a cylindrical shape with an active area of 78 mm², and the diode pitch is 5 mm within the central area of 6 x 6 cm², and 10 mm for the rest of the area of 20 x 20 cm² [101-103]. The Delta⁴ has a diameter of 22 cm and length of 40 cm. The design of the Delta⁴ is a cylindrical shape with orthogonal detector planes, which allows for irradiation from 360° around the cylinder. Delta⁴ also has an inclinometer that is attached to the LINAC head to measure the gantry angle independently during the arc delivery [101].

2.5.2.2 ArcCHECK

A new 3-D diode array is the ArcCHECK system (Sun Nuclear, Melbourne, Florida), which was developed for the routine QA of IMRT and VMAT [104]. It is a cylindrical phantom (PMMA) containing an array with 1383 diodes in a helical shape, with the active area of each diode being 0.8 mm x 0.8 mm and the diode pitch being 10 mm. The ArcCHECK array diameter is 21 cm, with a length of 21 cm. There is a central cavity in the ArcCHECK of 15 cm in diameter to insert and hold the ion chamber for absolute dose measurement [104, 105]. ArcCHECK uses real-time readout and fast dose verification. It allows measuring every gantry angle with high spatial resolution, and measuring the entry dose in front of the isocentre and exit

dose behind the isocentre [104]. This feature means that the errors presented in the isocentre can be seen by ArcCHECK.

2.6 Silicon detector limitations

Many parameters should be considered when using a silicon diode in radiation therapy as a dosimeter [106]. Silicon diodes have angular dependence and can over-respond to energy lower than 200 keV due to a large photoelectric cross-section [106, 107] and therefore the energy dependence of the silicon diode should also be taken into account [108, 109]. The essential drawback of silicon detectors is the radiation damage produced by irradiation [109-111]. The following section describes the effects of radiation on the performance of a silicon diode.

2.7 Radiation damage in silicon

2.7.1 Silicon radiation detectors: radiation hardness and sensitivity variation

A silicon diode is principally a p - n junction, which can be obtained by creating a superficial thin layer of p + (donor dopant) or n + (acceptor dopant) by implantation or diffusion into a doped bulk of silicon of the opposite dopant [112]. A p - n junction is referred to as a ' p -on- n ' type when using a doping impurity from group III (usually boron) into an n -type substrate, and is referred to as an ' n -on- p ' type when using a doping impurity from group V (such as phosphorus) into a p -side substrate.

In order to understand the operation of a silicon diode, it is necessary to consider the behaviour of the diode in equilibrium conditions at room temperature. In this situation, the p - and n -type regions join to form the p - n junction, and there is no voltage applied across the junction. Thereafter, the electrons and holes start to diffuse into a p - and n -region, respectively. The negative charge tends to drift from n - to p -type, while the positive charge tends to drift from p - to n -type. Such drifting stops

when, locally, the electric field generated by the minority carriers equals the one generated by the majority carriers. As a result, a built-in potential, Ψ_0 is created due to the distribution of the carriers in proximity of the junction, which prevents the further diffusion of charge across the junction [96, 113]. In this manner, in equilibrium conditions, there is a balance between drift and diffusion in the silicon diode, and thus no current flow [114, 115]. If the diode is not in equilibrium conditions, the current flow in the p - n junction depends on the polarity of the applied voltage on the diode. When the forward bias is applied on the diode, the current increases exponentially with the applied voltage. Under reverse bias, the amount of current flowing through the p - n junction is limited to the leakage current. This condition is used for silicon diodes as detectors, and passive mode is the polarisation condition used specifically for medical applications due to the absence of the leakage current.

The mechanism of operating the silicon detector in passive mode is represented in Figure 2.3 [96, 113]. The incident of ionising radiation produces electron-hole pairs across the diode [96]. The mean ionising energy needed to produce electron-hole pairs in silicon is 3.6 eV [109], although the bandgap of silicon is only 1.12 eV. The excess minority carriers (electrons in p -type and holes in n -type) diffuse towards the p - n junction, and are collected by the electrodes, which are polarised by the built-in potential, Ψ_0 . When an external ionising radiation source excites the detector, it generates electron-hole pairs across the whole detector substrate or within the distance of total absorption in silicon for the specific radiation particle. The charge carriers collected by the electrodes are only those produced within a diffusion length: L_p for n -type and L_n for p -type. These carriers can be collected and consequently

allow the generation of a detectable current that can be measured by the electrometer [96].

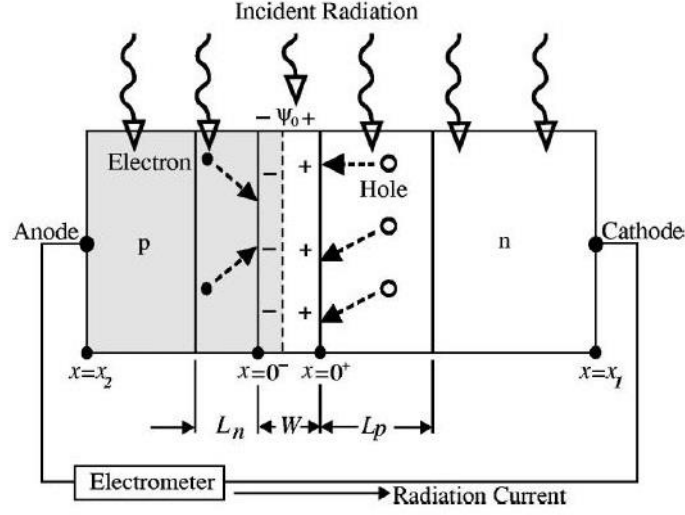


Figure 2.3: Schematic of a silicon p - n junction diode [113]

If a silicon junction is used to detect radiation, it demonstrates a variation in sensitivity due to the damage caused by radiation. The sensitivity of a passive detector is directly proportional to its active volume (V), which is defined as the product of the area of the detector, and the minority carrier diffusion length, $L_{n/p}$. The diffusion length for electrons is defined as:

$$L_n = \sqrt{D_n \tau}$$

where L_n or L_p is the diffusion length for electrons and holes, D_n or D_p is the diffusion constant of electrons and holes, and τ is the minority carrier lifetime [113]. In both n - and p -type doped detector substrates, the carrier lifetime is inversely proportional to the concentration of deep-level defects, and is responsible for deteriorating the sensitivity of the detector with the accumulation of dose. The presence of deep energy-level defects and trapped charge at the Si/SiO₂ interface also increases the leakage current if the detector is operated in reverse bias; however, this effect is often

mitigated by using the silicon detector in passive or unbiased mode [116, 117]. The variation in the carrier lifetime by irradiation with a photon beam is mainly due to the creation of generation and recombination centres (GRCs) via the interaction of the secondary electrons with a minimum energy of 260 keV with the detector substrate [118]. The concentration of GRC can be managed via defect engineering techniques, such as doping by oxygen or specialised silicon crystal growing technologies. These techniques have been used in the past to mitigate the effect of radiation damage by doping the substrate with impurities, thereby tailoring the transport mechanism of carriers in the lattice generated by the radiation [119].

Brookhaven National Laboratories first developed the oxygen-enriched floating zone (diffusion oxygenated float zone) substrate using oxygen as an aggregator of vacancy defects (V-O complex). This reduces the probability of having divacancy-oxygen complexes, which have a deeper energy level in the forbidden gap (approximately 0.55 eV) and are responsible for creating GRCs. This technique is particularly useful to mitigate the effects of photon irradiation by Co-60 [120]; however, the reproducibility of the fabrication process is very poor and the performance improvement is minimal in comparison to standard floating zone silicon diodes [121]. The same approach was tested using platinum (Pt) as the dopant for *n*-type silicon substrates [122] with similar reliability issues.

More recent investigations have explored the use of silicon *p*-type materials [123]. These studies were motivated by the phenomenon known in *n*-type substrate detectors of doping inversion after approximately 10^{12} cm^{-2} 1 MeV neutron-equivalent radiation fluence for high-resistivity silicon substrates. Inverting the effective doping concentration from *n*- to *p*-type changes the carrier type responsible for generating the electrical signal collected at the electrodes of the detector. The

inversion is due to the divacancy-oxygen complexes, which are electron-acceptor traps. The use of a p -type substrate avoids this effect by employing electrons as minority carriers, thereby making the substrate almost insensitive to the deep energy-level traps generated by the divacancy-oxygen complexes. By manufacturing a detector on a p -type substrate with active region dimensions smaller than the minority carrier diffusion length, it is expected that the sensitivity will remain largely stable and independent of accumulated dose. A small sensitive volume permits using the device in 'passive mode', or with no potential difference between the cathode and anode, thereby generating a depleted region of a few microns depending only on the built-in potential.

Radiation damage research has focused great attention on improving the performance of silicon devices as radiation dosimeters in radiotherapy [124]. Radiation damage manifests its effects by increasing leakage current and varying sensitivity as a function of the accumulated dose [109, 116, 125-127]. Degradation of the silicon p - n junction performance in the radiation field is due to alteration in the electric properties of the silicon junction and silicon oxide layer, SiO_2 [118, 128, 129]. Thus, two categories of radiation damage can affect the efficiency of silicon detectors. The first type refers to bulk damage and is caused by non-ionising energy loss (NIEL), which displaces the atoms from the silicon lattice [130-134]. The second type is surface damage and is caused by ionising energy loss (IEL), which manifests in accumulated positive charges and is trapped in the SiO_2 layer and Si/SiO_2 interface [130-132, 135]. The amount of dose deposited in each type is dependent on the energy and radiation type [136]. The effects of bulk damage and surface damage are discussed in the following sections.

2.7.2 Bulk damage

Bulk damage in silicon detectors can be caused by protons, neutrons, electrons and even gamma rays. Figure 2.4 displays the bulk damage (or ‘displacement damage’) of silicon by charge particles relative to 1 MeV neutrons. Bulk damage is produced by the displacement of a silicon atom from its substitution place to an interstitial place to create a Frenkel pair by fast neutrons, as shown in Figure 2.5. The most essential type of bulk damage is the Frenkel defect [66]. The mechanism of bulk damage by fast neutrons is related to the transfer of energy from the neutron to the recoil atom via inelastic interaction. If the energy transferred to the atom exceeds 70 keV, it can displace the atom and produce the Frenkel pair. If it has sufficient energy, this recoil atom creates a cascade of many interactions [125, 132-134, 137, 138]. As a result, the point defects and clusters are produced, taking into account that the relative number of point defects is higher for protons due to the Coulomb interaction [134]. In the case of charge particles, such as proton and pions, the bulk damage formation is partial clusters and point defects. For gamma radiation using Co-60, the only type of defect created is a Frenkel pair. This mechanism of displacement damage occurs due to Compton electrons. The maximum energy of electrons is around 1 MeV, which is insufficient to produce clusters via gamma radiation. In other words, vacancies and interstitial (Frenkel pairs) are the primary lattice defects in the silicon bulk, as shown in Figure 2.6 [133, 139]. The threshold energy required to dislodge an atom from a lattice site via electrons in the non-ionising energy loss approximation is approximately 200 keV [127, 132, 140], with a cross-section relative to 1 MeV neutron of approximately 10^{-3} .

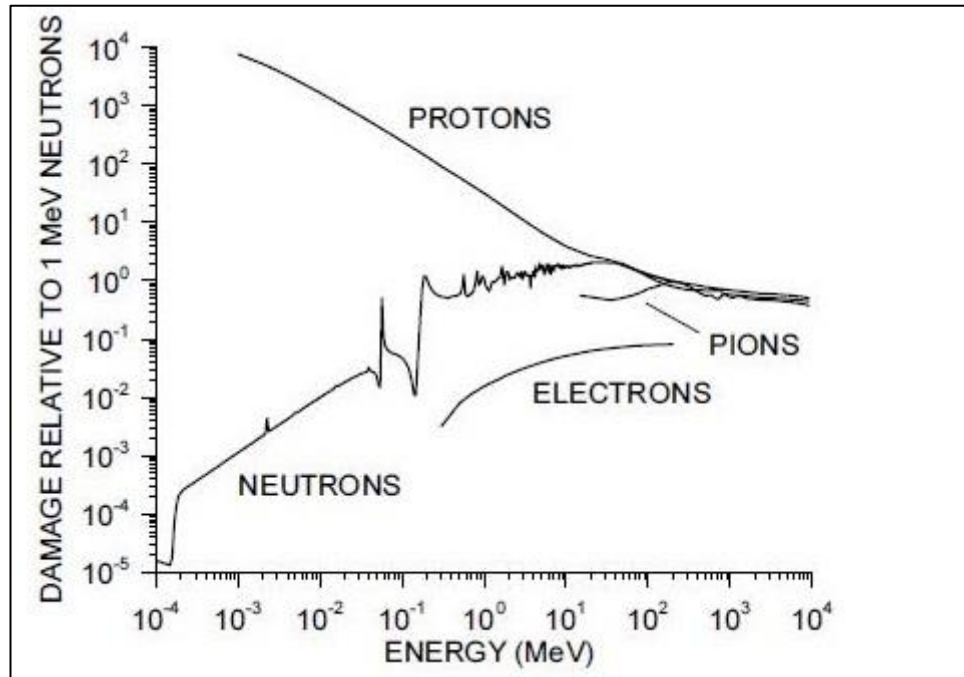


Figure 2.4: Displacement damage v. energy for neutrons, protons, pions and electrons plotted relative to 1 MeV neutrons [132]

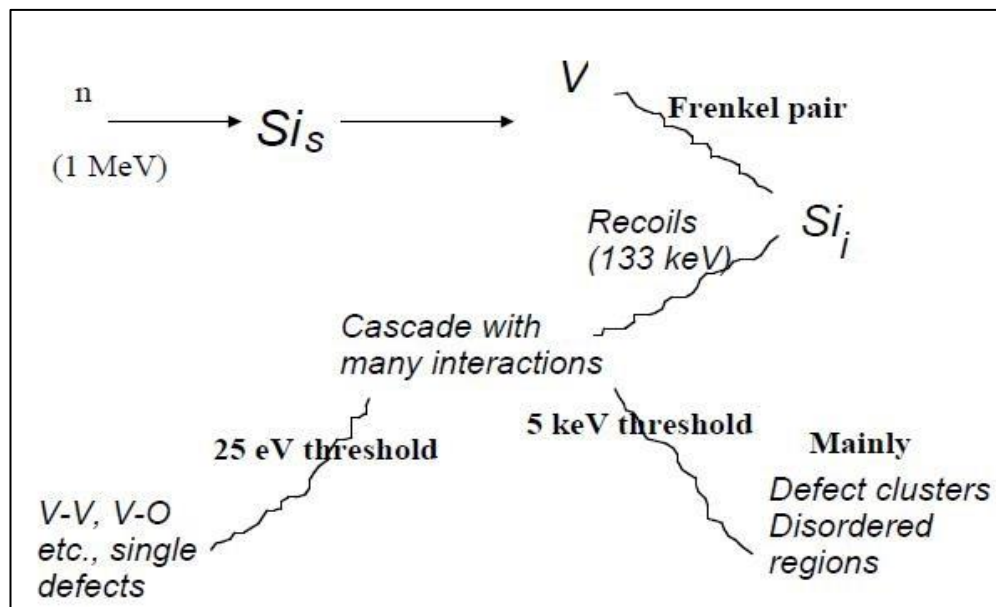


Figure 2.5: Primary and secondary defects in silicon (Si) caused by fast neutrons [125]

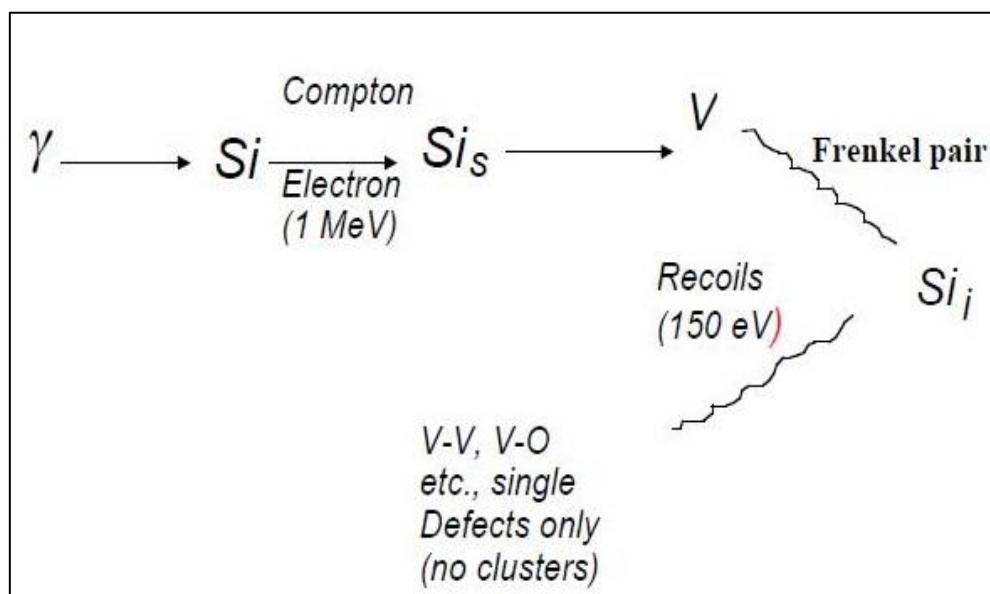


Figure 2.6: Primary and secondary defects in silicon (Si) caused by Co-60 [125]

As seen from the above figures, there are different structures of defects in silicon caused by different radiation types. Table 2.3 qualitatively summarises the defect structures caused by different types of energy. In order to compare the defects caused by different types of radiation, it is necessary to normalise all the effects to the equivalent fluence of 1 MeV neutron [138, 141].

Table 2.3: Different types of defect structures produced by different types of radiation [125]

Partical type	Single defects	Defect clusters
n	x	xxxxx
Charge particles (p, π , etc.)	xxxx	xx
γ , e	xxxxxxx	

Note: The number of 'x's is a qualitative indicator of the amount.

Displacement damage is associated with non-ionising energy loss, which is dependent on the amount of energy and radiation type. Inside the silicon bulk, the displacement damage has several effects on the efficiency of the detector [127, 138]. Several studies have been undertaken to examine defects with different measurement

techniques, such as deep-level transient spectroscopy and thermally stimulated currents [141]. The following sections explore the influence of radiation on the bulk of a silicon detector.

2.7.3 Changing the detector properties

2.7.3.1 Leakage current

It has been already shown that the leakage current increases after radiation for silicon detectors [123, 125, 134, 142, 143]. The increase of leakage current is due to the formation of defects, which form recombination centres in the bulk, with the energy levels of these centres situated in the mid-band gap [132, 141, 144, 145]. The effect of increasing the leakage current is often mitigated by using the silicon detector in passive or unbiased mode [142]. Additionally, many parameters are affected by increasing the leakage current in a silicon diode, including decreasing the signal-to-noise ratio, increasing power consumption and degrading energy resolution [134, 141]. The leakage current density (current per unit volume) also increases linearly with fluence [127, 131, 134, 146].

2.7.3.2 Effective doping concentration (N_{eff})

Another effect observed in silicon diodes after radiation is alteration of the effective doping concentration (N_{eff}) and the voltage required for full depletion (V_{dep}) [123, 131, 146-148]. The effective doping concentration (N_{eff}) and depletion voltage (V_{dep}) are determined from capacitance-voltage (C-V) measurements. The full depletion voltage depends on the effective doping concentration, and is given by the equation:

$$V_{dep} \cong \frac{q_0}{2\epsilon\epsilon_0} |N_{eff}| W^2$$

The radiation-induced generation of deep acceptors in n -type silicon causes the space charge to vary from positive to negative. In view of this, n -type substrates experience

a phenomenon called ‘substrate type inversion’ [66, 131]. Moll, Fretwurst and Lindström described the influence of oxygen concentration on radiation-induced alterations in the effective doping concentration of silicon diode. They found that the high concentration of oxygen enrichment decreases donor removal [147].

2.7.3.3 Charge collection efficiency—trapping

A further effect of bulk damage in silicon diodes is that the charge collection efficiency (CCE) is observed to decrease due to the carrier capture [144]. CCE variation is dominated by three main parameters of the detector: minority carrier lifetime, distribution of the electric field and detector physical volume. Variation of the CCE of silicon detectors is mainly due to the creation of GRC in the substrate via the photon and electron interactions with the detector materials, and accumulation of holes trapped in the silicon dioxide passivation layers.

2.7.4 Surface damage

The second effect seen in silicon detectors after radiation is the appearance of surface damage in the device [141]. Ionisation radiation induces surface damage that leads to positive charge building (holes are trapped into dielectrics permanently) in passivation layers and in the SiO₂ interface [149]. After irradiation, the silicon oxide interface in silicon diodes is distinguished by the existence of a net density of positive charges in the SiO₂/Si interface and by the presence of interface traps [141]. As in the bulk of the silicon detector, electron-hole pairs are formed in the SiO₂ due to the absorbed energy in the material. The energy of ionisation is different to the energy required to produce pairs in the bulk ($E_i = 18$ eV). All the effects created in the passivation layers and SiO₂/Si interface are linked to ionisation radiation (ionising energy loss) [134, 138]. When electron-hole pairs are produced and pass across the passivation layers, they have a high possibility of recombining. The

number of recombined electrons and holes depends on the type of radiation and strength of the electric field. Due to the escaped electrons from the initial recombination, they leave holes behind. Additionally, the mobility of holes in oxide is lower than the electrons. Thus, the holes towards the SiO_2/Si interface are trapped, depending on the direction of the electric field. These holes are captured by oxygen vacancies, thereby causing more positive charges in the oxide, until reaching saturation at a high dose making oxide charge (N_{ox}). Figure 2.7 illustrates the mechanism of formation of oxide charges and interface traps in a metal-oxide semiconductor (MOS).

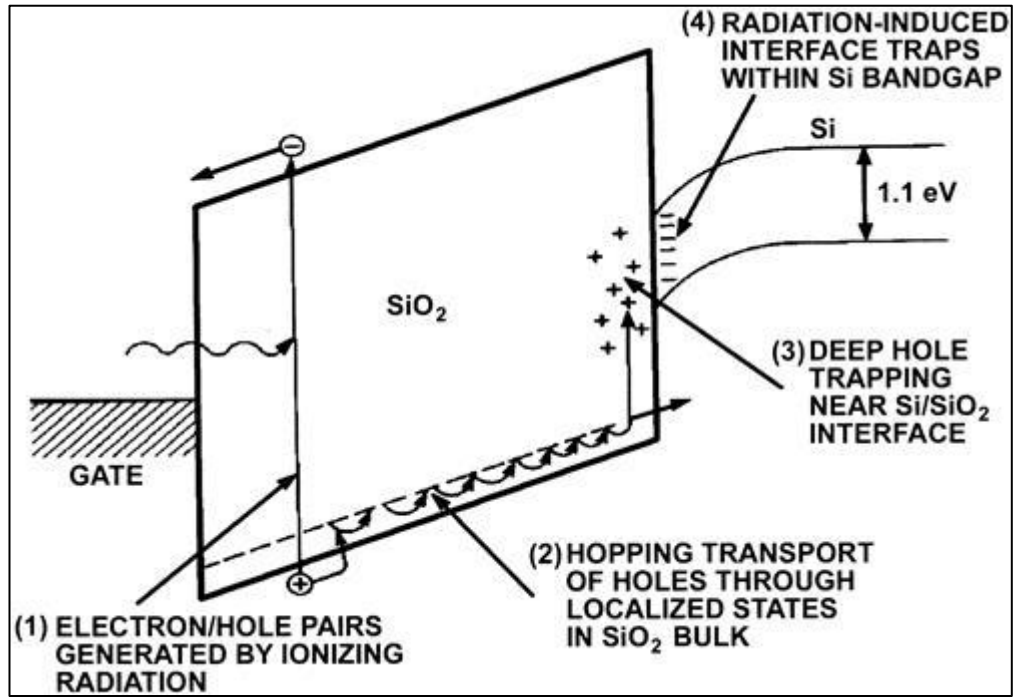


Figure 2.7: The mechanism of surface damage in an MOS [150]

2.7.5 Photoneutron damage

A large number of high-energy medical accelerators with energy above 10 MeV are employed in radiation therapy and have become part of clinical routine [151, 152]. These machines produce photoneutrons that may affect patients in the treatment room and people working in the area [153], as well as affecting the performance of the detectors used for QA. This phenomenon arises when the photon incident has energy greater than the threshold energy of the (γ , n) reaction, and the neutrons are created by photonuclear reaction. These reactions occur in different materials in the LINAC, such as targets, flattening filters and collimation systems [154, 155]. The average energy of the neutrons emitted from the target are 1 to 2 MeV, and these neutrons lose energy until they thermalise due to elastic collisions ($E = 0.0253$ eV) [156]. Further, low-energy neutrons are produced due to scattering events in the room treatment from the wall, maze and floor [157]. Thus, it is important to estimate

the effect created by the neutrons generated by the LINAC to estimate the lifetime of the instrument and the occurrence of recalibration required in such a radiation environment.

2.8 CMRP semiconductor dosimetry solutions

Based on the aforementioned criteria for dosimetry, the CMRP has developed several solutions for dosimetry in EBRT applications. For large area 2-D arrays, a new single epitaxial silicon diode based on a low resistivity *p*-type substrate epitaxial layer was designed and manufactured. The EPI diode was designed specifically for IMRT and VMAT applications for in-phantom dosimetry and *in vivo* photon flux monitoring. The use of ‘transmission mode’ (photon beam fluence is monitored constantly during the patient treatment) requires very high radiation hardness because the detector is exposed to more frequent use than a detector employed only for QA in a phantom. Chapter 3 presents the characterisation of this unusual silicon detector with particular emphasis on its radiation hardness performance. QA dosimetry for modalities such as SBRT and SRS requires very high spatial resolution. CMRP proposes the MP512 detector, which is a monolithic 2-D array of silicon diode manufactured on *p*-type substrate. An important accessory for the MP512 is the rotatable phantom, designed to allow high accuracy positioning of the detector in order to compensate for the intrinsic angular dependence of MP512, and to allow 2-D and 3-D dose reconstruction for pre-treatment QA. For small field radiotherapies adopting circular beam fields, such as stereotactic radiosurgery or Gamma Knife, the CMRP offered a 2-D silicon array named ‘DUO512’, with high spatial resolution and diodes organised only in two perpendicular strip arrays. The following chapters present this collection of devices, and discuss their performance and applications in dosimetry for EBRT.

CHAPTER 3: CHARACTERISING AN INNOVATIVE P-TYPE EPITAXIAL DIODE FOR DOSIMETRY IN MODERN EBRT

3.1 Introduction

This chapter describes the characterisation of the innovative *p*-type EPI diode used in this thesis. It also presents the experimental techniques, setup and simulation by Technology Computer Aided Design (TCAD). It begins by presenting an overview of the materials and devices used. The focus of this chapter is on a complete characterisation of the detector, and discussing its performance in terms of stability and radiation hardness for medical QA applications. The experimental results are compared to a simulation model of the device developed by Sentaurus TCAD (Synopsys, Bulgaria) to enable a deeper understanding of the radiation damage mechanism of the technology adopted to manufacture the silicon diode. Electrical characteristics were measured to determine the leakage currents as a function of irradiation dose, while applied voltage, CCE and radiation hardness were determined by irradiating the detectors by a Co-60 gamma source and an 18 MV medical LINAC with photon-neutron mixed radiation field.

3.2 Materials and methods

3.2.1 Design and fabrication

The silicon diodes presented in this chapter were designed and developed at the CMRP and fabricated at the facility of SPA-BIT (Ukraine). They were used as a sensitive element of MP121—an 11 x 11 array of diodes for 2-D and 3-D dosimetry in EBRT [4]. Figure 3.1 presents the detector structure manufactured on a 50 μm thick *p*-type (100 $\Omega\text{-cm}$) silicon EPI layer grown onto a 375 μm p^+ thick (0.001 $\Omega\text{-cm}$) silicon substrate. The advantage of using an epitaxial layer in radiation detectors is that the sensitive volume is limited via fabrication to the epitaxial layer, and this

limits the effect of variation of the diffusion time by irradiation damage, which is experienced in conventional bulk silicon detectors [142]. The sensitive area of the diode was $0.6 \times 0.6 \text{ mm}^2$, and was defined by an n^+ boron ion-implanted junction. The silicon oxide was grown by water vapour passivation at 900°C . A phosphosilicate glass (PSG) was also deposited on the detector surface for passivation. The detector had an overlap (overhang) of the front aluminium contact of p^+ and n^+ junctions over the oxide layer of $5 \text{ }\mu\text{m}$. A detailed knowledge of the technology used to manufacture the device is crucial for correctly evaluating the damage mechanisms involved in a radiation hardness study. The thickness of the oxides, protection layers, metallic contacts and doping concentrations of the junctions were attentively assessed and modelled by TCAD with the assistance of the manufacturer.

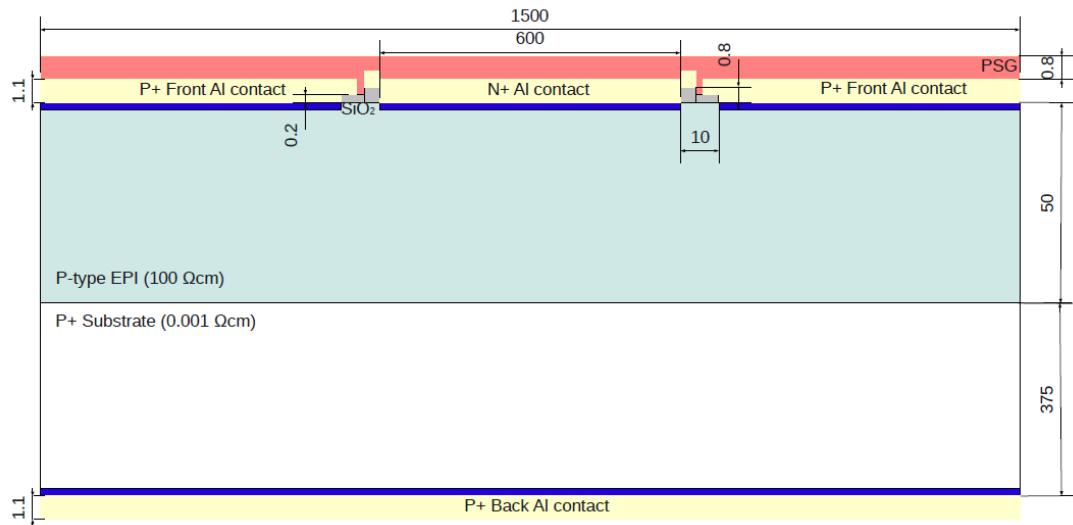


Figure 3.1: EPI diode schematic representation

3.2.2 Detector packaging

The detectors were assembled onto a 0.6 mm thick Kapton pigtail using a specialised technique named ‘drop-in’ [4], which is used to minimise energy dependence and

dose enhancement in a photon field due to the high Z materials that are typically used to package silicon dies. The Kapton pigtails are shielded with thin (70 μm) aluminium foil and grounded to minimise radio frequency noise [158].



Figure 3.2: EPI diode—(a) EPI shielded by aluminium and (b) EPI sensitive volume protected by Kapton

3.2.3 TERA readout system

Each diode was read out individually by a multichannel charge-to-frequency converter preamplifier called ‘TERA06’, designed by the *Istituto Nazionale di Fisica Nucleare*, Turin Division, and the University of Turin microelectronics group [159]. The TERA chip is an application-specific integration circuit (ASIC) designed to readout pixel and strip detectors [160]. The device is capable of zero dead-time readout of the integrated charge over a variable acquisition time (for the experiments presented in this chapter, this was set to 100 ms per frame). TERA was originally designed for ionising chambers and used in a system called the ‘Magic Cube’—a pixel ionisation detector for hadron therapy—and in commercial devices, such as MatriXX from IBA (Germany) [159, 161].

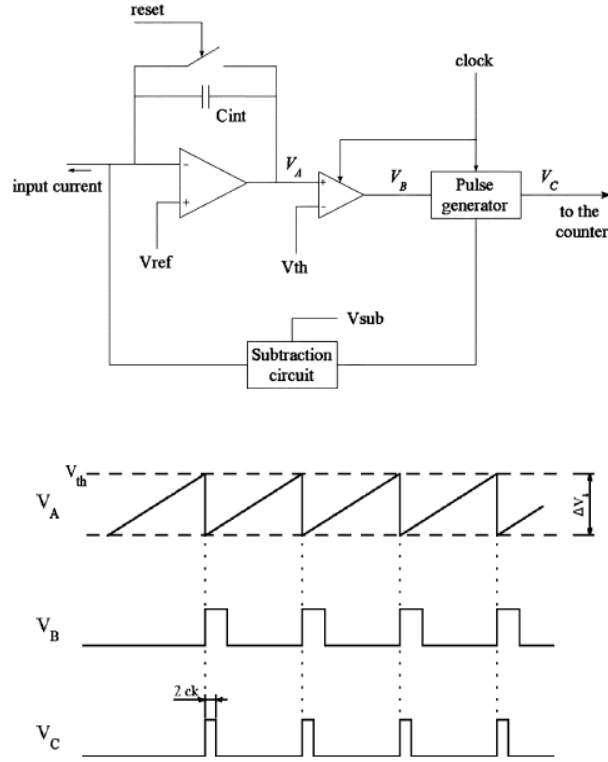


Figure 3.3: Schematic diagram of the TERA readout [159]

3.2.3.1 Brief description of how TERA works

The TERA ASIC is based on a current-to-frequency converter, followed by a 16-bit digital counter with large dynamic range (65535 counts), as depicted in Figure 3.3. The conversion from current (I) to frequency (F) is based on the charge-balancing integration technique [160]. In this regard, the charge can be measured by counting the number of pulses emitting from the convertor at a given time. When the radiation incidents on the silicon diode, it creates electron-hole pairs in the silicon and thus creates a current measurable at the electrodes. This current is called the ‘input current’ (I_{in}). The I_{in} is integrated through a capacitor (C_{int}) by the operational transconductance amplifier (OTA). The integrator output that results from the OTA is the voltage ramp (V_A). In the comparator, the ramp voltage is compared with the constant voltage (V_{th}). If the ramp voltage $V_A > V_{th}$, the comparator fires a calibrated

pulse (V_B), which is sent to the circuit input by the pulse generator (PG). The calibrated pulse (V_B) triggers the PG to output two pulses—the first must be sent to the digital counter and the second to the subtraction circuit. Therefore, the pulse generated by the PG to the subtraction circuit charges up 200 fF of subtraction capacitor (C_{sub}). Figure 3.4 shows that the output response of the C_{sub} to V_{sub} is two waveforms that have similar current pulses, but different polarity.

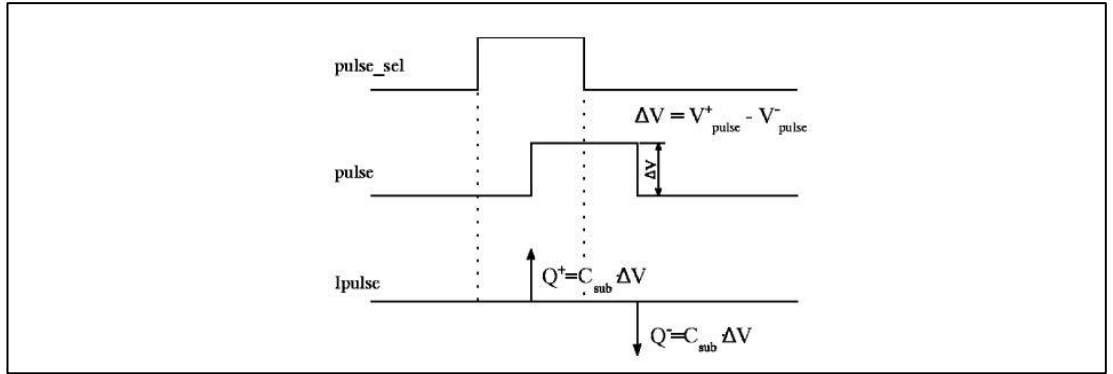


Figure 3.4: Charge subtraction waveforms [159]

The amplitude of the V_{sub} is defined by the difference of two voltages: V_{pulse+} and V_{pulse-} . Consequently, a fixed amount of charge (quantum charge) is subtracted from the input current, and the pulse with the voltage output that has the same polarity is shorted to the OTA. This results in a sharp reduction in charge across C_{int} , proportional to the charge released by the subtraction circuit [159]. When the input voltage still exceeds the threshold voltage in the comparator, the pulses continue to be sent to the counter and the subtraction circuit by the PG. The PG will stop sending pulses when the integrated charge through the C_{int} is below V_{th} . Using the charge-balancing technique, the fixed amount of quantum charge is subtracted from the main integrator capacitor (C_{int}) [159]. As a result, the main capacitor, C_{int} , continues to integrate. In that situation, the dead-time is introduced when the capacitor is resting

due to the conventional resetting of the C_{int} being high. The charge quantum can be defined as the Q_c being the unit charge needed for one count. The charge quantum can be expressed by the equation:

$$Q_c = C_{sub} \cdot \Delta V \quad (3.1)$$

where ΔV is the difference between V_{p+} and V_{p-} . These parameters are set externally and used to clarify the charge quantum. The charge quantum can be changed depending on the application. However, there is a minimum limit to set the charge quantum, which is dependent on the resolution of the comparator, which is 100 fC. The frequency of pulses is proportional to the input current, and can be described by:

$$f = \frac{I_{in}}{Q_c} \quad (3.2)$$

There is a limit of the maximum input current, which is determined by the PG. The limit of the current-to-frequency convertor is 5 MHz, and the lowest time between two pulses is 0.2 μ s. Therefore, the limit of the maximum input current is 3 μ A. When the current is overloading, the subtraction circuit cannot follow with integrated charge throughout C_{int} . In this regard, the voltage input to the comparator, V_A , continues to be higher than V_{th} . This leads to issue pulses with a maximum speed by the PG, until the overload is removed and $V_A < V_{th}$.

When using LINAC radiation, the beam generates a pulse in a 470 μ m *p*-type silicon substrate, corresponding to a current of approximately 7 μ A within a very short pulse width of 3.5 μ s. In the case of 100 to 600 MU/min recurrence rate, the range of pulse period may be from 16 to 2.7 ms. With a short pulse width of 3.5 μ s, the high input current charges the main integrator capacitor, C_{int} , to be more than V_{th} . In this case, it is impossible to bring the charge below the threshold value with a single charge quantum, Q_c , pulse. Consequently, at a maximum speed, the PG is run to issue pulses

to the subtraction circuit until the overload is removed. LINAC pulses have the advantage of having a long period (1.6 to 2.7 ms), which means the subtraction circuit has sufficient time to remove the overload before reaching the next pulse. It is important to ensure that the input current generating voltage on the capacitor does not go above the positive rail voltage. If this occurs, the output counts will be saturated. In that case, the generation of counts will be constant, even if the input current increases. Intuitively, setting the Q_c to a high value enables subtraction of the input current to occur at a faster rate. This is created at the expense of a lower sensitivity of the counts generated.

The data acquisition system (DAQ) used for the EPI diodes employs two TERA chips, with each TERA ASIC containing 64 independent channels—a total of 128 channels. All channels were coupled to an individual digital counter, followed by a 16-bit register with a common load command. This helped the counters collect the counts and readings at specific times. The next section describes the DAQ system used in this chapter.

3.2.3.2 DAQ

The DAQ software was written by QT C++ (Nokia, Sweden). This software, developed by CMRP, has the ability to allow online and offline analysis. Figure 3.5 shows the layout of the software—named ‘Rad-X Dose View’—that was employed to acquire all the response data of the detectors. The Rad-X Dose View interface allows the user to see the response of the detectors in real time. Further, the integral response of the detectors at the time of integration set by the operator can be visualised. The readout frequency is between 50 Hz and 1 kHz, and can be defined by the user.

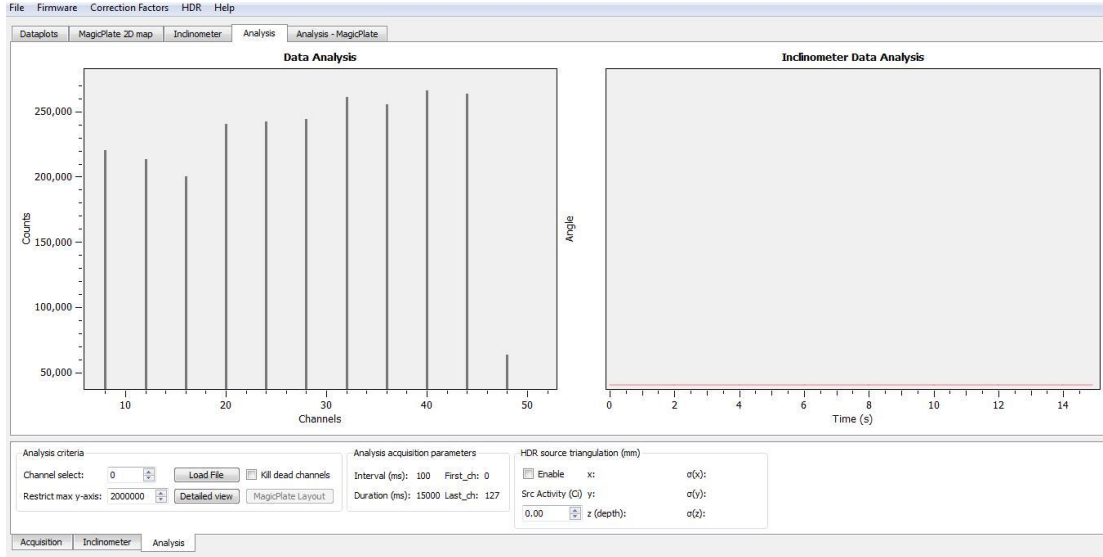


Figure 3.5: Rad-X Dose View interface

The software stores each acquisition to calculate the total dose, dose rate and timing behaviour of the input signal. The interval time can be set from 0.1 to 100 ms, and this parameter is used to determine how long accruing occurs for each frame measurement. The duration time is used to determine how long the total measurement takes, and can be set from 30 ms to 10 minutes.

3.3 Pre-irradiation characterisation

3.3.1 Current-voltage characteristics

For ideal p - n junctions, the current density is given by the ideal diode equation (shown in Equations 3.3 to 3.8), obtained from [162]:

$$J = J_s \left(e^{qv/kT} - 1 \right) \quad (3.3)$$

where: J_s = the saturation current density

q = the fundamental charge

V = the applied bias

T = the temperature of measurement.

When a reverse bias is applied, the current density saturates at $-J_s$, which is given by the sum of the diffusion currents only. For silicon junctions, the ideal diode equation can only give qualitative agreement due to the generation and recombination of the charge carriers in the depletion region. The current density due to the generation/recombination (GR) of carriers in the depletion region is given by two contributions: band-to-band GR current density and Shockley-Read-Hall (SHR)–GR current density:

$$J_{b-b} = q \int_{-x_p}^{x_n} n_i^2 (e^{V_a/V_t} - 1) dt = q n_i^2 b w (e^{V_a/V_t} - 1) \quad (3.4)$$

The SHR-GR current density can be expressed by:

$$J_{SHR} = \frac{q n x_i}{2\tau} (e^{V_a/2V_t} - 1) \quad (3.5)$$

where: x_i = the width of the depletion region
 τ = the generation lifetime of the carriers
 n = the intrinsic carrier density.

This is the case if the number of acceptors, \mathbb{T} , is far greater than the number of donors, and the reverse voltage, V , is greater than 3 kT/q . The reverse current density can be approximated by the sum of the diffusion current in the neutral regions and the generation current in the depletion regions, which is given by:

$$J_R = J_{\text{Diffusion}} + J_{\text{gen}} = q \sqrt{\frac{D_p}{\tau_p}} \frac{n_i^2}{N_D} + \frac{q n_i W_d}{\tau_g} \quad (3.6)$$

where: W_D = the depletion layer width
 τ_g = the generation lifetime.

For silicon, the intrinsic carrier density is relatively small; thus, the above equation is dominated by the generation current density term. As a result, the reverse current density is approximately proportional to the depth of the depletion region of the p - n

junction. The width of the depletion region is also increased by the applied reverse bias and expressed by the equation:

$$x_d = \sqrt{\frac{2\epsilon_0\epsilon_{Si}(V_{bi} - V_R)}{qN_{eff}}} \quad (3.7)$$

where: ϵ_{Si} = the dielectric constant of silicon
 ϵ_0 = the permittivity of free space
 Ψ_0 = the built-in potential of the p - n junction
 V_R = the external applied reverse bias.

Equation 3.6 indicates that the square of the depletion region width is proportional to the applied external bias. Thus, from Equation 3.5, it can be said that the reverse current density is also related to the applied external bias by the same proportionality. The macroscopic effect on the device characteristics is the variation of the effective resistivity ρ , which becomes:

$$\rho = \frac{1}{\mu_p N_{eff}} \quad (3.8)$$

where: μ_p = the hole mobility.

Therefore, Equation 3.7 indicates that the depletion width, and hence the reverse current density, is proportional to the square root of the resistivity of the silicon bulk.

3.3.2 Experimental methods

In this chapter, 20 samples of EPI diodes were tested before and after irradiation. Prior to detector irradiation, a current-voltage (I-V) analysis of the detectors was performed using a Keithley 230 programmable voltage source to apply the detector bias, coupled to a Keithley 199 System DMM/scanner and Keithley 614 electrometer to measure the reverse current across the detector. I-V curves can be used to assess

the uniformity of the detectors' performance within the batch of production, and to determine any radiation damage effects after the detectors were irradiated.

A negative bias (from 0 to -100 V) was applied on the bulk p^+ substrate, and current was measured across the junction defined by the n^+ region. During the measurement process, the detector was placed in a light-tight chamber at atmospheric pressure and ambient room temperature (~ 295 K) to replicate the conditions in which the detectors would likely be used during clinical applications. Figure 3.6 shows the diagram of I-V setup for testing the EPI diodes.

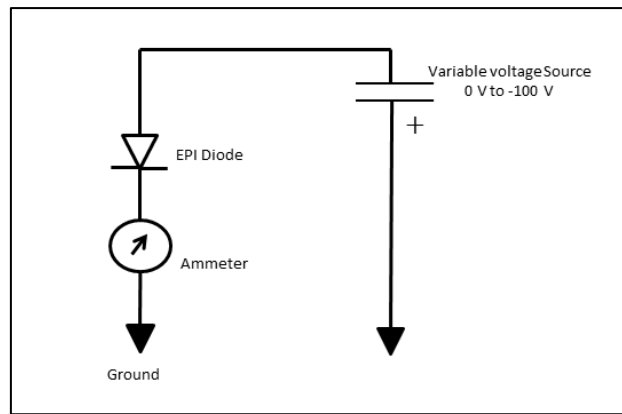


Figure 3.6: Measurement of I-V circuit diagram—EPI without guard ring

The data measurements and parameters were driven by a custom LabVIEW software driver. This software has the ability to define the parameters of the experiment, such as voltage range (from 0 to -100 V), step amplitude (-0.5 V) and delay time interval (two seconds). In addition, the interface displays the variation of the current as a function of the bias applied with the increment defined by the operator (set to 0.5 V for this set of measurements). The uncertainties for all I-V plots were dependent on the 6.5 digit accuracy scale of the instrument that was used in this experiment. Uncertainties were calculated as two SDs of five repetitions.

3.3.3 Capacitance-voltage characteristics

The C-V characteristic is an essential test to evaluate the effects of radiation on the effective doping concentration of the device [139]. Further, C-V tests are extremely important to estimate the depletion bias. This can be achieved by measuring the capacitance against an applied reverse bias. Increasing the voltage in the device leads to a decrease of capacitance, where:

$$C \propto \frac{1}{\sqrt{V}} \quad (3.8)$$

The capacitance decreases until reaching full depletion. Applying voltages higher than the depletion voltage does not alter the depletion width. The capacitance of the junction is given by:

$$C = \frac{\epsilon_0 \epsilon_{si}}{x_d} = \sqrt{\frac{q \epsilon_0 \epsilon_{si} N_{eff}}{2(V_{bi} - V_R)}} \quad (3.9)$$

where:

- ϵ_{si} = the dielectric constant of silicon
- ϵ_0 = the permittivity of free space
- q = the charge of an electron
- x_d = the width of the depletion region
- V_{bi} = the junction built-in potential
- V_R = the externally applied reverse voltage.

3.3.4 Experimental methods

Twenty samples of EPI detectors were tested. The C-V characteristics were determined using a Boonton 7200 Bridge Capacitance Meter. This meter imposes a sinusoidal signal of 1 MHz into the $p+$ input of the detector. The capacitance measured in this manner is a differential capacitance equivalent to the parallel equivalent capacitance of the depletion area altered by the negative bias applied at the $p+$ contact.

The data measurements and parameters were driven by a custom LabVIEW software interface. A negative bias was applied (from 0 to -50 V with a step size of -0.2 V) and delay time of 100 ms to allow for stabilisation of the capacitance after applying the bias. For this series of measurements, the detectors were kept in a light-tight chamber at atmospheric pressure and ambient room temperature (~ 295 K). The uncertainties for all C-V plots were dependent on the 3.5 digit accuracy scale of the instrument. Figure 3.7 shows the diagram of the C-V setup.

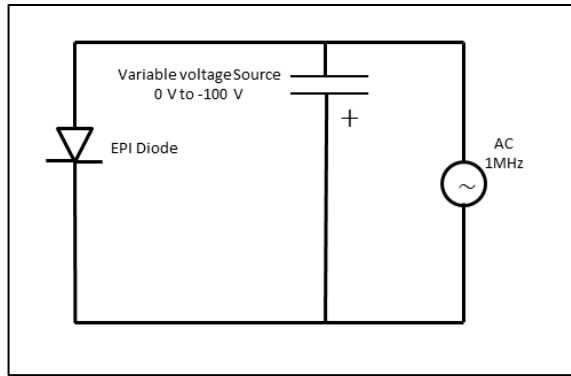


Figure 3.7: Measurement of the C-V circuit diagram—EPI without guard ring

3.3.5 Diode response measurements

The EPI diode response, before and after irradiation, was tested at the Illawarra Cancer Care Centre of Wollongong using a Varian 2100C LINAC under conditions typical for radiation therapy treatments. The response of the detector was measured at zero Mrad by collecting the charge generated in the EPI diode for an absorbed dose of 100 cGy in water, using 6 MV x-rays at a dose rate of 600 MU/min and a 20 x 20 cm² field size. The diodes were placed at an SSD of 100 cm and depth of 1.5 cm in a water-equivalent phantom. The EPI detectors were placed on top of a 30 x 30 cm² solid water block. The use of solid water materials was to provide scatter around

the detectors. Figure 3.8 (right) shows the EPI samples inserted into an electronic board connected with the TERA readout system. The pre-irradiation response test was performed for all samples and repeated after each Co-60 and photoneutron irradiation from the 18 MV LINAC. Figure 3.8 (left) displays the experimental setup.

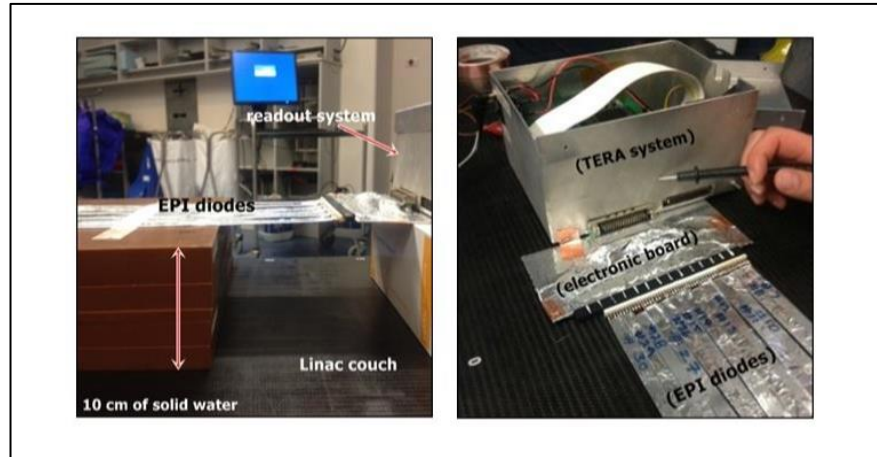


Figure 3.8: Experimental setup for EPI diodes with LINAC readout system (left) and TERA readout system (right)

3.3.6 Radiation hardness characterisation

3.3.6.1 Introduction

The samples were irradiated using the Gamma Technology Research Irradiator (GATRI) at the Australian Nuclear Science and Technology Organisation (ANSTO) facility in Lucas Heights, New South Wales. GATRI uses a Co-60 source, and the dose rate delivered by the source was in the range of 0.1 to 4 kGy/h. The Co-60 has two photopeaks with energies of 1.17 and 1.33 MeV. The mean energy of the Co-60 was considered approximately 1.25 MeV.

After determining the response before irradiation by the 6 MV x-ray accelerator, the detectors were irradiated up to the 120 kGy water-equivalent absorbed dose using the highest dose rate available (approximately 3.2 kGy/h at the time of irradiation). The

dose (measured in water) was delivered in 10 kGy irradiation steps to a total of 40 kGy, and then in increments of 20 kGy up to 120 kGy. Irradiation was performed while keeping the temperature below 30°C, and no bias was applied to the detector in order to mimic the standard use of the device during clinical operation. The response of the detectors after each irradiation step was performed by the 6 MV rays at a dose rate of 600 MU/min and 20 x 20 cm² field size. The diodes were placed at an SSD of 100 cm and depth of 1.5 cm in a water-equivalent phantom.

3.3.6.2 Radiation hardness study by photoneutrons

The radiation damage due to photoneutrons was evaluated by stimulating the samples in an 18 MV photon field using a medical LINAC at Saint George Cancer Care Centre (Kogarah, Sydney). Photons with energy higher than approximately 7 MeV can produce secondary neutrons via the (γ ,n) interaction [163, 164] with gantry head materials, such as the tungsten of primary collimators and jaws. Further, there is a study that shows the photoneutron can be produced from 6 MV [203]. It is important to estimate the effect of the neutron dose from a LINAC because of the different nature of radiation damage induced by radiation in the substrate, in comparison with photons. The neutrons generated by an 18 MV LINAC have an average energy of 1 to 2 MeV [155-157, 163], and thermalise travelling into the phantom. At this energy range, the neutrons produce cluster defects with the displacement of silicon atoms in the crystalline lattice. These defects generate highly packed (very high density in space) recombination centres with energy ranges localised deep in the forbidden gap, which reduces the responsiveness of the detector.

Radiation damage in EPI diodes produced by the 18 MV LINAC was assessed by delivering a 285 Gy photon dose in water to 20 samples placed at the surface of a water-equivalent phantom at an SSD of 90 cm. Under these conditions, the on-axis

photoneutron dose was approximately 1.2 Sv, based on the neutron dose equivalent per unit photon dose of 4.5mSv/Gy, evaluated by D’Errico for a GE-Saturne 20 LINAC [163]. It has been assumed that the spectrum and intensity of photoneutron fluence is not strongly affected by the machine model and manufacturer, as demonstrated in a study by Howell et al. [165]. Following this, the response of the EPI detectors was investigated under the same conditions as those used to measure the response before irradiation.

3.3.7 Simulation

3.3.7.1 Introduction

TCAD simulations were performed to investigate the intimate mechanisms of radiation damage behind the macroscopic variation of the detector response. The model of the device developed to simulate the leakage current, capacitance and CCE took into account the real junction doping concentrations, substrate initial doping and geometry of the EPI diodes.

3.3.7.2 Detector simulation

The CCE and built-in potential distribution of the detector structure were simulated by means of TCAD Sentaurus Device (Synopsys, Bulgaria) [166]. This software is based on a finite-element method that incorporates several physical models to describe carrier transport and generation and recombination processes. Given that it is based on a finite-element method, the model is discretised by a grid (called ‘mesh’) and equations are solved in each node of the mesh, which is optimised for the specific geometry of the device. The model used in the physics session of the Sentaurus Device command file for transport simulation is the *Mobility (DopingDep, HighFieldsat, Enormal)* model, which includes Poisson and mobility equations, as well as the dependence of the carrier mobility from doping concentration and

mobility saturation in the presence of high electric fields. The model used to simulate the recombination processes is *Recombination (SRH, DopingDep)*, which takes into account the variation of the effective doping concentration with radiation damage by including the optional model named *Traps*. The model used to represent the minimum ionising particle (MIP) and calculate the CCE is *HeavyIon (Let_f; length; wt_hi; time; location; direction)*, where *Let_f* represents the charge deposited by the particle along a track with a defined length and lateral exponential distribution with a half-distance of *wt_hi* hitting the detector surface at a certain instant time, location and direction.

The *Traps* model used to simulate the effects of radiation damage enables the parameterisation of the trapped charge at the S_i/S_iO_2 interface and the definition of point defects uniformly distributed in the silicon substrate. This model specifies the GRC energy levels in the forbidden band gap, the defect concentration proportional to the irradiation dose in water ($D_{(kGy)}$) and the cross-sections for electrons and holes. This approach has been successfully used in the past to model the radiation damage in a *p*-type silicon device for the irradiation total dose scenario predicted for the large hadron collider [123, 148]. Defects generated in a silicon substrate by Co-60 photon irradiation are principally related to the interstitial carbon-oxygen complex (C_i-O_i) and divacancy (V_2), with no experimental evidence of cluster or deep energy-level defects [167]. These can be simulated by a two-level radiation damage model, as summarised in Table 3.1.

Table 3.1: Two-level radiation damage model

Energy (eV)	Type of defect	Introduction rate (cm ⁻¹)	Cross-section (cm ⁻²)	
			Electrons	Holes
$E_v + 0.36$	C_i-O_i Donor	$1.826 \cdot 10^{12} D_{(kGy)}$	$2.5 \cdot 10^{-14}$	$2.5 \cdot 10^{-15}$
$E_c - 0.42$	$VV^{(-/0)}$ Acceptor	$3.04 \cdot 10^{12} \cdot D_{(kGy)}$	$2 \cdot 10^{-15}$	$2 \cdot 10^{-14}$

As discussed by Moll et al., irradiation by a photon field also contributes to the generation of a positive trapped charge in the Si/SiO_2 interface [167]. The main effect is the accumulation of a negative inversed charge layer in proximity to the interfaces. A TCAD model has been developed by taking into account the introduction of a uniform layer of positive charges at the interface from 10^9 to $10^{13} \text{ e}^-/\text{cm}^2$ for an irradiation range from 1 to 10 Mrad in silicon dioxide. For particles with low linear energy transfer, such as Co-60 gammas, pair volume density in silicon oxide increases at first approximation linearly with irradiation, and is equal to approximately $4 \times 10^{12} \text{ cm}^{-3} \text{ rad}^{-1} (\text{SiO}_2)$ [168], taking into account a fractional yield of 0.5 at zero volt biasing. Saturation typically occurs at $10^{-12} \text{ e}^-/\text{cm}^2$ in wet grown silicon dioxide, as demonstrated by several experimental studies [168].

3.4 Results

3.4.1 Electrical characteristics

The I-V and C-V characteristics of the silicon EPI detector were measured before and after irradiation in order to certify the simulation model. Figure 3.9 shows the I-V characteristic in reverse bias for EPI diodes. This was measured prior to irradiation. Some variation between detectors was observed, which was expected due to the growth process. The detectors' reverse current increased as expected for a pad detector, without breakdown up to 100 V. Some samples show the reverse current increasing linearly with voltage, identifying a shunt resistance associated with the reverse saturation current of approximately $400 \text{ } \Omega$, which is in good agreement with the results obtained from different groups working on low resistivity pad *p*-type silicon detectors [142].

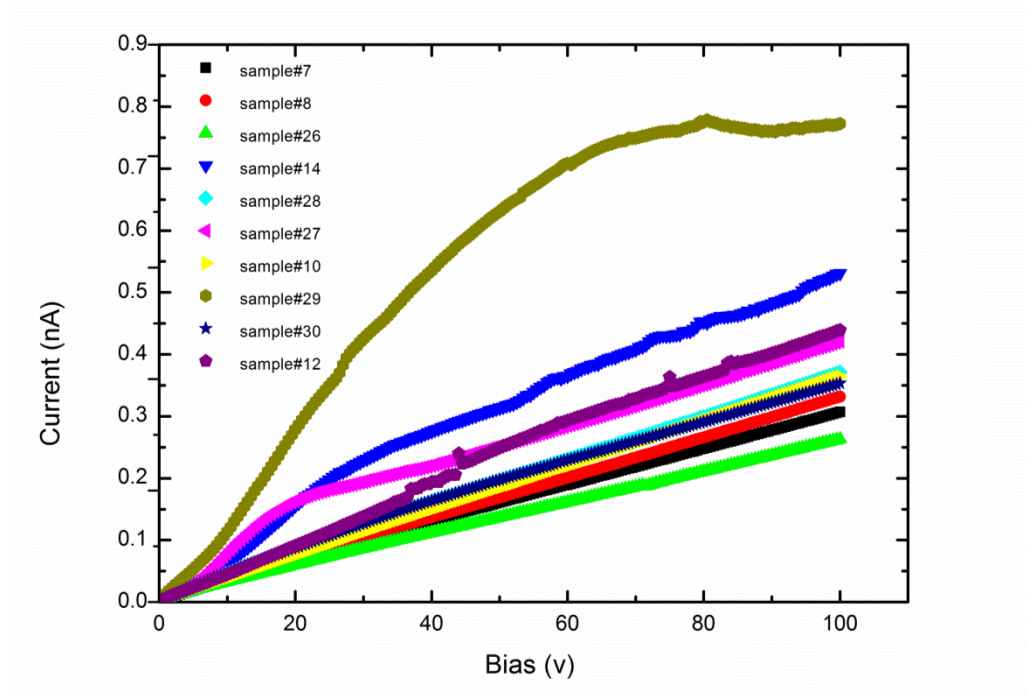


Figure 3.9: I-V characteristics from a few samples of EPI diodes, without guard ring

Figure 3.10 shows the C-V characteristic of EPI diodes, which are derived from the depletion region capacitance measured in reverse bias. All EPI detectors indicate a steep fall in capacitance at low voltage, then variations to a gradual fall. When the voltage increases, the fall in capacitance becomes negligible. The initial reduction of the capacitance of EPI detectors is due to an increase of the depletion width as the voltage increases. As the lateral and bulk depletion reach their limit of $50\ \mu\text{m}$ (defined by the lateral distance of the pad detector from the p^+ superficial implant and from the epitaxial layer), the fall in the capacitance is negligible, which indicates that the diodes are fully depleted.

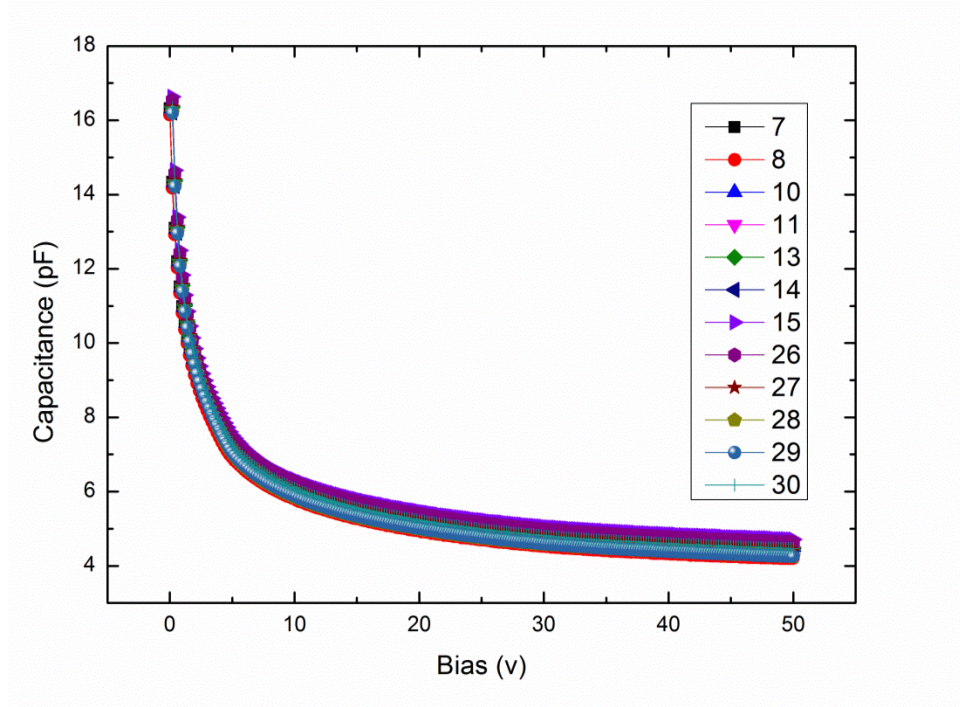


Figure 3.10: C-V characteristics from a few samples of EPI diodes, without guard ring

Figure 3.11 shows the validation of the simulation model by using experimental results obtained from a few samples from the same production batch. The doping concentrations and profiles of the simulated device were tuned to fit the experimental results and to remain compatible with the process parameter ranges adopted by the manufacturer. Figure 3.11 shows the trend of the simulated leakage current as a function of the reverse bias, compared with the measurements taken from four samples. The simulation data follow the ideal $n + p$ junction I-V, proportional to the square root of the reverse potential. The simulation considers the generation of surface leakage currents, which has little or no effect when the detector is not irradiated. However, the experimental data show a range of slopes of the I-V of the samples that varies from 80 to 150 pA at 10 V. This variation could be related to the specific position of the sample in the wafer during the manufacturing process, or the

surface defects induced by the mechanical stress created during the cutting of the samples. The simulation model fits the range of the measured leakage current within $\pm 25\%$.

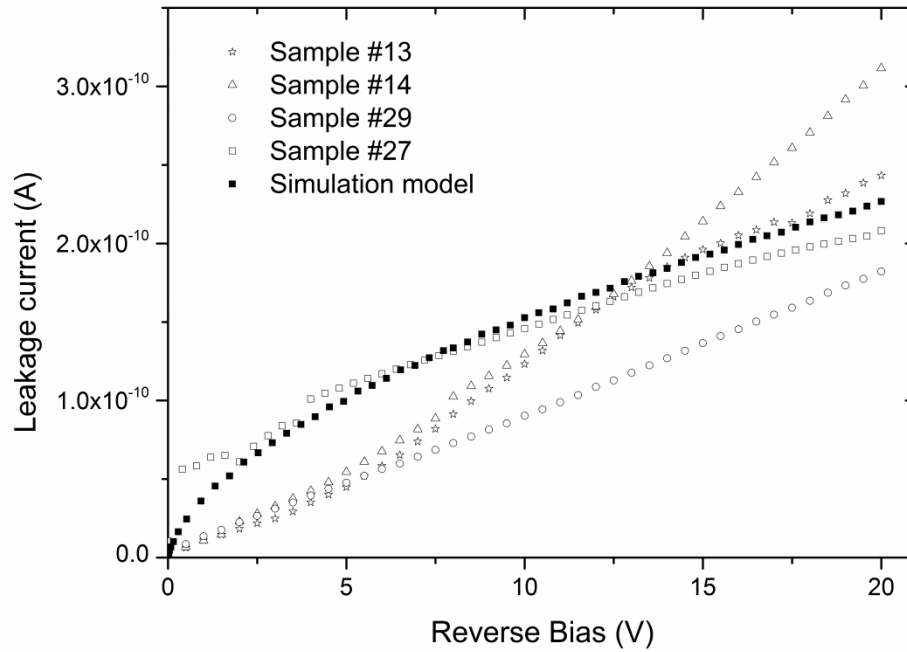


Figure 3.11: Collection of I-V experimental results from a few samples, and comparison with the I-V of the simulation model

The same detector model was used to simulate the capacitance as a function of the reverse bias, and was compared with the measurements, as shown in Figure 3.12. The discrepancy between simulations and measurements was due to the effect of the packaging of the detector, which increased the equivalent detector capacitance of approximately 2 pF for the entire range of bias measured.

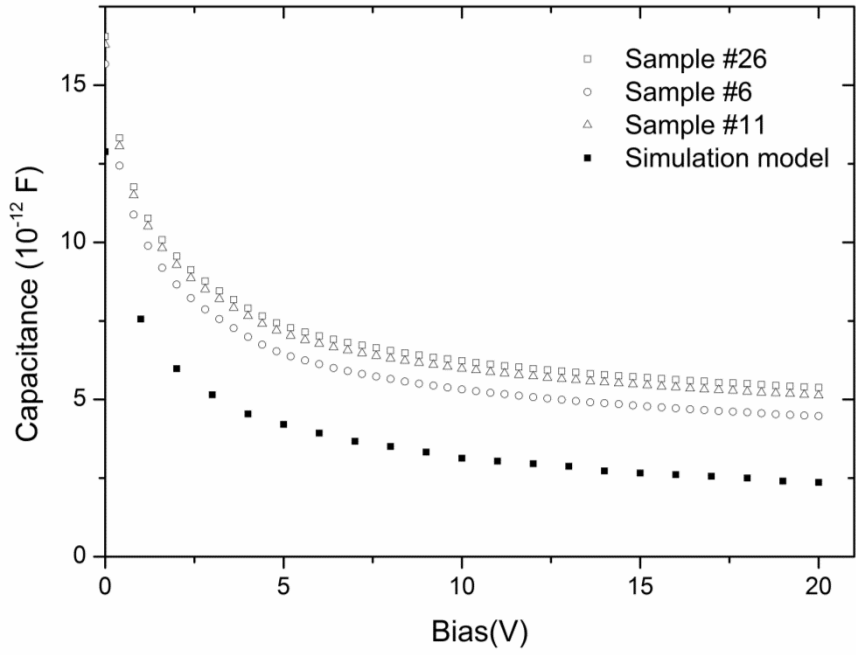


Figure 3.12: Collection of I-V experimental results from a few samples, and comparison of the measured and simulated C-V of the EPI diode

Note: The fixed gap of approximately 2 pF is due to the effect of the packaging on the equivalent capacitance seen by the instrument.

3.4.2 Damage rate calculation (α)

The current increases due to radiation-induced defects. The leakage current, ΔI , can be calculated by determining the difference between the current measured before and after irradiation. Figure 3.13 shows the volumetric leakage current density measured at a reverse bias of 20 V as a function of accumulated dose. Each point represents the average of three samples irradiated by the same dose, and the error bars represent two times the SD. Variation of the leakage current due to increase in the concentration of radiation-induced defects in the device substrate and S_i/S_iO_2 interfaces is often represented by the radiation damage rate, α , as supported by other studies [167, 169]. The damage rate was estimated at $\alpha = 1.76 \pm 0.2 \cdot 10^{10}$ A/cm³Gy.

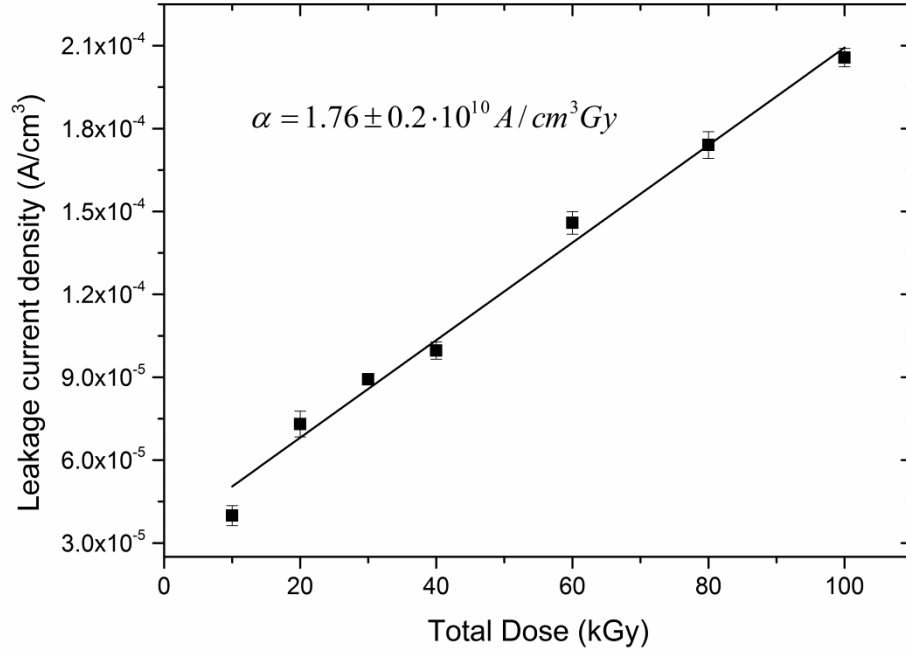


Figure 3.13: Average leakage current density of a set of 20 samples as a function of the total dose measured at 20 V

3.4.3 CCE

Based on results from the literature [96, 110, 142, 170], the expected trend of the CCE is represented by a drop of the response as a function of the accumulated dose. This characteristic is well understood and obtained by the variation of the carrier lifetime as a function of the concentration of GRC in fully depleted detector substrates. In medical radiation applications, silicon detectors are used mainly in passive mode (zero volts applied at the electrodes) to minimise variation in the leakage current and consequent variation in the baseline of the signal, which requires time-consuming and frequent recalibration procedures. This operative modality dramatically changes the macroscopic effects of the radiation damage in a silicon device because the collection volume is defined only by the area of the junction and

the depletion layer generated by the built-in potential, which corresponds to few microns in a 100 Ω -cm substrate.

The TCAD simulation of the depleted layer thickness variation as a function of the radiation damage (taking into account both the bulk GRC and oxide trapped charge), showed that the depth of the depleted region was approximately 4 μm . It indicated that its variation with the accumulated dose was minimal. In contrast, the lateral depletion increased by a factor of three due to the generation of an accumulation layer of negative charge at the Si/SiO_2 interface, as seen in Figure 3.14.

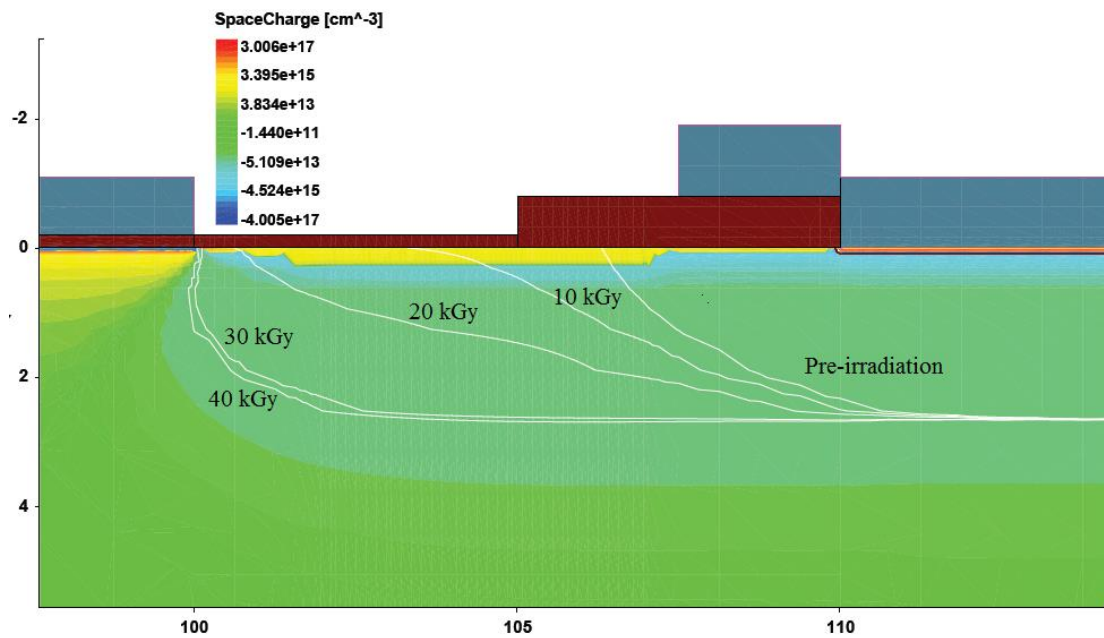


Figure 3.14: The space charge distribution and variation of the lateral depletion region as a function of the irradiation dose (white line)

Note: The distance units are microns.

The CCE variation as a function of the radiation damage was evaluated by simulating an MIP hitting the device perpendicularly, with no bias applied at the electrodes. TCAD simulates the transience of the current generated at the electrode and induced

by the diffusion of the charge generated by the MIP (80 e/h pairs μm). The collected charge is calculated as the integral of the current signal over several hundreds of nanoseconds. A non-irradiated device was simulated with an initial concentration of trapped charge at the Si/SiO₂ interfaces of 10^7 cm^{-2} , with no point defects in the substrate. The simulation was repeated by increasing the trapped charge and bulk GRC concentrations based on the radiation model described previously. The simulated charge collected before irradiation was $1.25 \times 10^{-16} \text{ C}$, corresponding to the charge generated in approximately a 9 μm thick silicon layer by an MIP, as seen in Figure 3.15 (left). The trap concentration values that were simulated considered previous studies, where measurements of the trapped charge were performed on similar planar devices [118].

The data obtained were strongly dependent on the geometry of the detector and dimensions of the silicon oxide grown around the $n + p$ junction. Figure 3.15 (right) shows the measurement of the relative response of a collection of 20 samples as a function of the accumulated dose when operated in passive mode. The CCE increased by a factor of four after 40 kGy (H₂O) and remained stable until 120 kGy (H₂O), with $\pm 5\%$. The experimental results showed an increase of the response even higher than that simulated by TCAD. This residual increase could be related to a beneficial radiation ‘gettering’ effect, related to the transfer of the energy generated by the radiation in the superficial layers of the device to the lattice and the Si/SiO₂ interfaces, which relax the mechanical stresses generated by the ion implantation and the silicon oxide growing. Despite the limited literature available about such a mechanism [171-173], it has been proven that irradiation of a device may cause a decrease in the structural defect density, the mechanical relaxation of stress in multilayer structures, and the saturation of the GRC produced during the

manufacturing process of oxides—especially in oxygen-enriched vapour atmospheres. All these mechanisms could explain the further improvement of the CCE observed in the experimental measurements, in addition to the effect of the inverse layer in p-Si below the Si/SiO₂ interface due to the build-up of the positive charge in SiO₂. Figure 3.16 shows the evolution of charge diffusion in the diode substrate as a function of time, when the MIPs hit the detectors.

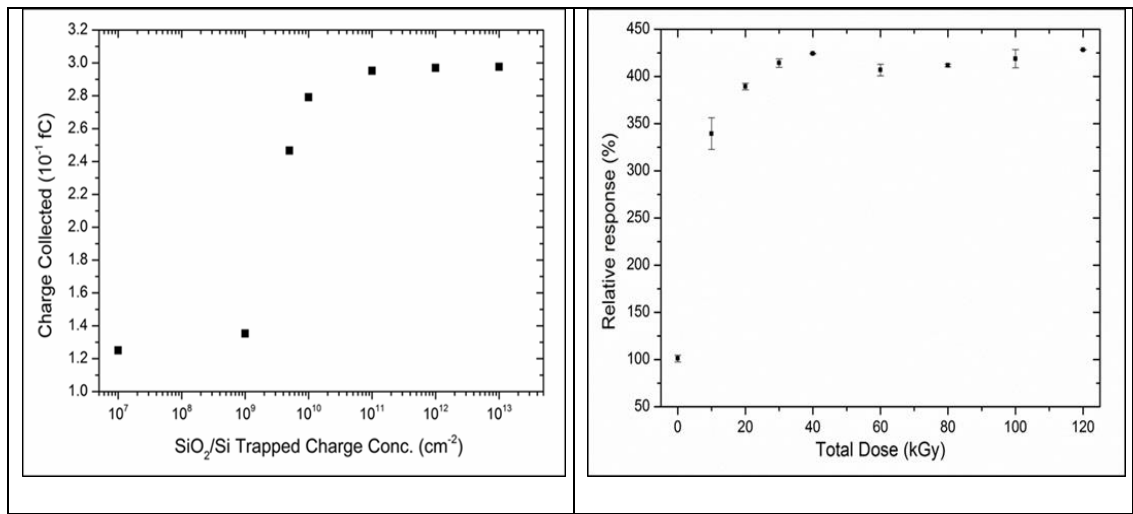
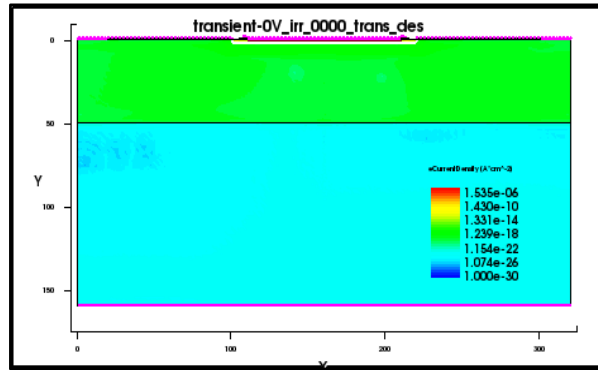


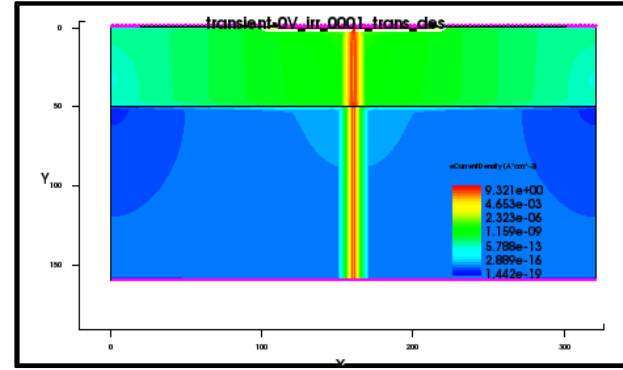
Figure 3.15: Simulated CCE as a function of the concentration of positive charge trapped at the Si/SiO₂ interface (left) and the experimental measure of the EPI diode response normalised to pre-irradiation CCE as a function of the accumulated dose (right)

Note: The ratio between the CCE with no irradiation and a trapped charge concentration of 10¹² cm⁻² is approximately three.

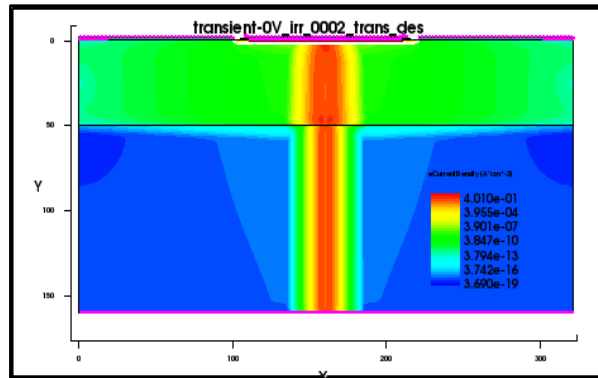
a



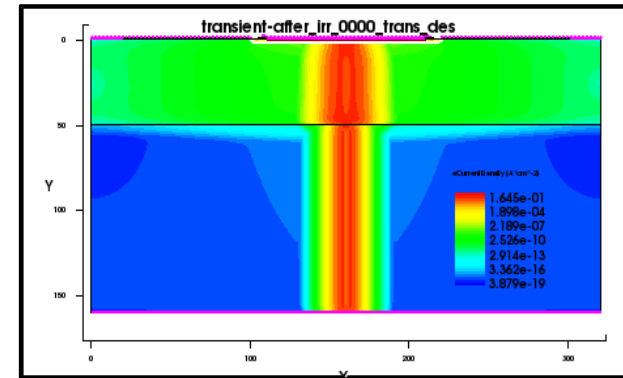
b



c



d



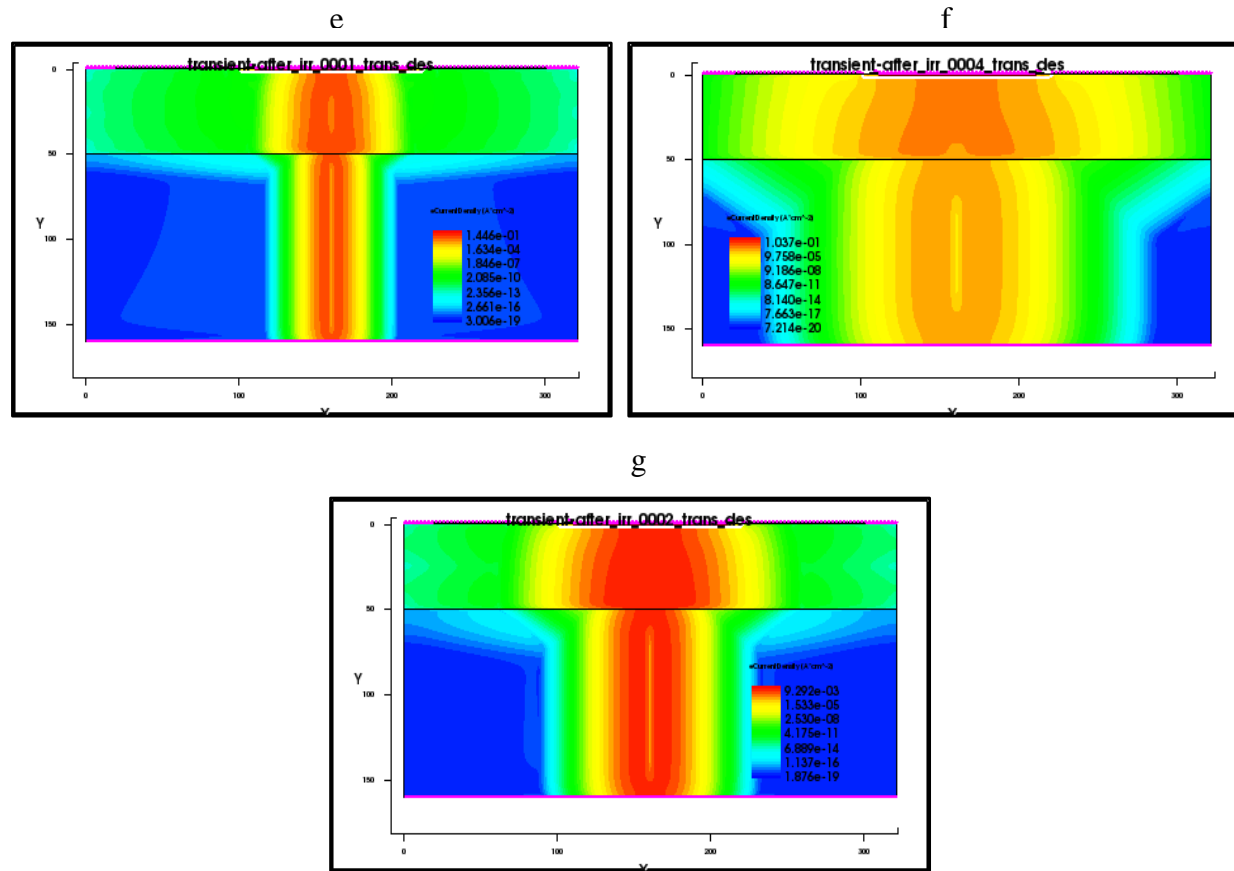


Figure 3.16: TCAD simulation of the diffusion of the charge generated inside the silicon substrate by a Minimum Ionising Particle (MIP) corresponding to 80 Frenkel pairs per micron in silicon. a) Initial conditions with no event; b) generation of the charge at the moment of the event occurs; c-d-e-f-g) evolution of the charge diffusing toward the electrodes as a function of time

3.4.4 Radiation damage by 18 MV photon beam

Figure 3.17 shows the average normalised response of the EPI diode after irradiation by a mixed photon-neutron field produced by an 18 MV medical LINAC. Detector samples were tested after pre-irradiation (4 Mrad in water) by a Co-60 source, and read out in passive mode. The decrease in response, and subsequently the CCE induced by irradiation, was less than 1.5%/300 Gy. This can be attributed to the generation of cluster defects in the EPI layer due to the presence of fast secondary neutrons inducing the creation of recombination centres with a very deep energy level in the silicon forbidden band gap (often attributed to the energy level $E_c-0.50$ eV) [123, 148, 167]. The measured reduction of the CCE in the radiation field from the 18 MV photon beam in the EPI diodes is comparable to other devices developed for medical applications [174, 175].

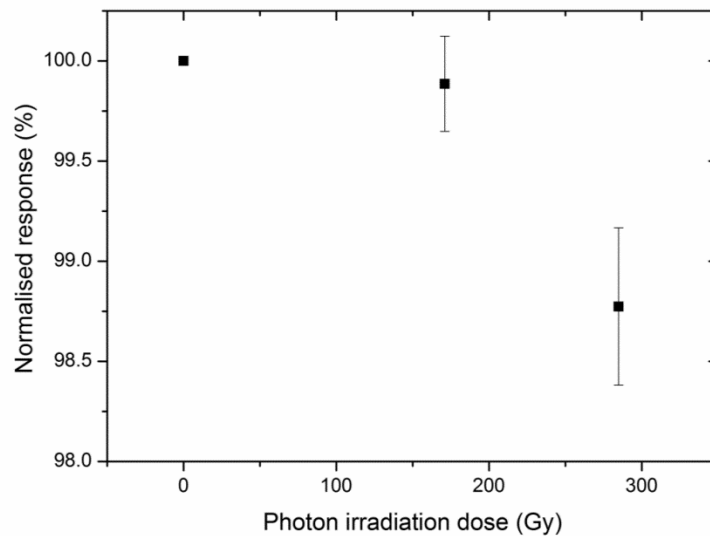


Figure 3.17: The response of the EPI diode as a function of the irradiation dose delivered by an 18 MV medical LINAC photon beam

Note: Detector samples were tested after pre-irradiation (4 Mrad) on a Co-60 source. Each value represents the average response of 20 samples, and error bars were calculated as two times the SD of the average response measured by all the samples.

3.5 Conclusion

This chapter examined the experimental measurements and numerical simulation techniques performed to characterise a new EPI diode developed at CMRP for dosimetry in EBRT, which demonstrated an unusual total dose radiation response. The developed EPI diodes demonstrated an increase in sensitivity with gamma irradiation in contrast to commercial diodes. Validation and fine-tuning of the simulation model were undertaken by comparing the simulated data with the electrical characteristics (I-V and C-V) of the device. The radiation hardness characterisation of the detector was performed by evaluation diode response using radiation fields from the Co-60 gamma source and 18 MV medical LINAC. The detectors showed a stable response within 5% for 120 kGy of the gamma irradiation dose (Co-60), following 40 kGy of pre-irradiation on a Co-60.

The mechanism of radiation damage induced by the photon beam was studied via the simulation of the effect of the concentration of trapped charge in the S_i/S_iO_2 interfaces on the lateral extension of the depleted region when the detector operated in passive mode. The model developed fits the experimental data fairly well, and the main mechanisms of variation in the response of the device were explained by combining a CCE induced by the trapped charge at the S_i/S_iO_2 interfaces and by the radiation ‘gettering’ effect. The effect of the radiation damage induced by photoneutrons generated in the 18 MV photon beam was quantified as 0.5%/100 Gy, demonstrating the high grade of radiation hardness of this new EPI diode, with a potential lifetime—for standard clinical QA usage—of approximately 70 cGy/week, or more than eight years.

CHAPTER 4: RADIATION HARDNESS FOR 2-D SILICON DIODE ARRAY (MP512) USED IN EBRT

4.1 Introduction

The purpose of this study is to characterise an innovative silicon 2-D array detector for dosimetry in small field EBRT. In this chapter, single diode test structures are fabricated onto the same wafer for preliminary characterisation of the performance expected by the final prototype. This chapter also studies the basic electrical properties of I-V and C-V for the test structures and silicon 2-D array. The single test diodes are fabricated onto a set of *p*-type silicon substrates with three different *p*-stop implantation densities. The purpose of these tests is to determine the optimal configuration of the *p*+ top-implantation realised between the *n*+ diode junctions to minimise the crosstalk between pixels due to the generation of conductive channels between the sensitive elements.

4.2 Materials and methods

4.2.1 MP512 array design and fabrication

The MP512 is a monolithic pixel array of 512, $0.5 \times 0.5 \text{ mm}^2$ ion-implanted diodes of on a bulk *p*-type 470 μm thick silicon substrate. The total array area is $52 \times 52 \text{ mm}^2$, with 2 mm diode pitch. The silicon detector array is wire-bonded to a thin tissue-equivalent printed circuit board (PCB) and covered by a layer of protective epoxy to avoid accidental damage to the wire bonding. The PCB provides the fan-out for connecting the sensor to the readout electronics. The MP512 silicon detector operates in passive mode, with no bias voltage applied to the diodes. In this study, the MP512 detector was placed between two 5 mm thick PMMA slabs. The PMMA envelope of the detector served two purposes: (i) protecting from mechanical damages and (ii) shielding the sensor from ambient light [4]. Figure 4.1 shows a

diagram of the detector embedded in the PMMA envelope (left) and an image of the detector mounted on the flexible PCB (right).

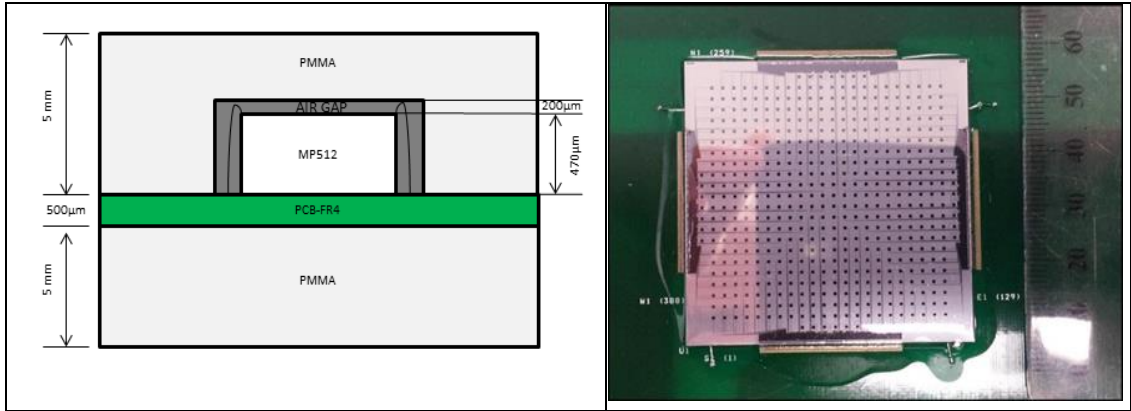


Figure 4.1: Schematic of the M512 packaging between two PMMA slabs (not to scale) (left) and the MP512 detector mounted and wire-bonded to the thin PCB, with detector and wire bonding protected by a thin layer of epoxy resin (right)

Two different substrates of the MP512 array are examined in this chapter. Every sample had its own number to distinguish between different implantation charge, different substrate manufacturer and resistivity. Table 4.1 illustrates the ion implantation and substrate resistivity of each device. Two sets of silicon substrates were examined—one from a United States silicon provider (CMRP) and one from a European silicon facility (KDB).

Table 4.1: Ion implantation and resistivity of two arrays

Array sample number	Ion implantation, p^+	Substrate resistivity and type
21	100 μC	10 $\Omega\text{-cm}$ (CMRP substrate)
24	30 μC	10 $\Omega\text{-cm}$ (KDB substrate)

The ion implantation charge (μC) describes the total ion charges deposited in the substrate of the array to produce the p-stop junctions between the pixels of MP512.

The energy of the incident particles was 67 keV, which gave a 0.08 μm depth of penetration. The dopant concentrations available are summarised in Table 4.2.

Table 4.2: Amount of dopant concentrations for the samples used in this thesis

Name of the device + ion implantation	Dopant concentrations Particles/cm ³
MP512 # 100 μC	7.74×10^{19}
MP512 # 30 μC	2.32×10^{20}
Test structure # 10 μC	7.74×10^{20}

4.2.2 Test structures design and fabrication

The test structures in this study were supplied by SPA-BIT in the Ukraine and manufactured on the same type of wafer as the detector array. These structures were very useful tools to verify the effect of changing the parameters of the production process on the performance of the single detector. The test structures were initially produced on the same p -type silicon substrate of 470 μm thick with a p^+ back junction (to realise the back ohmic contact), with a p^+ p-stop junction and n^+ diode junction. Single diode test structures were fabricated onto the same wafer for preliminary characterisation of the performance expected by the final prototype. Two configurations of the test structures are evaluated in this chapter. Figure 4.2 shows the first design with a guard ring, which was n^+ 5 μm in width and 5 μm from the edge of the anode. Figure 4.3 shows the second design of test structure, which was without a guard ring. The sensitive volume of the diode was 0.5 mm for each configuration.

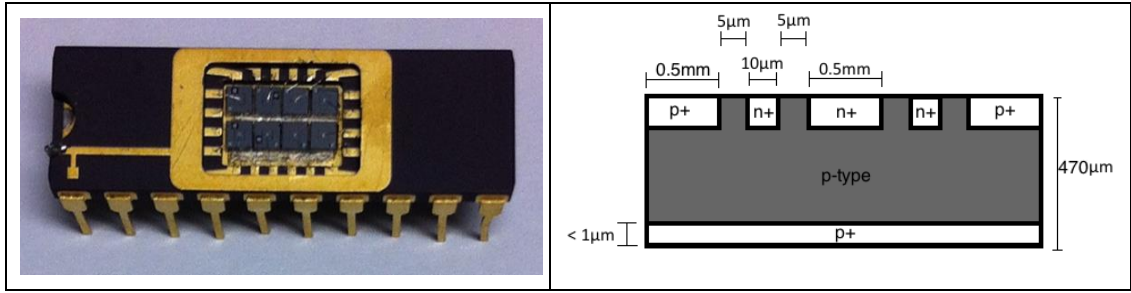


Figure 4.2: Real and schematic diagram of the test structure with guard ring

The test structures were placed on dual in-line (DIL) ceramic packages containing either six or eight diodes with a common back contact. A range of samples was examined, with different boron dopant implantation charges of 10, 30 and 100 μC . In addition, two different types of substrate were investigated: a 1 $\Omega\text{-cm}$ and 10 $\Omega\text{-cm}$ substrate from the CMRP foundry and a 10 $\Omega\text{-cm}$ substrate from the KDB foundry. The dopant implantation and substrates were grouped to determine which substrate and dopant implantation grouping was the best choice to use the silicon diode as a dosimeter in the clinical field. The data presented in this chapter were calculated as an average of all the diodes on a specific DIL ceramic package, for both the CMRP and KDB substrates.

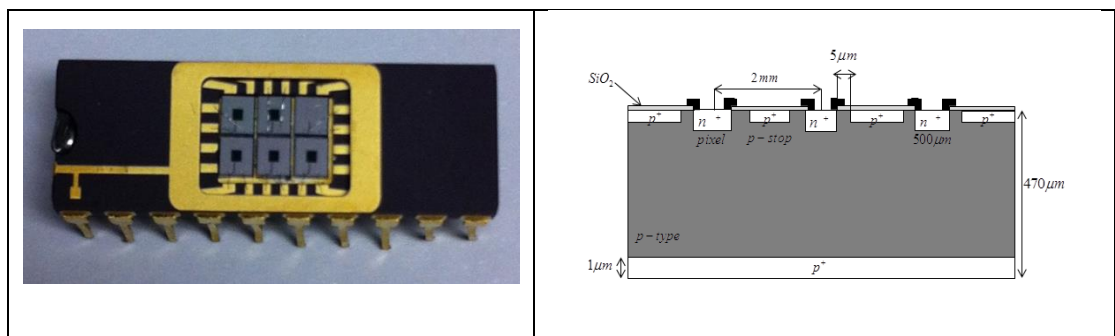


Figure 4.3: Real and schematic diagram of the test structure without guard ring

4.2.3 Readout system

The readout system used to perform the measurements was the TERA system, which was discussed in Section 3.2.3.

4.2.4 I-V characteristics for test structure and MP512

Characterisation of the test structures and MP512 in terms of I-V allowed determination of the baseline signal by applying a reverse voltage bias through the diode. This signal or leakage current was produced by the diode in the absence of ionising radiation or light.

4.2.5 Experimental method

I-V characteristics were determined using a Keithley 230 programmable voltage source to apply a bias through the diodes, and the current was measured using a Keithley 614 electrometer and Keithley 199 System DMM/scanner. These experiments evaluated two configurations of test structures—with and without a guard ring. The MP512 full array was also tested via the same setup. The reverse voltage was applied to the diodes from 0 to -25 V, with an incremental step amplitude of -0.5 V, and the delay time was 1000 ms (between the application of the bias and current sampling to achieve the full stabilisation of the current). The test structure and MP512 were placed in a dark aluminium sealed container in order to protect the device from the photocurrent generation due to the ambient light and electromagnetic interference. The detectors were also kept at room temperature (approximately 295 K).

For the test structure, the data points were acquired as an average of all the diodes on a particular DIL ceramic package, which all had the same geometry and substrate characteristics, with the substrate resistivity and pre-irrigation ion implantation

displayed on the plots. Uncertainties for all I-V plots were based on the 6.5 digit accuracy scale of the equipment used in this experiment. The scale of the instrument was variable, between a range of 20 pA to 200 nA, and the uncertainties ranged from 0.0002 to 2 pA. The first I-V test was performed on the test structure diodes that did not have a guard ring. The test was also undertaken on different substrate resistivity and pre-irradiation dopant implantations. Figure 4.4 shows the diagram of the experiment, with the negative bias applied to the p^+ region and the ammeter connected to the n^+ region. In this experiment, the negative voltage was applied from 0 to -25V, with a step increment of -0.5 V.

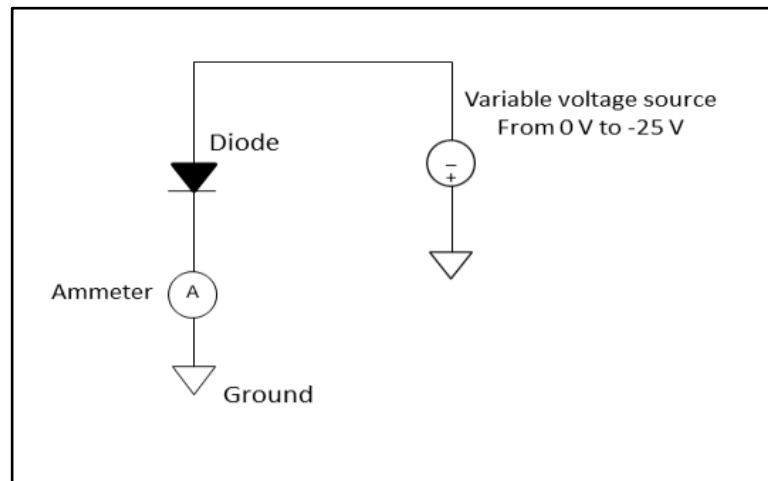


Figure 4.4: Schematic of the I-V test for test structure without guard ring

The second I-V test was performed on the test structure diodes with the guard ring. The experiments were undertaken when the negative bias was applied to the p^+ region from 0 to -25 V with an increment of -0.5 V, and the ammeter was connected to the n^+ region of the diode pad. The guard rings in this test were either kept grounded (see Figure 4.5—left) or floating (see Figure 4.5—right).

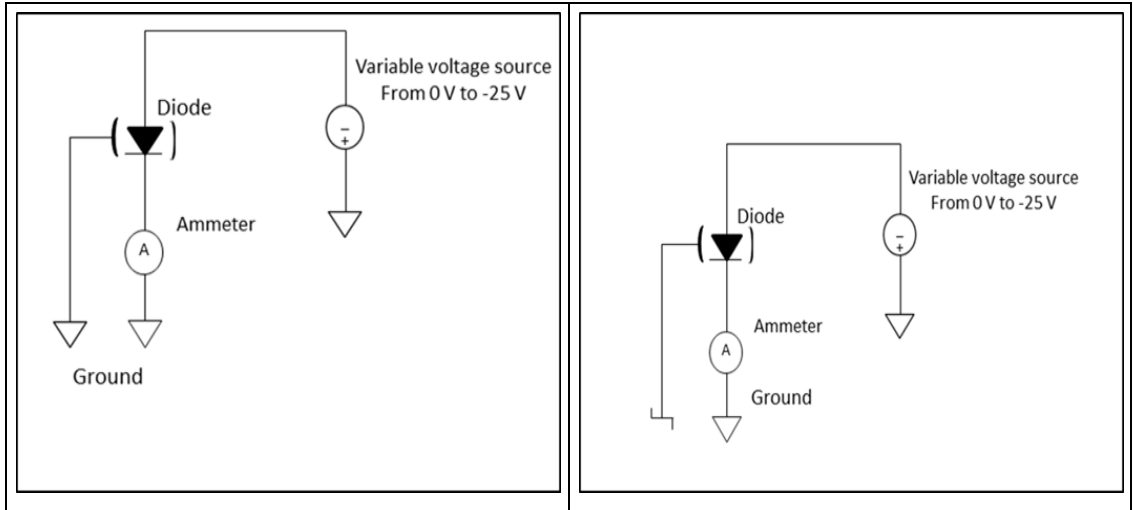


Figure 4.5: Schematic of the I-V test for the test structure with a guard ring that is grounded (left) and floating (right)

The third I-V experiment was undertaken on the MP512 full array. The negative bias was applied to the uniform p^+ region via one of the bias pins available on each side of the MP512 detector die, while the ammeter was connected to the n^+ region of each individual diode. The full array sample tested in this experiment was not equipped with a guard ring. The schematic of the test is shown in Figure 4.6. The voltage was set from 0 to -14 V with -0.5 V increments because the MP512 exhibited breakdown around -14 V, unlike the rest of the test structure, which was up to -25 V.

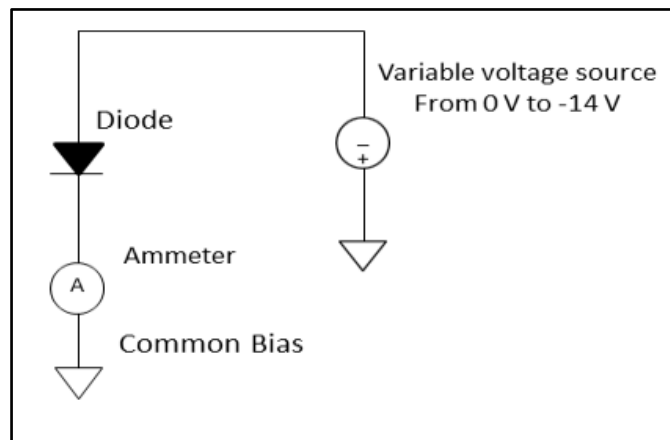


Figure 4.6: Schematic of the I-V test for the MP512 array

The test of MP512 diodes was performed by selecting diodes in different positions across the array. Figure 4.7 shows the position of the detectors tested. The I-V characteristic was performed for both arrays of CMRP #21 and KDB #24. Due to having the same geometry in both arrays, the locations of the tested diodes were the same in both arrays. The idea behind testing the I-V of MP512 in different locations was to determine whether the geometry of the detector had any effect on the leakage current. Figure 4.7 shows the locations of the detectors tested.

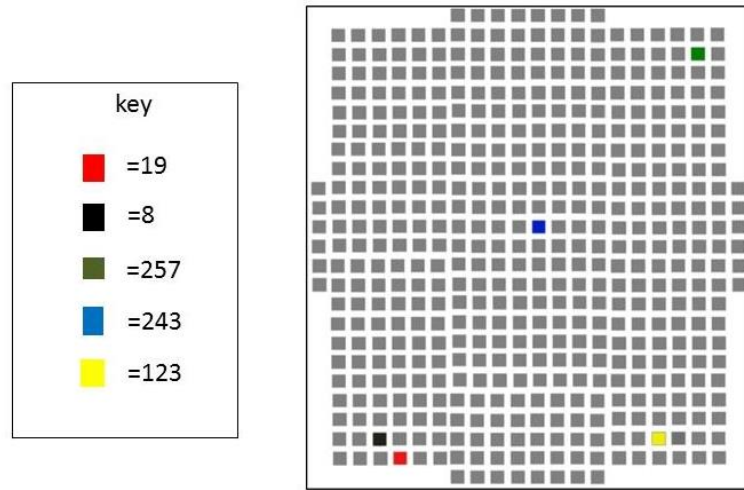


Figure 4.7: Locations of diodes tested on MP512

4.2.6 C-V characteristics

As discussed in Section 3.3.2, the C-V characteristic is used to determine the depletion bias of detectors. The capacitance of the detector is also an important parameter to design the readout front end, which must tolerate the output equivalent capacitance presented by the detector at the preamplifier input. This is particularly important when the detector is used in passive mode, where the capacitance has its

maximum value. As for any real silicon detector, the C-V curve evaluation is not as simple as for an ideal p - n junction device as the one discussed in Chapter 3. This is due to the presence of multiple depletion steps that occur between the diode junction towards the lateral p -stop junction (only 10 μm apart) and towards the back ohmic contact of the substrate. Despite the difficult analysis of the experimental results, it is still important to measure the C-V characteristic of complex devices to define the alternating current small signal behaviour of the devices.

The instrumentation (as described in Chapter 3) was the bridge capacitance meter Boonton 7200. This allows the application of positive and negative bias up to 100 V. For the test structures, this study measured the capacitance by applying a bias from 0 to -60 V, with -0.5 V increments, with the delay time set to 1000 ms. Using the same parameters and setup, three different configurations were tested: no guard ring, guard ring grounded and guard ring floating. The uncertainties for all C-V plots were dependent on the 3.5 digit accuracy scale of the machine. The scale used in the experiments was pF with two decimal places recorded, and the uncertainty for each data point presented was $\frac{0.01}{\sqrt{12}} \text{ pF}$.

4.2.7 Radiation hardness characterisation

4.2.7.1 Radiation hardness study by photons and photoneutrons for test structures

In terms of radiation damage by photons, all test structures were irradiated up to 40 kGy water-equivalent dose, in steps of 10 kGy, as indicated in Table 4.3. Further, all test structures were exposed to the photoneutrons using a medical LINAC, which produced 18 MV.

Table 4.3: The dose received of each samples from test structures

Sample	Ion implantation μC	Dose received-kGy
1 Ω -cm (CMRP)	100	10
10 Ω -cm (CMRP)	10	10
10 Ω -cm (CMRP)	30	20
10 Ω -cm (CMRP)	100	10
10 Ω -cm (CMRP)	100	40
10 Ω -cm (KDB)	10	20
10 Ω -cm (KDB)	10	30
10 Ω -cm (KDB)	30	20
10 Ω -cm (KDB)	30	30
10 Ω -cm (KDB)	100	10
10 Ω -cm (KDB)	100	40

4.2.7.2 Photon damage—experimental method

After irradiation, the response of all test structures was measured at the Illawarra Cancer Care Centre of Wollongong Hospital using a Varian 2100C LINAC. This test evaluated the effect of irradiation by Co-60. The diodes were placed on top of the couch using a 30 x 30 cm² solid water phantom. The response of the detectors was performed by 6 MV x-rays at a dose of 100 MU with a dose rate of 600 MU/minute and a 20 x 20 cm² field size. The diodes were placed at an SSD of 100 cm and 1.5 cm depth in a water-equivalent phantom. The responses of all diodes before exposure to radiation were recorded, and a post-irradiation response was measured and normalised to the zero dose. All data acquisition was undertaken by the Rad-X Dose View acquisition system, as discussed in Section 3.2.3.2.

4.2.7.3 Photoneutron damage—experimental method

To assess the effect of photoneutrons on silicon detectors using a LINAC, the detectors were irradiated for a prolonged period with an 18 MV beam. The response was measured before any course of irradiation using 6 MV, as clarified earlier. This point was used as a reference against which the irradiated detectors could be compared and the response normalised. The response of the detectors was measured at the Saint George Care Hospital in Sydney using a Varian iX LINAC. The

irradiation of the detectors was performed via 18 MV x-rays at a dose of 9795 MU with a dose rate of 600 MU/minute and a $40 \times 40 \text{ cm}^2$ field size. The diodes were placed at the surface of the phantom to avoid any thermalisation of the neutrons at an SSD of 90 cm, and placed at the surface of 130 mm of water-equivalent phantom as back-scatter material. This study used a field size larger than $10 \times 10 \text{ cm}^2$ to produce the largest possible number of photoneutrons and reduce the exposure time. Due to using the large field size, the dose was increased to achieve an approximate equivalent dose of 300 Gy.

A further test was performed with the test structure using the same parameters as above, except the detector was placed at d_{max} of 18 MV within $30 \times 30 \text{ cm}^2$ of a solid water phantom. Following this, the response of the detectors was investigated with the same conditions used to measure the response before irradiation.

4.2.7.4 Radiation hardness study by photons and photoneutrons for MP array (MP512)—experimental method

The same conditions adopted to test the test structures were used for the characterisation of two full array samples: MP512 sample #24 with 10 Ω -cm and 30 μC ion implantation KDB substrate, and MP512 sample #21 with 10 Ω -cm and 100 μC ion implantation CMRP substrate. The setup of the photon study is shown in Figure 4.8. The detectors were placed at an SSD of 100 cm, and placed at d_{max} . In the top of the detector was 0.5 cm bolus, using 10 cm of water-equivalent phantom as back-scatter material.

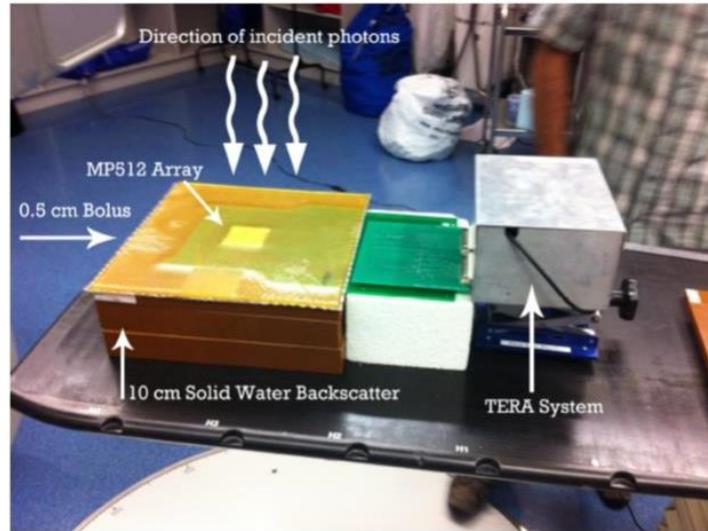


Figure 4.8: The setup of the response test for the arrays

4.3 Results

4.3.1 Electrical and I-V characteristics for test structure

Figure 4.9 shows the I-V characteristics for the test structures without a guard ring, for both the CMRP and KDB substrates. All test structures expressed the predicted trend, which was an increase in leakage current with increased negative bias. This figure also exhibits a range of variation of slopes of the I-V results for the test structures, which differed from 15 to 125 pA at a maximum negative voltage of 25 V. Some detectors demonstrated a breakdown at voltage -25 V, while others had a leakage current lower than 100 pA.

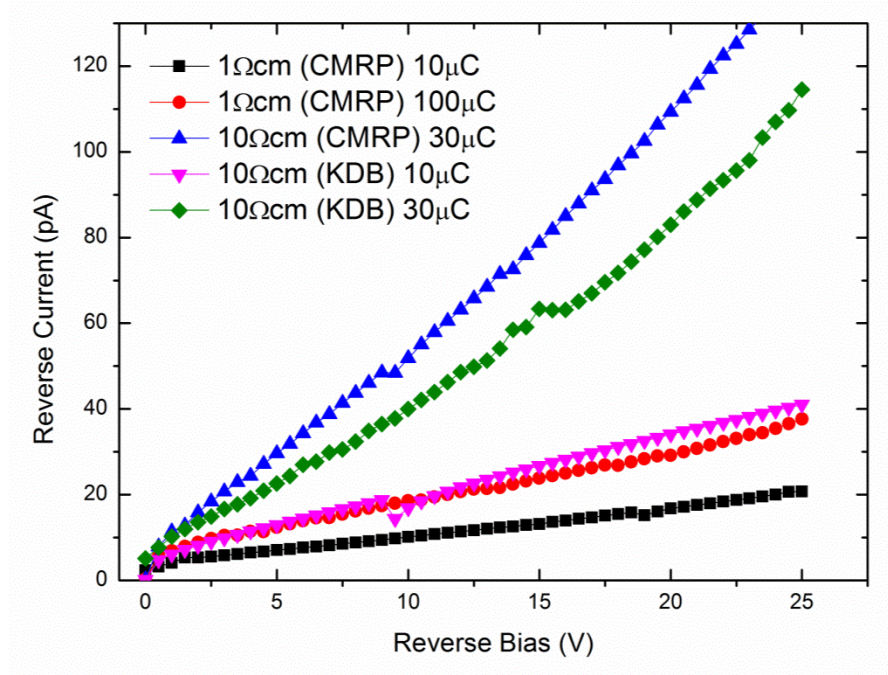


Figure 4.9: I-V characteristics for all test structures without guard ring

Figure 4.10 shows the I-V of the test structures with 1 Ω -cm CMRP substrate, with guard rings both floating and grounded. The sample with 10 μ C shows that the floating guard ring did not have any effect on the leakage current, which was unexpected. Instead, the sample with 100 μ C revealed a leakage current almost double when the guard ring was left floating, which showed that the geometry and structure of the guard ring was fully functioning, but required a steeper doping charge profile to be effective in such low resistivity substrate. The guard ring was an $n+$ junction 10 μ m apart from the $n+$ junction of the pad diode. Between them, the p-stop junction must have at least 100 μ C to avoid the guard ring, and the diode junctions were shorted by the electron channel generated by the induction of the positive charge trapped in the Si/SiO₂ interface.

According to Mishra et al. [176], detectors with a grounded guard ring show a lower leakage current than do those with a floating guard ring, which is in substantial agreement with the results obtained by the sample with 100 μC implantation charge.

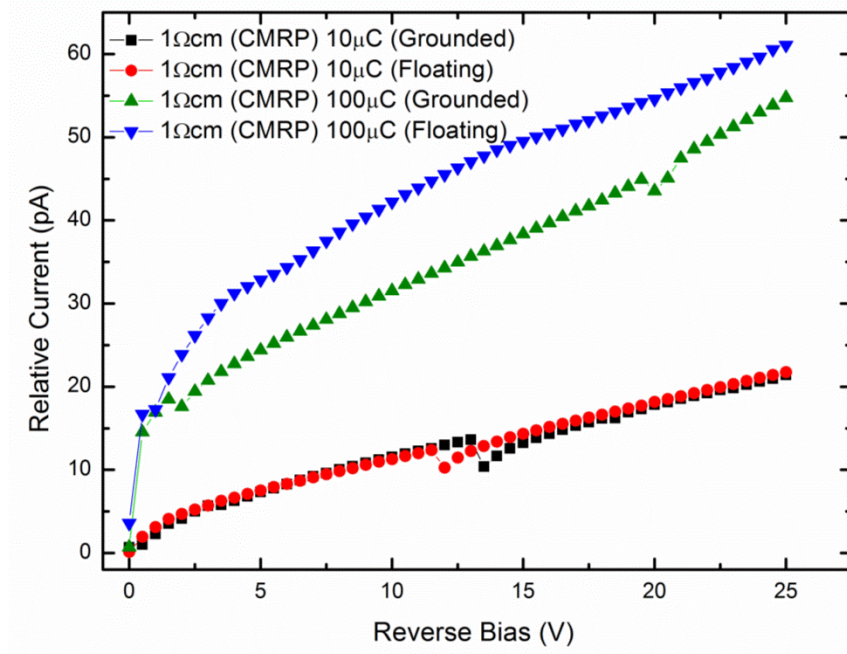


Figure 4.10: I-V characteristics for 1 Ω -cm CMRP substrate, showing different ion implantations with guard ring grounded and floating

Figure 4.11 shows the I-V of the test structure with KDB substrate 10 Ω -cm, with a guard ring floating and grounded. The results obtained with the KDB substrate substantially confirmed the data obtained on the CMRP substrate—to make the guard ring effective, a minimum charge of 100 μC is required. This is illustrated by the sample 100 μC in Figure 4.11, which showed a double leakage current at -20 V if the guard ring was not polarised. The sample of 10 μC and 30 μC showed no effect of polarisation of the guard ring on the leakage current, with an average value of the current higher at the same bias voltage as the 100 μC samples with the guard ring grounded. The results from the 100 μC KDB substrate were consistent with Mishra

et al.'s results [176]. The results from the I-V of the CMRP substrate with 10 Ω -cm confirmed the results obtained for the other substrates.

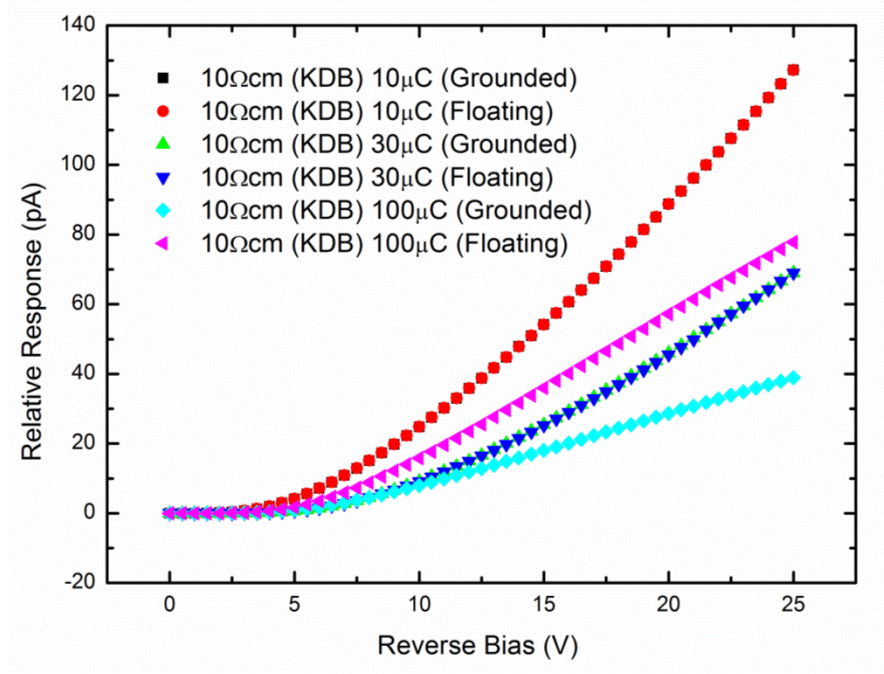


Figure 4.11: I-V characteristics for 10 Ω cm (KDB) substrate, different ion implantation with guard ring grounded and floating

In conclusion, the guard ring structure had no effect if the p-stop implantation charge was lower than 100 μ C, which limits options for manufacturing the full array. The use of a guard ring is also very problematic in a large number of channel arrays, and requires definition of extra contacts, which can be difficult in terms of routing the contacts. The characterisation by I-V convinced the researchers to avoid using a guard ring for a full array.

4.3.2 Electrical characterisation of MP512 full array

Figure 4.12 shows the I-V characteristics for the diodes that were selected (as shown in Figure 4.7) for array sample #21 (CMRP substrate) and sample #24 (KDB

substrate). Due to the large extent of the leakage current at the breakdown, the logarithmic scale was applied to attain a better demonstration of the trend.

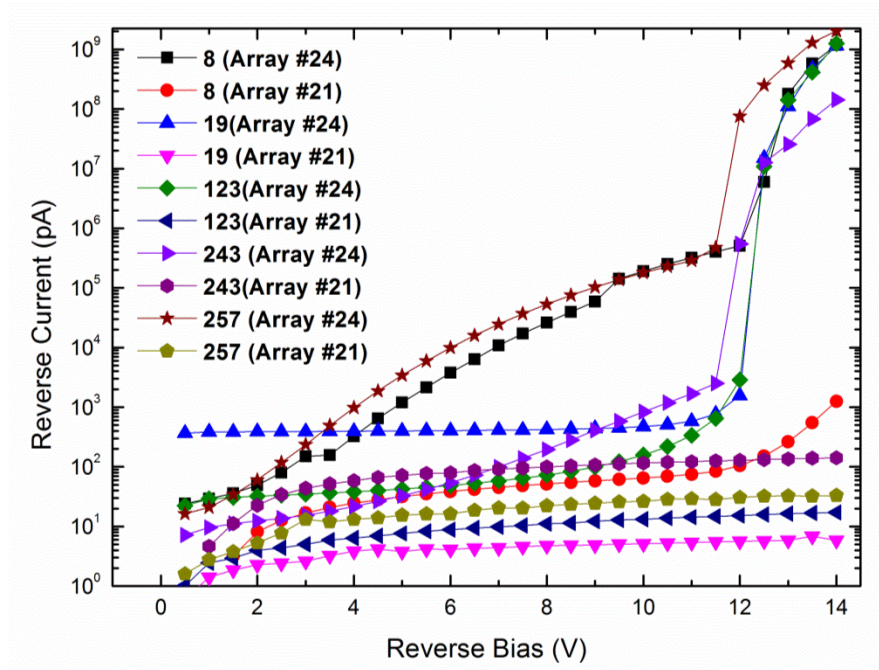


Figure 4.12: I-V characteristics for both arrays from the MP512 CMRP and KDB substrates and same pixels are tested in both arrays in the positions of MP. MP with KDB substrate shows high leakage current compared to MP with CMRP substrate.

Investigating the leakage current from the #21 array indicated that the trend for all diodes tested was consistent up to -12 V, where a sharp increase in leakage current occurred. Diodes #19, #123 and #257 showed the lowest leakage current, with a maximum current of 6, 18 and 33 pA, respectively. These were conspicuously lower than diode #243, which reached a maximum leakage current of 141 pA, and diode #8, which rose steadily to approximately 70 pA before a sharp increase at -12 V. From 0 to -12 V, the leakage current ranged from 1 to 100 pA for all diodes from the #21 array. Although this appeared to be a significant deviation, these results were comparatively far better than those demonstrated for the #24 array.

The leakage current observed for sample #24 of the KDB substrate exhibited more inconsistency than did sample #21. Fluctuating trends were observed with the diodes from array #24, and the breakdown was observed for all diodes at approximately -12 V. Diode #19 displayed a relatively constant leakage current, similar to the diodes from array #21; however, the current was significantly higher—around 400 pA—before breaking down at -12 V. With applied negative bias, the leakage current was increased for diodes #123 and #243. However, diode #243 showed a sharp increase of leakage current from -7 V. Similar behaviour was observed for diode #123, yet starting from -10 V. Both diodes showed breakdown at around -12 V. For diodes #8 and #257, the leakage current increased similarly to the previous diodes; however, the rate of increase was considerably higher.

In terms of comparison between the two substrates, the lower leakage current was observed from sample #21 of the CMRP substrate with 10 Ω -cm resistivity. The KDB substrate—nominally 10 Ω -cm, like the CMRP substrate—showed larger leakage currents in the full array, with pixels consistently breaking down at approximately -12V. Therefore, the CMRP substrate device may be operated at a far greater negative voltage range than the KDB device. The test was performed for diodes from different positions on the array. Thus, the results from both arrays demonstrated that there was no clear relationship between leakage current and geometrical position. The results also showed that the manufacturing process could achieve good uniformity in terms of ion implantation across the entire four-inch wafer, where the detector array covered almost 40% of the area.

4.3.3 Capacitance characteristics (C-V) of test structures

Figure 4.13 shows the C-V characteristics of the test structures of both substrates without a guard ring. All devices demonstrated the expected trend, which displayed a

maximum capacitance with no bias applied, and a quadratic reduction when a negative voltage was applied.

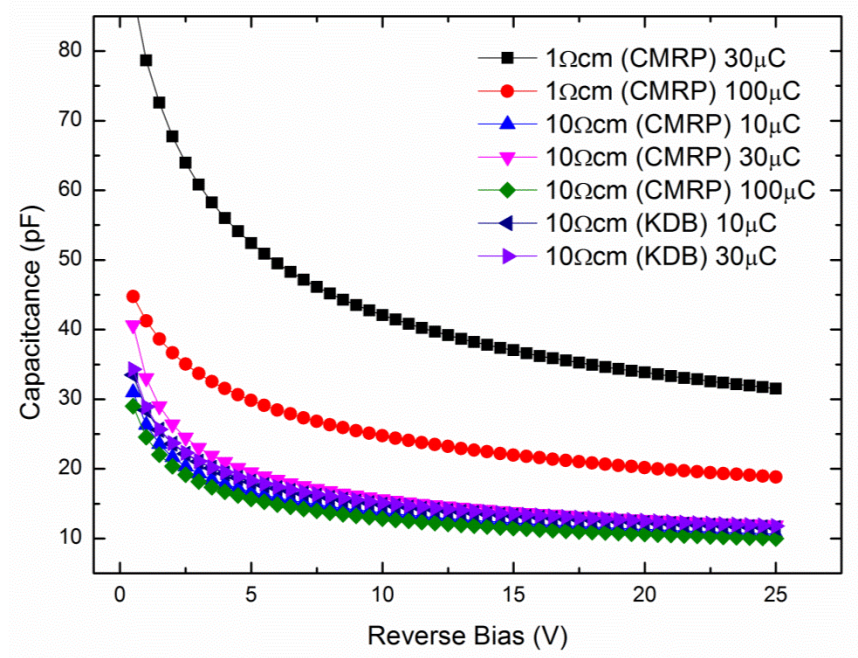


Figure 4.13: C-V characteristics for the test structure of both substrates without a guard ring

However, the two samples from 1 Ω -cm showed high capacitance and the response was relatively worse than for the 10 Ω -cm samples. The higher response of the capacitance was found for the sample with 1 Ω -cm, 30 μ C ion implantation and approximately 88 pF at zero bias, which reduced to a minimum value of 31 pF at -25 V. In contrast, the sample from the same substrate (CMRP) with different ion implantation (100 μ C) showed a better response for capacitance, with a maximum value of 44.7 pF at zero bias, and a reduction to 20 pF at -25. For both tested structures (CMRP and KDB), the 10 Ω -cm substrates demonstrated similar results and predictable trends. For the CMRP sample with 10 Ω -cm and 30 μ C, the initial capacitance was 40 pF. For the KDB sample with the same resistivity and ion

implantation charge, the initial capacitance was 34 pF. Excluding these two samples, the remaining tested structures with all 10 Ω -cm substrates (both the CMRP and KDB) presented an initial capacitance from 28 to 34 pF. As the negative bias increased, all test structures with 10 Ω -cm substrate recorded a capacitance value from 10.5 to 11.73 pF.

In all cases, the results were in qualitative good agreement with the theory that relates the junction capacitance to doping concentration and bias applied by the following relationship:

$$C_j = \sqrt{\frac{q\epsilon}{2(\varphi - V_a)} \times \frac{N_a N_d}{N_a + N_d}}$$

where φ is the built-in potential, V_a is the bias applied, and N_a and N_d are the concentrations of the acceptor and donor dopants, respectively.

The famous plot reported by Blankenship et al. [177] summarises the general trends and suggests a methodology to verify the data obtained experimentally—see Figure 4.14.

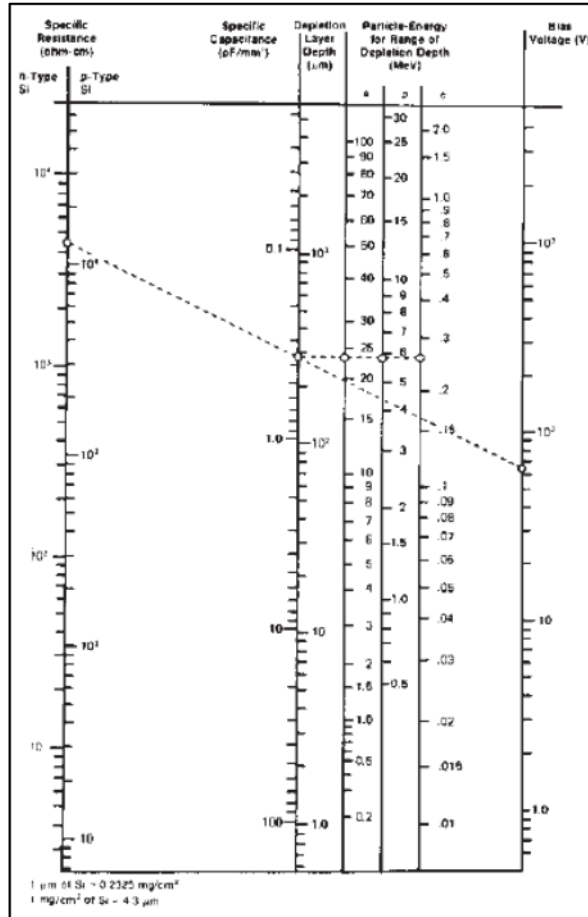


Figure 4.14: Silicon detector parameters monograph [177]

Figure 4.15 shows the C-V characteristics of the sample of 1 Ω-cm CMRP substrate for different ion implantations with a guard ring. The guard ring in this assessment was tested as both grounded and floating. It was difficult to distinguish between the capacitance for a diode when the guard ring was grounded and floating; however, it was observed that the capacitance of the sample with 10 μC was considerably higher than the other samples with the same substrate and resistivity.

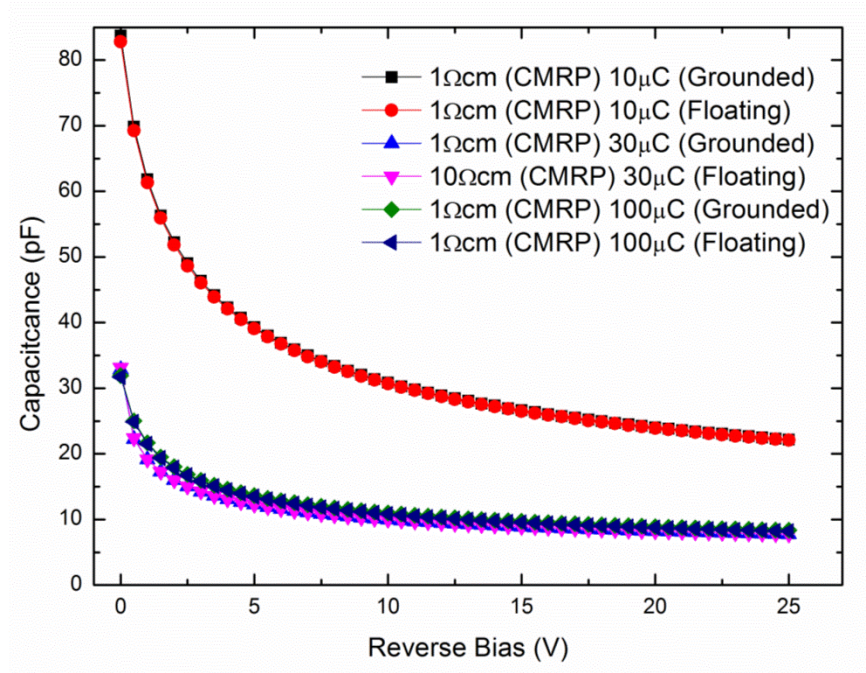


Figure 4.15: C-V characteristics for test structure 1 Ω -cm CMRP with guard ring

Figure 4.16 shows the C-V characteristics of the sample of 10 Ω -cm CMRP substrate and different ion implantation with a guard ring. The guard ring in this assessment was tested as both grounded and floating. The plots indicate that the sample with 30 μ C ion implantation showed a significantly lower capacitance than did the 10 and 100 μ C samples.

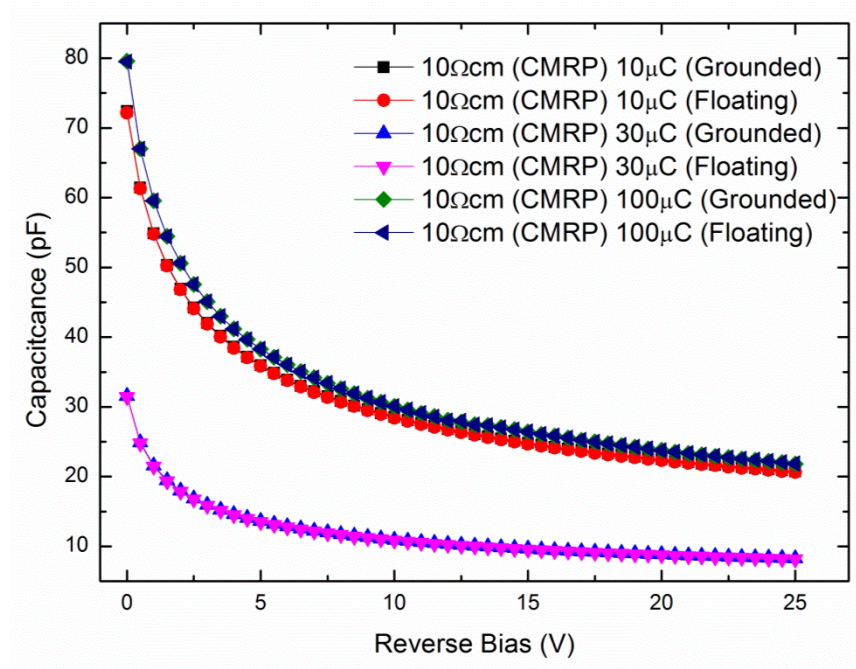


Figure 4.16: C-V characteristics for test structure 10 Ω -cm CMRP with guard ring

Figure 4.17 shows the C-V characteristics of the samples of 10 Ω -cm KDB substrate and different ion implantation with a guard ring. The guard ring in this assessment was tested as both grounded and floating. However, it was difficult to distinguish between the plots when grounded and floating. Despite this, the results indicated that the KDB substrate was more consistent than the CMRP substrate.

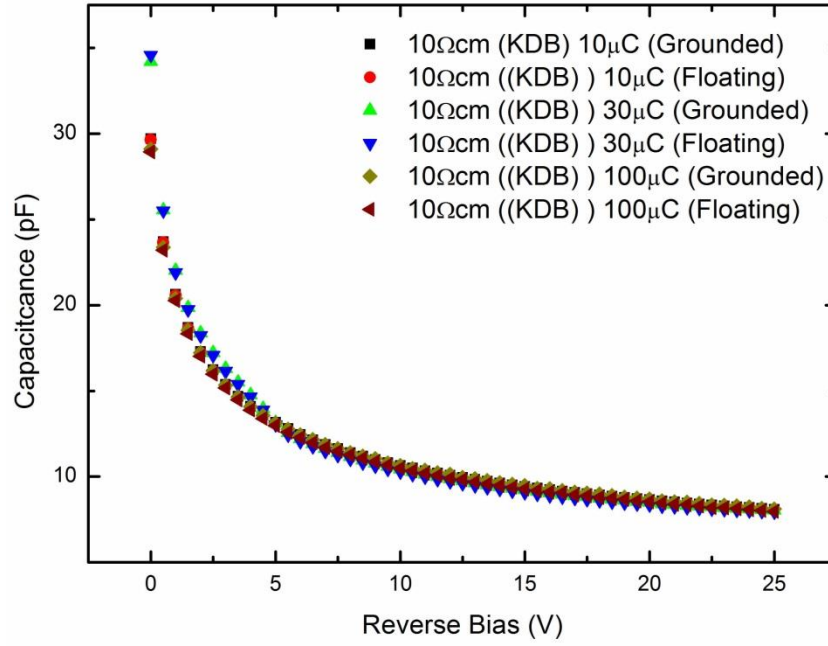


Figure 4.17: C-V characteristics for test structure 10 Ω -cm KDB with guard ring

To conclude, with the exception of the test structures with 1 Ω -cm CMRP substrate shown in Figure 4.15, the difference between the capacitance of the other test structures was insignificant. In terms of the effect of doping concentration, this study observed a relationship between decreasing the capacitance for silicon and increasing the doping concentration [178] of the substrate. To conclude the effect of the guard ring on the capacitance of the silicon, there was little effect on the capacitance of the devices. The maximum deviation recorded between the floating and grounded guard ring for all substrates and different ion implantations was 1 pF. This represents a deviation of approximately 1 to 3% of the capacitance through all samples tested. Thus, the guard ring may have a slight influence on the noise in a readout system.

4.3.4 Radiation damage for test structures and MP

4.3.4.1 Photon damage for test structure

Figure 4.18 shows the relative response as a function of the accumulated dose for the test structures with 1 and 10 Ω -cm CMRP substrate and 10 Ω -cm KDB substrate with different ion implantation charges. All the samples showed a reduction of the response down to approximately 55% at 40 kGy, with a stabilisation between 30 and 40 kGy within 3%. All the plots trend were found to agree with previous works [142, 170]. Further, the KDB substrate suffered a larger decrease of response, and also showed a stabilisation between 30 and 40 kGy at 57%, which made it a good candidate to be selected for the final production of the full array.

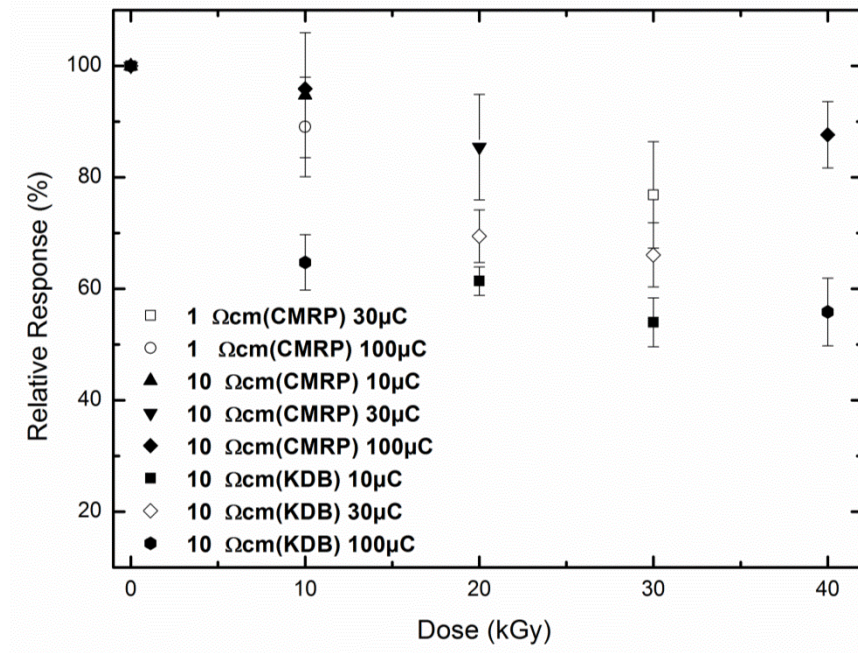


Figure 4.18: Relative response for test structures as a function of accumulated dose

4.3.4.2 Photoneutron damage for test structure

Figure 4.19 shows the relative response of a few samples of test structures decreasing, which were irradiated using 18 MV. The sample of 10 Ω -cm for the

CMRP substrate of both ion implantations charge showed consistent results and better performance than did the 10 Ω -cm KDB samples. The plot also indicates that the ion implantation affected the response of the detectors. For both substrates, the lower dopant concentration showed a significantly decreased response.

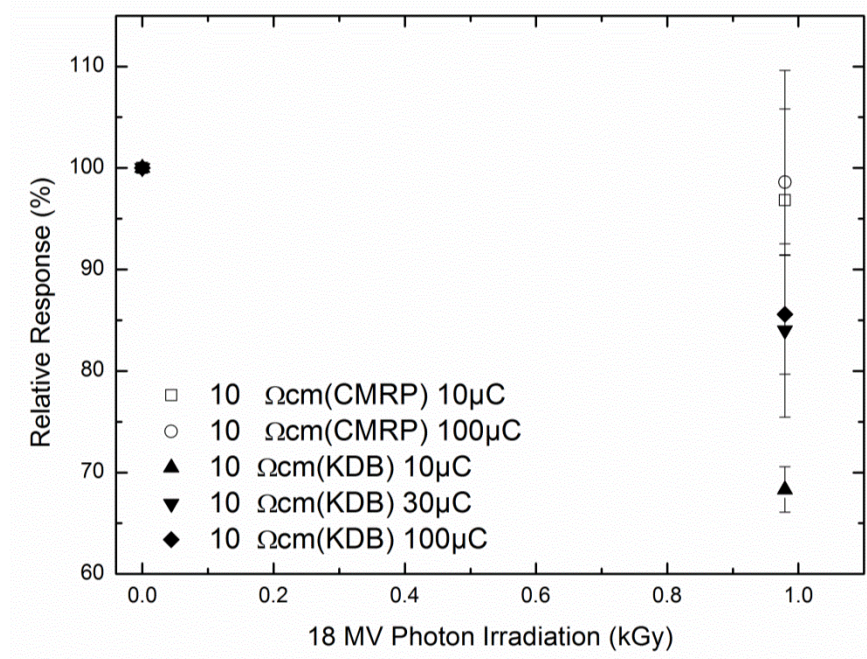


Figure 4.19: Relative response for test structures as result of photoneutrons

Further, the reduction in the response of the detectors was observed as a result of photon dose, while the decreased response was negligible due to the neutrons.

Table 4.4: The relative response alterations due to the photoneutrons

Sample		Post-irradiation response (%)	Error (%)
10 Ω -cm (CMRP)	10 μ C	96.84	12.70
10 Ω -cm (CMRP)	100 μ C	98.60	7.21
1 Ω -cm (CMRP)	100 μ C	99.21	2.21
10 Ω -cm (KDB)	10 μ C	68.33	2.23
10 Ω -cm (KDB)	30 μ C	83.79	8.54
10 Ω -cm (CMRP)	100 μ C	85.56	5.88

Table 4.4 indicates that the response of the sample of 10 Ω -cm with CMRP 100 μ C exhibited a 1.4% drop, compared to a 14.4% drop for the sample with the same pre-

ion implantation, but a different substrate (KDB). Such low sensitivity to photoneutron radiation damage exhibited by the CMRP samples suggests a very short lifetime of the non-pre-irradiated material, which is a sign of a low quality silicon substrate. In the same manner, the sample of 10 Ω -cm KDB 10 μ C demonstrated a large drop in response of 31.67%, in comparison to 3.16% for the CMRP substrate with the same pre-ion implantation.

To conclude the damage by photons, the KDB sample results with 10 Ω -cm with different ion implantations charge were in good agreement with theory and the previous results obtained by Bruzzi et al. [142]. In contrast, the CMRP showed very unusual results for photoneutron irradiation, and the results again showed that the material has very poor quality and small reproducibility across the samples, with the error bars among samples exceeding 9%.

To conclude the damage by 18 MV irradiation, the samples for the 10 Ω -cm CMRP substrate were less sensitive to radiation damage than the 10 Ω -cm KDB. The most important conclusion obtained from this test was of the effect of dopant implantation on response decrease. As specified previously, the greatest percentage decrease of response was observed with a sample with the lowest dopant concentration. The samples with high dopant concentration showed the smallest percentage decrease against radiation damage by photons. In conclusion, samples with 100 μ C and 30 μ C pre-irradiation ion implantation showed better performance than did samples with 10 μ C ion implantation. This was because the higher doping concentration in the p^+ junction helped produce a higher doping gradient between the junction and p -type substrate. This phenomenon caused a higher electric field through the junction, which extended the space charge region and CCE of the detector, especially when polarised in passive mode.

4.3.4.3 Photon damage for MP512 array

The radiation damage test was performed on the MP512 arrays for both the CMRP and KDB substrates. Figures 4.20 and 4.21 show the relative response as a function of accumulated dose for array #24 (KDB) substrate, which had 10 Ω -cm and 30 μ C, and sample #21(CMRP) substrate, which had 10 Ω -cm and 100 μ C. The choice of these two specific arrays was based on the outcomes acquired from the test structures' results in order to validate the best manufacturing configuration of substrate type and ion implantation charge. The sample with 10 μ C ion implantation charge from the test structure did not show a positive result, which led the focus to the other samples with 30 and 100 μ C. The test structure with the KDB substrate and 100 or 30 μ C showed a large response resulting from high CCE, and demonstrated a comparatively lower sensitivity to radiation damage. Ideally, this study would have opted for the 100 μ C ion implantation; however, due to technical issues during the manufacture process, this study opted for the 30 μ C ion implantation for the KDB substrate, which is not far from the optimum. The CMRP substrate showed an overall low response; however, a very small sensitivity to radiation damage for both gamma and photoneutrons was observed. Thus, this study selected the sample with 30 μ C ion implantation charge.

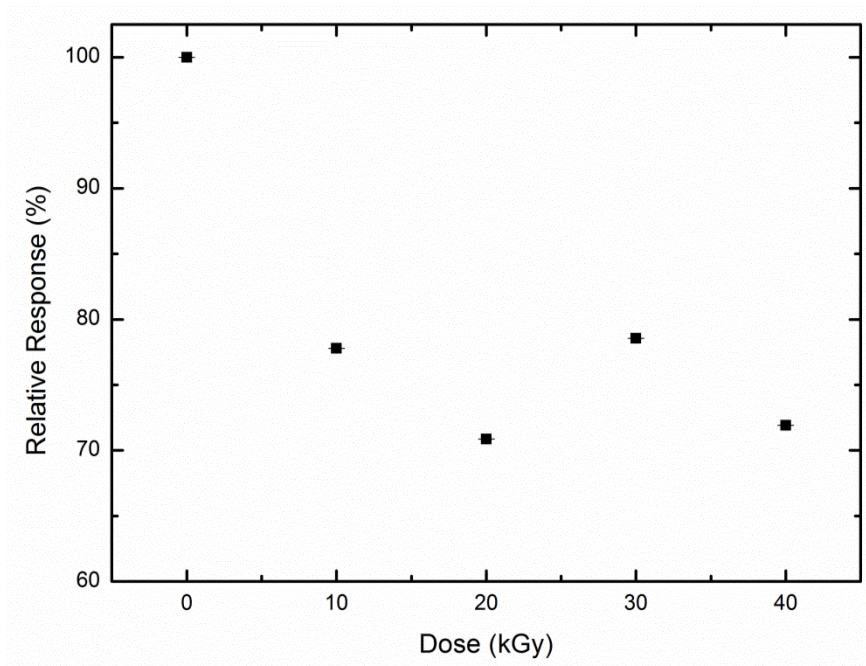


Figure 4.20: Relative response for MP512 sample #24 with KDB substrate at d_{\max}

Figure 4.20 shows a significant relative response change between the responses before and after irradiation by Co-60 up to 10 kGy. The percentage difference of relative response from pre-irradiation to 10 kGy was approximately 31%. After being irradiated up to 40 kGy, the response stabilised at 20, 30 and 40 kGy with a difference between the responses of approximately $\pm 4.5\%$, with fluctuations probably due to annealing effects related to the samples being stored at room temperature for long periods.

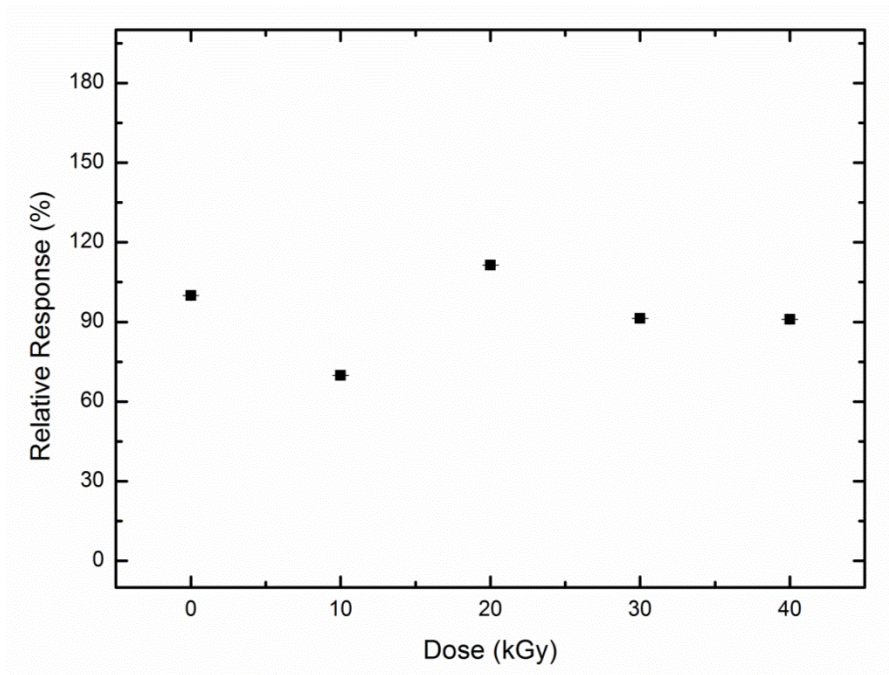


Figure 4.21: Relative response for MP512 sample #21 with CMRP substrate at d_{\max}

Based on Figure 4.21, it is problematic to make any accurate assessment of the dose and relative response of the CMRP array. This large fluctuation of the response of the diodes was due to fluctuation of the baseline, which also produced large fluctuation in the absolute response. The lower sensitivity seems to be associated with the quality of the substrate, which was rich in the GRCs responsible for the lack of CCE. Sample #24 was found to be the sample most suitable to be used in the clinical characterisation performed during this study.

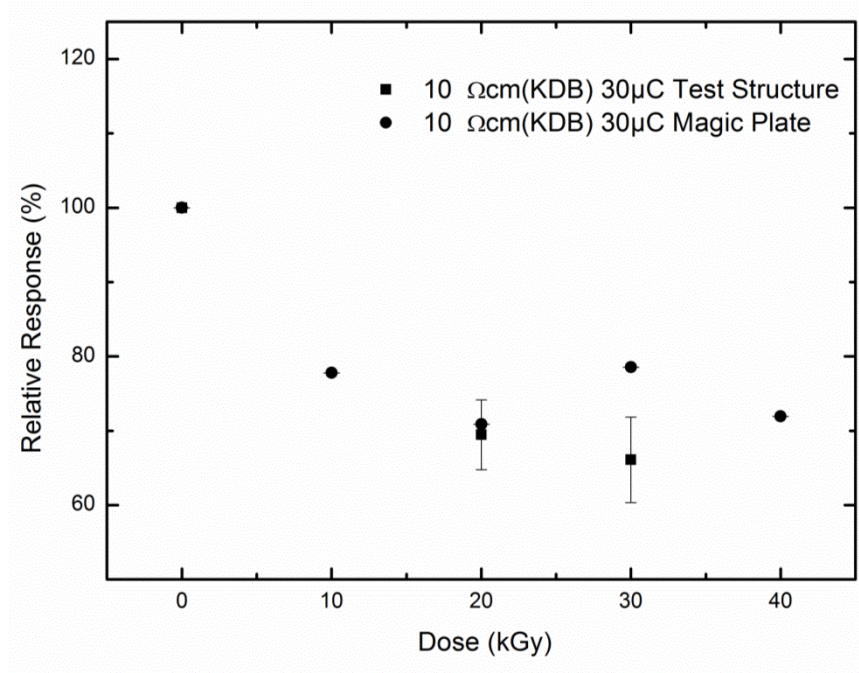


Figure 4.22: Comparison of the response of the test structures and MP512 full array as a function of accumulated dose

The radiation hardness study performed on the test structures was confirmed by repeating the same test on an MP512 full array. This comparison was required to evaluate the effect of radiation damage on the cross talk between pixels, and the effect of distribution of the electric field on the response of the pixels, and also to establish the reproducibility of the experimental setup and manufacturing process. Figure 4.22 shows the comparison of the MP512 array and correspondent test diode. The deviation between the test structure and array response was less than 4.5% at 20 kGy, and less than 2.5% at 30 kGy, thereby confirming the validity of the method adopted.

4.3.4.4 Photoneutron damage for MP512 array

Figure 4.23 shows the radiation damage after irradiation by photoneutron field for the MP with 30 μC for the KDB substrate. It shows that the decreased response was

less than 2.6%/300 Gy. This may refer to the generation of cluster defects in the Si-Oi₂ layer due to the creation of recombination centres [179].

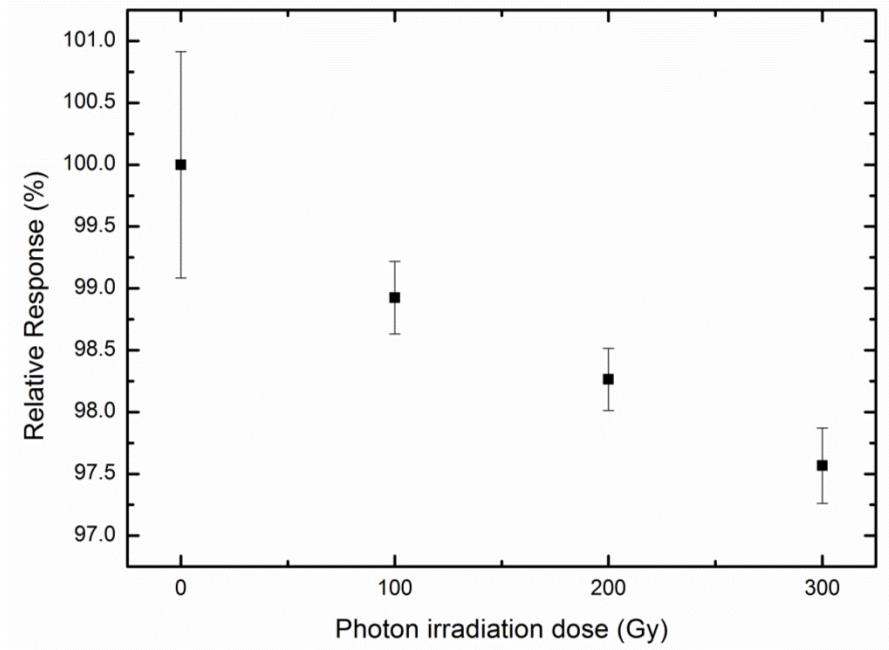


Figure 4.23: A normalised response as a function of the irradiation dose using an 18 MV medical LINAC photon beam

4.4 Conclusion

This study has tested the performance of silicon detectors in terms of their electrical characteristics and radiation hardness to determine the optimum substrate resistivity and pre-irradiation ion implantation for use in radiation therapy as a 2-D dosimeter. The I-V characteristic showed that there is no relationship between the amount of ion implantation and leakage current for test structures without a guard ring. Further, the I-V results indicated that, although a guard ring could help reduce the leakage current in a topology adopting at least 100 μC , it adds significant complexity to the architecture of a large 2-D array without a direct measurable benefit. This led this study to avoid using a guard ring in the final detector array design. The C-V results

indicated that there was a small influence on capacitance when using a guard ring in the test structures. The characterisation of the test structures indicated that the best performance in terms of radiation hardness can be achieved by generating a p -stop junction between the pixels with a boron concentration of $100 \mu\text{C}/\text{cm}^2$. Even if the detector was unbiased, the presence of a strong boron concentration gradient mitigated the effect of reducing the carrier lifetime as the irradiation dose increased. The same conclusion could be reached by considering the effect of irradiation from photoneutrons generated by an 18 MV medical LINAC. The characterisation was performed on the test structures, and the methodology was confirmed by comparison with the measurement of the response of a full detector array, which agreed with the single diodes within 4%.

In terms of comparing the test structure and MP array, this study indicated that the test structure response decreased less than the MP response. For the MP512 sample #21, the fluctuation of the response of the diodes was due to fluctuation of the baseline and the annealing effects. The results were obtained from the MP512 sample #24, which was supported by the simulation performed by Petasecca et al. [123]. The previous work was based on simulating an $n^+/p/p^+$ silicon structure with a TCAD radiation damage model for p -type substrates. Moreover, this study proved that a decreased CCE is associated with increased fluence. These results correlate with the data presented in Figure 4.20.

As a result, sample #24 of MP512 with $30 \mu\text{C}$ was used to determine the feasibility of the device for clinical use, especially for small field beams. The next chapter presents the experiments conducted related to dose linearity, uniformity, PDD, DPP, OF and beam profile. The MP512 was also used with a movable phantom to

characterise the beam profile in 2-D (X and Y) and to enable a comparison with EB3 film, which will be discussed in Chapter 7.

CHAPTER 5: A TWO DIMENSIONAL SILICON DETECTORS ARRAY FOR QUALITY ACCURANCE IN SBRT—MAGICPLATE-512

5.1 Introduction

The MP512 detector was pre-irradiated up to 40 kGy using a Co-60 gamma source to stabilise its response. Its radiation hardness performance was extensively characterised by irradiation with photons from a Co-60 gamma source, and on a mixed photoneutrons radiation field from 18 MV LINAC. This demonstrated very good radiation stability, with variation in response of approximately 1%/10 kGy (H₂O) of Co-60 and 0.9%/10 kGy (H₂O) on 18 MV LINAC. Therefore, based on the results obtained from the previous chapter, the silicon detector array of MP512 with 30 μ C and KDB substrate was chosen.

5.2 Materials and methods

5.2.1 MP detector array

A description of the MP512 was presented in Section 4.2.1.

5.2.2 DAQ

The DAQ system is an essential component of any multichannel detector device. The prototype of the MP512 DAQ system was custom designed by CMRP, based on a multichannel electrometer chip. The chip named ‘AFE0064’ (Texas Instruments) is a 64-channel current integrator that provides an analogue differential output proportional to the charge accumulated in a capacitor during a configurable, pre-settable timeframe for each channel. The chip is set electronically through a serial protocol interface on the lowest gain available to span the full scale up to 9.6 pC, with a resolution of 16 bit and a non-linearity of less than 0.1% [180]. Each current integrator is equipped with a double sampler for subtraction of the baseline—a

feature that is particularly important when a high signal-to-noise ratio is required, as in medical instrumentation.

The DAQ system uses eight chips, for a total of 512 channels that are readout in parallel by four analogue-to-digital (ADC) converters. The analogue front end and converters are handled by a field programmable gate array (FPGA) that provides the clocks and synchronisation circuitry to manage the trigger signal provided by the LINAC to synchronise the acquisition when the beam is on. A physical connection between the FPGA DAQ and LINAC is necessary by means of a coaxial cable. The FPGA also manages the USB 2.0 link with the host computer, where a graphical user interface (designed at CMRP for EBRT applications) provides real-time visualisation and all the commands necessary for the user to control the instrumentation. The DAQ system also allows asynchronous acquisition of the detector signals by generating an internal trigger with a frequency of up to 5 kHz. It resolves and reports the amount of charge generated in each silicon detector/pixel for each LINAC pulse. This feature is unique and extremely important because it allows visualisation and quantitative analysis of the transient dose-rate effect of the radiation generated by the LINAC. For further details of the DAQ, refer to Fuduli et al. [181].

5.2.3 Detector packaging characterisation

Dosimetry is strongly affected by the scattering and attenuation of a given radiation field by the materials surrounding the sensitive volume of the detector. The MP512 was wire-bonded to a 0.5 mm thick flexible fibreglass PCB carrier. The detector and PCB carrier were designed to avoid using high Z contact pads, resulting in dose enhancement effect. The water equivalency on the MP512 was evaluated by placing the detector at a depth of 1.5 cm in a solid water phantom with 10 cm of back-scattering material at an SSD of 100 cm, and irradiating the device with a 6 MV

photon beam of $10 \times 10 \text{ cm}^2$ in size. The same measurement was repeated for the backside-irradiated detector. Figure 5.1 shows the setup of the experiments under LINAC.

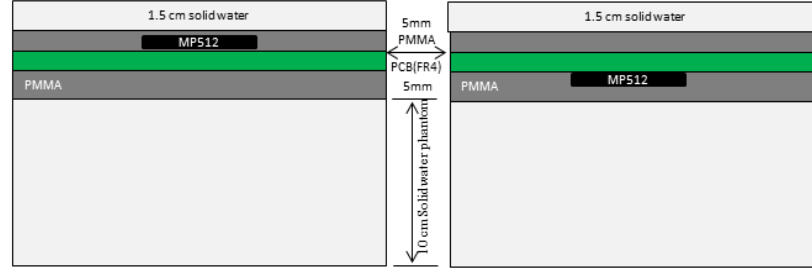


Figure 5.1: Schematic of the M512 packaging, inserting the MP512 upside down

5.2.4 Uniformity

The MP512 consisted of 512 pixels implanted on bulk *p*-type silicon substrate and connected to a readout of multichannel electronics. The response of a channel is the combination of the sensitivity of each pixel and the gain of its corresponding preamplifier channel, which can generally lead to small variations of the response from pixel to pixel. Typically, this issue can be addressed by an equalisation procedure, based on calculating a multiplication factor array, which can be used to equalise the response of the entire system, as reported earlier by Wong et al. [4]. The equalisation factor was obtained by irradiating the device at 100 cm SSD in a solid water phantom with a $20 \times 20 \text{ cm}^2$ field of 6 MV energy photons at a depth of 10 cm. The setup of this test is shown in Figure 5.2. At a depth of 10 cm, the dose cross-profile of a LINAC equipped with flattening filter was considered flat and the response from the MP512 was recorded, generating the vector X_i . Based on the hypothesis that the stimulus for all pixels is the same, the average response from all

channels ($\langle X \rangle$) was calculated. The equalisation factor vector F_i , and equalised detector response, X_{eq-i} , were then:

$$F_i = \frac{x_i}{\langle x \rangle}; X_{eq-i} = \frac{x_i}{F_i} \quad (5.1)$$

The uniformity of the array was calculated as a differential response from each pixel:

$$X_{\%} = \frac{x_{eq-i} - x_{eq-(11,12)}}{x_{eq-(11,12)}} \times 100 \quad (5.2)$$

where $x_{eq-(11,12)}$ is the response of the central detector after the normalisation procedure described above, and can be visualised by a statistical histogram.

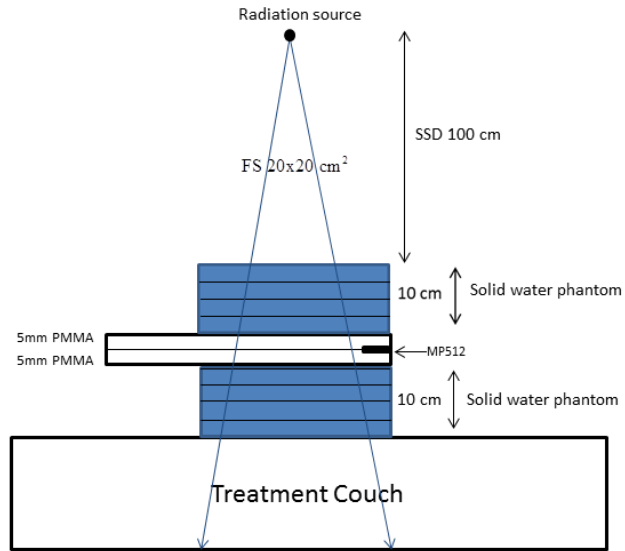


Figure 5.2: Schematic of the equalisation setup

5.2.5 Dose linearity measurement

Ideally, the dosimeter should have a linear response with the delivered MUs. The linearity response of MP512 was verified by inserting the device into a solid water phantom with a size of 30 x 30 cm² at 1.5 cm depth and 10 cm of back-scattering material, at an SSD of 100 cm. The response to a 6 MV photon beam with field size

of $10 \times 10 \text{ cm}^2$ was registered as a function of the total accumulated irradiation dose up to 500 cGy, with 50 cGy increments.

5.2.6 Percentage depth dose measurements

The MP512 was inserted into a PMMA holder composed of a slab of 5 mm on the top and bottom of the detector. Sections of $30 \times 30 \text{ cm}^2$ of solid water were used to provide the proper scattering conditions, with a slab 10 cm thick for the back-scattering material and several slabs to obtain the depth dose profile from 1.5 to 30 cm depth. The device was irradiated with 100 MU by a field of $10 \times 10 \text{ cm}^2$ at 100 cm SSD, by a 6 MV photon beam. The result was compared with measurements taken by a Markus IC (PTW-Freiburg, Germany) under the same experimental conditions (in solid water).

5.2.7 Dose per pulse measurements

The DPP dependence measurements were made for the range of $0.9 \cdot 10^{-5}$ to $3.4 \cdot 10^{-4}$ Gy/pulse. This was achieved using a field size of $10 \times 10 \text{ cm}^2$ at 6 MV with a fixed dose rate of 600 MU/min, and changing the SSD and depth of the detector in a water-equivalent phantom. The DPP reference measurement was performed using IC CC13 at d_{max} , and the response from MP512 was normalised to the chamber response ($2.78 \cdot 10^{-4}$ Gy/pulse). Characterisation of DPP by changing the depth of the detector in a phantom can potentially be affected by variation in the response of the detector with the spectrum of the radiation. The measurement of percentage depth dose shows that MP512 is energy independent up to a depth of 25 cm. To determine the very low DPP, the depth was kept constant at 25 cm and the SSD was varied from 90 to 350 cm, as suggested by previous studies [182, 183].

5.2.8 Beam profile measurement

A beam profile of an x-ray photon beam is comprised of the inter-umbral regions (the region between two penumbral regions), penumbral regions (the region included between 20% and 80% of the maximum dose intensity) and out-of-field regions [97]. Both penumbra and output factor (OF) measurements were determined with the MP512 placed at a 10 cm depth in a solid water phantom at the isocentre. The square field size was collimated by the means of the jaws, ranging from 0.5 to 10 cm, keeping the MLC completely retracted in order to avoid the problems of interleaf and round leaf-end leakages that are typical for MLCs.

The beam profile was evaluated using the central row of the detector array with 22 sampling points and a 2 mm pixel-to-pixel pitch. The alignment of the central pixel of the central row in respect to the beam was achieved by irradiating the detector with a $0.5 \times 0.5 \text{ cm}^2$ beam, and moving the detector laterally relative to the beam with steps of 1 mm in both directions. The central position was identified when the corresponding detector pixel attained the maximum response. The measured data points for the profiles were calculated as the mean value of five repetitions, and the error bars of each data point were calculated as two SDs.

5.2.9 Beam profile measurements by EBT3 film

Gafchromic EBT3 film (Ashland, Wayne, New Jersey) was used as the benchmark for the measurements of the beam profiles. The EBT3 films were cut into sections of $10 \times 10 \text{ cm}^2$ and positioned at the centre of the solid water phantom at the isocentre. They were scanned with an A3 flatbed scanner (Epson Expression 10000XL). To ensure a proper scanner warm up and better film analysis consistency, each film was scanned six times and only the last three scans were kept to perform the analysis [184]. The films were scanned in 48-bit RGB colour mode with a scanning resolution

of 70 dpi (equivalent to a pixel size of 0.362 mm); however, only the red channel was used for pixel-to-dose conversion, based on the calibration curve. Care was taken to scan the film in the same orientation at the centre region of the scanner to reduce scanner-induced non-uniformity [185].

The images were analysed using both the Image J Version 1.43U (National Institute of Health, United States) and MATLAB (The MathWorks Inc., Natick, Massachusetts) software tools. A set of calibration films was also prepared, exposed in the same experimental session and analysed following the same protocol. A 3 x 3 pixel 2-D median filter was applied to reduce image noise [184]. The data points located in the same position of the central row of MP512 were sampled for comparison of the profiles and calculation of the full width at half maximum (FWHM) of the beam. The error bar values for the film dosimetry measurements (not reported in the final plot for clarity) were determined from the uncertainty confidence limits resulting from the conversion of pixel value to dose by the optical density function:

$$OD = \log_{10}\left(\frac{I_0}{I}\right) \quad (5.3)$$

The intensity (I) and background intensity (I_0) values were measured from the image pixel values of the film scan with associated statistical errors, σ_I and σ_{I_0} , respectively. SDs were calculated across three image datasets (repeated scans of the same film). The optical density was calculated from these intensity values and converted to dose in cGy via the dose calibration curve. A second-order polynomial function was fitted to the measured data of the dose calibration curve:

$$Dose = A + Bx + Cx^2 \quad (5.4)$$

The polynomial function depends on associated fitting constants: A, B and C, with errors σ_A , σ_B and σ_C , respectively. The SDs were determined statistically by repeating the fitting process across three film scan image sets. Thus, the final error (in cGy) in the calculated dose values from the EBT3 film measurements was dependent on the values and errors associated with the measured quantities of I and I_0 , as well as the fitting constants of the second-order polynomial:

$$\begin{aligned} \therefore (\sigma_{Dose})^2 = & \left[\left(\frac{B}{I_0 \times \ln 10} + \frac{2C \times \ln \frac{I_0}{I}}{I_0 \times \ln^2 10} \right) \sigma_{I_0} \right]^2 + \left[\left(\frac{-B}{I \times \ln 10} + \frac{-2C \times \ln \left(\frac{I_0}{I} \right)}{I \times \ln^2 10} \right) \sigma_I \right]^2 + [\sigma_A]^2 + \\ & \left[\left(\log_{10} \left(\frac{I_0}{I} \right) \right) \times \sigma_B \right]^2 \left[\left(\log_{10} \left(\frac{I_0}{I} \right) \right)^2 \times \sigma_C \right]^2 \quad (5.5) \end{aligned}$$

The average uncertainty calculated across all field size measurements was approximately $\pm 1.9\%$.

5.2.10 OF measurements

The OF was defined as the ratio of dose per MU at a specific field size to the reference field size [35]. The reference field size for this study was 10 x 10 cm², measured at the isocentre (10 cm in depth at an SSD of 90 cm) [35]. The OF was calculated by acquiring the response of the detector in the central pixel (row 11 and column 12) for a field size ranging from 0.5 x 0.5 to 30 x 30 cm². The measurement setup was the same as described in Section 2.8. The OF measured by MP512 was directly compared with the MOSkin—a silicon MOSFET detector developed for skin dosimetry [95, 186]. MOSkin is a MOSFET with a water-equivalent depth measurement of 70 μ m, which presents the advantage of a very small sensitive volume of approximately 3·10⁻⁶ mm³, and a minimal size of silicon die of approximately 0.5 mm². It is mounted in fully tissue-equivalent packaging, avoiding

wire bonding and high Z materials, thereby minimising the potential radiation field perturbation associated with OF measurements. The *MOSkin* measurements for OF determination were undertaken at the British Columbia Cancer Agency, Victoria, British Columbia, Canada. The American Association of Physicists in Medicine TG-51 protocol was used by placing *MOSkin* at the isocentre in a solid water phantom (RMI Gammex) at a depth of 10 cm. A 6 MV photo beam was delivered from a Varian 21EX medical LINAC for this testing. The OF measurements taken by MP512, *MOSkin* and EBT3 films were also compared with several detector studies taken from the literature (Farmer ion chamber, Pinpoint ion chamber, Diamond PTW 60003 and Scanditronic diode unshielded) [187].

5.3 Results

5.3.1 Uniformity

Figure 5.3 shows the uniformity statistics of the MP512 response after the equalisation factors were applied. Uniformity was evaluated considering two SDs from the mean value as small as 0.25% after equalisation was applied.

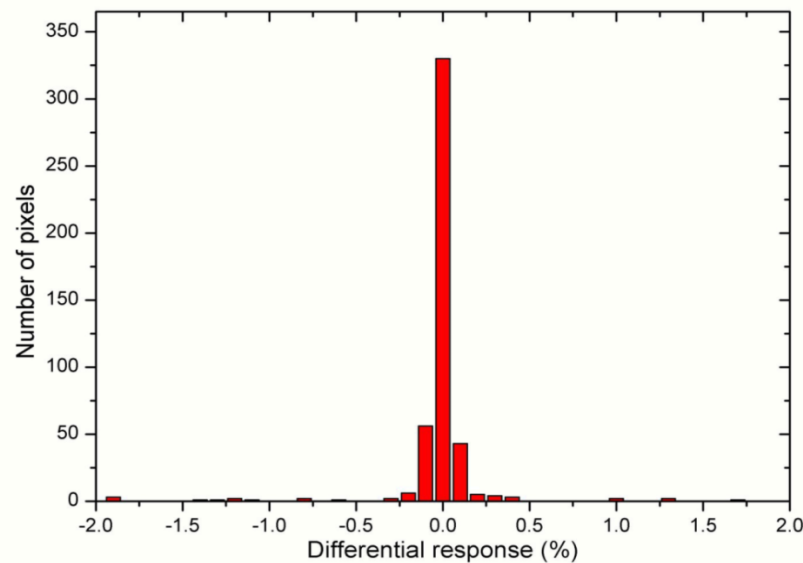


Figure 5.3: Differential response of MP512 after equalisation

5.3.2 Dose linearity

Figure 5.4 shows the dose linearity of MP512 for accumulated doses ranging from 50 to 500 MU, with 50 MU increments. The adjusted regression coefficient, R^2 , was 0.9988 and vertical error bars were calculated by two SDs over five repetitions. From the slope of the linear fit, the conversion factor from counts to dose was 1825.19 counts/cGy, which corresponded to 175.2 pC/cGy.

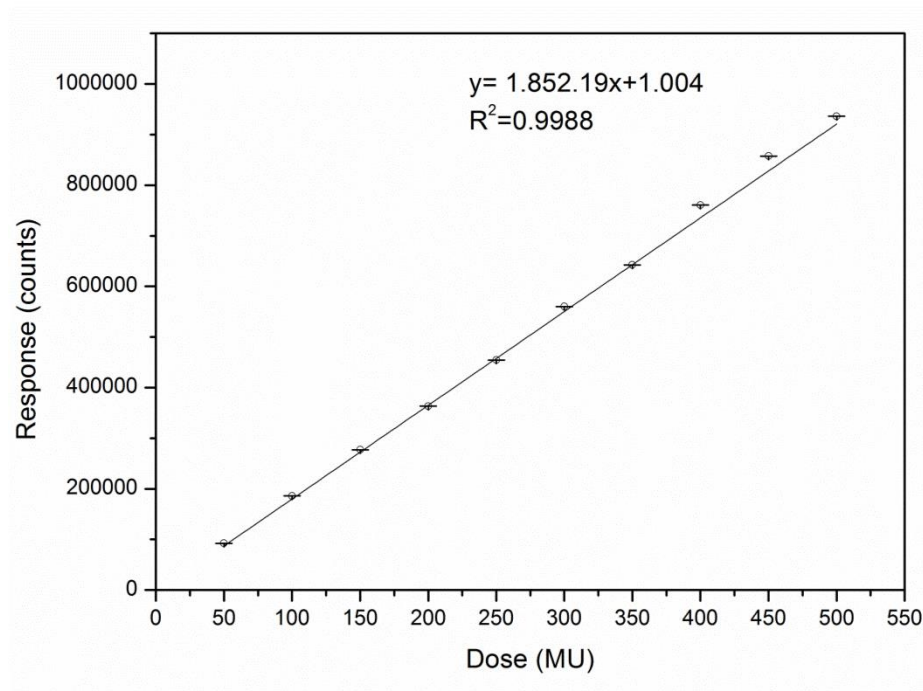


Figure 5.4: Accumulated dose response of the central pixel

Note: The solid line represents the linear fit.

5.3.3 Detector packaging

Evaluation of the effect on dose measurement of packaging MP512 on a 500 μm thick flexible PCB was performed by irradiating the detector in the phantom in both face-up and face-down orientations. The relative difference in response of the MP512 in face-up and face-down was found to be $+0.64\% \pm 0.1\%$. This showed that

the flexible thin PCB was a valid option for packaging a monolithic 2-D detector array.

5.3.4 Percent depth dose

Figure 5.5 presents the PDD for MP512 measured in a solid water phantom in comparison to the PDD measured for the same radiation field with a Markus IC. The minimum depth of measurements was 5 mm water-equivalent depth (WED). The observed maximum difference between PDDs was approximately $\pm 1\%$. Error bars were calculated as two SDs over five repetitions.

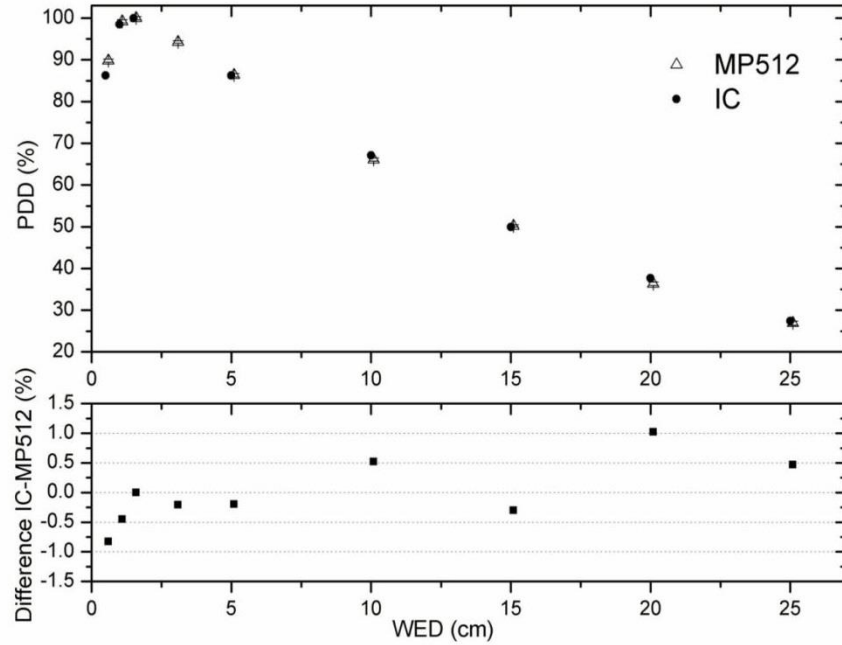


Figure 5.5: PDD measured with MP512 of 6 MV photons and $10 \times 10 \text{ cm}^2$ field in comparison with a Markus ion chamber

5.3.5 Dose per pulse dependence

Figure 5.6 shows the DPP response of the MP512, normalised to $2.78 \cdot 10^{-4} \text{ Gy/pulse}$, representing the response of the IC at d_{max} (for a 6 MV photon beam with a field size of $10 \times 10 \text{ cm}^2$). The error bars representing the uncertainties of the MP512

measurements were two SDs. For each dose rate, the response of the MP512 was normalised to the dose measured by the IC placed next to the MP512. This assumed that the CC13 was dose-rate independent. The results obtained (maximum DPP dependence was approximately 5% in the whole range of dose rate evaluated) were in substantial agreement with the data measured by Zhu et al. [183] on commercially available single diodes for dosimetry in radiotherapy and manufactured on a *p*-type silicon substrate.

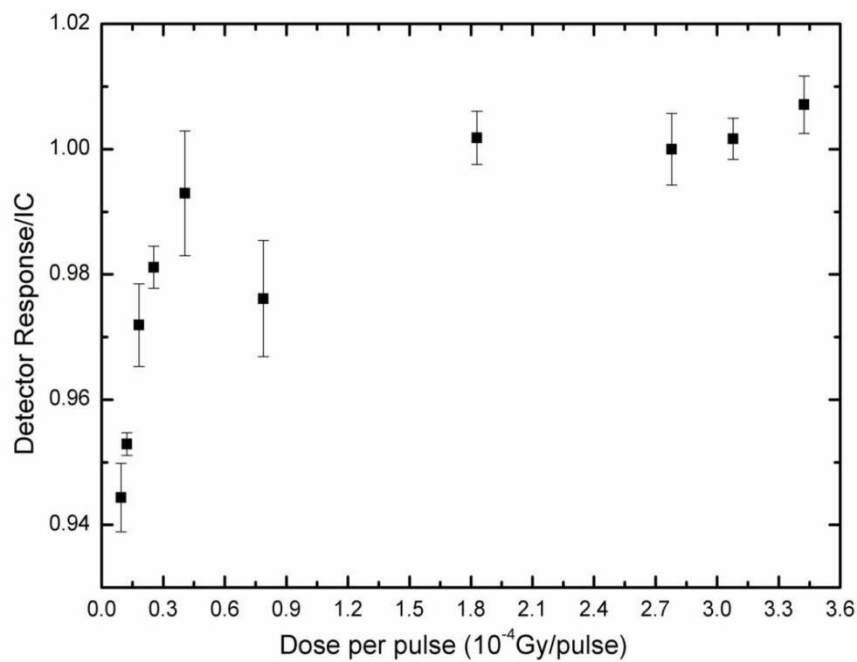


Figure 5.6: DPP response for MP512 normalised to the DPP of 2.78×10^{-4} Gy/pulse

Note: DPP was estimated at a depth of 1.5 cm and SSD of 100 cm. The x-axis represents the DPP in the order of 10^{-4} Gy/pulse.

5.3.6 Beam profile measurements

Figure 5.7 shows the measurements of the beam profile for square beam sizes ranging from 0.5 to 5 cm. The plot compares the data measured by a set of EBT3 Gafchromic radiotherapy films (Ashland, Wayne, New Jersey) with the

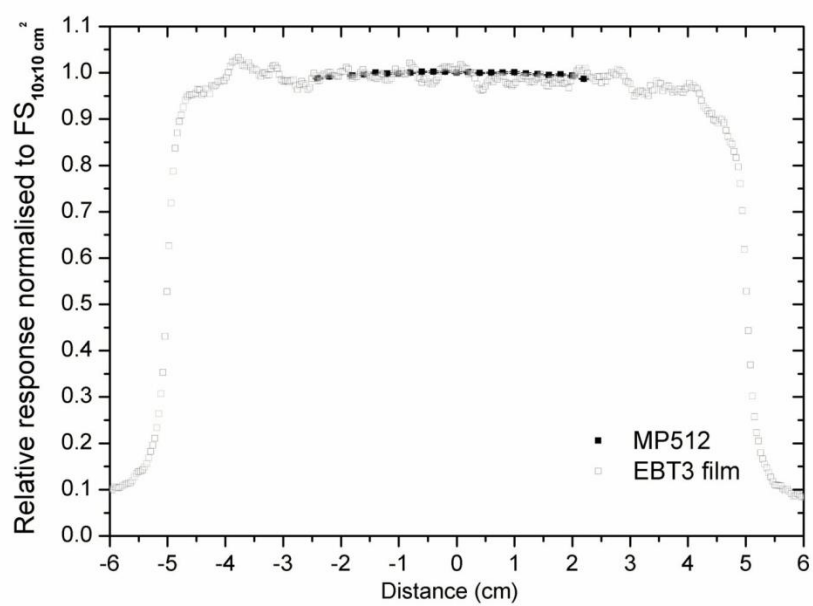
measurements performed by the MP512. All MP512 profiles were normalised to the response of the central axis pixel (CAX) at row 11 and column 12, and aligned with the corresponding EBT3 profile to the value at 50% of CAX. Profiles for 5 x 5 and 10 x 10 cm² (Figure 5.7a and b) were aligned to the response of the CAX because the value at 50% was not available since the detector was too small for such field sizes (Figures 5.7a and b). The profile measured with EBT3 films was normalised to the average value of a 2 x 2 mm² area around the central axis of the beam profile. For a more accurate evaluation of the agreement between film and MP512, the datasets were analysed with MATLAB (MathWorks, Natick, Massachusetts) to generate a fit using the Curve Fitting Toolbox. The FWHM and penumbra (80%-20%) were evaluated by interpolating the data points using the interpolation shape-preserving fit (with a resolution step of 0.01 mm), as summarised in Table 5.1.

Table 5.1: EBT3 and MP512 FWHM and penumbra width (80%-20%) study for different square field sizes at 10 cm depth and isocentre

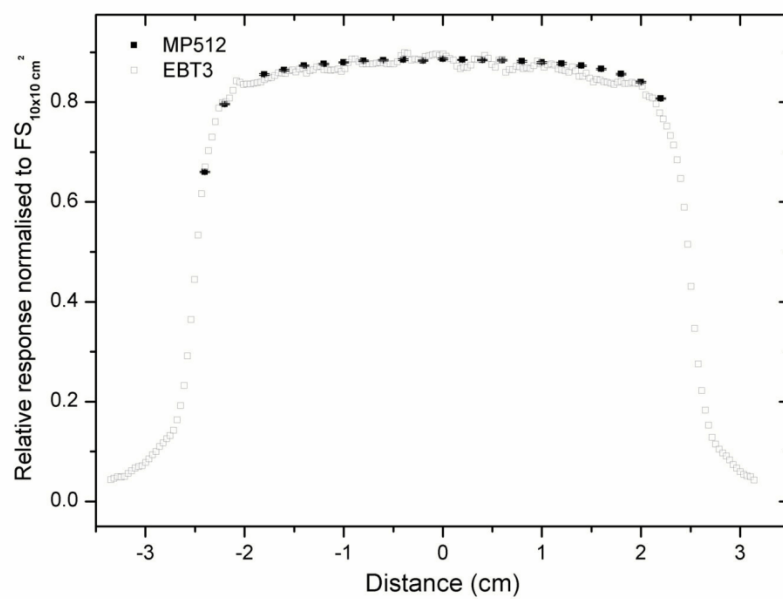
Field size (mm)	EBT3		MP512		$\frac{MP512 - EBT3}{EBT3} \times 100$	
	FWHM (mm)	Penumbra (mm)	FWHM	Penumbra	Δ FWHM (%)	Δ Penumbra (%)
100	100.46	3.60	-	-	-	-
50	49.98	3.31	-	-	-	-
40	39.96	3.16	40.16	3.61	+0.5	+14.2
30	29.88	3.02	29.89	3.49	+0.03	+15.5
20	19.91	2.74	20.08	3.17	+0.85	+15.6
10	9.96	2.46	10.08	2.89	+1.2	+17.4
5	5.15	1.97	5.22	2.36	+1.36	+19.7

The MP512 and EBT3 films showed good agreement to within 1.36% in the evaluation of the FWHM of the field size. The MP512 gave penumbral widths (80%-20%) that were nominally about 0.4 mm wider than those derived from the EBT3 film measurements. Additionally, the relative discrepancy increased with the decrease of the field size, suggesting an effect of averaging due to the size of the

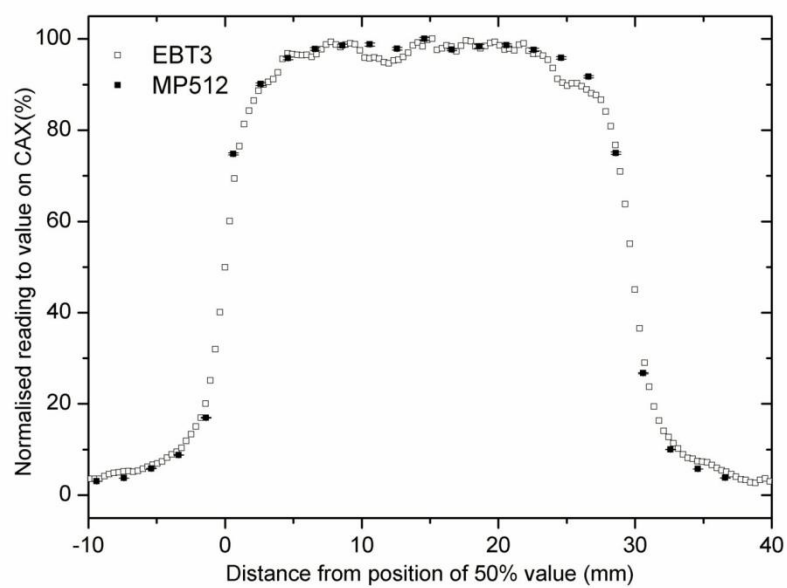
detector sensitive area ($0.5 \times 0.5 \text{ mm}^2$). Also contributing was the effect of the detector pitch size (2 mm), which became too large relative to the steep gradients of the penumbra width, especially for very small field size beams. A detailed analysis of this effect was presented by Wong et al. [26]. However, the absolute value of the discrepancy was lower than 0.4 mm for the penumbra of the smallest field of $5 \times 5 \text{ mm}^2$. Hence, the overestimation was acceptable for clinical use, considering that the general criterion for plan verification in small field therapies is approximately 1 mm distance to agreement.



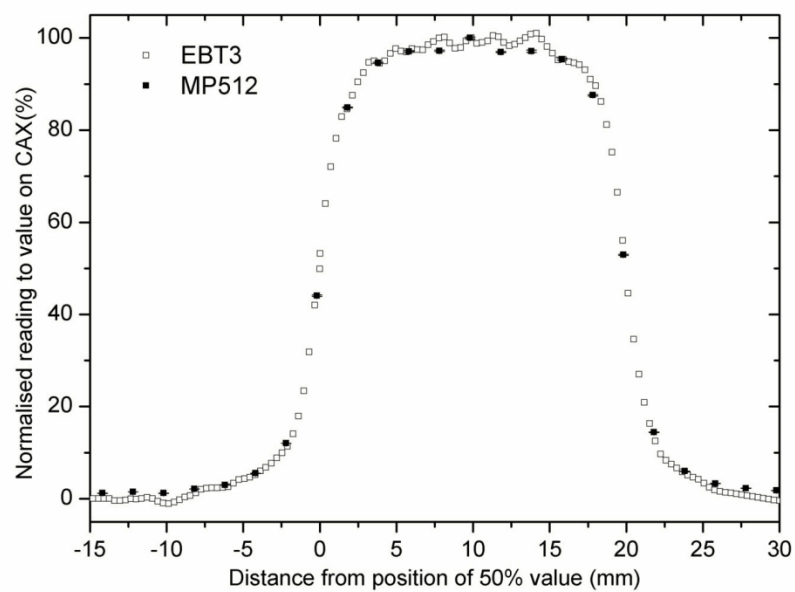
(a) $FS = 10 \times 10 \text{ cm}^2$



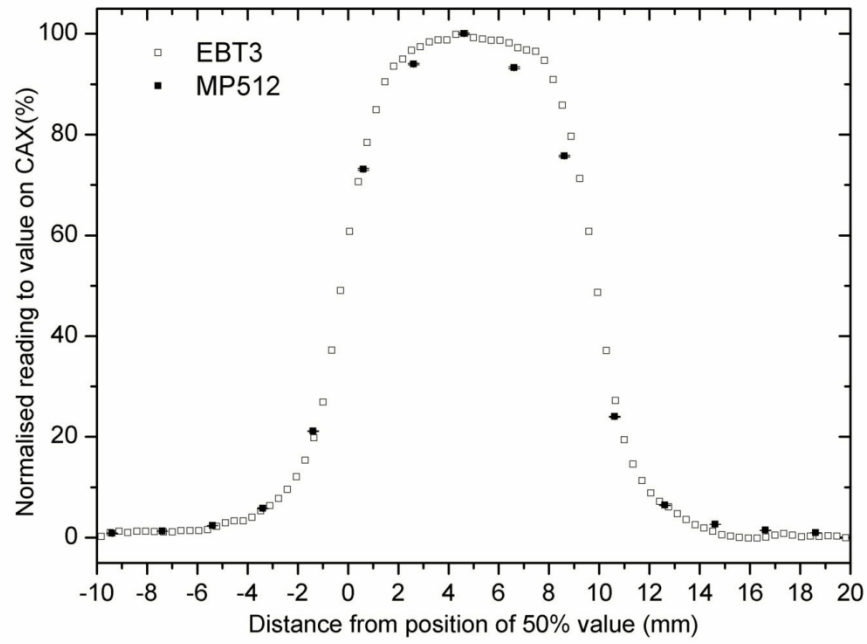
(b) $FS = 5 \times 5 \text{ cm}^2$



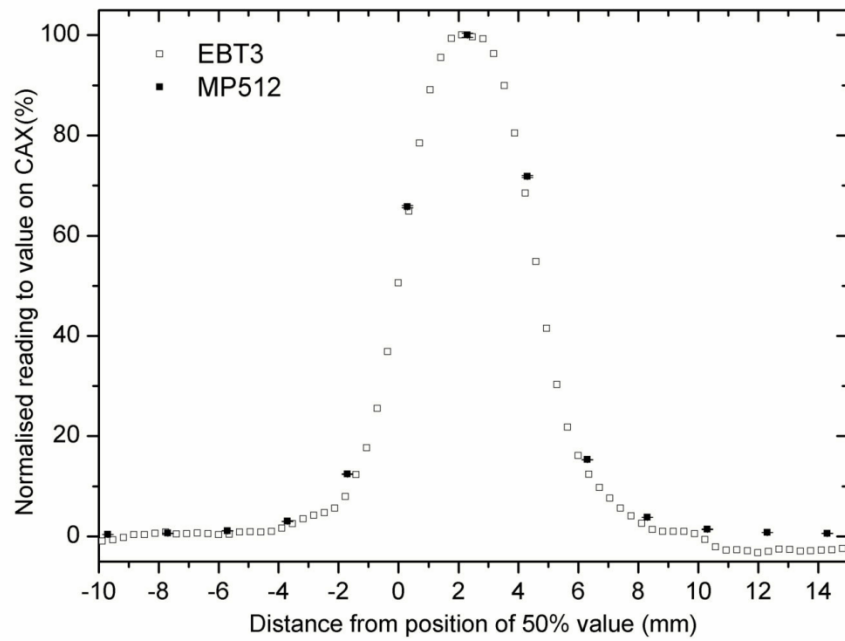
(c) $FS = 3 \times 3 \text{ cm}^2$



(d) $FS = 2 \times 2 \text{ cm}^2$



(e) FS = $1 \times 1 \text{ cm}^2$



(f) FS = $0.5 \times 0.5 \text{ cm}^2$

Figure 5.7: Beam profiles measured with MP512 and EBT3 films for radiation fields ranging from 0.5×0.5 to $10 \times 10 \text{ cm}^2$

Note: FS = field size.

5.3.7 OF measurements

Figure 5.8 shows the response of the central diode of the MP512, *MOSkin* detector and EBT3 film as a function of the field size at the isocenter and at a depth of 10 cm for a 6 MV photon beam, normalised to the 10 x 10 cm² field size. For field sizes smaller than 1 x 1 cm², the MP512 over-responded (less than 4%); effect which has been observed earlier for point silicon diodes as well. This effect is due to perturbation of the radiation field by the silicon and the package material of the diode. With decreasing field size, the relative portion of the beam directly interacting with the silicon and surrounding materials of the packaging increased. This causes the electrons scattered from the silicon and packaging material take a more dominant role in the response of the detector. In contrast, the large field response was dominated primarily by electrons that were scattered from the solid water. By reducing the size of the nontissue equivalent detector and its packaging, this effect can be minimised. It almost disappears when a very small size point silicon detector, surrounded by no high Z materials—such as the *MOSkin*—is used to measure the OF. The *MOSkin* showed excellent agreement with the EBT3 films, having a response difference within 1.5%. The *MOSkin*'s 'drop-in' technology adopts only quasiwater equivalent materials, thereby minimising the effect of the dose enhancement of materials with a high atomic number.

These results were compared with measurements taken by several research groups worldwide using commercial detectors in the same experimental conditions (Figure 5.9) [187]. Although this comparison involved measurements taken by different LINACs, it showed that the results obtained in this study fit very well with the trend obtained by very different detector types. Both the Farmer and Pinpoint ICs exhibited

a lower response when compared to other detectors due to the averaging effect of the sensitive volumes of 0.6 and 0.13 cm³, respectively. For field sizes equal to 1 x 1 cm² and larger, the MP512 results agreed generally within 1%. It is possible to compensate for the over-response of the MP512 for these small field sizes using a small air gap above each pixel to ideally match the EBT3 film [188, 189].

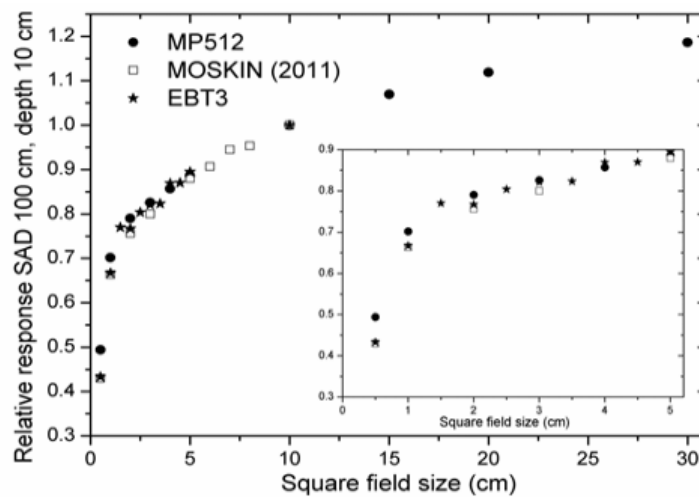


Figure 5.8: Field size dependence response of MP512, MOSkin and EBT3 film normalised to response at 10 x 10 cm² field size

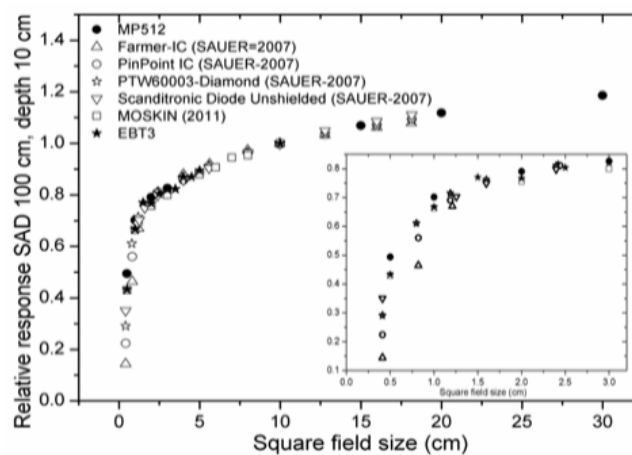


Figure 5.9: Comparison of output factor for a different detector type and size from Sauer et al. [187]

5.4 Conclusion

The MP512 is a 2-D array monolithic pixelated detector based on ion-implanted *p*-type silicon technology. It comprises 512 pixels arranged in a 22 x 22 array with seven extra elements for each detector side, covering an area of 52 x 52 mm². The sensitive volume of each diode is 0.5 x 0.5 x 0.1 mm³, and the detector pitch is 2 mm. Variation of the response between the diodes in a flat field was $\pm 0.25\%$ after uniformity correction. Characterisation of the MP512 for phantom dosimetry QA in SRT applications was performed. PDD measurements of the MP512 were compared to those with ionising chambers and agreed to within 1.5% for depth. Dose rate dependence of the MP512 was evaluated by comparing the response to an ionising chamber. MP512 showed a DPP dependence within 1% down to $3.5 \cdot 10^{-5}$ Gy/pulse (approximately one order of magnitude lower than in-field DPP), while it showed approximately 5% at the lowest DPP of $0.9 \cdot 10^{-5}$ Gy/pulse.

The normalised beam profile distributions for square field sizes between 0.5 and 4 cm were measured with the MP512 and compared to Gafchromic EBT3 film. The MP512 showed excellent performance in beam profile reconstruction (FWHM discrepancy less than 1.3%). But in spite of much higher spatial resolution and pixel size of the available 2-D diode array, the MP512 produced a discrepancy in the penumbra of less than 0.4 mm for the smallest fields. This discrepancy still falls within the acceptance criteria of 1 mm generally accepted for small field dosimetry penumbra. A detailed comparison of the OFs and beam profiles measured by the EBT3 and MP512 showed that the MP512 is suitable for beam profile reconstruction down to a 10 mm square field size with a discrepancy of the relative response of the central channel of less than 2%. The MP512 showed an over-response (less than 4%)

with the $5 \times 5 \text{ mm}^2$ field size because the scattering produced by the silicon surrounding the central pixel is not negligible. To prove this hypothesis, a single small silicon detector with tissue equivalent (TE) packaging (*MOSkin*) was tested and compared with the EBT3 film measurements. The *MOSkin* agreed to within 1.5% of the EBT3 film measurements down to a 5 mm field size.

Further improvement of the MP512 for field sizes smaller than $10 \times 10 \text{ mm}^2$ can be achieved by reducing the pixel pitch and pixel size down to $200 \text{ }\mu\text{m}$ and introducing a small air gap above the detector to mitigate the dose enhancement produced by the silicon chip die. Before MP512 can be used as a patient-specific QA device, few more experiments should be undertaken to enable complete characterisation in a clinical scenario such as effect of MLC on dosimetry and characterisation of the energy dependence. Further, any 2-D detector array demonstrated angular dependence; however, no angular dependence study was performed. This is because we developed a new QA tool that allows the detector to be exposed perpendicularly to the beam. This was labelled a ‘rotatable phantom’, and is introduced in the next chapter.

CHAPTER 6: ROTATABLE PHANTOM FOR AUTOMATIC ALIGNMENT OF MP512 WITH THE LINAC BEAM

6.1 Introduction

The rotatable phantom was designed and produced by CMRP to avoid the angular dependence of the detector. Inserting the MP512 in a rotatable cylindrical phantom that rotates synchronically with the gantry head of the LINAC helps the beam constantly incident perpendicularly to the detector. The design of such devices demands high accuracy and attention to detail. A 3-D computer-aided drawing package, SolidWorks (Dassault Systems SolidWorks Corporation, Massachusetts), was used to design the rotatable phantom model and technical drawings.

6.2 Rotatable phantom description

The rotatable phantom was designed to have a cylindrical shape to allow the detector to rotate in an angular range of $\pm 180^\circ$, with a bidirectional accuracy position of ± 0.25 degree. It can be rotated in a clockwise direction and its movement can be controlled either manually or automatically. The rotatable phantom angle can be determined using an inclinometer attached to the LINAC gantry head. The rotatable phantom was made from PMMA material (PMMA density 1.17 g/cm³), which is close enough to tissue equivalent for 6 MV photon beam energy. The physical dimensions of the rotatable phantom are 30 cm diameter and 40 cm length, which approximately corresponds to the length of the thoracic duct of an adult. The rotatable phantom weight is 35 kg. The MP512 was held by thin PCB board and inserted into the phantom slot, which has a width of 13 cm and a depth of 15 cm. The MP512 was sandwiched between 25 + 25 mm solid water slabs, and was placed on the centre of rotation. The solid water insert was necessary to accurately mimic the scattering conditions of water close to the detector in order to avoid the dose enhancement

generated by denser materials such as PMMA. At 6 and 10 MV, the maximum range of secondary electrons was approximately 15 and 25 mm, respectively. Using such an insert around the detector enables greater charge particle equilibrium (CPE) to be achieved.

The rotatable phantom was synchronised with the LINAC by a stepper motor (NEMA 24) with a torque of 2.74 N-m. The motor was driven by the same acquisition system that managed the data collection of the detector signal. The stepper motor was placed on the large plate and attached with a small gear (the small gear has 18 teeth, while the large one has 64 teeth) that drove the large gear via a timing belt. The length of the timing belt was between 620 to 650 mm, and it had lateral flanges to avoid misalignment. The large gear was attached directly to the cylindrical phantom by the aluminium shaft (10 mm length). The position of the detector was monitored by an optical encoder (Absolute Encoder Multiturn ATM 60 SSI servo flange) attached at the phantom's shaft, and the LINAC head position was measured by an inclinometer placed on the accessory tray. This system of sensors was necessary to instantaneously maintain the alignment of the detector with the beam with discrepancy within $\pm 1^\circ$. The rotating encoder was used to determine the position of the phantom precisely with accuracy within a measuring step of 0.043 degree. The digital interface used with the optical encoder was RS 422. Figure 6.1 (left) presents a drawing of the final design of the rotatable phantom by SolidWorks, while Figure 6.1 (right) presents a photograph of the phantom under the LINAC gantry.

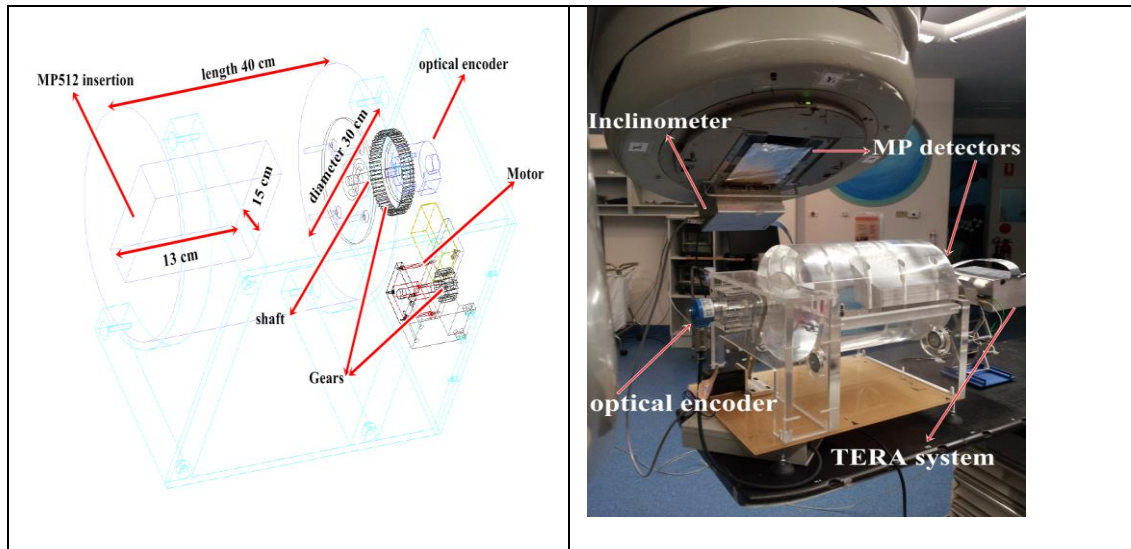


Figure 6.1: Final design of the rotatable cylindrical phantom by SolidWorks (left) and actual rotatable cylindrical phantom with an inclinometer attached to the LINAC head (right)

Inserting the MP512 in the rotatable cylindrical phantom that rotates synchronically with the gantry of the LINAC, helps to maintain the beam constantly perpendicular to the detector. Figure 6.2 shows the actual phantom following the LINAC gantry, with the beam constantly remaining perpendicular to the MP512.

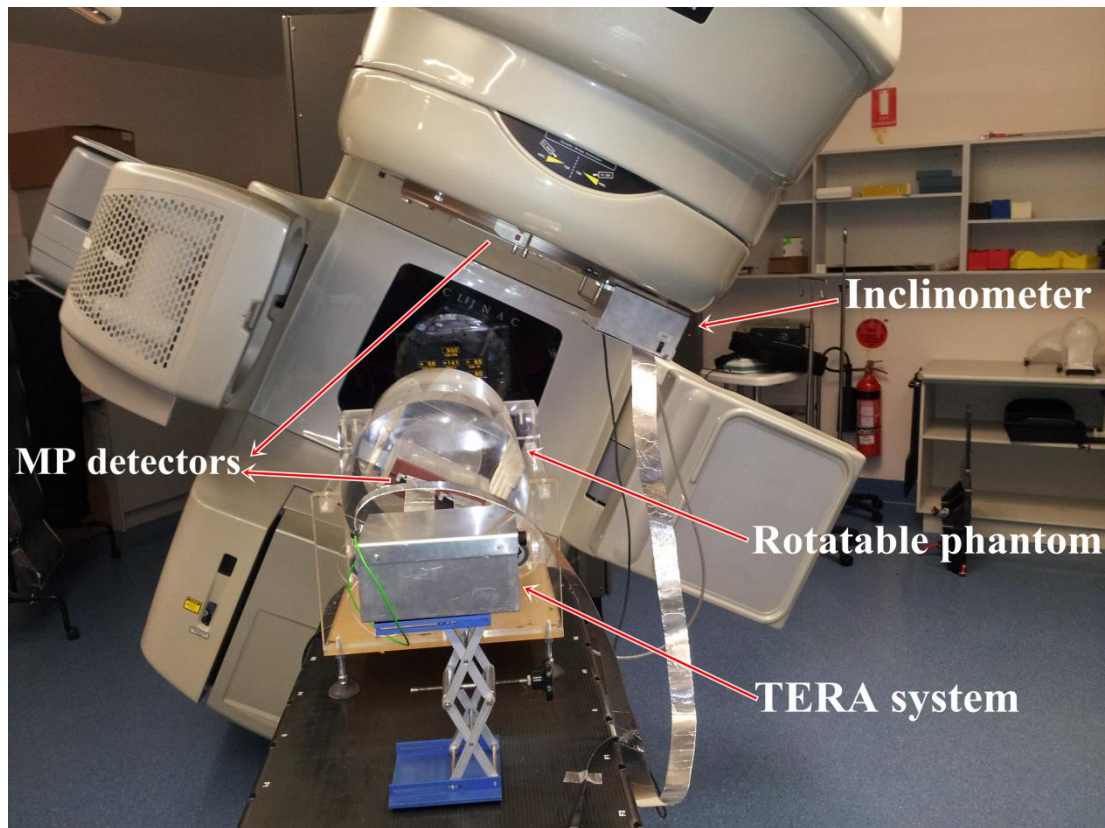


Figure 6.2: Phantom with mechanical parts under the LINAC gantry

6.3 X-ray CT for rotatable cylindrical phantom

Before dose is delivered to the patient, it is necessary to check the dose calculations of the treatment planning using a phantom. Such dose verification procedure is based on simulating the same plan calculated for the patient on the phantom geometry [190]. The next step involves measuring the dose by IC, semiconductors or films, then comparing it with the calculated dose. The rotatable phantom is used as a QA tool to verify the dose distribution. The rotatable phantom is scanned using CT simulation. CT simulation has the ability to provide accurate internal and external contour information for the phantom, converting CT numbers into electronic density of the different parts of the phantom. Figure 6.3 presents the CT image taken for the rotatable phantom in 3-D. The image clearly shows the solid water slabs (dark part,

MP insertion) that have density and CT number comparable to water (solid water density =1.02 g/cm, CT number =17). PMMA show higher CT numbers compared to water (CT number =133).

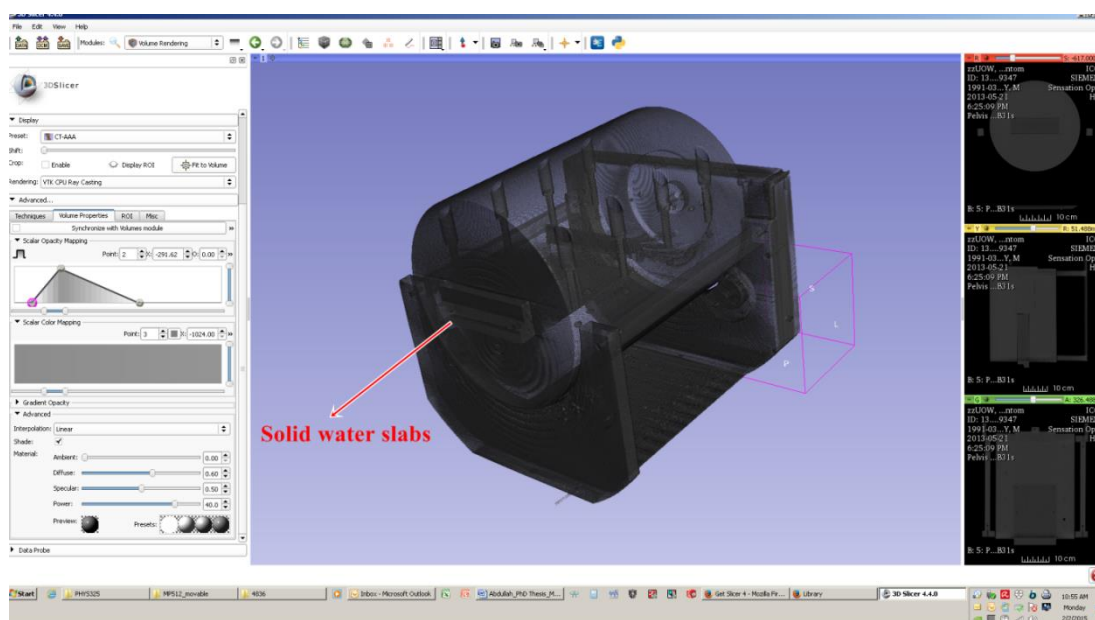


Figure 6.3: CT image of the rotatable phantom in 3-D

Based on the CT simulation, data were collected and used in the treatment planning system to simulate the proper radiation beams. Figure 6.4 shows the simulation of the incident beam by the treatment planning system on the rotatable phantom.

Further testing of the accuracy of the dose distribution in the rotatable phantom compared to TPS calculations is not part of this work and will be analysed and reported by other students.

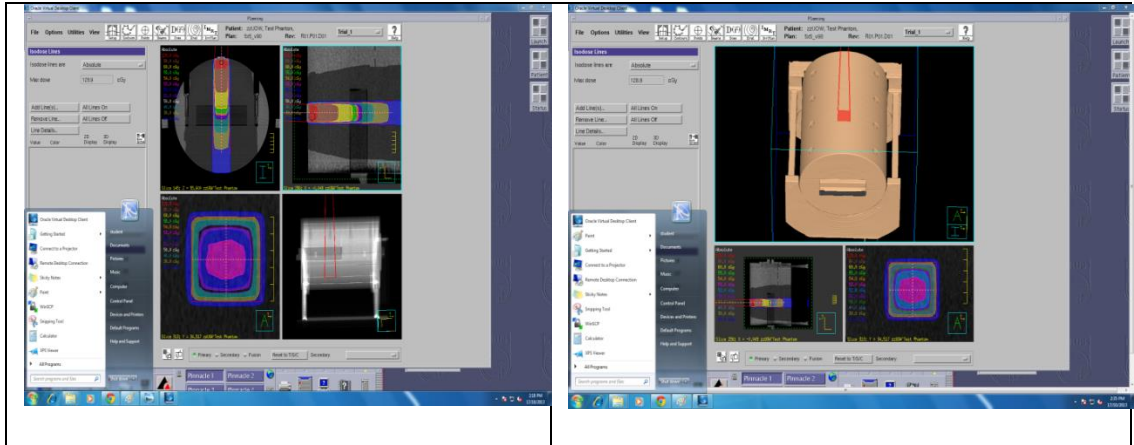


Figure 6.4: 2-D isodose plan of the rotatable phantom

6.4 Mechanical and electronics parts of the rotatable phantom system

The system is composed of three modules: (i) a digital inclinometer placed on the LINAC accessory tray, (ii) a rotating encoder attached at the phantom drum, and (iii) a slow-control module that includes the PMMA phantom equipped with a stepper motor and the power supply that provides all the power rails required by the system.

Figure 6.5 presents a schematic representation of the rotatable phantom system.

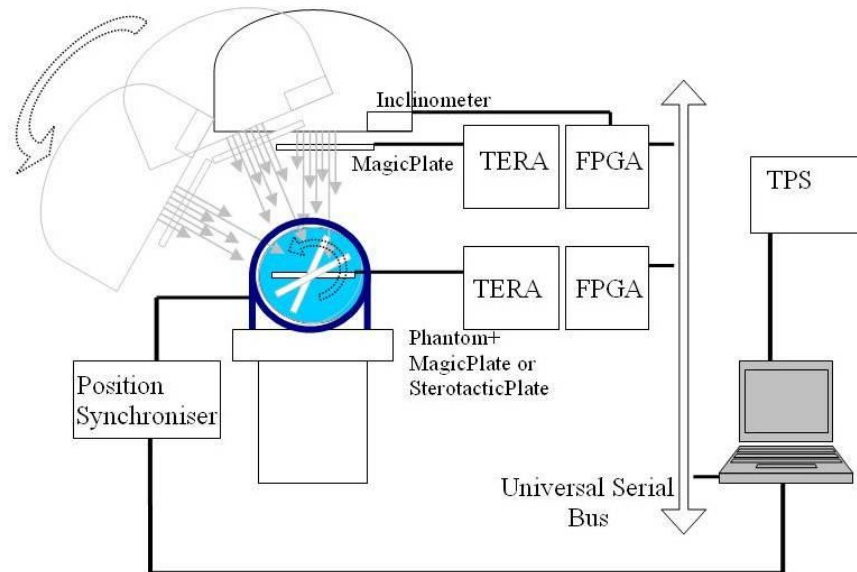


Figure 6.5: Schematic diagram of the rotatable phantom system

Note: The position synchroniser and DAQ of the analogue front-end electronics were embedded in the FPGA module, but are presented separately here for clarity.

The inclinometer, optical encoder and slow control were the modules responsible for the active alignment of the detector, which was always kept perpendicular to the beam. The inclinometer is a commercial chip made by Analogue Devices. It is a 14-bit digital gyroscopic sensor that has a resolution of 0.025° on the rotating angle. The FPGA controls the inclinometer with a Serial Peripheral Interface (SPI), and requests all information needed, such as the instantaneous position during normal operation, or parameters such as the power supply or the SPI status, in case it is operated in debugging mode [191]. The FPGA also manages the zeroing procedure for aligning the angle read by the inclinometer on the LINAC and by the encoder on the phantom, via using a simple command on the host computer's graphical user interface. The position of the inclinometer is used to make the rotation of the gantry compatible with the full range of the sensor, which is $\pm 180^\circ$. The slow control lies in the set of commands sent by the FPGA to control the stepper motor and read out the rotating optical encoder. The encoder is a multi-turn, 24-bit digital output, rotating sensor that adopts a RS-422 or SSI protocol [192] to communicate with the FPGA.

The 12 'most significant bits' are dedicated to the number of revolutions and the 12 'least significant bits' are used to divide 360° into 4096 steps, giving a resolution of 0.088° per step. The absolute position of the zero degree is set by sending a command from the host computer's graphical user interface, and this remains in the memory of the encoder unless changed by the user. A commercial stepper motor is used to rotate the phantom according to the information obtained from the inclinometer and encoder. The nominal resolution of the motor is 1.8° per step. The

stepper motor driver is a commercial microstep device called ‘G203V’ from Gecko [193]. It is optically insulated to minimise the propagation of the noise. It divides each step of the motor by 10 to give a resolution of 0.18° per step. A system of gears and belt physically connects the motor to the phantom, allowing for a further increase in resolution by a factor of 3.34, which brings the effective rotating resolution of the phantom up to 0.054° per step.

6.5 Slow control and DAQ digital design

The main feature of the proposed rotatable phantom is the ability to detect the position of the gantry and activate the stepper motor to keep the detector perpendicular to the beam, based on numerical information from the inclinometer and encoder. The acquisition of inclinometer and encoder data is synchronised with the acquisition of the detectors so that each detector snapshot of the dose delivered in a frame also has information relative to the position of the LINAC head and the phantom.

For the alignment of the phantom, the angle read from the inclinometer is compared to the angle read by the encoder and the absolute difference between the two data, scaled by the conversion factor given by the number of steps necessary to reach the desired position. Additional controls are added to determine the direction of the rotation of the motor, allowing for full bi-directional tracking of the gantry. Another constraint is related to the way the gantry moves: it spans all 360° , from -180° to $+180^\circ$; however, it always returns to the position of 0° (crossing from the -180° to $+180^\circ$ position is not allowed). Controls guarantee that the phantom follows the same path. Figure 6.6 shows the firmware block diagram.

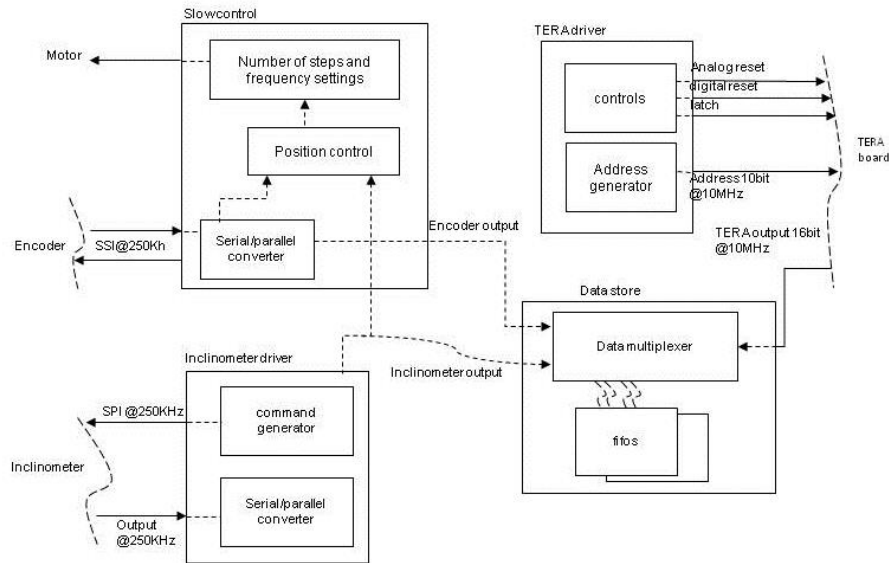


Figure 6.6: Simplified block diagram of the rotatable phantom architecture

The difference between the angles recorded by the inclinometer and encoder also drives the frequency of the steps, which determines the speed of the motor to reach the final expected position. Many theories suggest that using a proportional-integral-derivative (PID) control system is the optimal method for open loop control. Thus, a PID module was implemented in the FPGA firmware. A PID involves multiple calculations that remember past positions and generate an output that smoothly follows the behaviour of the input. In the proposed system, that means changing the frequency of the motor at each acquisition timing frame of 100 ms, 50 ms or even faster, depending on the application.

An alternative solution was designed to avoid an overload of calculation—called ‘discrete angle control’ (DAC). The DAC approach simplifies the algorithm of the speed selection and allows for the use of a combinatorial network, instead of a complicated sequential arithmetic logic unit. The DAC approach appears to be very simple to implement; however, it can be slow to catch up with the gantry if the

LINAC accelerates because it has no memory of the previous position and relies on absolute error. A third solution, called Adaptive Discrete Angle Control (ADAC), has been designed in order to add some flexibility to the DAC mode. The ADAC approach checks the position's error and sets the initial speed of the motor in the same manner as the DAC mode; however, the last error estimation is remembered. As the system acquires again, the algorithm compares the new error with the previous error, and, even if the value falls in the same step, it increases or decreases the speed of a fixed amount in order to quickly track a speed variation of the gantry.

6.6 Experimental results: control system tuning and comparison at the workbench

A test bench of the system was designed to verify the functioning of the three modules by internally generating the information about the position of the gantry moving at $2^\circ/\text{s}$ to $7^\circ/\text{s}$. First, the PID was tuned using the Ziegler-Nichols method [194]. Figure 6.7 shows how the response of the system changes at different gains. At the minimum gain ($K_p = 1$), the control was not fast enough to track the test signal, which simulated a continuous movement from 0° to 65° and backwards at the speed of $7^\circ/\text{s}$. Various values of the gain were used to attempt to reach the point of instability ($K_p = 50$), then the three factors of the PID (K_p , K_i and K_d) were calculated following the Ziegler-Nichols equations. The optimised PID was then tested, and appeared to be fast enough to track the test signal and be stable.

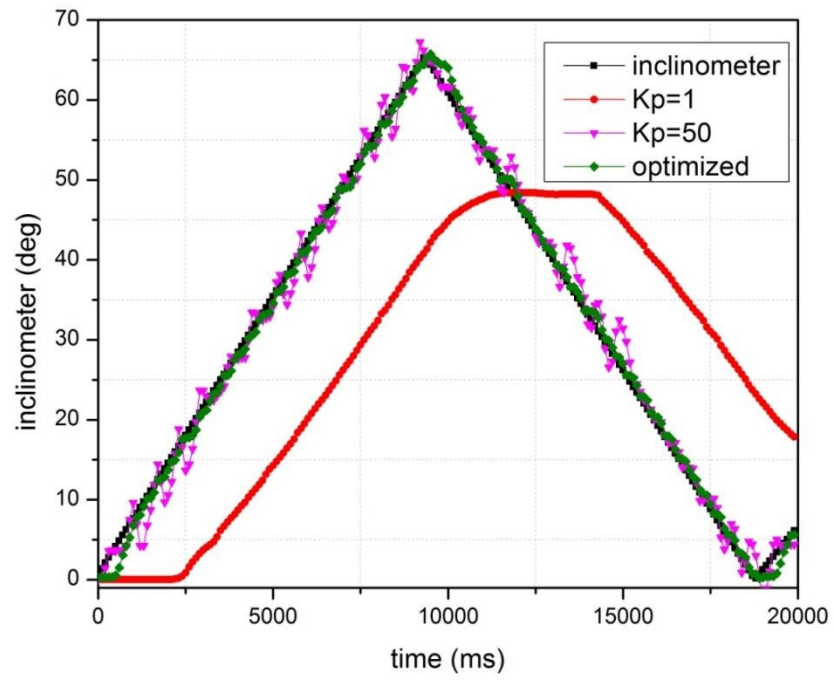


Figure 6.7: PID tuning tracking mode

To compare the performance of the three models by using an internal generated angle pattern (to simulate the data provided by the inclinometer), this study defined rising time, overshoot and settling time as per Figure 6.8 for the step response.

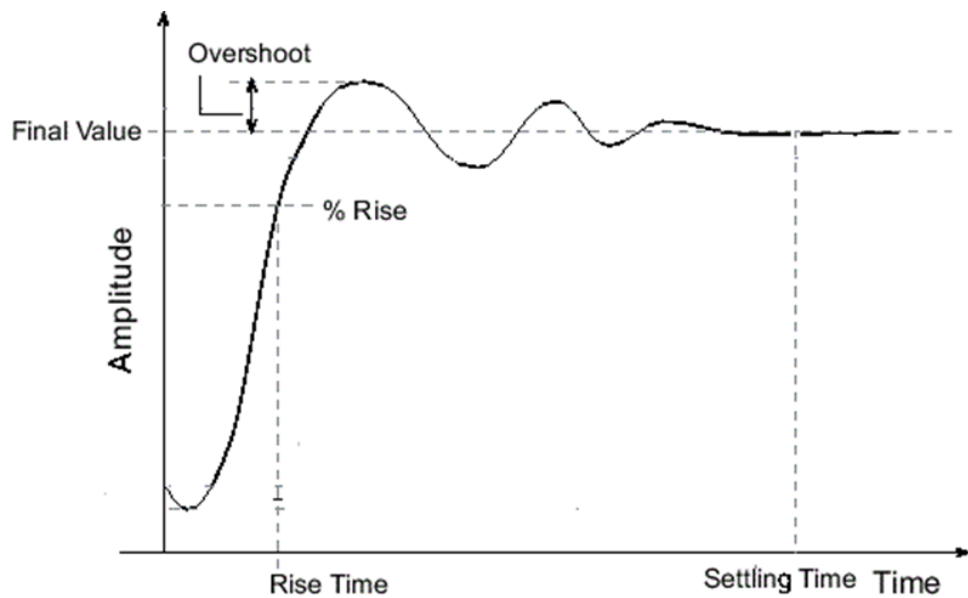


Figure 6.8: Timing parameters

Figure 6.9 shows the response of the three control solutions (PID, DAC and ADAC) to a step of 90° (constant speed in one direction from -45° to $+45^\circ$). Looking at the timing performances summarised in Table 6.1, the ADAC method appears to have more performance control over the phantom. In particular, the step response has no overshoot—a characteristic that is particularly relevant for the phantom due to its large mass inertia.

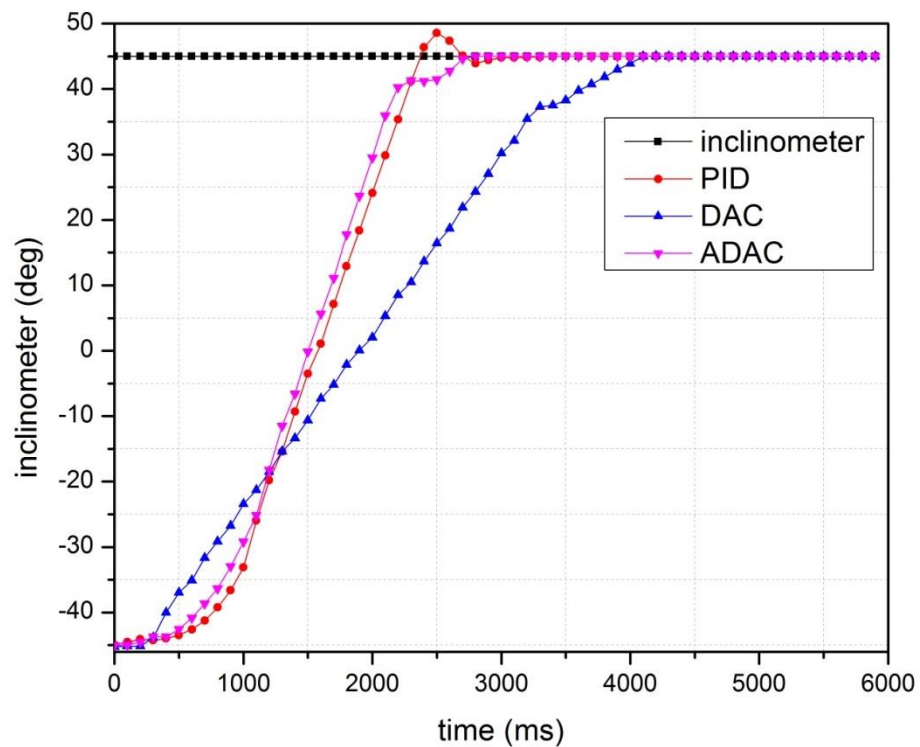


Figure 6.9: Step response

Table 6.1: Timing performances

Step response	DAC	ADAC	Optimised PID
Rising time @ 90% (s)	3.4	2.3	2.4
Overshoot (deg)	0.056	0	4.664
Settling time (s)	1	0.6	1.1
Std tracking mode (deg)	0.21	0.19	0.39
Std global (deg)	0.7	0.39	0.55

6.7 Experimental results using a medical LINAC

The system was tested at the Illawarra Cancer Care Centre by using the Varian 2100EX Clinic and installing the inclinometer into the LINAC's accessory tray. As a preliminary test, the three control methods were compared using the same criteria evaluated in the test bench for the step response and for the tracking modality of operation. The speed of the gantry was calculated using the output of the inclinometer by the sampling rate, and ranged from 5.6 to 5.8°/s. The timing response of the three control systems was comparable with those calculated using the test bench; however, while the best performance was achieved using the ADAC method in the test bench, the DAC method had the best performance because of the lower speed of rotation of the gantry and the noise immunity of the DAC method (purely combinatorial—with a Look-Up Table 6.2) to parasitic vibrations. In addition, higher uncertainties resulted from having the inclinometer mounted on the LINAC head.

Table 6.2: Timing parameters in three modalities in clinical environment using a LINAC

Step response	DAC	ADAC	Optimised PID
Rising time @ 90% (s)	1.9	1.9	2
Overshoot (deg)	0	0	5.526
Settling time (s)	0.3	0.4	1.2
Std global (deg)	0.266 ± 0.003	0.348 ± 0.1	0.517 ± 0.07

6.8 Conclusion

The rotatable phantom as a QA tool for dose verification was designed by CMRP to overcome the angular dependence. The MP512 combined with the use of the rotatable phantom is a powerful tool, with real-time, accurate 2-D—and potentially 3-D—dose reconstruction capabilities for pre-treatment QA for SBRT and SRS verification. The rotatable phantom has the ability to rotate $\pm 180^\circ$ with accuracy by direction position within ± 0.25 . The residual angle due to the beam divergence over a

small field size (between 0.5 and 4 cm) was less than 1° and could be considered to have a negligible effect on the response of the pixels across the detector.

CHAPTER 7: A 2-D SILICON DETECTOR ARRAY (MP512) USED AS A TOOL TO STUDY MOVING TARGETS IN RADIOTHERAPY

7.1 Introduction

The accuracy of the treatment in SBRT is proven to be affected by organ motion. It can be challenging to control tumours while minimising the dose of radiation delivered to healthy tissue during radiotherapy. Real-time DMLC tracking is the method used for intra-fraction motion management, which keeps healthy tissue away from the beam by tracking the tumour's movement. However, dose verification is required due to the presence of geometric and dosimetric uncertainties. In this study, a silicon detector array was used for the QA of a small field beam, such as in SBRT and SRS. In this study, the MP512 was used to reconstruct 2-D dose distributions of small field beams (1×1 , 2×2 and $3 \times 3 \text{ cm}^2$) in combination with a Calypso and DMLC tracking system. The 2-D dose distributions were performed using a movable platform called HexaMotion in the following scenarios: (i) without motion, (ii) with motion and (iii) with motion and DMLC tracking enabled.

7.2 Method and materials

7.2.1 The detector system and packaging

A 2-D silicon detector array MP512 was introduced in Section 4.2.1, while the readout system was discussed in Section 5.2.2. When combining the MP512 detector with the Calypso system, there is a concern about the fluctuations of the signal baseline produced by electromagnetic field. This is because the induced current affects the detector cabling and electronic system. To resolve this problematic, radiofrequency (RF) aluminium shielding was designed. The aluminium sheet works as shielding box for the preamplifier boards, and the thickness was calculated to allow no more than 5% of RF to be transmitted through the aluminium sheet to the

electronic system. The next section presents the RF shielding calculations and shows the diagram of the detector in combination with the aluminium sheet and solid water.

7.2.2 Aluminium shielding calculation and simulations

In this study, an aluminium shielding sheet was employed by being placed on top of the detector. The main advantage of using aluminium shielding is to attenuate the effect of the RF noise in the detector and electronic parts that are exposed to the Calypso system. The thickness of the aluminium used was approximately 2 mm, which reduced 95% of the initial intensity of the electromagnetic field. Table 7.1 presents the main electromagnetic parameters used to calculate the proper thickness.

Table 7.1: Parameter values for calculating aluminium thickness

Parameter	Description	Typ. value	Units
ϵ_0	Permittivity in free space	$8.854 * 10^{-12}$	F/m
μ_0	Permeability in free space	$4 \pi * 10^{-7}$	H/m
μ_r	Relative permeability	1	This value was obtained from [176]
ω	Oscillation	$2 \pi * 500 * 10^3$	Hz
σ	Conductivity	$3.54 * 10^4$	(Ω cm) ⁻¹

The approximation of a plane-wave incident perpendicularly on the aluminium and the displacement current term of the Maxwell equation have the form:

$$\frac{\partial^2 E}{\partial z^2} = i\mu\mu_r\epsilon\epsilon_r\omega\frac{\partial E}{\partial t} + \mu\mu_r\sigma\frac{\partial E}{\partial t} \quad (6.1)$$

$$\omega\epsilon_r\epsilon_0 \ll \sigma,$$

$$\frac{\partial^2 E}{\partial z^2} = \mu\mu_r\sigma\frac{\partial E}{\partial t} \quad (6.2)$$

The answer to the partial mixed derivative equation has the form of:

$$E = E_0 \exp(-\alpha z) \exp i(\omega t - \beta z) \quad (6.3)$$

where:

$$\beta = \alpha = \sqrt{\frac{\mu\mu_r\sigma\omega}{2}} \quad (6.4)$$

The skin depth for the electromagnetic wave propagated by Calypso at a frequency of 500 kHz is approximately:

$$\delta = \frac{1}{\alpha} = \sqrt{\frac{2}{\mu\mu_r\sigma\omega}} = 700 \mu m \quad (6.5)$$

For an attenuation of 95%, this leads to:

$$\frac{E_0 \exp\left(\frac{-z}{7 \cdot 10^{-4}}\right)}{E_0} = 0.05 \rightarrow z \approx 2 mm \quad (6.6)$$

where z refers to the aluminium thickness sheet which is 2 mm.

Further, PMMA slabs and solid water were placed on top of the detector with the aluminium sheet, as shown in Figure 7.1. These layers were equivalent to 1.5 cm depth, which matched the d_{\max} for a 6 MV photon beam generated by the LINAC. This method was similarly used by Huang et al. in a single detector for entrance dosimetry, using covering metal (either aluminium or brass) to replicate the desired thickness corresponding to d_{\max} for energy ranges of MV photons [195].

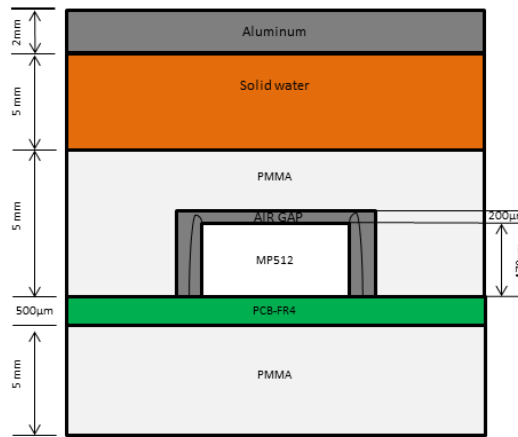


Figure 7.1: Schematic of the MP512 with PMMA, solid water and an aluminium sheet

To verify the dose perturbation with the influence of the insertion of 2 mm of aluminium sheet on the top of the MP512 detector, the Monte Carlo Geant4 version 10.0p01 simulations were performed [196]. A 6 MV x-ray with square field beams of 1 x 1, 2 x 2 and 3 x 3 cm² were simulated when the x-ray passed through the solid water slabs of 30 x 30 x 30 cm³. The simulation was based on replacing the 2 mm water with aluminium—the reference simulation when the entire phantom is water. The aim of this simulation was replicated by placing the 2 mm aluminium sheet on top of the PMMA detector at an SSD of 100 cm. The beams were incident from phase space files formed by EGSnrc Monte Carlo, which models a Varian 2100C LINAC [197]. Standard physics packages were used for the simulation, which embraced Compton scattering and gamma conversion (photons), ionisation, photoelectric effect and positron annihilation (leptons) and Bremsstrahlung. The physics parameter of particle range was fixed to 0.1 mm, while the maximum step length of electron/positron was set to 0.1 mm. The dose was counted inside the

phantom at a voxel resolution of 1 mm³. Each simulation was fragmented into 10 parallel jobs each with unique seeds and the mean dose stated. Further, the uncertainties were evaluated by taking the SD across 10 simulations. For each field size, the 4 x 10³ primary histories were simulated (primary histories refer to the number of electrons striking the x-ray target in the LINAC head). At a depth of 1.5 cm at the beam central axis (CAX) for each field size, the dose uncertainty was found to be approximately $\pm 1\%$ of the dose.

7.2.3 Baseline study

The evaluation the efficiency of the aluminium sheet was measured by acquiring the baseline (leakage current) of the detector. The baseline measurements were performed with the following configurations:

1. with Calypso off
2. with Calypso activated and MP512 unshielded
3. with Calypso activated and the aluminium sheet placed on top of the phantom, as shown in Figure 7.1.

To attain a large number of samples, acquisition of the baseline was performed to 120 seconds with a sampling rate of 360 Hz. Statistical analysis of the leakage current was measured and presented by calculating the average of the baseline and plotting the frequency distribution of its SD in each channel of MP512 in the three different configurations listed above.

7.2.4 Calypso four-dimensional (4-D) localisation system

An important component in the experiment was the Calypso system provided by Varian, designed for radiotherapy and real-time target localisation in 4-D. The Calypso system can provide the most accurate and precise position of the target during treatment using transponders called 'beacons'. The value of these beacons is

that they are not required to connect to the cable to track the object. The Calypso system consists of a 4-D electromagnetic array that can localise the beacon positions using RF. This array is placed above the beacons, then the 4-D electromagnetic array emits RF signals to excite the beacons, and each of these beacons has its own resonant frequencies. The electromagnetic array detects the signal from the beacons after being absorbed, and their positions are subsequently identified, as shown in Figure 7.2. The Calypso system can also display the position of the beacons in real time prior to the test beginning [60, 198].

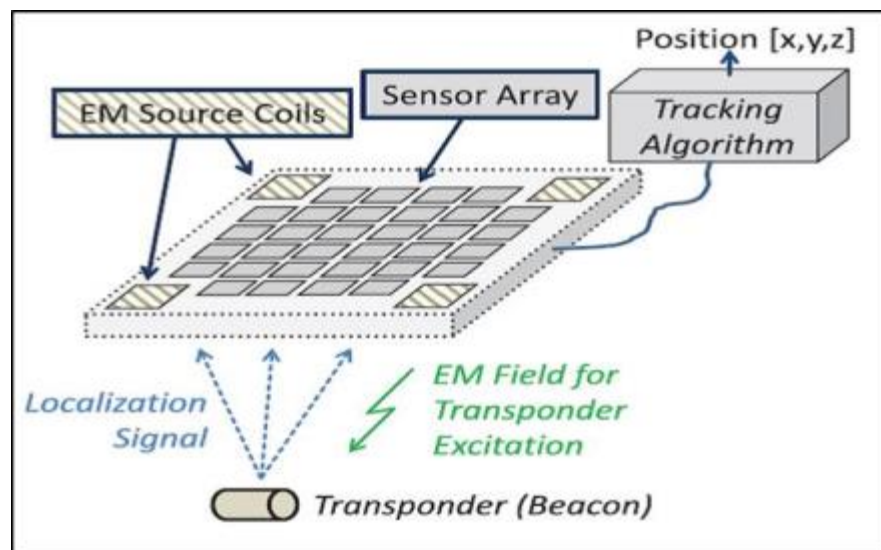


Figure 7.2: Principle of electromagnetism with beacon in the Calypso system

Note: In this study, the Z component was eliminated [199].

7.2.5 Lung motion mimicking

To study the performance of a silicon detector array with target movement, a real lung temporal pattern was used. This was extracted from a real patient's lung

movement recorded using a 4-D CT scan. A simplified version of the motion pattern was used with no vertical (Z) component of the movement. The pattern was a text file with absolute position frames between X and Y every 25 ms. The text file was uploaded to the HexaMotion platform. The motion was provided using the HexaMotion platform, which is discussed in the following section. Figure 7.3 shows the temporal pattern adopted for this test in X and Y directions.

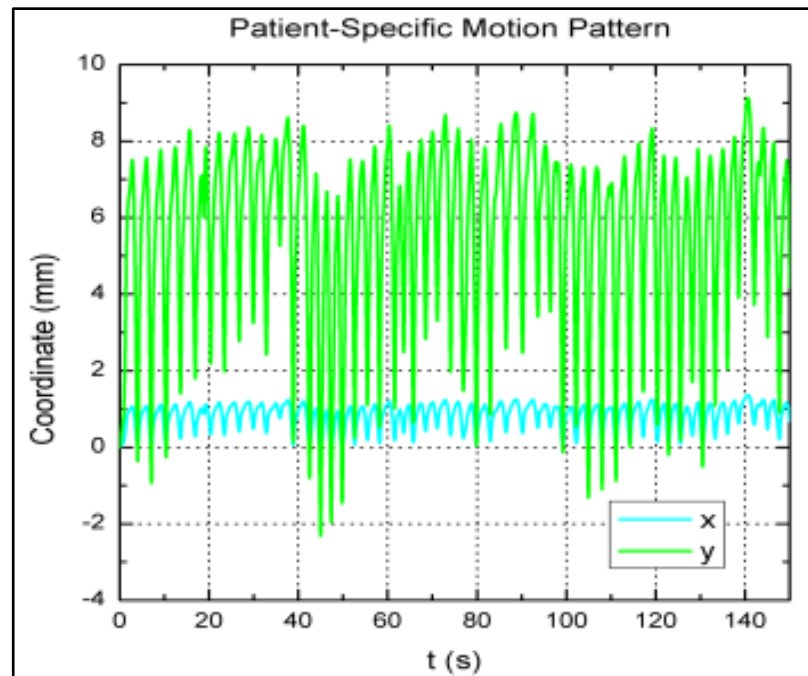


Figure 7.3: Lung trace motion in X (blue) and Y (green) coordinates

7.2.6 HexaMotion six-dimensional (6-D) motion platform

A 6-D motion platform (HexaMotion, ScandiDos, Uppsala, Sweden) was used in this study to mimic organ motion. The HexaMotion platform was manufactured as an accessory for Delta⁴ and has the ability to simulate tumour motion in 6-D and read the position data from a text file. This study performed the motions in only two axes

(X and Y), following the lung temporal motion pattern described previously. The HexaMotion platform can be controlled from the treatment room using a software program. The platform was modified using a flat wood plate to carry the MP512 detector and DAQ system during the delivery of the beam, with the positioning accuracy of the platform being better than 0.5 mm. Figure 7.4 presents the experimental setup.

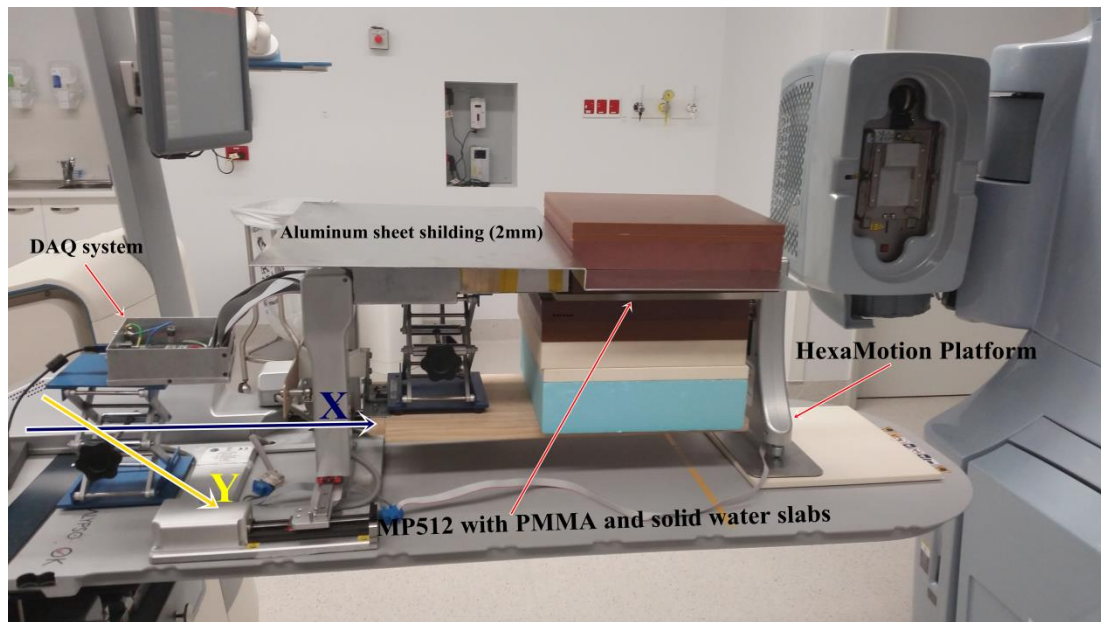


Figure 7.4: Experimental setup of the MP512 carried by the HexaMotion platform

Note: The flat wood plate of HexaMotion was adapted to support the detector, PMMA, solid water and aluminium sheet.

7.2.7 Experimental setup

7.2.7.1 Dynamic wedge study

The MP512 has the ability to measure pulse by pulse, which is very important for dose QA, especially in motion adaptive radiotherapy. Further, the MP512 has high temporal resolution in dose mapping and can be used to test and improve the performance of the feedback algorithm, which is used to drive the DMLC to track the

target movement measured by Calypso. To investigate the 3-D dose reconstruction (X, Y and t) of MP512, a dynamic wedge was tested. This wedge was combined with the lung motion pattern described in Section 7.2.5. The dynamic wedge study was performed on a solid water slab positioned above the HexaMotion platform, testing three different scenarios. The wedge was tested using 6 MV beam energy with a total dose of 1000 MU and 600 MU/min. The MP512 was positioned at a depth of 1.5 cm and SAD of 100 cm. To avoid the effects of the angular response of the detector, the LINAC gantry was fixed perpendicularly.

7.2.7.2 Beam profile measurements using MP512

Beam profiles of 1×1 , 2×2 and $3 \times 3 \text{ cm}^2$ were performed in three scenarios: (i) no motion, (ii) motion without DMLC tracking and (iii) motion with DMLC tracking. The square field beams were collimated by the MLC, and jaws were retracted 1 cm in each direction, as shown in Figure 7.5. This was to minimise the end-of-lead leakage and permit the full range of movement in X and Y directions to 2 mm and 8 mm, respectively. Beam profiles were tested along the X and Y directions using the MP512 and EBT3 films. Both detectors irradiated with 6 MV, 1000 MU and a dose rate of 600 MU/min at a depth of 1.5 cm. They were aligned to an SAD of 100 cm.

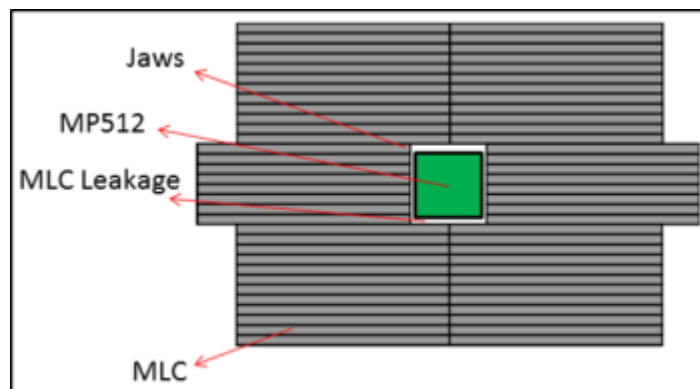


Figure 7.5: Diagram of jaws defining the square field size

For the no-motion study, the MP512 was placed on top of the movable phantom above the 6 cm of solid water as back-scatter material. A black cloth was used to cover the parts to protect the detector from ambient light. The beacons were positioned on the top and the Calypso system was activated as shown in Figure 7.6. For the motion study, a similar setup was used to the no-motion study, and the HexaMotion platform was operated based on the lung temporal pattern described in Section 7.2.5. The Calypso system was activated, except without DMLC tracking enabled. The final study performed involved motion with DMLC tracking enabled. In this study, the MP was moved with the HexaMotion platform, and the Calypso system was activated. The beacon provided positional information related to cameras installed in the room that registered the position of the array relative to the coordinate system of the LINAC. This allowed localisation by the Calypso system. This position was then sent to DMLC tracking. In real time, the DMLC tracking software calculated the new positions of the MLC [200, 201]. All beam profiles of the MP512 were normalised to central pixel response (row 11, column 12) and aligned with the corresponding EBT3 profile to the value at 50% of the central pixel response. The responses of each detector (MP512 and EBT3 film) were calculated based on five repetitions of the same field. The error bars of each data point presented in the plot were calculated as two SDs. The MP512 was equalised using similar methods for MP-121, and the response variation across the whole detector was 0.5% [4].

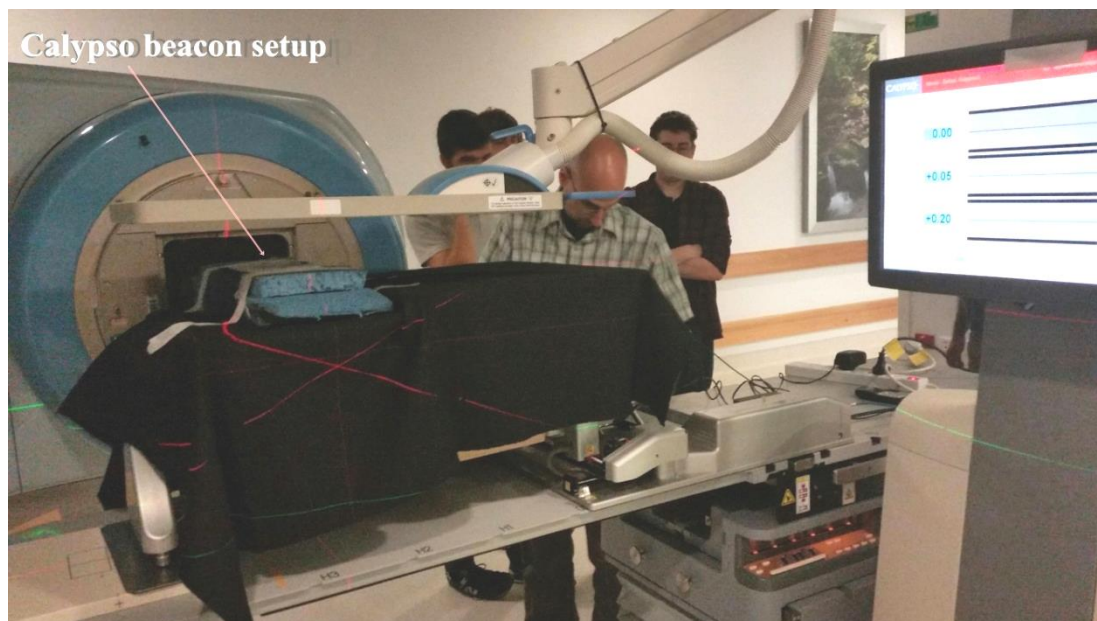


Figure 7.6: The final setup, showing the transponders (beacons) positioned on the foam top of the detector and localised relative to the room coordinate system

Note: The same setup was used for the three different scenarios.

7.2.7.3 Beam profile measurements using EBT3 film

Gafchromic EBT3 film was used as the benchmark for beam profile in the three different scenarios: no motion, motion without DMLC tracking and motion with DMLC tracking. The same procedures as in Section 5.2.9 were used in this test to scan the film and calculate its response.

7.3 Results

7.3.1 DAQ

An important feature of the data acquisition of the MP512 is the graphical user interface, which provides a real-time visualisation of the charge collected by each pixel in a fixed integration time, as shown in Figure 7.7 (left). Additionally, the response of each single channel of the MP512 can be presented, as shown in Figure

7.7 (right). All measurements were conducted with a delivery of 1000 MU to allow the LINAC beam to reach an appropriate stabilisation condition.

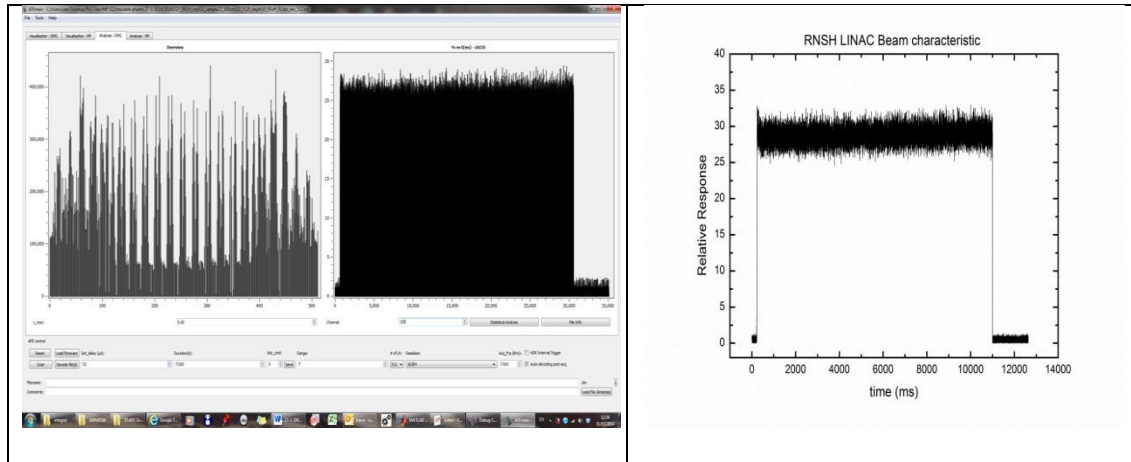


Figure 7.7: Graphical user interface of the data acquisition (left) and investigation of the initial LINAC beam characteristics (right)

7.4 2-D maps of MP512

The value of using MP512 is the ability to present the dose distribution in 2-D. Figure 7.8 shows the projected beam of different field sizes for three scenarios: (i) no motion, (ii) with motion and the tracking system disabled and (iii) with motion and the tracking system enabled. This study found that MLC leakage affects the dose distribution of a square plan for all field sizes. Moreover, visualisation of the effect of the motion indicated that the larger field size resulted in large dose redistribution. The LINAC output was confirmed to be the same for all configurations, regardless of the dose distribution across the detector.

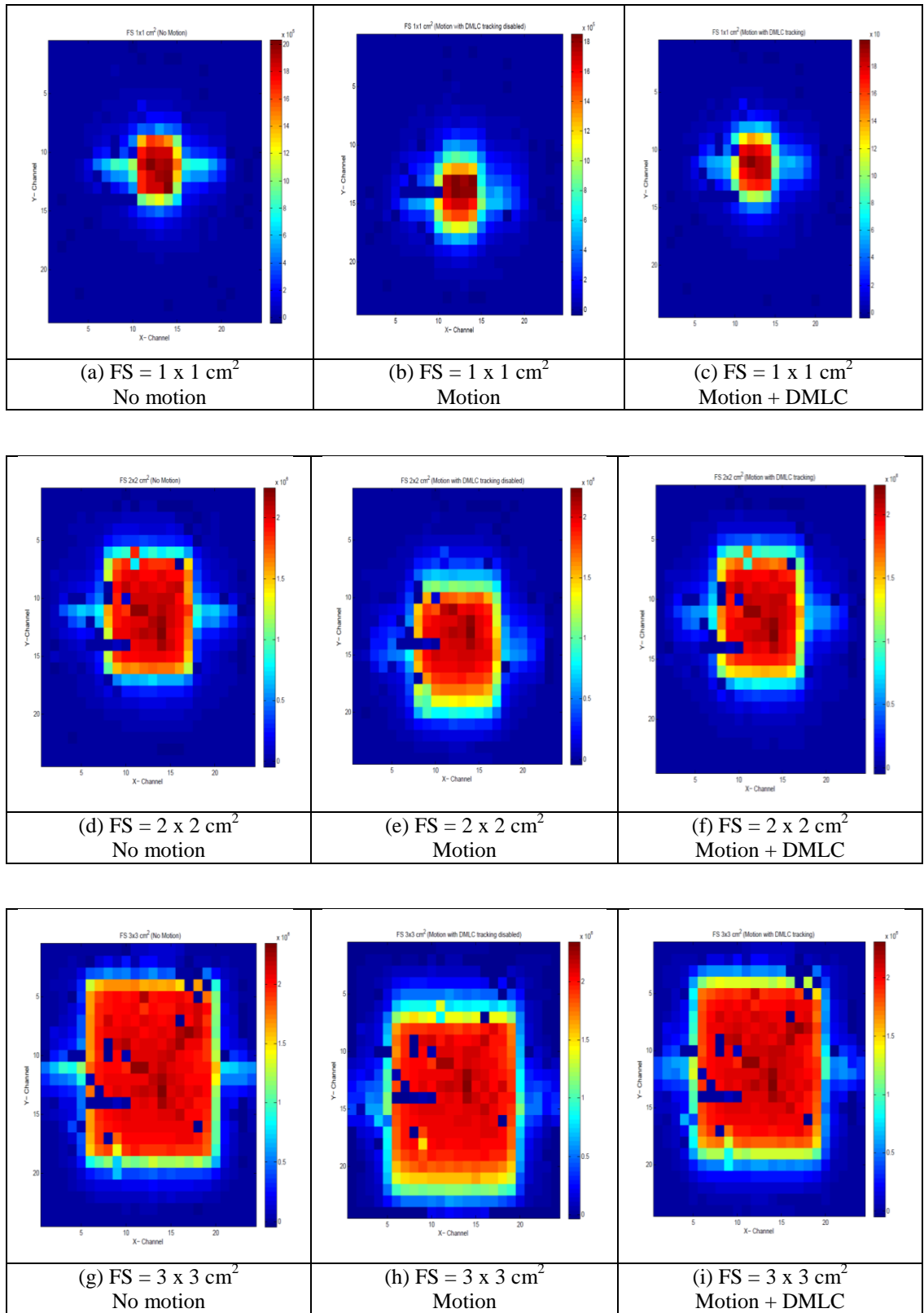


Figure 7.8: 2-D dose distribution at d_{\max} of MP512 for different field sizes in three cases

Note: Pitch is 2 mm, X and Y axes present the channel numbers, and FS = field size.

7.4.1 Geant4 simulation of aluminium sheet effect and RF noise destruction performance

Figure 7.9 shows the MP512 without shielding and the RF on, which is generated by Calypso. The baseline fluctuation measured up to 9% of the full signal scale during the beam delivery. This large fluctuation was estimated and showed a relatively small frequency count with a maximum of 25 occurrences (events/second) at 6%. Despite this, the fluctuation significantly affected the accuracy of the measurement. As a result, a stochastic current signal was produced that could not be distinguished from the signal generated by the beam. Further, this fluctuation affected the accuracy of the dose distribution in the out-of-field and penumbra areas. Using aluminium shielding completely removed the large amplitude fluctuation component, as shown by the blue bars in Figure 7.9.

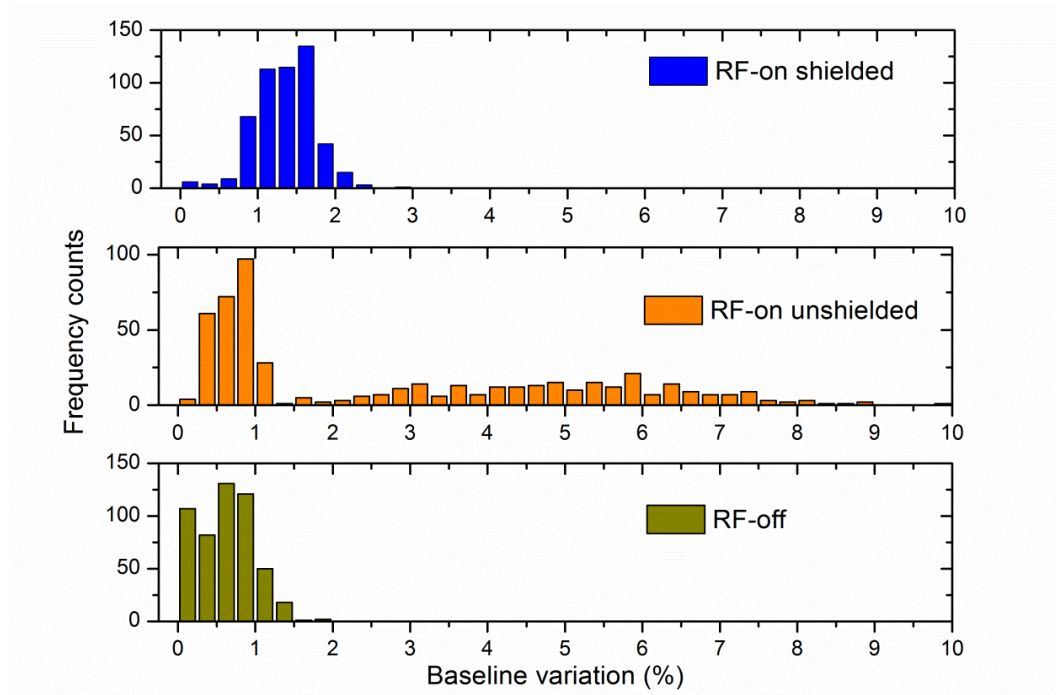


Figure 7.9: Baseline fluctuation distribution acquired with Calypso on (with and without aluminium sheet shielding—blue and orange bars, respectively) compared to the baseline fluctuation with Calypso off (green bars)

Figure 7.10 (left) shows the results of the Monte Carlo simulation of the depth dose profiles for 1 x 1, 2 x 2 and 3 x 3 cm² field sizes. Further, the cross-profiles were presented at a depth of 1.5 cm, as shown in Figure 7.10 (right). Using 2 mm of aluminium sheet on top of the detector had a very small effect on the dosimetry. A minimum dose was decreased and can be show that in percentage depth dose measured by the central pixel of MP512 compared with IC beyond 14 mm depth. The simulation uncertainties were within 1%. In contrast, no substantial changes were exhibited in the cross-profiles for all field sizes. Further, there was an increase in the energy deposition in water in the first 14 mm build-up region due to the large amount of secondary electron fluence produced by aluminium compared to the same thickness of water equivalent material (aluminium density 2.7 g/cm³).

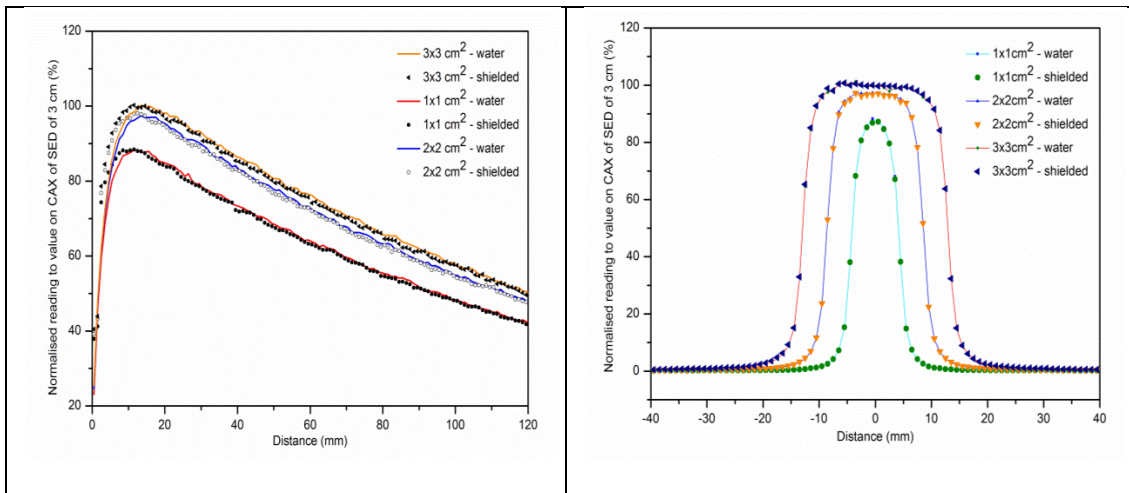


Figure 7.10: Comparison of the Geant4 simulations of present depth dose (left) and dose profile (right) for 1 x 1, 2 x 2 and 3 x 3 cm² field sizes with and without the aluminium sheet

Note: The response was normalised to the central pixel response corresponding to the dose profile of a 3 x 3 cm² radiation field.

7.4.2 Dynamic wedge measurement

Figure 7.11 shows the dose profile measured by MP512 for no motion, motion, and motion with DMLC tracking of the dynamic wedge. The difference between no motion and motion with DMLC not activated was estimated, and found to be an average of -18% along the wedge. Further, at the peak of +75% in the penumbra region, the displacement of dose distribution was found to be approximately 0.8 to 1 cm. The comparison between no motion and motion with DMLC tracking activated was that the integral response could rise to a maximum difference of approximately +15% in the region corresponding to the right side penumbra of the wedge, while keeping the disagreement with the no-motion scenario within -3% along the wedge.

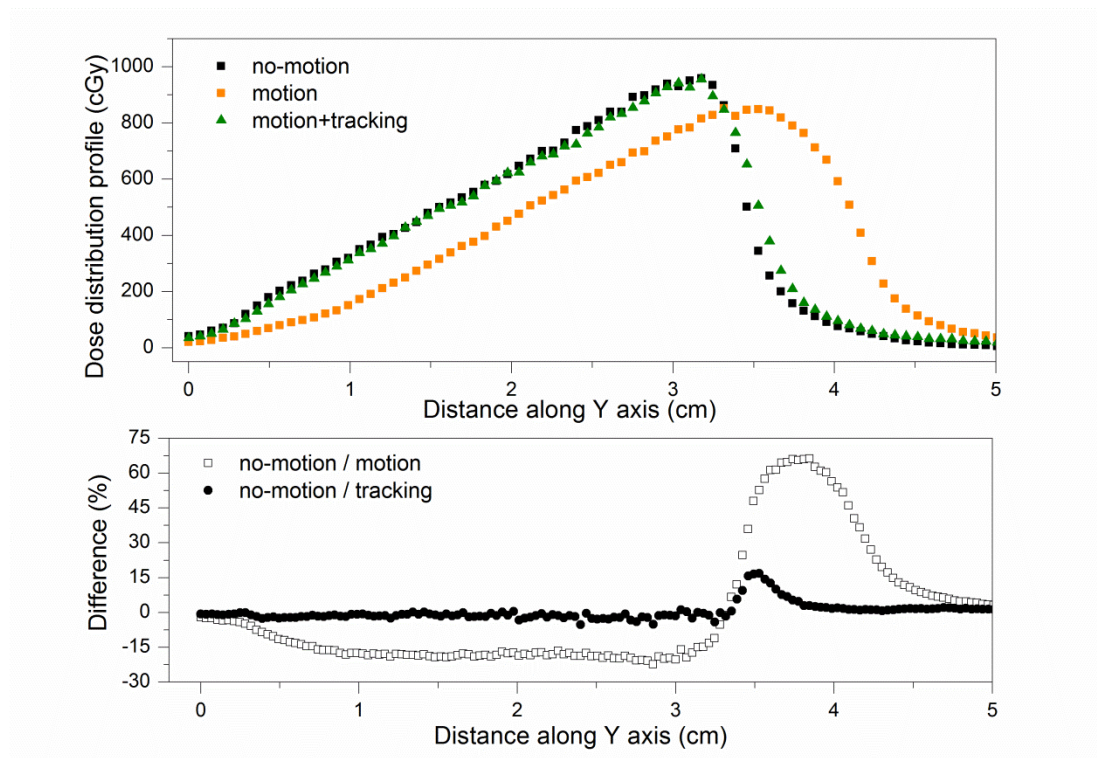


Figure 7.11: Dynamic wedge integral dose profiles taken in the central Y axis of MP512 (upper plot) and the percentage difference that normalised to the no-motion peak integral dose response (lower plot)

7.4.3 Beam profiles

For the clinical lung motion pattern, the motion was generated by the HexaMotion platform, which included six movement axes following a patient-specific motion pattern. The motion pattern was provided by the Royal North Shore Hospital, Sydney. The pattern was simplified to 2-D motion in the X and Y directions, with the Z direction suppressed in order to diminish the effect of variation in the intensity of the beam due to changes in the SSD of the phantom. Figure 7.12 shows the dose profile measurements for different square field sizes (1 x 1, 2 x 2 and 3 x 3 cm²) in the Y direction of the MP512 and EBT3 films for different sets (no motion, motion with DMLC tracking disabled, and motion with DMLC tracking enabled). All MP512 dose profiles were compared with EBT3 film. All MP512 dose profiles were normalised to the response of the central pixel (row 11, column 12). The EBT3 film dose profiles were normalised to the mean value of a 2 x 2 mm² area, which surrounded the central axis of the beam profile. Profiles measured by MP512 and EBT3 film were aligned to the value at 50% of CAX.

The agreement between MP512 and EBT3 film was evaluated quantitatively using MATLAB (Mathworks Inc.) by creating a fit with the curve fitting toolbox. The penumbral width (80%-20%) was measured by interpolating the data points using the interpolation shape preserving fit. The FWHM and right hind side (RHS) penumbra width (80%-20%) calculations are shown in Table 7.2. The right side of the penumbra (80%-20%) displays the large distortion produced by the lung motion pattern. This was due to the offset of approximately 4 mm created by the motion in the +Y direction, which corresponded to the positive direction of the distance informed in Figure 7.12. The results showed that the tracking technique can mitigate

the dose smearing due to the orange motion. The variation of the penumbra between the no-motion and motion was evaluated quantitatively to determine the efficiency, and found to be 2.4 mm. Further, this value was reduced down to 0.7 mm when the tracking was active. The comparison between the MP512 and EBT3 film showed that agreement was within 3% and 0.4 mm for the FWHM and penumbra width, respectively.

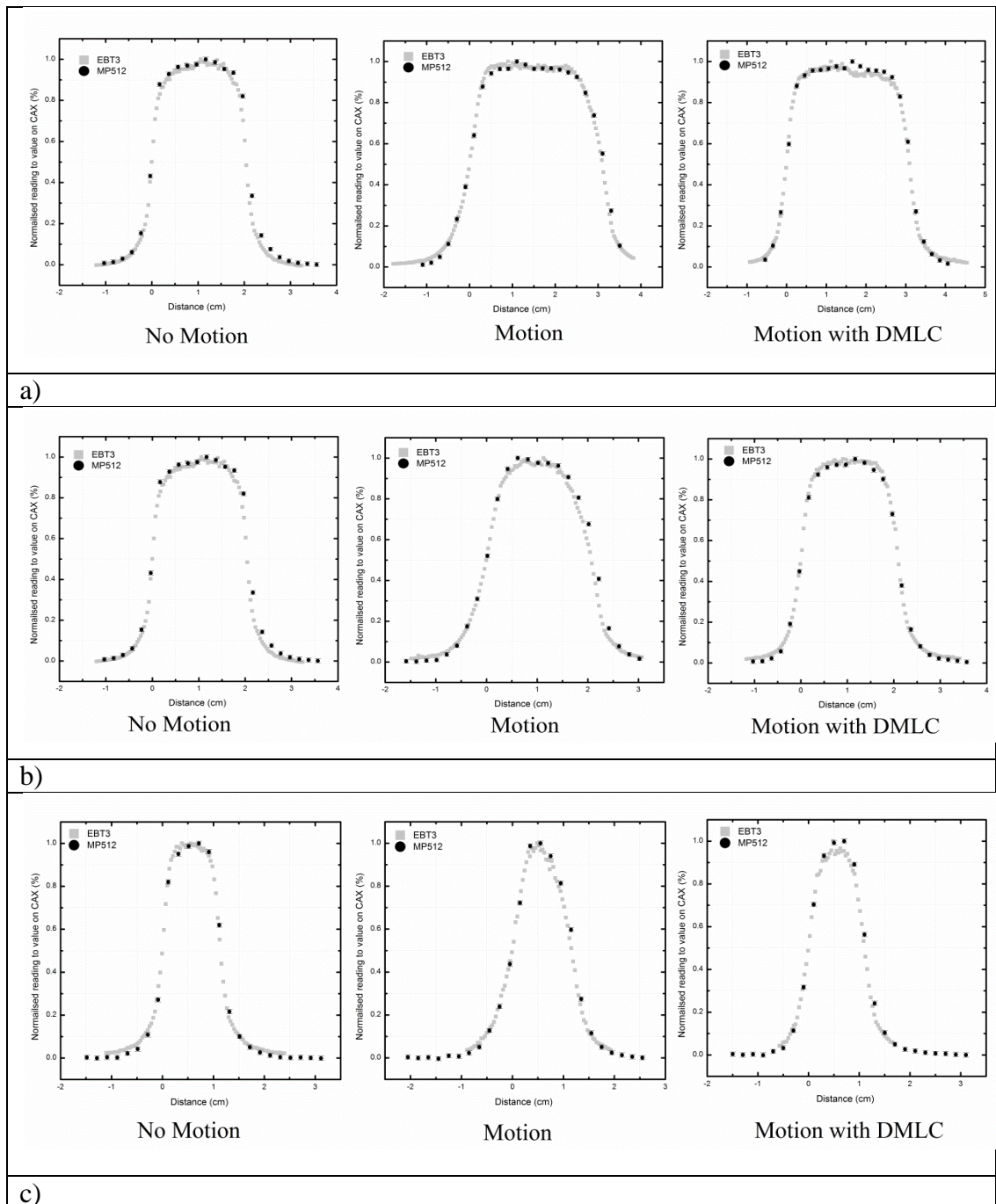


Figure 7.12: MP512 dose profile in different cases comparing the data measured by EBT3 for field sizes of (a) 3 x 3 cm², (b) 2 x 2 cm² and (c) 1 x 1 cm² in the Y direction

Table 7.2: Summary of calculations of FWHM and RHS penumbra width (80%-20%) in the Y direction of all field sizes measured by MP512 and EBT3 film

Y direction						
EBT3						
	No motion		Motion		DMLC	
FS (cm ²)	FWHM +/- 0.1(mm)	RHS Penumbra +/- 0.1(mm)	FWHM +/- 0.1(mm)	RHS Penumbra +/- 0.1(mm)	FWHM +/- 0.1(mm)	RHS Penumbra +/- 0.1(mm)
1 x 1	11.4	2.6	11.6	5	11	3.5
2 x 2	20.4	2.7	20.7	5.4	21	3.4
3 x 3	30.6	3	31	5.3	31	3.5
MP512						
	No motion		Motion		DMLC	
FS (cm ²)	FWHM +/- 0.1(mm)	RHS Penumbra +/- 0.1(mm)	FWHM +/- 0.1(mm)	RHS Penumbra +/- 0.1(mm)	FWHM +/- 0.1(mm)	RHS Penumbra +/- 0.1(mm)
1 x 1	11.7	2.5	12.1	5.1	11.4	3.7
2 x 2	21	3	21.5	5.6	21	3.8
3 x 3	31.6	2.9	31.5	5.7	31.2	3.9

Note: FS = field size.

Figure 7.13 shows the profiles measured by MP512 compared with EBT3 film in the X direction. The lateral movement generated by the lung motion pattern in the X direction was approximately ± 1 mm and the minimum leaf width in that direction was 2 mm. Therefore, when the tracking was activated, the leaf could not move more than 1 mm. Further, for all field sizes, it was observed that the beam profiles generated in case of motion were more comparable to the beam profiles when there was motion and DMLC tracking activated. This can be explained by the fact that the tracking system is not too sensitive in the X direction compared to the Y direction. The pattern of the beam profiles below 30% of the maximum dose was correlated to radiation leakage between the edges of closed leaves and did not exist in the profiles

measured in the Y direction. The FWHM and RHS penumbra width (80%-20%) calculations are shown in Table 7.3.

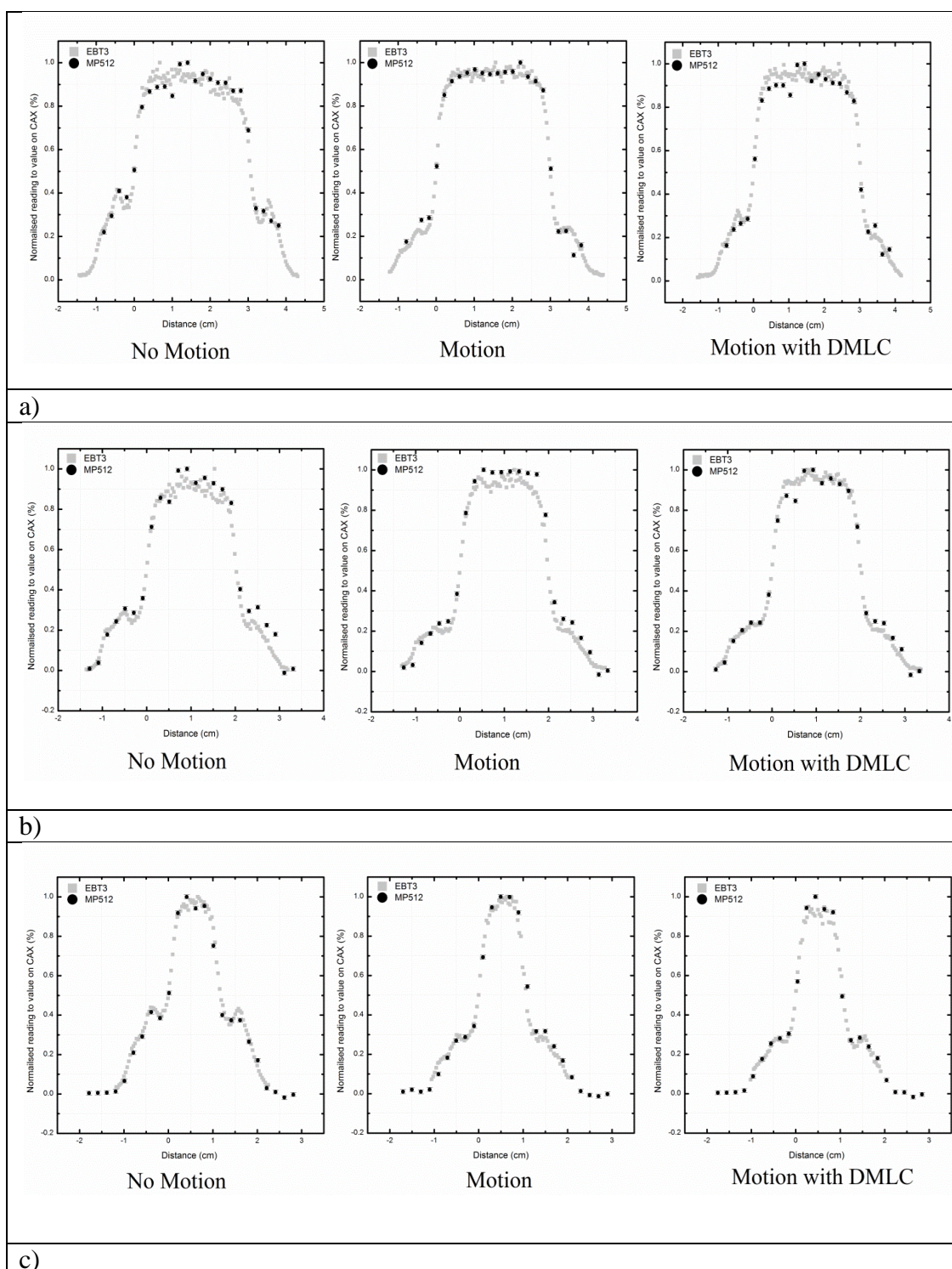


Figure 7.13: MP512 dose profile in different cases comparing the data measured by EBT3 for field sizes of (a) 3 x 3 cm², (b) 2 x 2 cm² and (c) 1 x 1 cm² in the X direction

Table 7.3: Summary of calculations of FWHM and RHS penumbra width (80%-20%) in the X direction of all field sizes measured by MP512 and EBT3 film

X direction						
EBT3						
	No motion		Motion		DMLC	
FS (cm ²)	FWHM +/- 0.1(mm)	RHS Penumbra +/- 0.1(mm)	FWHM +/- 0.1(mm)	RHS Penumbra +/- 0.1(mm)	FWHM +/- 0.1(mm)	RHS Penumbra +/- 0.1(mm)
1 x 1	11.7	9.92	10.6	8.1	10.6	8
2 x 2	20	10.9	19.9	7.8	20.1	7.6
3 x 3	30.6	10.7	29.9	7.4	30.2	8.7
MP512						
	No motion		Motion		DMLC	
FS (cm ²)	FWHM +/- 0.1(mm)	RHS Penumbra +/- 0.1(mm)	FWHM +/- 0.1(mm)	RHS Penumbra +/- 0.1(mm)	FWHM +/- 0.1(mm)	RHS Penumbra +/- 0.1(mm)
1 x 1	11.3	9.4	11.2	8.31	10.3	8.5
2 x 2	20.5	10.3	20.5	7.6	20.2	8.8
3 x 3	30.9	10.3	30.2	6.2	29.9	8.7

Note: FS = field size.

7.5 Penumbra width

The penumbra width in a dose profile is defined as the distance between the 80% and 20% at d_{max} . Figures 7.14 and 7.15 show the comparison of penumbra width (80 %-20%) in the Y and X directions for a field size of 1 x 1 cm² (top), 2 x 2 cm² (middle) and 3 x 3 cm² (bottom). The penumbra agreement between MP512 and EBT3 film of Y and X was presented in Tables 7.2 and 7.3, respectively.

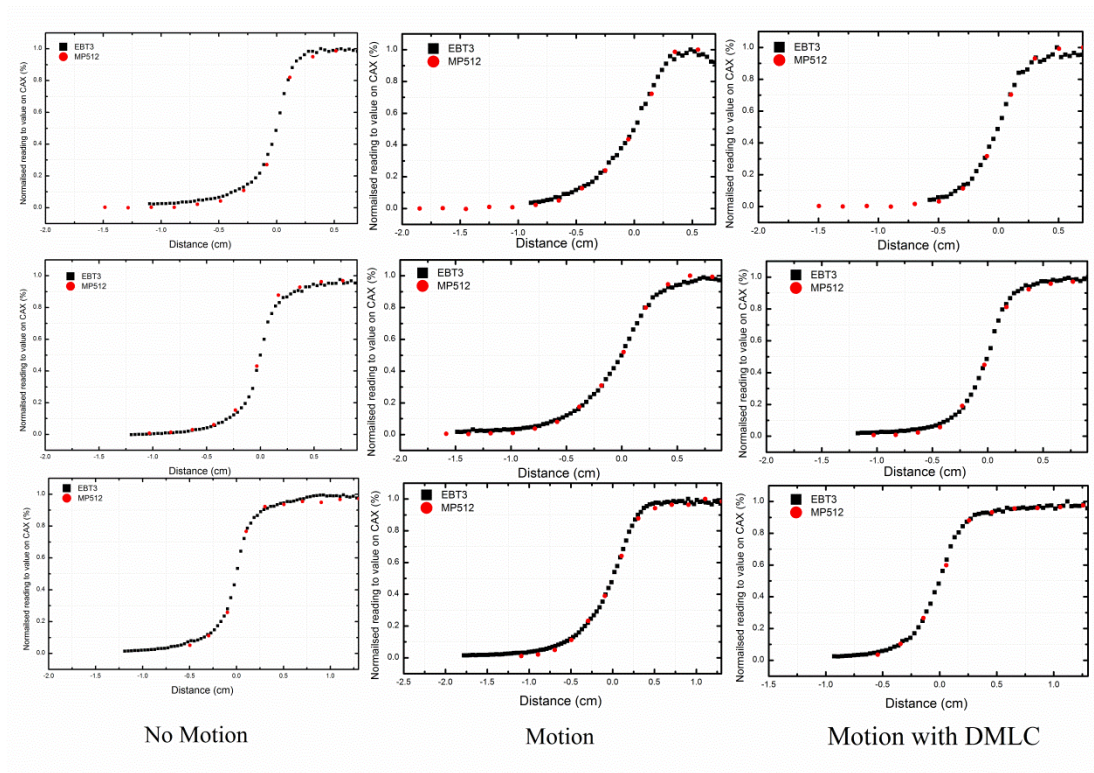


Figure 7.14: Comparison of penumbra width between MP512 and EBT3 film for field sizes 1 x 1, 2 x 2 and 3 x 3 cm² in the Y direction

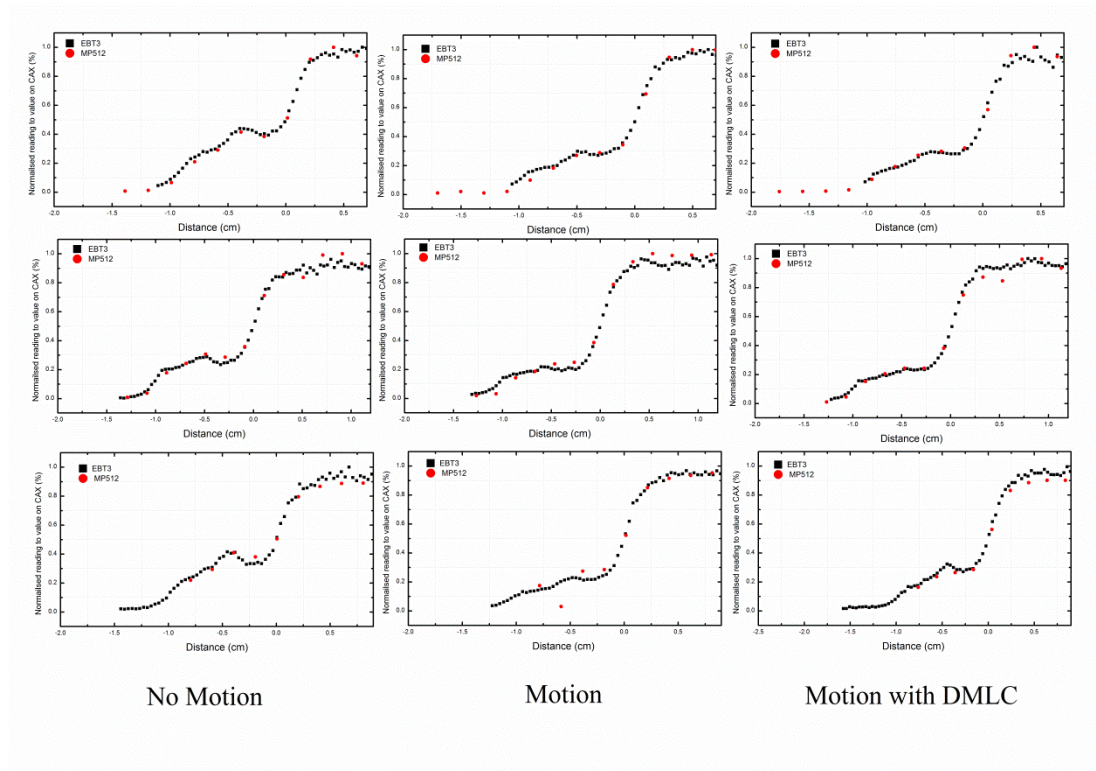


Figure 7.15: Comparison of left hand profiles for 1 x 1, 2 x 2 and 3 x 3 field sizes along the X- direaction of EBT3 and MP512 measurments. Both the devices show the dose distribution generated by the leaf leakage with a minimal (within 2%) discrepancy

7.6 Conclusion

The SBRT and SRS are widely used techniques for small field beam radiation therapy. Organ motion during the course of the treatment presents a challenge for clinicians. This issue has been taken into account by increased the PTV or using image guidance to shape the beam and intensity delivered to the movable targets, and by introducing DMLC tracking and 4-D Calypso systems. In response to this, an advanced QA system is required, especially with high spatial and temporal resolution.

The 2-D array MP512 was developed and tested with the Calypso system as a dose verification of moving targets in radiotherapy. The Calypso system is a 4-D localisation system based on real time that uses transponders (beacons) to localise the position of the object. The DMLC tracking system demonstrated the ability to account for target motion during treatment by performing measurements using the MP512. The MP512 results showed good agreement between the static and tracked measurements in terms of beam profile, and displayed a maximum difference of 2.8%. Supplied motion induced a spatial displacement component; however, this displacement was compensated for by the DMLC tracking system. The MP512 detector was proven to be an effective tool for pre-treatment verification of real-time adaptive deliveries with both high spatial resolution for dose profiling and high temporal resolution for pulse-by-pulse reconstruction. The MP512 has the ability to measure the dose in 2-D dose distribution, as shown for all field sizes. In comparison with EBT3 film, a discrepancy was found within 0.4 mm for FWHM and 4% for penumbra width. Using the HexaMotion platform with MP512 was successfully examined, with the motion of the HexaMotion platform provided via a lung motion pattern. The dose distribution measured by MP512 was compared with EBT3 film for no motion, motion, and motion with DMLC tracking system.

The aluminium sheet with 2 mm thickness was introduced successfully on a surface of 10 mm thick solid water (2 mm aluminium + 10 mm solid water equivalent to d_{\max} for 6 MV) to minimise the baseline fluctuation due to the RF emitted by Calypso. Using the 2 mm aluminium sheet did not perturb the radiation field for any field size tested, as proven by Monte Carlo simulations. The PDD study with aluminium sheet showed agreement within 1% below d_{\max} in comparison to dose measured in water without using aluminium sheet. Using a 3-D lung motion pattern did not show any

effect on the detector response due to the ability of the design of the electronic readout system to minimise the noise. The MP512 has the ability to measure the dose in 2-D dose distribution, as shown for all field sizes. In comparison with EBT3 film, the discrepancy was found within 0.4 mm for FWHM and 4% for penumbra width. However, this study was performed only using one motion (lung motion pattern), and movement was restricted to the X and Y directions. Further, this study did not take into account the variation of the MP512 SSD from the LINAC source. Changing SSD leads to variation in the dose rate measured by the MP512 due to the presence of the motion in the Z direction. Further, this study used a fixed gantry position, rather than using the gantry as it is employed in real SBRT or SRS modalities.

CHAPTER 8: HIGH SPATIAL RESOLUTION MONOLITHIC SILICON ARRAY FOR STEREOTACTIC RADIOSURGERY

8.1 Introduction

This chapter introduces a new silicon detector array—named ‘DUO512’—that features a high spatial resolution and unusual geometry of sensitive volumes to those used in contemporary instrumentation in radiotherapy. This 2-D silicon detector array can be used in very small fields for stereotactic radiosurgery. The aim of this chapter is to investigate the effect of ionising radiation on DUO512. This chapter also presents the electric characteristics of the device for I-V and C-V. Moreover, the DUO512’s uniformity, dose linearity and reproducibility are presented, as well as the results of radiation damage studies using two modalities—photons (by irradiation with a Co-60 source) and photoneutrons (by irradiation with 18 MV LINAC).

8.2 Materials and methods

8.2.1 Design and fabrication

The DUO512 is a monolithic dosimeter array that contains 512 microstrips of phosphorous ions implanted on a bulk *p*-type silicon KDB substrate and organised in a cross shaped topology. The total area of silicon is $52 \times 52 \text{ mm}^2$, with a $200 \text{ }\mu\text{-strip}$ pitch. The sensitive area of the single strip is $20 \times 800 \text{ }\mu\text{m}^2$, with a $100 \text{ }\mu\text{C}$ p-stop implantation charge between each strip. The silicon detector array is covered by a thin layer of protective resin epoxy to avoid accidental damage to the connections. The board is not tissue equivalent, but is fibreglass (FR4) with a $500 \text{ }\mu\text{m}$ thickness. The resistivity of the substrate is $10 \text{ }\Omega\text{-cm}$ and the substrate is $500 \text{ }\mu\text{m}$ thick—see Figure 8.1 (left). Figure 8.1 (right) shows the DUO512 assembled on the PCB carrier.

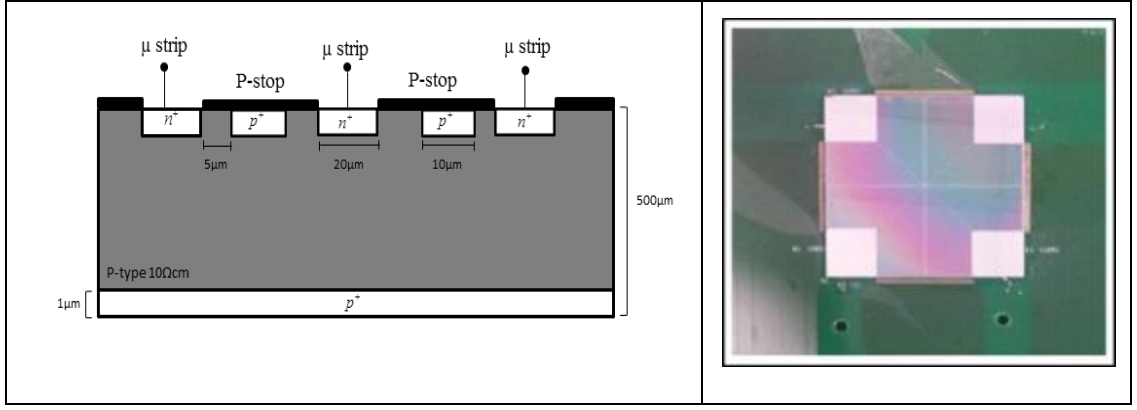


Figure 8.1: DUO512 pixel structure diagram (not to scale) (left) and DUO512 silicon detector array (right)

8.2.2 Readout system

The AFE readout system was employed to readout the current signal from the DUO512. The full description of this system was introduced in Section 5.2.2.

8.2.3 I-V characteristics

The I-V characteristics were determined using a Keithley 230 programmable voltage source to apply a bias through the diodes. The current was measured with a Keithley 614 electrometer. The reverse voltage applied to the diodes ranged from 0 to -20 V, with an incremental step amplitude of -0.5 V. The delay time between the applied bias and current sampling to achieve the full stabilisation of the current was 1000 ms. The detector was placed in a dark sealed container to shield the device from photocurrent due to ambient light. All detectors were kept at room temperature (approximately 295 K). The I-V test of the DUO512 silicon array was performed by selecting diodes in different positions across the array.

8.2.4 C-V characteristics

The C-V was performed using the Boonton 7200 Bridge Capacitance Meter. The reverse voltage applied to the diodes ranged from 0 to -20 V. The incremental step amplitude was -0.5 V and the delay time was 1000 ms.

8.2.5 Uniformity

The uniformity was also measured for the DUO512 using the same methods performed with the MP512 in Section 5.2.4. The uniformity was presented as a comparison before and after the equalisation factor was applied.

8.2.6 Dose linearity

The study of the dose linearity for the DUO512 was performed in a field size of 10 x 10 cm², set up at an SSD of 100 cm in a solid water phantom, and placed at a depth of 1.5 cm. The response of the DUO512 was registered as a function of irradiation. The dose linearity was evaluated for the selected dose, starting from 50 to 500 cGy.

8.2.7 Reproducibility

To study the reproducibility of the detector, the array was irradiated 10 times under standard conditions, and the corresponding average and SD were calculated. The array was irradiated with 100 MU.

8.2.8 Damage rate calculation (α)

The damage caused by irradiation can be represented by the damage rate constant, which is defined as the rate of increase in leakage current as a function of the total dose at a specific voltage [202]. In this study, the damage rate constant was measured at -20 V. The detector was irradiated up to 14 Mrad using Co-60 at ANSTO.

8.2.9 Radiation hardness study

8.2.9.1 Photon damage

The test of response was performed after each irradiation by the Co-60 source to evaluate the effect of the accumulated dose on the silicon detector array. The response was tested at the Illawarra Cancer Care Centre of Wollongong, using a Varian 2100C LINAC. The response of the detectors was measured by collecting the charge created in the diodes for an absorbed dose of 100 cGy, using 6 MV x-rays at a dose rate of 600 MU/minute and a 10 x 10 cm² field size. The detectors were placed at an SSD of 100 cm and placed at d_{\max} in a water equivalent.

8.2.9.2 Photoneutron damage

To evaluate the effect of photoneutrons on silicon detectors using the LINAC, the response must first be measured at 6 MV under standard conditions. This point of measurement was used as a reference against which the irradiated detector's response was compared and normalised. The irradiation to detectors by photoneutrons was performed using 18 MV x-rays at a dose of 9795 MU three times, with a dose rate of 600 MU/minute and a 20 x 20 cm² field size. The arrays were placed at an SSD of 90 cm and placed at the surface in a 10 cm water-equivalent phantom as back-scatter material. The response was tested at the Saint George Care Hospital in Sydney using a Varian iX LINAC.

8.3 Results

8.3.1 Electrical characteristics (I-V and C-V)

Figure 8.2 presents the I-V characteristics of the selected pixels from the silicon detector array DUO512. The logarithmic scale was applied to attain a better demonstration of the breakdown. All pixels exhibited a gradual increase of leakage current proportional to reverse bias. The effect of the applied reverse bias was clearly

observed in all tested pixels from the detector. In addition, the current showed breakdown at -20 V. Figure 8.3 shows the C-V characteristic, which exhibited the expected trend of reducing the capacitance with increased bias.

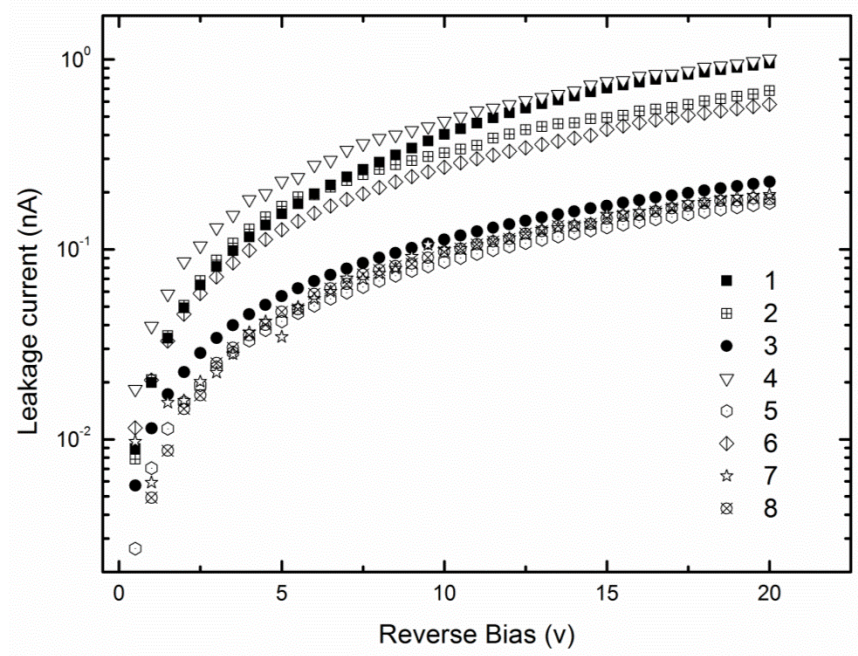


Figure 8.2: Pre-irradiation leakage current of the selected pixels

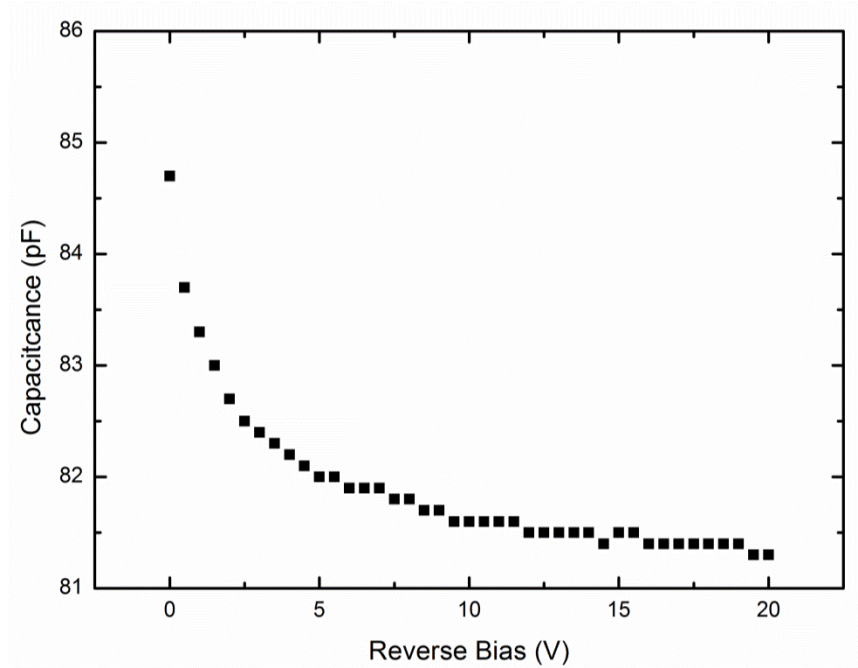


Figure 8.3: Measurement of the C-V characteristic of the DUO512

8.3.2 Uniformity

Figure 8.4 presents the responses of each detector channel before and after equalisation. The response of the array was normalised to the central detector in each case (before and after equalisation). The variation between all channels before applying the equalisation factors was within 1 to 1.5%. After applying the equalisation factors, the variation between all channels was below 0.5%.

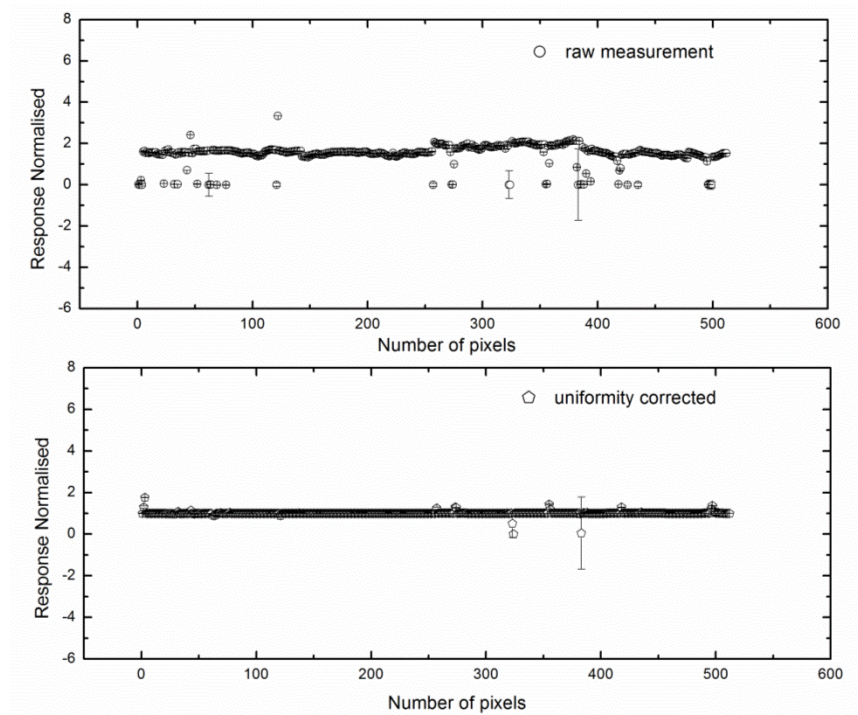


Figure 8.4: Detector response before and after equalisation was applied

8.3.3 Dose linearity

Figure 8.5 show the dose linearity of DUO512 for accumulated doses ranging from 50 to 500 MU, with 50 MU increments. The R^2 was equal to one and the vertical error bars were calculated by taking two SDs over three measurements. The

conversion factors from counts to dose were calculated from the linear fit as 1445.59 counts/cGy.

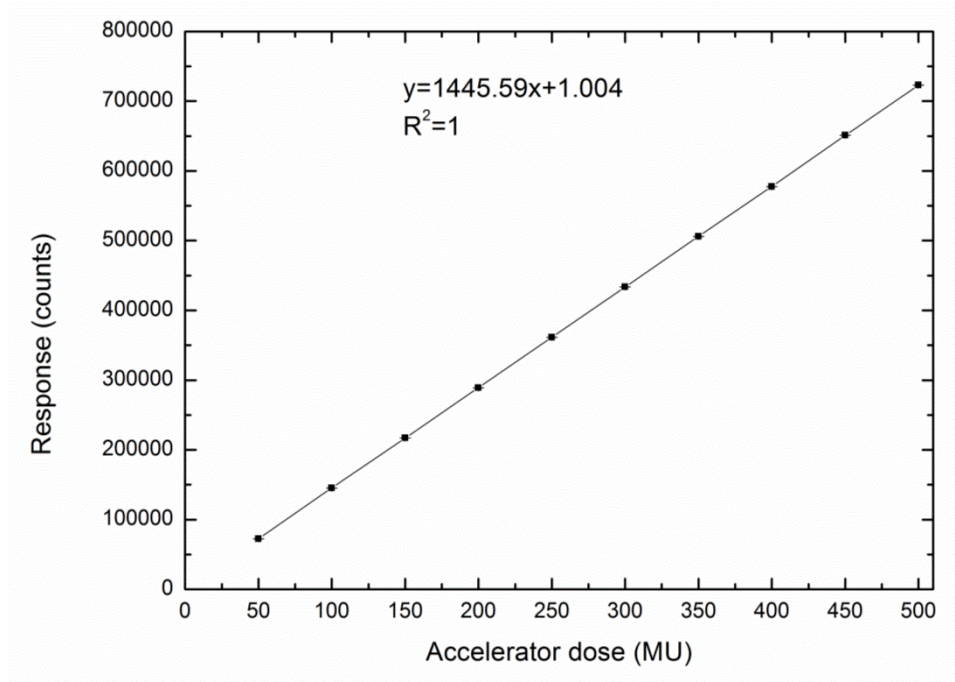


Figure 8.5: Measurement of the linearity of the central pixel, error bars are included but barely visible even considering a variation corresponding to two standard deviations over five repetitions.

Note: The solid line represents the linear fit.

8.3.4 Reproducibility

The reproducibility was measured by irradiating the device several times with a constant number of MUs. Reproducibility quantifies the variation in the response of the different channels on the array [99]. All the pixels' responses showed a maximum SD within 0.019% over the dynamic full scale of 9.6pC at 100 μ s integration time.

8.3.5 Damage rate calculation (α)

Figure 8.6 shows the volumetric leakage current density measured at a reverse bias of -20 V as a function of accumulated dose for the DUO512. The leakage current increased due to the increase in concentration of radiation-induced defects in the

detector substrate and Si/SiO₂ interfaces. This is often represented by the radiation damage rate, α , which aligns with another study [167]. The damage rate was calculated as $\alpha = 1.03 \times 10^{-10} \text{ A/cm}^3\text{Gy}$.

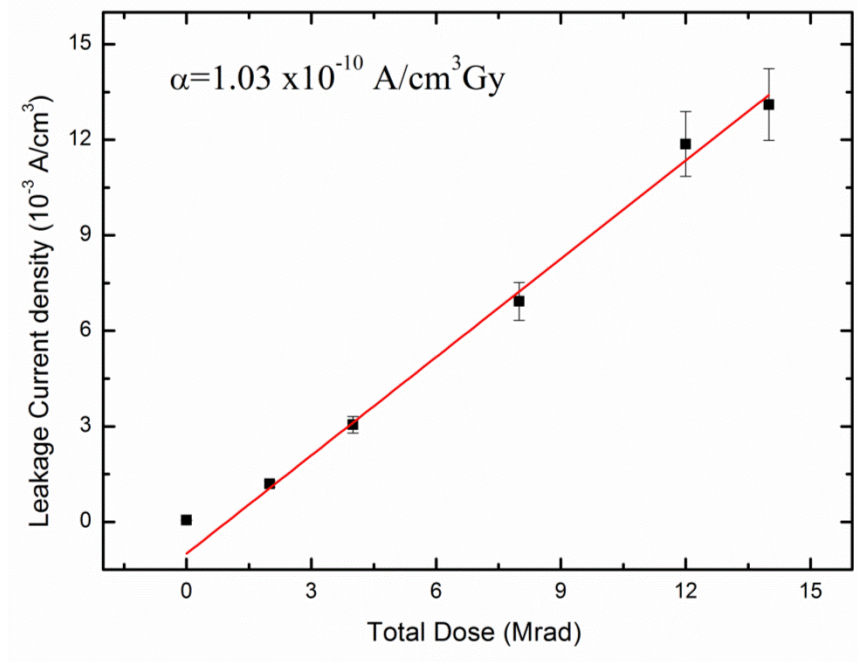


Figure 8.6: Leakage current density as a function of irradiation dose, measured at negative 20 V bias.

8.3.6 Photon damage

Figure 8.7 shows that the relative sensitivity decreased after pre-irradiation. This result agrees with the literature, which indicates a drop in sensitivity after irradiation [96, 142, 170, 179]. This trend relates to variation in the carrier lifetime as a function of the concentration of GRCs in the depleted detector substrate [179]. In this study, the decrease in sensitivity was observed at 12 kGy irradiation. This can be explained by the minimum size of the sensitive volume, which has too short a carrier lifetime. In addition, the sensitivity of the detector is based on the diffusion length, which decreases with the accumulated dose. To use a silicon detector with patients, it must

be operated in passive mode to decrease the variation in leakage current. It is also important to consider the effect of radiation damage. This means that the detector should be pre-irradiated before use to eliminate reduction of the sensitivity after irradiation and to reduce the time required to calibrate the detector [116].

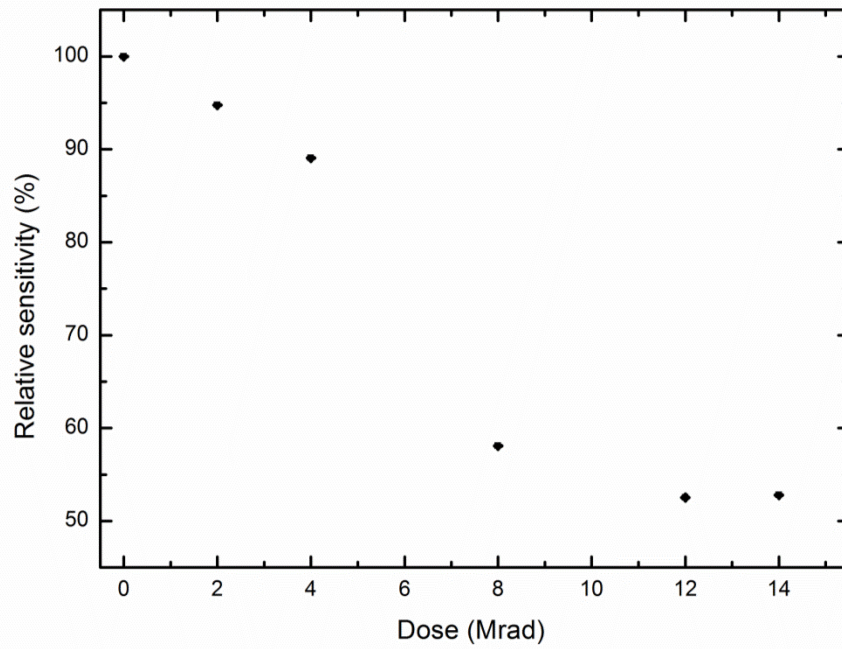


Figure 8.7: Measurement of relative sensitivity as a function of pre-irradiation dose up to 14 Mrad

Note: The error bars represent one SD.

8.3.7 Radiation damage by 18 MV photon beam

Figure 8.8 shows the normalised response after irradiation using a mixed photon-neutron field generated by an 18 MV medical LINAC. During this test, the response reduced and CCE induced by irradiation were less than 11%/300 Gy. This was due to the generation of cluster defects in the layer of the silicon. This can be explained by the presence of fast secondary neutrons. This also leads to creating recombination centres at the very deep energy level of the silicon forbidden band gap [179]. The

small amount of reduction indicates that the detector was very sensitive to the neutron field. Therefore, the silicon detector array seems unstable for use at energy levels above 10 MV.

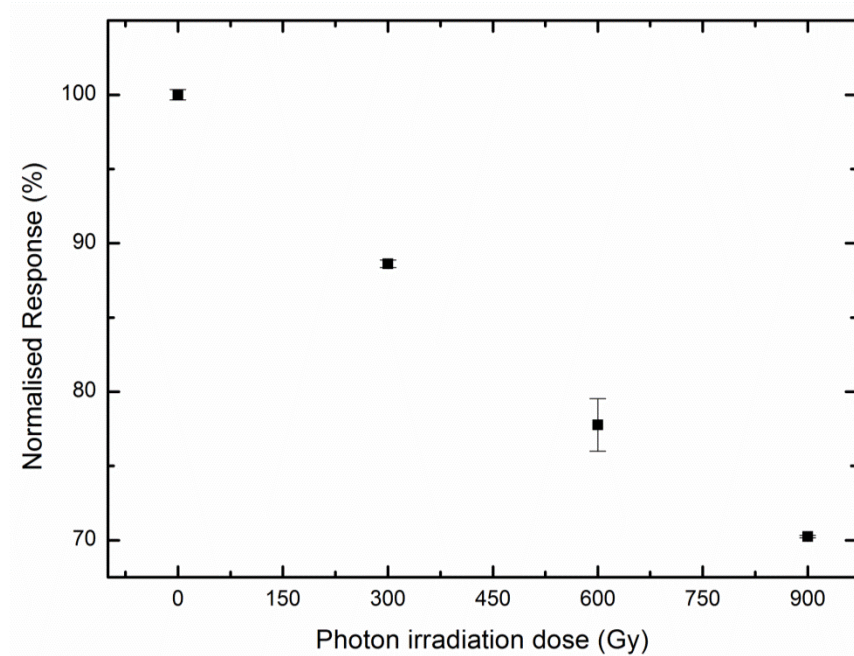


Figure 8.8: Normalised response of silicon detector array as a function of the irradiation dose delivered by an 18 MV medical LINAC photon beam

Note: The error bars represent the SD of the measurements.

8.4 Conclusion

This chapter has studied a 2-D array based on a *p*-type silicon substrate in terms of basic characterisations. This array comprised 512 pixels implanted on an area of 52 x 52 mm², arranged in four arms, with each arm containing 128 pixels. The sensitive volume of each single strip was 20 x 800 μm², and the detector pitch was 200 μm. Experimental measurements were performed to characterise the array developed at CMRP for dosimetry in small fields for stereotactic radiosurgery. These studies were

very important to evaluate the detector before use in medical applications and for 4-D radiation therapy purposes. This was achieved by testing the electrical properties of the array and studying the response after irradiation by Co-60 and photoneutrons from LINAC.

The equalisation method was applied to equalise the response between the pixels, and the variation after equalisation was below 0.5%. The linearity of the array was measured and $R^2 = 1$. Reproducibility was performed, which showed that the maximum SD did not exceed 0.01. The radiation damage showed a stable response at 120 kGy using a gamma irradiation dose (Co-60). Additionally, the radiation damage by photoneutrons produced using the 18 MV medical LINAC was 11%/300 Gy. The silicon detector array DUO512 was found to be unsuitable for use at energy levels above 10 MV for dosimetry in radiation therapy due to the detector being too sensitive to photoneutrons.

CHAPTER 9: CONCLUSION

This thesis has investigated a selection of dosimeter systems based on silicon substrates. It has described a single diode system (the EPI diodes), sensitive volume of the 2-D detector array MP121, and monolithic 2D arrays (the MP512 and DUO512). These systems were successfully characterised in terms of radiation damage using high energy photons emitted by a Co-60 source before being used for medical applications. They were then positively employed for dosimetric verification of IMRT, SBRT modalities and for verification of DMLC tracking techniques. This chapter summarises the main outcomes of this thesis regarding using the EPI, MP512 and DUO512, discussing the advantages and drawbacks of these three systems. Further, this chapter presents future potential developments for these systems' use in medical applications.

9.1 EPI diode

The silicon EPI diode without a guard ring was characterised by assessing its electrical properties and radiation hardness. The EPI diode was used as a sensitive element of the MP121 and an 11 x 11 array of diodes for 2-D and 3-D dosimetry in EBRT. It was a 50 μm thick p -type with a resistivity (100 $\Omega\text{-cm}$) based on an EPI layer growing onto a 375 μm thick p^+ , with a resistivity of 0.001 $\Omega\text{-cm}$ silicon substrate. The sensitive area of the diode was 0.6 mm^2 , and was defined by an n^+ boron ion-implanted junction. The current-voltage and capacitance characteristics of the detectors were examined to determine the leakage current and depletion bias. The radiation damage rate, α , was calculated through the leakage current density as a function of the accumulated dose. The radiation damage rate calculation was found to agree with the literature. Experimental and numerical simulation techniques were used to validate the radiation damage results.

Simulation has been used also to verify the radiation damage mechanism underpinning the EPI diode's unusual total dose radiation response. The EPI diode developed at CMRP for dosimetry in EBRT exhibited an increase in the sensitivity with gamma radiation, as opposed to commercial diodes. The experimental measurements of the electrical characteristics (I-V and C-V) as a function of reverse bias were compared with the simulation, and showed to fit the ideal behaviour expected by the $n + p$ junction simulated taking into account the geometry and doping concentrations. In order to study the radiation damage of the detectors, the CCE was evaluated using a radiation field from a Co-60 gamma source and 18 MV medical LINAC. Using gamma radiation of Co-60, the detector showed a stable response within $\pm 2.5\%$ for 120 kGy. A simulation of the effect of the concentration of trapped charge in the Si/SiO₂ interface was performed and verified to be the mechanism of radiation damage by photon beam responsible for the detector response increase when operated in passive mode. The simulation indicated that variation in the response of the diodes was due to the combination of CCE induced by the trapped charge at the Si/SiO₂ interface, and by the radiation gettering effect. Using an 18 MV medical LINAC, the radiation damage induced by photoneutrons was estimated to be 0.5/100 Gy. The device demonstrated a long lifetime as a dosimeter for clinical QA.

9.2 MP512

9.2.1 Radiation damage study

The MP512 is a monolithic 2-D array detector based on ion-implanted p -type silicon technology. The MP512 used in this thesis had 512 detectors and a detector pitch of 2 mm. The pixels were arranged in a 22 x 22 array, with seven extra elements for each detector side, covering an area of 52 x 52 mm². The sensitive volume of each

pixel was $0.5 \times 0.5 \times 0.1 \text{ mm}^3$. Two samples of MP512 with different type of substrates were characterised in Chapter 4. The bulk silicon of both substrates was examined to determine the optimum substrate resistivity and ion implantation for use in 2-D radiation therapy. The electrical characteristics of I-V and C-V were examined. The CCE of both test structures and the MP512 were studied.

The I-V results showed that there is no relationship between the amount of ion implantation and leakage current for test structures without a guard ring. The test structures with higher amounts of ion implantation of $100 \text{ } \mu\text{C}$ with different substrates showed consistent results, while the samples with lower ion implantation exhibited lower leakage current but large variation between pixels. When using the guard ring in the test structures, the samples showed inconsistent results in terms of leakage current when the guard ring was grounded, while the floating guard ring configuration showed the opposite effect. There was no evidence indicating that introducing a guard ring to the detector diminished the leakage current. Therefore, it is has not been necessary to design a detector array with a guard ring. Further, the C-V proved that the guard ring had a slight influence on the capacitance of the test structures. The CMRP substrate showed lower leakage current than did the KDB substrate. The radiation damage study showed a consistent result for the MP512 array with test structures in the CMRP substrates. The MP512 with $10 \text{ } \Omega\text{-cm}$ CMRP substrate showed lower response reduction than did the MP512 with $10 \text{ } \Omega\text{-cm}$ KDB substrate. The response of the array with CMRP substrate was very low, which made accurate assessment impossible due to the large uncertainty in the data. The MP512 $30 \text{ } \mu\text{C}$ with KDB substrate also exhibited a low response; however, the data were more reproducible and stable for dosimetry. Likewise, the radiation damage by photoneutrons generated using an 18 MV medical LINAC was also evaluated. Both

test structures and the MP512 were tested, and showed high sensitivity to the photoneutron field. Thus, the detector is not suitable for dosimetry for energy larger than 10MV.

Therefore, the MP512 array of 30 μC with KDB substrate was chosen for clinical use to perform the basic characterisation in terms of uniformity, PDD, beam profile, OF and DPP. All these measurements were presented in Chapter 5. Further, the detector was used in a movable phantom with a DMLC tracking system for dose verification, as discussed in Chapter 7.

9.2.2 Radiation response and basic characteristics

The response and basic characteristics of the MP512 as a dosimeter for QA in SBRT were described in Chapter 7. The response of the MP512 showed variation of $\pm 0.25\%$ after the uniformity corrections. The MP512 PDDs were compared with ionising chambers, and showed agreement within 1.5% for percentage depth dose. Further, the dose-rate dependence of the detector was evaluated by comparing the response to an ionising chamber. The MP512 displayed a dose per pulse dependence within 1% to 3.5×10^{-5} Gy/pulse. MP512 is suitable for beam profile reconstruction down to a $10 \times 10 \text{ mm}^2$ field size. The central pixel response showed a discrepancy of less than 2%. As the field size became narrower—such as when using $5 \times 5 \text{ mm}^2$ —the MP512 demonstrated an over-response of approximately 4%. This was because of the scattering produced by the silicon surrounding the central pixel. This was proven by using the small single detector, *MOSkin*, and comparing it to the EBT3 film. The *MOSkin* showed agreement with the EBT3 film within 1.5% for field sizes down to 5 mm. The rotatable cylindrical phantom was designed by the CMRP to overcome the angular dependence. The MP512 combined with the rotatable phantom

is a powerful tool, with real-time, accurate 2-D—and potentially 3-D—dose reconstruction capabilities for pre-treatment QA for SBRT and SRS verification.

9.2.3 MP512 used as dose verification for movable target

The MP512 was also combined with the Calypso system as a tool to study moving targets in radiotherapy. The MP512 was compared with the EBT3 film in terms of dose profile. The dose profiles were studied with different field sizes for three different scenarios: no motion, motion, and motion with DMLC tracking system. The MP512 showed excellent agreement with the EBT3 film in terms of FWHM and penumbra (80%-20%). MP512 was proven to be an effective tool for pre-treatment verification of real-time adaptive deliveries with both high spatial resolution for dose profiling and high temporal resolution for pulse-by-pulse reconstruction.

9.3 DUO512

A 2-D detector array based on the *p*-type substrate was tested in Chapter 8. The detector array—called DUO512—was 52 x 52 mm², with a 200 μm diode pitch. The detectors were implanted on fibreglass (FR4) with a 500 μm thickness. The pixel element was a strip detector that was 20 μm and 800 μm long, with 10 Ω-cm resistivity of the substrate. The final goal of this study was to characterise the detector in terms of the electric properties and radiation damage in order to validate using the detector as a 2-D dosimeter in EBRT, especially for a small field beam.

An analysis of the I-V and C-V characteristics of the silicon detector array was performed. The detector current exhibited breakdown at -20 V. The detector array showed the ideal trend of the *p-n* junction, with the current increasing with applied voltage. The I-V of the detector was measured before and after pre-irradiation by Co-60 to calculate the constant damage rate, which was found to be $1.03 \times 10^{-10} \text{ A/cm}^3$.

An equalisation method to correct the uniformity was applied, and the variation in response after equalisation was below 0.5%. Basic characterisation in terms of the radiation damage by photons and photoneutrons was performed. The dose linearity showed the ideal trend of the detector, which increased the response with the dose. The radiation damage test for the array showed a stable response at 120 kGy using a gamma irradiation dose (Co-60). Further, the radiation damage by photoneutrons produced using an 18 MV medical LINAC was determined to be 11%/300 Gy. The silicon detector array DUO512 was shown to be unsuitable for use at energy levels above 10 MV for dosimetry in radiation therapy due to the detector being too sensitive to photoneutrons.

Further characterisation of MP512 is planned to enable a complete characterisation for clinical scenarios, including determining the effect of MLC on dosimetry and characterising the energy dependence. Moreover, further characterisation of DUO512 is planned, including determining the feasibility of the array for profiling of very small fields such the one adopted for SRS. These experiments will include PDD, OF, DPP and beam profile comparison with EBT3 film. Further, this detector is also planned to be used with the movable phantom.

REFERENCES

1. World health statistics, 2009. [Online]. Available:
<http://www.who.int/mediacentre/factsheets/fs297/en/index.html>
2. Benedick, F., D. Karen, H. Margie, et al., *American Association of Physicists in Medicine Radiation Therapy Committee Task Group 53: quality assurance for clinical radiotherapy treatment planning*. Medical Physics, 1998. **25**(10): p. 1773-1829.
3. Webb, S., *Advances in three-dimensional conformal radiation therapy physics with intensity modulation*. Lancet Oncology, 2000. **1**(1): p. 30-36.
4. Wong, J.H.D., I. Fuduli, M. Carolan, et al., *Characterization of a novel two dimensional diode array the "magic plate" as a radiation detector for radiation therapy treatment*. Medical Physics, 2012. **39**(5): p. 2544-2558.
5. Webb, S., *The physical basis of IMRT and inverse planning*. The British journal of radiology, 2003. **76**(910): p. 678-689.
6. Martin, D.D., *Review of Radiation Therapy in the Pregnant Cancer Patient*. Clinical Obstetrics and Gynecology, 2011. **54**(4): p. 591-601.
7. Van Dyk, J., *The Modern Technology of Radiation Oncology: a Compendium for Medical Physicists and Radiation Oncologists*. 1999, Madison, Wis: Medical Physics Pub.
8. Fuks, Z. and A. Horwich, *Clinical and Technical Aspects of Conformal Therapy*. Radiotherapy and Oncology, 1993. **29**(2): p. 219-219.
9. Nutting, C., D.P. Dearnaley, and S. Webb, *Intensity modulated radiation therapy: a clinical review*. The British journal of radiology, 2000. **73**(869): p. 459-469.

10. Brahme, A., J.E. Roos, I. Lax, et al., *Solution of an integral equation encountered in rotation therapy*. Physics in Medicine and Biology, 1982. **27**(10): p. 1221-1229.
12. Arthur, L.B., A. Larry, F. Aaron, et al., *A review of electronic portal imaging devices (EPIDs)*. Medical physics, 1992. **19**(1): p. 1-16.
13. Matuszak, M.M., D. Yan, I. Grills, et al., *Clinical Applications of Volumetric Modulated Arc Therapy*. International journal of Radiation Oncology, Biology, Physics, 2010. **77**(2): p. 608-616.
14. Bedford, J.L., *Treatment planning for volumetric modulated arc therapy*. Medical Physics, 2009. **36**(11): p. 5128-5138.
15. Yu, C.X., *Intensity-modulated arc therapy with dynamic multileaf collimation: an alternative to tomotherapy*. Physics in Medicine and Biology, 1995. **40**(9): p. 1435-1449.
16. Teoh, M., C.H. Clark, K. Wood, et al., *Volumetric modulated arc therapy: a review of current literature and clinical use in practice*. The British journal of radiology, 2011. **84**(1007): p. 967-996.
17. Lartigau, E., *Stereotactic body radiotherapy*. British Medical Journal, 2011. **343**: p. 1-2.
18. Martin, A. and A. Gaya, *Stereotactic Body Radiotherapy : A Review*. Clinical Oncology, 2010. **22**(3): p. 157-172.
19. Bijlani, A., G. Aguzzi, D.W. Schaal, et al., *Stereotactic radiosurgery and stereotactic body radiation therapy cost-effectiveness results*. Frontiers in oncology, 2013. **3**(77): p. 1-9.
20. Benedict, S.H., K.M. Yenice, D. Followill, et al., *Stereotactic body radiation therapy: The report of AAPM Task Group 101*. Medical Physics, 2010. **37**(8): p. 4078-4101.

21. Holt, A., D. Van Gestel, M.P. Arends, et al., *Multi-institutional comparison of volumetric modulated arc therapy vs. intensity-modulated radiation therapy for head-and-neck cancer: a planning study*. Radiation oncology, 2013. **8**(1): p. 1-11.
22. Aldosari, A.H., P. Metcalfe, M. Carolan, et al., *A two dimensional silicon detectors array for quality assurance in stereotactic radiotherapy: MagicPlate-512*. Medical Physics, 2014. **41**(9): p. 1-10.
23. Heydarian, M., P.W. Hoban, and A.H. Beddoe, *A comparison of dosimetry techniques in stereotactic radiosurgery*. Physics in Medicine and Biology, 1996. **41**(1): p. 93-110.
24. Balagamwala, E.H., S.T. Chao, and J.H. Suh, *Principles of radiobiology of stereotactic radiosurgery and clinical applications in the central nervous system*. Technology in cancer research & treatment, 2012. **11**(1): p. 3-13.
25. Yamada, Y., M.H. Bilsky, D.M. Lovelock, et al., *High-Dose, Single-Fraction Image-Guided Intensity-Modulated Radiotherapy for Metastatic Spinal Lesions*. International Journal of Radiation Oncology, Biology, Physics, 2008. **71**(2): p. 484-490.
26. Wong, J.H.D., A.B. Rosenfeld, T. Knittel, et al., *The use of a silicon strip detector dose magnifying glass in stereotactic radiotherapy QA and dosimetry*. Medical Physics, 2011. **38**(3): p. 1226-1238.
27. Li, X.A., M. Soubra, J. Szanto, et al., *Lateral electron equilibrium and electron contamination in measurements of head-scatter factors using miniphantoms and brass caps*. Medical Physics, 1995. **22**(7): p. 1167-1170.
28. Manolopoulos, S., C. Wojnecki, R. Hugtenburg, et al., *Small field measurements with a novel silicon position sensitive diode array*. Physics in Medicine and Biology, 2009. **54**(3): p. 485-495.
29. Pappas, E., T.G. Maris, F. Zacharopoulou, et al., *Small SRS photon field profile dosimetry performed using a PinPoint air ion chamber, a diamond*

- detector, a novel silicon-diode array (DOSI), and polymer gel dosimetry. Analysis and intercomparison. Medical Physics, 2008. 35(10): p. 4640-4648.*
30. García-Vicente, F., M.J. Béjar, L. Pérez, et al., *Clinical impact of the detector size effect in 3D-CRT. Radiotherapy and Oncology, 2005. 74(3): p. 315-322.*
 31. Laub, W.U. and T. Wong, *The volume effect of detectors in the dosimetry of small fields used in IMRT. Medical Physics, 2003. 30(3): p. 341-347.*
 32. Kornelsen, R.O. and M.E.J. Young, *Changes in the dose-profile of a 10 MV x-ray beam within and beyond low density material. Medical Physics, 1982. 9(1): p. 114-116.*
 33. Dawson, D.J., J.M. Harper, and A.C. Akinradewo, *Analysis of physical parameters associated with the measurement of high-energy x-ray penumbra. Medical Physics, 1984. 11(4): p. 491-497.*
 34. Rice, R.K., J.J. Hansen, G.K. Svensson, et al., *Measurements of dose distributions in small beams of 6 MV X-rays. Physics in Medicine and Biology, 1987. 32(9): p. 1087-1099.*
 35. Westermarck, M., J. Arndt, B. Nilsson, et al., *Comparative dosimetry in narrow high-energy photon beams. Physics in Medicine and Biology, 2000. 45(3): p. 685-702.*
 36. Low, D.A., J.M. Moran, J.F. Dempsey, et al., *Dosimetry tools and techniques for IMRT. Medical Physics, 2011. 38(3): p. 1313-1338.*
 37. Ibbott, G.S., M.J. Maryanski, P. Eastman, et al., *Three-dimensional visualization and measurement of conformal dose distributions using magnetic resonance imaging of BANG polymer gel dosimeters. International Journal of Radiation Oncology, Biology, Physics, 1997. 38(5): p. 1097-1103.*
 38. Vergote, K., Y.D. Deene, W. Duthoy, et al., *Validation and application of polymer gel dosimetry for the dose verification of an intensity-modulated arc therapy (IMAT) treatment. Physics in Medicine and Biology, 2004. 49(2): p. 287-305.*

39. Horowitz, Y.S., *The theoretical and microdosimetric basis of thermoluminescence and applications to dosimetry*. Physics in Medicine and Biology, 1981. **26**(5): p. 765-824.
40. McKerracher, C. and D.I. Thwaites, *Assessment of new small-field detectors against standard-field detectors for practical stereotactic beam data acquisition*. Physics in Medicine and Biology, 1999. **44**(9): p. 2143-2160.
41. Benedict, S.H., J. Cai, B. Libby, et al., *SRT and SBRT: Current practices for QA dosimetry and 3D*. Journal of Physics: Conference Series, 2010. **250**: p. 1-11.
42. Bortfeld, T., K. Jokivarsi, M. Goitein, et al., *Effects of intra-fraction motion on IMRT dose delivery: statistical analysis and simulation*. Physics in Medicine and Biology, 2002. **47**(13): p. 2203-2220.
43. Seco, J., G.C. Sharp, J. Turcotte, et al., *Effects of organ motion on IMRT treatments with segments of few monitor units*. Medical Physics, 2007. **34**(3): p. 923-934.
44. Schwarz, M., J. Van der Geer, M. Van Herk, et al., *Impact of geometrical uncertainties on 3D CRT and IMRT dose distributions for lung cancer treatment*. International journal of Radiation Oncology, Biology, Physics, 2006. **65**(4): p. 1260-1269.
45. Zelefsky, M.J., A. Jackson, M. Skwarchuk, et al., *Clinical experience with intensity modulated radiation therapy (IMRT) in prostate cancer*. Radiotherapy and Oncology, 2000. **55**(3): p. 241-249.
46. Langen, K.M. and D.T. Jones, *Organ motion and its management*. International journal of Radiation Oncology, Biology, Physics, 2001. **50**(1): p. 265-278.
47. Saw, C.B., E. Brandner, R. Selvaraj, et al., *A review on the clinical implementation of respiratory-gated radiation therapy*. Biomedical Imaging and Intervention Journal, 2007. **3**(1): p. 1-8.

48. Grégoire, V. and T.R. Mackie, *State of the art on dose prescription, reporting and recording in Intensity-Modulated Radiation Therapy (ICRU report No. 83)*. Cancer/Radiothérapie, 2011. **15**(6): p. 555-559.
49. Zimmerman, J., S. Korreman, G. Persson, et al., *DMLC motion tracking of moving targets for intensity modulated arc therapy treatment: a feasibility study*. Acta Oncologica, 2009. **48**(2): p. 245-245.
50. Benedict, S.H. Schlesinger, D.J. et al., *Stereotactic radiosurgery and stereotactic body radiation therapy*. 2014, Boca Raton, Florida: CRC Press.
51. Paul, J.K., R.M. Brad, R.R. Chester, et al., *The management of respiratory motion in radiation oncology report of AAPM Task Group 76*. Medical Physics, 2006. **33**(10): p. 3874-3900.
52. Mah, D., J. Hanley, K.E. Rosenzweig, et al., *Technical aspects of the deep inspiration breath-hold technique in the treatment of thoracic cancer*. International Journal of Radiation Oncology, Biology, Physics, 2000. **48**(4): p. 1175-1185.
53. Blomgren, H., I. Lax, I. Näslund, et al., *Stereotactic high dose fraction radiation therapy of extracranial tumors using an accelerator. Clinical experience of the first thirty-one patients*. Acta Oncologica, 1995. **34**(6): p. 861-870.
54. Keall, P., S. Vedam, R. George, et al., *The clinical implementation of respiratory-gated intensity-modulated radiotherapy*. Medical Dosimetry, 2006. **31**(2): p. 152-162.
55. Giraud, P., E. Yorke, S. Jiang, et al., *Reduction of organ motion effects in IMRT and conformal 3D radiation delivery by using gating and tracking techniques*. Cancer/Radiothérapie, 2006. **10**(5): p. 269-282.
56. Keall, P.J., V.R. Kini, S.S. Vedam, et al., *Potential Radiotherapy Improvements with Respiratory Gating*. Australasian Physical & Engineering Sciences in Medicine, 2002. **25**(1): p. 1-6.

57. Keall, P.J., V.R. Kini, S.S. Vedam, et al., *Motion adaptive x-ray therapy: a feasibility study*. Physics in Medicine and Biology, 2001. **46**(1): p. 1-10.
58. Ryan, M., P. Lech, and R. Dharanipathy, *Dynamic-MLC leaf control utilizing on-flight intensity calculations: A robust method for real-time IMRT delivery over moving rigid targets*. Medical Physics, 2007. **34**(8): p. 3211-3223.
59. Depuydt, T., M. Hoogeman, G. Storme, et al., *Geometric accuracy of a novel gimbals based radiation therapy tumor tracking system*. Radiotherapy and Oncology 2011. **98**(3): p. 365-372.
60. Shah, A.P., P.A. Kupelian, T.R. Willoughby, et al., *Expanding the use of real-time electromagnetic tracking in radiation oncology*. Journal of Applied Clinical Medical Physics, 2011. **12**(4): p. 34-49.
61. Houdek, P.V., J.L. Bujnowski, J.G. Schwade, et al., *Computer controlled stereotaxic radiotherapy system*. International Journal of Radiation Oncology, Biology, Physics, 1992. **22**(1): p. 175-180.
62. Santanam, L., C. Noel, T.R. Willoughby, et al., *Quality assurance for clinical implementation of an electromagnetic tracking system*. Medical Physics, 2009. **36**(8): p. 3477-3486.
63. Kupelian, P., D. Liu, D. Beyer, et al., *Multi-institutional clinical experience with the Calypso System in localization and continuous, real-time monitoring of the prostate gland during external radiotherapy*. International Journal of Radiation Oncology, Biology, Physics, 2007. **67**(4): p. 1088-1098.
64. Willoughby, T., S. Hadley, j. Wei, et al., *Target localization and real-time tracking using the Calypso 4D localization system in patients with localized prostate cancer*. International Journal of Radiation Oncology, Biology and Physics, 2006. **65**(2): p. 528-534.
65. Attix, F.H., *Introduction to radiological physics and radiation dosimetry*. 2004, Weinheim, Germany: Wiley-VCH.

66. Knoll, G.F., *Radiation detection and measurement*. 2000, New York: J. Wiley.
67. Frelin, A.M., J.M. Fontbonne, G. Ban, et al. *Scintillating fiber dosimeter*. IEEE Symposium Conference Record Nuclear Science, 2004. **4**: p. 2221-2225.
68. McCarthy, D., S. O'Keeffe, E. Lewis, et al. *Optical fibre X-ray radiation dosimeter sensor for low dose applications*. IEEE Sensors Proceedings, 2011. p. 121-124.
69. Aznar, M.C., C.E. Andersen, L. Bøtter-Jensen, et al., *Real-time optical-fibre luminescence dosimetry for radiotherapy: physical characteristics and applications in photon beams*. Physics in Medicine and Biology, 2004. **49**(9): p. 1655-1669.
70. Marsolat, F., D. Tromson, N. Tranchant, et al., *Diamond dosimeter for small beam stereotactic radiotherapy*. Diamond and Related Materials, 2013. **33**: p. 63-70.
71. Guerrero, M.J., D. Tromson, M. Rebisz, et al., *Requirements for synthetic diamond devices for radiotherapy dosimetry applications*. Diamond and Related Materials, 2004. **13**(11): p. 2046-2051.
72. Venkataraman, S., K.E. Malkoske, M. Jensen, et al., *The influence of a novel transmission detector on 6 MV x-ray beam characteristics*. Physics in Medicine and Biology, 2009. **54**(10): p. 3173-3183.
73. Ezzell, G.A., C.X. Yu, J.M. Galvin, et al., *Guidance document on delivery, treatment planning, and clinical implementation of IMRT: report of the IMRT Subcommittee of the AAPM Radiation Therapy Committee*. Medical Physics, 2003. **30**(8): p. 2089-2115.
74. Bogucki, T.M., W.R. Murphy, C.W. Baker, et al., *Processor quality control in laser imaging systems*. Medical physics, 1997. **24**(4): p. 581-584.

75. E. B. Podgorsak, E. and R.P.D. Kristofer Kainz, *Radiation Oncology Physics: A Handbook for Teachers and Students*. 2006, Austria.
76. Amerio, S., F. Marchetto, U. Nastasi, et al., *Dosimetric characterization of a large area pixel-segmented ionization chamber*. Medical Physics, 2004. **31**(2): p. 414-420.
77. Li, J.G., G. Yan, and C. Liu, *Comparison of two commercial detector arrays for IMRT quality assurance*. Journal of Applied Clinical Medical Physics / American College of Medical Physics, 2009. **10**(2): p. 62-74.
78. McAuley, K.B., *Fundamentals of Polymer Gel Dosimeters*. Journal of Physics: Conference Series, 2006. **56**. p. 35-44.
79. Baldock, C., Y. De Deene, S. Doran, et al., *Polymer gel dosimetry*. Physics in Medicine and Biology, 2010. **55**(5): p. R1-R63.
80. Day, M.J. and G. Stein, *Chemical effects of ionizing radiation in some gels*. Nature, 1950. **166**(4212): p. 146-147.
81. Schreiner, L.J., T. Olding, and K.B. McAuley, *Polymer gel dosimetry*. Journal of Physics: Conference Series, 2010. **250**. p. 012014.
82. Ibbott, G.S., *Applications of gel dosimetry*. Journal of Physics: Conference Series, 2004. **3**. p. 58-77.
83. Guo, P.Y., J.A. Adamovics, and M. Oldham, *Characterization of a new radiochromic three-dimensional dosimeter*. Medical Physics, 2006. **33**(5): p. 1338-1345.
84. Adamovics, J. and M.J. Maryanski, *Characterisation of PRESAGE: A new 3-D radiochromic solid polymer dosemeter for ionising radiation*. Radiation protection dosimetry, 2006. **120**(1-4): p. 107-112.
85. Doran, S.J., *The history and principles of chemical dosimetry for 3-D radiation fields: Gels, polymers and plastics*. Applied Radiation and Isotopes, 2009. **67**(3): p. 393-398.

86. Brown, S., A. Venning, Y. De Deene, et al., *Radiological properties of the PRESAGE and PAGAT polymer dosimeters*. Applied Radiation and Isotopes, 2008. **66**(12): p. 1970-1974.
87. Ceberg, S., A. Karlsson, H. Gustavsson, et al., *Verification of dynamic radiotherapy: the potential for 3D dosimetry under respiratory-like motion using polymer gel*. Physics in medicine and biology, 2008. **53**(20): p. N387-N396.
88. Ceberg, S., G. Persson, A. Sawant, et al., *Tumor-tracking radiotherapy of moving targets; verification using 3D polymer gel, 2D ion-chamber array and biplanar diode array*. Journal of Physics: Conference Series, 2010. **250**. p. 012051-012239.
89. Martens, C., C.D. Wagter, and W.D. Neve, *The value of the PinPoint ion chamber for characterization of small field segments used in intensity-modulated radiotherapy*. Physics in Medicine and Biology, 2000. **45**(9): p. 2519-2530.
90. Aird, E.G.A. and F.T. Farmer, *The design of a thimble chamber for the Farmer dosemeter*. Physics in medicine and biology, 1972. **17**(2): p. 169-174.
91. Poppe, B., A. Blechschmidt, A. Djouguela, et al., *Two-dimensional ionization chamber arrays for IMRT plan verification*. Medical Physics, 2006. **33**(4): p. 1005-1015.
92. Dreindl, R., D. Georg, and M. Stock, *Radiochromic film dosimetry: considerations on precision and accuracy for EBT2 and EBT3 type films*. Med. Phys, 2014. **24**(2): p. 153-163.
93. Casanova Borca, V., M. Pasquino, G. Russo, et al., *Dosimetric characterization and use of GAFCHROMIC EBT3 film for IMRT dose verification*. Journal of applied clinical medical physics / American College of Medical Physics, 2013. **14**(2): p. 158-171.

94. Kumar, A.S., S.D. Sharma, and B.P. Ravindran, *Characteristics of mobile MOSFET dosimetry system for megavoltage photon beams*. Journal of medical physics / Association of Medical Physicists of India, 2014. **39**(3): p. 142-149.
95. Rosenfeld, A.B., *MOSFET dosimetry on modern radiation oncology modalities*. Radiation protection dosimetry, 2002. **101**(1): p. 393-398.
96. Rosenfeld, A.B., *Electronic dosimetry in radiation therapy*. Radiation Measurements, 2006. **41**: p. S134-S153.
97. Metcalfe, P., T. Kron, and P. Hoban, *The physics of radiotherapy x-rays and electrons*. 2007, Madison, Wis.
98. Létourneau, D., M. Gulam, D. Yan, et al., *Evaluation of a 2D diode array for IMRT quality assurance*. Radiotherapy and Oncology, 2004. **70**(2): p. 199-206.
99. Talamonti, C., M. Bruzzi, M. Bucciolini, et al., *Preliminary dosimetric characterization of a silicon segmented detector for 2D dose verifications in radiotherapy*. Nuclear Instruments and Methods in Physics Research Section A: Accelerators, Spectrometers, Detectors and Associated Equipment, 2007. **583**(1): p. 114-118.
100. Bocci, A., F.J. Pérez Nieto, M.A. Cortés-Giraldo, et al., *Silicon strip detector for a novel 2D dosimetric method for radiotherapy treatment verification*. Nuclear Inst. and Methods in Physics Research, A, 2012. **673**: p. 98-106.
101. Bedford, J.L., Y.K. Lee, P. Wai, et al., *Evaluation of the Delta4 phantom for IMRT and VMAT verification*. Physics in medicine and biology, 2009. **54**(9): p. N167-N176.
102. Fredh, A., J.B. Scherman, L.S. Fog, et al., *Patient QA systems for rotational radiation therapy: a comparative experimental study with intentional errors*. Medical Physics, 2013. **40**(3): p. 1-9.

103. Stine, K., *Dosimetric verification of RapidArc treatment delivery*. Acta Oncologica, 2009. **48**(2): p. 185-191.
104. Li, G., Y. Zhang, X. Jiang, et al., *Evaluation of the ArcCHECK QA system for IMRT and VMAT verification*. Physica Medica, 2013. **29**(3): p. 295-303.
105. Fakir, H., S. Gaede, M. Mulligan, et al., *Development of a novel ArcCHECKTM insert for routine quality assurance of VMAT delivery including dose calculation with inhomogeneities*. Medical Physics, 2012. **39**(7): p. 4203-4208.
106. Nilsson, B., B.-I. Rudén, and B. Sorcini, *Characteristics of silicon diodes as patient dosimeters in external radiation therapy*. Radiotherapy and Oncology, 1988. **11**(3): p. 279-288.
107. Ismail, A., J.Y. Giraud, G.N. Lu, et al., *Radiotherapy quality insurance by individualized in vivo dosimetry: State of the art*. Cancer Radiothérapie, 2009. **13**(3): p. 182-189.
108. Amarjit, S.S. and C.Z. Timothy, *Energy dependence of commercially available diode detectors for in-vivo dosimetry*. Medical Physics, 2007. **34**(5): p. 1704-1711.
109. Grusell, E. and G. Rikner, *Radiation damage induced dose rate non-linearity in an n-type silicon detector*. Acta Radiologica Oncology, 1984. **23**(6): p. 465-496.
110. Rikner, G. and E. Grusell, *Effects of radiation damage on p-type silicon detectors*. Physics in Medicine and Biology, 1983. **28**(11): p. 1261-1267.
111. Eremin, V., E. Verbitskaya, and Z. Li, *Effect of radiation induced deep level traps on Si detector performance*. Nuclear Instruments and Methods in Physics Research Section A: Accelerators, Spectrometers, Detectors and Associated Equipment, 2002. **476**(3): p. 537-549.

112. Li, S.S. and SpringerLink, *Semiconductor physical electronics*. 2006, New York: Springer.
113. Shi, J., W.E. Simon, and T.C. Zhu, *Modeling the instantaneous dose rate dependence of radiation diode detectors*. Medical physics, 2003. **30**(9): p. 2509-2519.
114. Thompson, M.T., Knovel, and Ebrary, *Intuitive Analog Circuit Design*. 2006, San Diego: Newnes.
115. Turner, J.E., *Atoms, radiation, and radiation protection*. 1992, New York: McGraw-Hill.
116. Grusell, E. and G. Rikner, *Evaluation of temperature effects in p-type silicon detectors*. Physics in Medicine and Biology, 1986. **31**(5): p. 527-534.
117. Moll, M., A. Barcz, K.M.H. Johansen, et al., *Development of radiation tolerant semiconductor detectors for the Super-LHC*. Nuclear Inst. and Methods in Physics Research, A, 2005. **546**(1): p. 99-107.
118. Wunstorf, R., H. Feick, E. Fretwurst, et al., *Damage-induced surface effects in silicon detectors*. Nuclear Instruments and Methods in Physics Research Section A: Accelerators, Spectrometers, Detectors and Associated Equipment, 1996. **377**(2): p. 290-297.
119. Fretwurst, E., A. Barcz, K.M.H. Johansen, et al., *Recent advancements in the development of radiation hard semiconductor detectors for S-LHC*. Nuclear Inst. and Methods in Physics Research, A, 2005. **552**(1): p. 7-19.
120. Fretwurst, E., G. Lindström, J. Stahl, et al., *Bulk damage effects in standard and oxygen-enriched silicon detectors induced by ⁶⁰Co-gamma radiation*. Nuclear Instruments and Methods in Physics Research Section A: Accelerators, Spectrometers, Detectors and Associated Equipment, 2003. **514**(1): p. 1-8.

121. Casati, M., M. Bruzzi, M. Bucciolini, et al., *Characterization of standard and oxygenated float zone Si diodes under radiotherapy beams*. Nuclear Inst. and Methods in Physics Research, A, 2005. **552**(1): p. 158-162.
122. Jursinic, P.A. and B.E. Nelms, *A 2-D diode array and analysis software for verification of intensity modulated radiation therapy delivery*. Medical Physics, 2003. **30**(5): p. 870-879.
123. Petasecca, M., F. Moscatelli, D. Passeri, et al., *Numerical simulation of radiation damage effects in p-type silicon detectors*. Nuclear Inst. and Methods in Physics Research, A, 2006. **563**(1): p. 192-195.
124. Bruzzi, M., *Radiation damage in silicon detectors for high-energy physics experiments*. Nuclear Science, IEEE Transactions on, 2001. **48**(4): p. 960-971.
125. Li, Z., *Radiation damage effects in Si materials and detectors and rad-hard Si detectors for SLHC*. Journal of Instrumentation, 2009. **4**(3): p. 1-31.
126. Dixon, R.L. and K.E. Ekstrand, *Silicon diode dosimetry*. The International Journal of Applied Radiation And Isotopes, 1982. **33**(11): p. 1171-1176.
127. Lindström, G., *Radiation damage in silicon detectors*. Nuclear Instruments and Methods in Physics Research Section A: Accelerators, Spectrometers, Detectors and Associated Equipment, 2003. **512**(1-2): p. 30-43.
128. Kuchinski, P., A. Petrunin, E. Savenok, et al., *The effect of impurities on the silicon detector's radiation hardness*. Nuclear Instruments and Methods in Physics Research Section A: Accelerators, Spectrometers, Detectors and Associated Equipment, 1997. **388**(3): p. 375-378.
129. Vayrynen, S. and J. Raisanen, *Effect of proton energy on damage generation in irradiated silicon*. Journal of Applied Physics, 2010. **107**(8): p. 0849030-084903-4.

130. Zhang, J., E. Fretwurst, R. Klanner, et al., *Investigation of X-ray induced radiation damage at the Si-SiO₂ interface of silicon sensors for the European XFEL*. Journal of Instrumentation, 2012. **7**(12): p. 1-11.
131. Moll, M., *Radiation tolerant semiconductor sensors for tracking detectors*. Nuclear Instruments and Methods in Physics Research Section A: Accelerators, Spectrometers, Detectors and Associated Equipment, 2006. **565**(1): p. 202-211.
132. Spieler, H. and Knovel, *Semiconductor detector systems*. 2005, New York: Oxford University Press.
133. Srour, J.R., C.J. Marshall, and P.W. Marshall. *Review of displacement damage effects in silicon devices*. IEEE Transactions on Nuclear Science, 2003. **50**(30) p. 653-670.
134. Wunstorff, R., *Radiation hardness of silicon detectors: Current status*. IEEE Transactions on Nuclear Science, 1997. **44**(3): p. 806-814.
135. Yoshida, S., T. Ohsugi, Y. Fukazawa, et al., *Radiation hardening of silicon strip detectors*. Nuclear Instruments and Methods in Physics Research Section A: Accelerators, Spectrometers, Detectors and Associated Equipment, 2003. **514**(1-3): p. 38-43.
136. Rosenfeld, A.B., M.I. Reinhard, D. Marinaro, et al. *A system for radiation damage monitoring*. IEEE Transactions on nuclear science, 1999. **46**(6): p. 1766-1773.
137. MacEvoy, B.C., G. Hall, and K. Gill, *Defect evolution in irradiated silicon detector material*. Nuclear Instruments and Methods in Physics Research Section A: Accelerators, Spectrometers, Detectors and Associated Equipment, 1996. **374**(1): p. 12-26.
138. Dąbrowski, W., *Radiation damage in Si detectors and front-end electronics*. Nuclear Physics B, 1995. **44**(1): p. 463-467.

139. Holmes-Siedle, A.G. and L. Adams, *Handbook of radiation effects*. 2001, Oxford: Oxford University Press.
140. Braunig, D. and F. Wulf, *Atomic Displacement and Total Ionizing Dose Damage in Semiconductors*. Radiation Physics and Chemistry, 1994. **43**(1): p. 105-127.
141. Borchì, E. and M. Bruzzi, *Radiation-Damage in Silicon Detectors*. Rivista Del Nuovo Cimento, 1994. **17**(11): p. 1-63.
142. Bruzzi, M., M. Bucciolini, M. Casati, et al., *Epitaxial silicon devices for dosimetry applications*. Applied Physics Letters, 2007. **90**(17): p. 1721090-1721093.
143. Lari, T., *Radiation hardness studies of silicon pixel detectors*. Nuclear Instruments and Methods in Physics Research Section A: Accelerators, Spectrometers, Detectors and Associated Equipment, 2006. **560**(1): p. 93-97.
144. Pintilie, I., G. Lindstroem, A. Junkes, et al., *Radiation-induced point- and cluster-related defects with strong impact on damage properties of silicon detectors*. Nuclear Instruments and Methods in Physics Research Section A: Accelerators, Spectrometers, Detectors and Associated Equipment, 2009. **611**(1): p. 52-68.
145. Moloi, S.J. and M. McPherson, *Current-voltage behaviour of Schottky diodes fabricated on p-type silicon for radiation hard detectors*. Physica B: Condensed Matter, 2009. **404**(16): p. 2251-2258.
146. Gill, K., G. Hall, S. Roe, et al., *Radiation-Damage by Neutrons and Photons to Silicon Detectors*. Nuclear Instruments & Methods in Physics Research Section A-Accelerators Spectrometers Detectors and Associated Equipment, 1992. **322**(2): p. 177-188.
147. Moll, M., E. Fretwurst, and G. Lindström, *Investigation on the improved radiation hardness of silicon detectors with high oxygen concentration*. Nuclear Instruments and Methods in Physics Research Section A:

Accelerators, Spectrometers, Detectors and Associated Equipment, 2000. **439**(2): p. 282-292.

148. Petasecca, M., F. Moscatelli, D. Passeri, et al. *Numerical Simulation of Radiation Damage Effects in p-Type and n-Type FZ Silicon Detectors*. IEEE Transactions on Nuclear Science, 2006. **53**(5): p. 2971-2976.
149. Schwank, J.R., M.R. Shaneyfelt, D.M. Fleetwood, et al. *Radiation Effects in MOS Oxides*. IEEE Transactions on Nuclear Science, 2008. **34**(4): p. 1833-1853.
150. Oldham, T.R. and F.B. McLean. *Total ionizing dose effects in MOS oxides and devices*. IEEE Transactions on Nuclear Science, 2003. **50**(3): p. 483-499.
151. Falcão, R.C., A. Facure, and A.X. Silva, *Neutron dose calculation at the maze entrance of medical linear accelerator rooms*. Radiation protection dosimetry, 2007. **123**(3): p. 283-287.
152. National Council on Radiation, P., C. *Neutron contamination from medical electron accelerators: recommendations of the National Council on Radiation Protection and Measurements*. 1984, The Council: Bethesda, Md.
153. Garnica-Garza, H.M., *Characteristics of the photoneutron contamination present in a high-energy radiotherapy treatment room*. Physics in Medicine and Biology, 2005. **50**(3): p. 531-539.
154. Kim, H.S. and J.K. Lee, *Assessment and Measurement of the Photoneutron Field Produced in the Varian Medical Linear Accelerator*. Journal of Nuclear Science and Technology, 2007. **44**(1): p. 95-101.
155. Stephen, F.K., M.H. Rebecca, S. Mohammad, et al., *Neutron spectra and dose equivalents calculated in tissue for high-energy radiation therapy*. Medical physics, 2009. **36**(4): p. 1244-1250.
156. Kry, S.F., M. Salehpour, D.S. Followill, et al., *Out-of-field photon and neutron dose equivalents from step-and-shoot intensity-modulated radiation*

- therapy*. International journal of radiation oncology, biology, physics, 2005. **62**(4): p. 1204-1216.
157. Hashemi, S.M., B. Hashemi-Malayeri, G. Raisali, et al., *The effect of field modifier blocks on the fast photoneutron dose equivalent from two high-energy medical linear accelerators*. Radiation protection dosimetry, 2008. **128**(3): p. 359-362.
 158. Petasecca, M., A. Bravin, V. Perevertaylo, et al., *X-Tream: a novel dosimetry system for Synchrotron Microbeam Radiation Therapy*. Journal of Instrumentation, 2012. **7**(7): p. 1-15.
 159. Mazza, G., R. Cirio, M. Donetti, et al. *A 64-Channel Wide Dynamic Range Charge Measurement ASIC for Strip and Pixel Ionization Detectors*. IEEE Transactions on Nuclear Science, 2005. **52**(4): p. 847-853.
 160. Mazza, G., F. Marchetto, V. Monaco, et al. *A large dynamic range charge measurement ASIC family for beam monitoring in radiotherapy applications*. IEEE Nuclear Science Symposium Conference Record, 2008. p. 1077-1080.
 161. Brusasco, C., M. Ruspa, A. Solano, et al., *Strip ionization chambers as 3-D detector for hadron therapy*. Nuclear Inst. and Methods in Physics Research, A, 1997. **389**(3): p. 499-512.
 162. Sze, S.M., K.K. Ng, *Physics of semiconductor devices*. 2007, Hoboken, N.J: Wiley-Interscience.
 163. Francesco, d.E., N. Ravinder, T. Luigi, et al., *In-phantom dosimetry and spectrometry of photoneutrons from an 18 MV linear accelerator*. Medical physics, 1998. **25**(9): p. 1717-1724.
 164. Naseri, A. and A. Mesbahi, *A review on photoneutrons characteristics in radiation therapy with high-energy photon beams*. Reports of Practical Oncology & Radiotherapy, 2010. **15**(5): p. 138-144.

165. Howell, R.M., S.F. Kry, and E. Burgett, *Secondary neutron spectra from modern Varian, Siemens, and Elekta linacs with multileaf collimators*. Medical Physics, 2009. **36**(9): p. 4027-4038.
166. *Process and device simulation tools*. 2013. [Online]. Available: <http://www.synopsys.com/Tools/TCAD/Pages/default.aspx>.
167. Moll, M., *Radiation damage in silicon particle detectors*. Ph.D. dissertation, Hamburg Univ., Hamburg, Germany, 1999.
168. McLean, F.B., T.R. Oldham, and M.D. Harry Diamond Labs Adelphi, *Basic Mechanisms of Radiation Effects in Electronic Materials and Devices*. Technical Report, 1987.
169. McEvoy, B., *Defect kinetics in silicon detector material for applications at the Large Hadron Collider*, Ph.D. dissertation, Imperial College-Rutherford Laboratories, London, U.K., 1996.
170. Rikner, G. and E. Grusell, *General specifications for silicon semiconductors for use in radiation dosimetry*. Physics in Medicine and Biology, 1987. **32**(9): p. 1109-1117.
171. Kulikov, A.V., V.A. Perevoshchikov, V.D. Skupov, et al., *Low-temperature radiation-stimulated gettering of impurities and defects in silicon by layers of porous silicon*. Technical Physics Letters, 1997. **23**(7): p. 507-508.
172. Lai, S.K., *Interface trap generation in silicon dioxide when electrons are captured by trapped holes*. Journal of Applied Physics, 1983. **58**(5): p. 2540-2546.
173. Grusha, S.A., A.M. Evstigneev, K.A. Ismailov, et al., *Electric field effect on radiation-induced gettering of defects in n plus -n-n plus plus GaAs*. Physica Status Solidi (A) Applied Research, 1984. **86**(1): p. k83-k86.
174. Zhu, X.R., *Entrance dose measurements for in-vivo diode dosimetry: Comparison of correction factors for two types of commercial silicon diode*

- detectors*. Journal of Applied Clinical Medical Physics, 2000. **1**(3): p. 100-107.
175. Jornet, N., M. Ribas, and T. Eudaldo, *In vivo dosimetry: Intercomparison between p-type based and n-type based diodes for the 16–25 MV energy range*. Medical Physics, 2000. **27**(6): p. 1287-1293.
 176. Mishra, V., V.D. Srivastava, and S.K. Kataria, *Role of guard rings in improving the performance of silicon detectors*. Indian Academy of Sciences, 2005. **65**(2): p. 259-272.
 177. Blankenship, J.L. and C.J. Borkowski, *Silicon Surface-Barrier Nuclear Particle Spectrometer*. IRE Transactions on Nuclear Science, 1960. **7**(2-3): p. 190-195.
 178. Nagai, K., T. Sekigawa, and Y. Hayashi, *Capacitance-voltage characteristics of Semiconductor-Insulator-Semiconductor (SIS) structure*. Solid State Electronics, 1985. **28**(8): p. 789-798.
 179. Aldosari, A.H., A. Espinoza, D. Robinson, et al., *Characterization of an Innovative p-type Epitaxial Diode for Dosimetry in Modern External Beam Radiotherapy*. Nuclear Science, IEEE Transactions on, 2013. **60**(6): p. 4705-4712.
 180. Texas Instruments, *64 Channel Analog Front End for Digital X-Ray Detector*. <http://www.ti.com/lit/ds/symlink/afe0064.pdf>. September 2009.
 181. Fuduli, I., M.K. Newall, A.A. Espinoza, et al., *Multichannel Data Acquisition System comparison for Quality Assurance in external beam radiation therapy*. Radtion measurements, 2014. **71**: p. 338-341.
 182. David, W., X.A. Li, C. Joanna, et al., *The effect of dose rate dependence of p-type silicon detectors on linac relative dosimetry*. Medical physics, 1997. **24**(6): p. 879-881.

183. Saini, A.S. and T.C. Zhu, *Dose rate and SDD dependence of commercially available diode detectors*. Medical Physics, 2004. **31**(4): p. 914-924.
184. Butson, M.J., T. Cheung, and P.K.N. Yu, *Scanning orientation effects on Gafchromic EBT film dosimetry*. Australasian Physics & Engineering Sciences in Medicine, 2006. **29**(3): p. 281-284.
185. Andrés, C., A. del Castillo, R. Tortosa, et al., *A comprehensive study of the Gafchromic EBT2 radiochromic film. A comparison with EBT*. Medical physics, 2010. **37**(12): p. 6271-6278.
186. Qi, Z.-Y., P. Metcalfe, A. Rosenfeld, et al., *In vivo verification of superficial dose for head and neck treatments using intensity-modulated techniques*. Medical Physics, 2009. **36**(1): p. 59-70.
187. Sauer, A. and J. Wilbert, *Measurement of output factors for small photon beams*. Medical Physics, 2007. **34**(6): p. 1983-1988.
188. Charles, P.H., C.M. Langton, J.V. Trapp, et al., *The effect of very small air gaps on small field dosimetry*. Physics in medicine and biology, 2012. **57**(21): p. 6947-6960.
189. Charles, P.H., S.B. Crowe, T. Kairn, et al., *Monte Carlo-based diode design for correction-less small field dosimetry*. Physics in Medicine and Biology, 2013. **58**(13): p. 4501-4512.
190. Takahashi, Y. and S.K. Hui, *Fast, simple, and informative patient-specific dose verification method for intensity modulated total marrow irradiation with helical tomotherapy*. Radiation oncology, 2014. **9**(1): p. 34-34.
191. "http://www.analog.com/static/imported-files/data_sheets/ADIS16209.pdf," Analog Device, 7 2012. [Online]. [Accessed 13 01 2014].
192. "http://www.sick-automation.ru/images/File/pdf/DIV01/atm60_atm90.pdf," Sick Stegmann. [Online]. [Accessed 13 01 2014].

193. "http://www.geckodrive.com/gecko/images/cms_files/G203V-REV-7-MANUAL.pdf," Gecko, 07 01 2010. [Online]. [Accessed 13 01 2014].
194. "http://en.wikipedia.org/wiki/Ziegler%E2%80%93Nichols_method," 28 02 2014. [Online]. [Accessed 31 03 2014].
195. Huang, K., J.W.S. Bice, and O. Hidalgo-Salvatierra, *Characterization of an in vivo diode dosimetry system for clinical use*. Journal of applied clinical medical physics / American College of Medical Physics, 2003. **4**(2): p. 132-142.
196. Agostinelli, S., G. Barrant, S. Sei, et al., *Geant4 - A simulation toolkit*. Nuclear Instruments and Methods in Physics Research Section A: Accelerators, Spectrometers, Detectors and Associated Equipment, 2003. **506**. p. 250-303.
197. BM, O., W. M, B. M, et al., *IMRT treatment Monitor Unit verification using absolute calibrated BEAMnrc and Geant4 Monte Carlo simulations*, Journal of Physics: Conference Series. 2014, **489**. p. 012020-012026.
198. Keall, P.J., E. Colvill, R. O'Brien, et al., *The first clinical implementation of electromagnetic transponder-guided MLC tracking*. Medical Physics, 2014. **41**(2): p. 1-5.
199. Mate, T.P., D. Krag, J.N. Wright, et al., *A new system to perform continuous target tracking for radiation and surgery using non-ionizing alternating current electromagnetics*. International Congress Series, 2004. **1268**: p. 425-430.
200. Pommer, T., M. Falk, P.R. Poulsen, et al., *Dosimetric benefit of DMLC tracking for conventional and sub-volume boosted prostate intensity-modulated arc radiotherapy*. Physics in medicine and biology, 2013. **58**(7): p. 2349-2361.
201. Keall, P.J., A. Sawant, B. Cho, et al., *Electromagnetic-Guided Dynamic Multileaf Collimator Tracking Enables Motion Management for Intensity-*

Modulated Arc Therapy. International Journal of Radiation Oncology, Biology and Physics, 2011. **79**(1): p. 312-320.

202. Foland, A.D., J.P. Alexander, P.I. Hopman, et al., *Radiation-induced surface leakage currents in silicon microstrip detectors*. IEEE Transactions on Nuclear Science, 1996. **43**(3): p. 1746-1750.
203. Derrico, F., B.M. Luszik, R. Nath, et al., *Depth dose-equivalent and effective energies of photoneutrons generated by 6-18 MV X-ray beams for radoptherapy*. Health Physics, 2001. **80**(1): p. 4-11.

APPENDIX A

An example of the scripting code used to simulate the electric field and space charge distribution of the EPI diodes as a function of the radiation damage by means of Synopsys TCAD Dessis as discussed in Chapter 3 is shown below:

```
Device EpitaxialDiode2D {
File      {Grid = "EpiDiode2D_CCE2_msh.tdr"
           Current = "epi2D"
           Plot = "epi2D"
           # Output = "epi2D"}

Electrode { {Name="P+back" Voltage=0.0 }
            {Name="P+top" Voltage=0.0 }
            {Name="N+" Voltage=0.0 }}

Physics      {Temperature=300
              Mobility (Doping Dependence HighFieldsat Enormal)
              Recombination (SRH (Doping Dependence))
#Scharfetter model for life time
              # HeavyIon(
              # Let_f=1.3e-5
              # Length=20e-4
              # Wt_hi=10e-6
              # Time=2.5e-9
              # Location=(x,y,z)
              # Direction=(x,y,z)
              # PicoCoulomb
              EffectiveIntrinsicDensity(Bennett)}
Physics (Material="Silicon")      {Traps ((Acceptor      Level
EnergyMid=0.42 fromCondBand
              Conc = 1.613e10 eXsection=2e-15 hXsection=2e-14)
              (Donor Level EnergyMid=0.36 fromCondBand
              Conc = 0.9e10 eXsection=2.5e-14 hXsection=2.5e-15))}

Physics (Material="Oxide") {charge(conc=5e9)}
Physics (MaterialInterface="Oxide/Silicon") {Traps (FixedCharge
Conc=5e9) }}

System      {EpitaxialDiode2D      trans      ("P+back"=nanode
"P+top"=nanode "N+"=ncatode)
              Vsource_pset v1 (ncatode 0) {dc=0}
              Vsource_pset v2 (nanode 0) {dc=0}}

Plot {eDensityhDensityCurrentPotentialPotentialElectricField
DonorConcentrationAcceptorConcentrationDoping
HeavyIonChargeDensitySpaceChargeeTrappedCharge hTrappedCharge
eCurrent hCurrent TotalCurrentDensity}
```

```

Math      {# parallelization on multi-CPU machine
          Number_Of_Threads = 4
          Digits=5
          Iterations=50
          NotDamped=50
          Method=Blocked
#          Method=ILS
          Submethod=Pardiso
          Extrapolate
          Derivatives
          #AvalDerivatives
          RelErrControl
          Erreff(electron)=1e3
          Erreff(hole)=1e3DirectCurrent}
Solve     {Coupled (Iterations=100){ Poisson }
          Coupled { poisson electron hole }
          Quasistationary (Goal {Parameter=v2.dc Voltage=0}
          Maxstep=0.01 Minstep=1.e-9 InitialStep=1.e-5)
          {Coupled          {Poisson Electron Hole}
          #Plot(Time=(0; 0.2; 0.45; 0.5; 0.65; 0.8; 0.95; 1)
          NoOverwrite)}
          Save(FilePrefix="QuasiStat_0V") }

```